2015

An investigation into the effect of interruptions on cathodic arc plasma deposited TiN films for machining applications, and the development of a cutting test method under controlled atmosphere

Theo Finley Sinkovits

University of Wollongong

An investigation into the effect of interruptions on cathodic arc plasma deposited TiN films for machining applications, and the development of a cutting test method under controlled atmosphere.

A thesis submitted in fulfilment of the requirements for the award of the degree

Doctor of Philosophy

From

UNIVERSITY OF WOLLONGONG

By

Theo Finley Sinkovits BEng. (Mech), GCert. BA

School of Mechanical, Mechatronics & Materials Engineering

2015

Acknowledgements.

I would like to acknowledge my supervisor Dr. Yue Zhao for his generous support, perseverance, and for allowing me the right of investigative freedom. I also thank the people and organisations named below.

The Defence Materials Technology Centre for funding the project. I must thank Professor Huijun Li for bringing me into the group.

The team at Sutton Tools and associates from the Royal Melbourne Institute of Technology. Co-supervisor Dr. Steve Dowey for his guidance in industry relevant research for metal cutting, and fixations with the use of appropriate statistical analysis techniques. Jimmy Toton for his kindness in sharing his knowledge of drill tests and conducting the tests shown here, as well as Dr. Antony Pilkington for a better understanding of vapour deposited film growth. In particular Professor Derry Doyle for offering many hours of his time to long and enthralling discussions about metal cutting physics, discussions that framed and guided experiments on chip formation conducted here.

Facilities within and members of the UOW Electron Microscope Centre. Dr. Azdiar Gazder and Dr. Ahmed Saleh for help with EBSD, and for their fascinating and fruitful conversations in times of need. Dr. Mitchell Nancarrow for his expertise in electron spectroscopy, and Dr. David Mitchell for making TEM accessible.

Undergraduate students who helped with experiments: Aaron Chhua, Dominic Gralton, Joel Ovington and especially Rebecca O'Brien.

My ever supportive parents Tom and Anthea; their positive (and negative) reinforcement assisted in many ways. My partner Loulou for supporting me during final editions. Lastly, my sister Jade for her encouragement to write and her meticulous edits.

Abstract.

There has been increased interest in hard coatings from the metal cutting industry in recent times and research has covered many new avenues for improvement. Methods for hard coating design cover improvements to hardness with microstructure and defect density control, elemental selection for oxidation resistance, layered structures, and nanostructures.

In the literature, interruptions during growth of physical vapour deposited films have been used to modify and control stresses to better understand the mechanisms that generate stress during growth. Experiments have covered lower energy systems such as thermal evaporation and some higher energy systems like magnetron sputtering, and have included monitoring stress in-situ. Investigations are made in ultra-high vacuum, with high purity targets to eliminate the influence of impurities on growth mechanisms and stress generation, allowing for less ambiguity in conclusions.

The influence of interruptions during cathodic arc plasma deposition (CAPD) on residual film properties, in high vacuum reactive environments, using commercial purity targets are not explored in the literature. It is beneficial to investigate this as an avenue for coating improvement for commercial use in metal cutting applications. In this work the effect of interruptions during CAPD of TiN, on film microstructure and mechanical properties are investigated.

Mechanical testing of interrupted TiN films consisted of nanoindentation for hardness, scratch testing for adhesion, and drill testing. With the introduction of interruptions, coating performance improved in indentation hardness and drill testing, and scratch tests remained inconclusive.

Film microstructure was closely examined with X-ray diffraction (XRD) residual stress analysis, X-ray photoelectron spectroscopy (XPS), electron backscatter diffraction (EBSD), transmission electron microscopy (TEM) diffraction and energy dispersive spectroscopy, and XRD characterisation with Rietveld analysis and glancing angle XRD.

Improvements in coated high-speed steel drill life were measured and linked to an increase in hardness. No obvious changes to microstructure, to explain improvements, were noticed

in electron microscopy. The combination of two stress analysis techniques revealed an increase in defects with the introduction of interruptions during film growth.

Crystallographic evidence of a segregated phase of ferrite was found in all TiN films. Glancing angle XRD showed an increased volume fraction of ferrite with the introduction of nine 5 minute long interruptions. Spectroscopy in the scanning electron microscope was incapable of providing chemical evidence of Fe due to groupings being too small, however TEM provided some chemical evidence of Fe. The source of Fe is most likely to be from commercially pure (Grade 2) Ti targets that contain a maximum of 0.3 % Fe impurity.

Gibbs free energy calculations and the ternary phase diagram of a Ti-Fe-N system explain that the ferrite phase is immiscible in TiN. Interruptions provide the right conditions and enough time for additional Fe segregation in the TiN lattice, and interruptions can allow higher diffusions rates of Fe along the free surface of the sample inside the vacuum chamber.

An increased interfacial strain component provided by the segregation of the secondary Fe phase is linked to the measured increase in hardness and compressive strain. Fe inclusions are likely to have a positive influence on hindering dislocation motion in the TiN lattice, accommodating strain, providing a modulated strain field. These factors increased the lifetime of coated high-speed steel drills.

While understanding coating performance improvement is critical, it is as important to develop a reliable cutting test methodology to test industrial cutting processes. Systematic control must be available to examine the effects of cutting parameters, tools, coatings and their reaction with atmosphere. A test designed to balance between real industrial practices and scientific experimentation was developed to assist in answering questions. Face milling tests showed some interesting results and controlled atmospheres has an influence on tool life for TiN and TiAlN coated tools. Control of the cutting environment was possible with Ar gas supplied, enabling comparative observations of oxidation resistance of coatings. However, analysis of cutting tools and chips was complex due to the dynamic tool and chip conditions of face milling.

An orthogonal cutting test using a lathe, with substantial cutting distances at industry practice cutting speeds and depths of cut, was developed to provide a testing system capable of filling the middle ground between industrial and scientific demands. The design also incorporated a quick-stop device to allow for examination of any changes to chip formation.

TiN coating performance in orthogonal cutting of Ti6Al4V was dependent on levels of oxygen. Tool wear was reduced with Ar supplied, possibly due to less oxidation of the film. No comparison with TiAlN in different atmospheric conditions was possible as the coating was completely removed with both samples.

Crystallographic analysis of quick-stopped Ti6Al4V chips, from observations made in EBSD, showed an inconsistent chip formation mechanism for both TiN and TiAlN coatings in Ar and compressed air atmospheres. Segmental and continuous deformation was visible within a single chip cut at a cutting speed of 50 m/min and this formation behaviour of Ti6Al4V was independent of oxygen levels, although some critical areas were unresolved with EBSD. Changes to atmosphere will most likely change deformation in the secondary shear zone as the chip is highly reactive when exposed to atmosphere, however, EBSD was unable to resolve crystallography in these areas due to high levels of deformation. Various deformation mechanisms were noticed in Ti6Al4V chip formation including: crystal rotation and twinning. Further work is required to take full advantage of the results obtained.

Table of Contents

Glossary of Terms.

AE	Acoustic Emission
ANOVA	Analysis of Variance
CAPD	Cathodic Arc Plasma Deposition
CGM	Crystallite Group Method
CNC	Computer Numerically Controlled
CVD	Chemical Vapour Deposition
EBSD	Electron Backscatter Diffraction
EDS	Energy-dispersive X-Ray Spectroscopy
EELS	Electron Energy Loss Spectroscopy
FIB	Focussed Ion Beam
HSS	High-Speed Steel
INT	Interrupted
IPF	Inverse Pole Figure
L_c	Critical Load
PVD	Physical Vapour Deposition
SAD	Selected Area Diffraction
SEM	Scanning Electron Microscope
STD	Standard
TEM	Transmission Electron Microscope
XPS	X-Ray Photoelectron Spectroscopy
XRD	X-Ray Diffraction

1. Introduction.

Metal cutting is a very important process in the production and manufacturing environment. It involves the removal of unwanted material to provide a component of desired dimension with appropriate tolerances and surface finish. Ideally this is completed at efficient speeds, allowing for a cost effective product. Costs in the production environment involve a balance of equipment and labour, maintenance (including tool changes), and cutting tools. As cutting speeds increase, the cost of cutting tools becomes increasingly important. Improving the lifetime and operating speeds of cutting tools can allow for a shift of the optimal cost of production to the right of Figure 1.1, thereby increasing productivity and profitability.

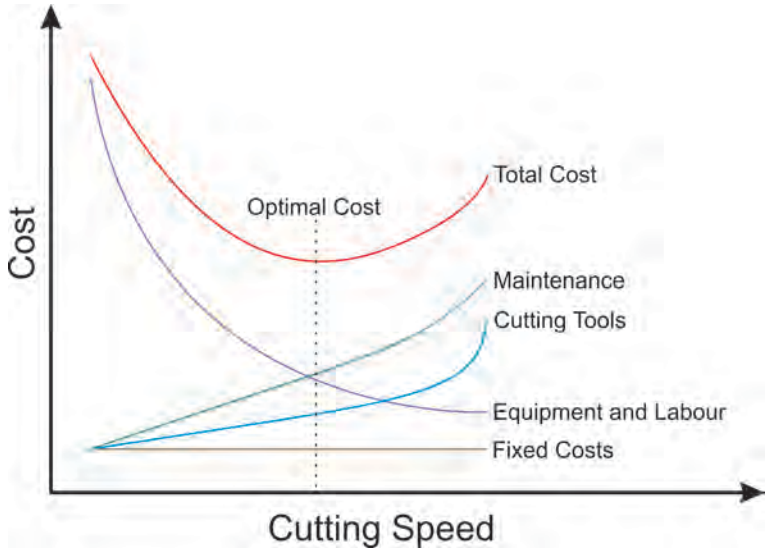

Figure 1.1: Dependence of machining costs on cutting speed. Adapted from [1]

The performance of tools depends on many factors some of which include: geometry, edge preparation (honing), roughness, and machine system properties such as stiffness, vibration characteristics and cutting fluids. These are extremely vital to the tool designer and machine operator but for the materials engineer, more recent developments in the application of hard coatings for cutting tools are of huge interest for the expansion of safe operating conditions for tools. To put their importance into perspective, approximately 90% of indexable cemented carbide inserts are coated for wear protection, 25 % of which are produced by physical vapour deposition (PVD) and the remainder by chemical vapour deposition (CVD) [2].

Other shank design tools such as end mills, drills and taps are commonly protected with hard coatings, mostly cemented carbide tools and especially those used for high speed and difficult-to-machine material applications. Difficult-to-machine workpiece materials can include Ti and Ni based alloys that exhibit dramatic work hardening and possess stability at high temperatures. The result of cutting these alloys is dramatic tool wear, and the essential requirement for coatings capable of protecting tools. High-speed steel (HSS) tools are also coated, but typically with films that have a similar ceiling for safe operation. The combination of TiN films on HSS substrates is very common for low speed tools such as spotting drills, taps and jobber drills.

Many coating architectures exist in the research literature however few of these laboratory tested designs translate to the commercial coated tool market due to difficulties in scaling up deposition technologies. An example being plasma-assisted chemical vapour deposition (PACVD) [1], which does have commercial deposition systems, but is a good example of a process difficult to upscale and commercialise. Other difficulties stem from the need to test coatings in controlled laboratory environments and with simple substrates in order to obtain data that is capable of allowing conclusions to be made for peer reviewed articles. Once the coatings experience real machining conditions at industrial operating speeds, they can fail to show the improvements observed in the laboratory. Not only are the practicalities of coating design important, but there must be a market for the product and it must be in the interest of the tool manufacturer to invest in its release. Attempts in overcoming these problems are made here by modifying industry standard deposition processes only very slightly to alter film microstructures, and by testing coatings on commonly used substrates, like HSS and cemented carbide, at typical cutting conditions. Laboratory techniques are also used to measure film properties, in an attempt to explain the source of improvements. Other areas such as tool geometry, edge preparation, machine system properties, substrate cleaning prior to deposition and in chamber cleaning are not examined.

Interruptions during film growth of low energy thermally evaporated and sputtered films have been used to understand in-situ stress development [3-10]. In-situ measurements of stress during high energy magnetron sputtering of TiN show some similarities [11] but observations of the effect of interruptions during cathodic arc plasma deposition (CAPD) of

TiN, on in-situ or residual film properties, have not been conducted to date. It is of interest to understand the effect of interruptions on the mechanical properties (particularly those important to metal cutting) and microstructure of CAPD TiN. The deposition process of a CAPD system, used for the large-scale deposition of coatings for cutting tools, is modified with the introduction of interruptions to the arc plasma producing process. Efforts are made to link improved mechanical properties to microstructure through careful analysis with X-ray diffraction (XRD) and electron microscopy.

Cutting tests are vital for hard research into coatings intended for tolling applications. They enable observations to be made at conditions of a tool and coating's intended application. A test designed to balance between real industrial practices and scientific experimentation was developed. The 3-dimensional process can be abridged into a 2-dimensional and more controlled process, commonly referred to as orthogonal cutting. The second part of this work covers the development of a cutting test that provides some medium ground between laboratory research and real industrial operating conditions. A controlled environment is used to provide conclusions about the effect of oxidation on the performance of TiN and TiAlN coated tools. The test also provided observation of Ti6Al4V chip formation, allowing for the possibility to study changes to coating performance stemming from changes to deformation mechanisms. The test rig can be used for many combinations of workpiece, tool and cutting atmosphere experiments in the future.

2. Literature Review.

The following literature review will cover the areas relevant to hard coating design for metal cutting applications, from chip and tool interactions to a detailed explanation of films used for protection, their deposition and microstructures.

2.1. Metal cutting.

Scientific knowledge in the area of metal cutting is, due to its complexity, relatively under developed. The process of metal cutting is best explained from a 2-dimensional point of view, via the orthogonal cutting model (Figure 2.1).

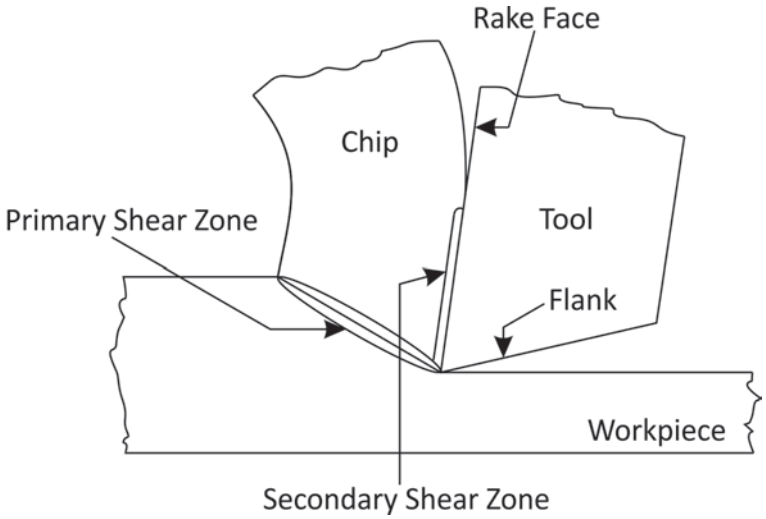

Figure 2.1: Schematic of the orthogonal cutting model displaying the two shear zones.

As the cutting tool is forced into the workpiece, the material deforms via shear as it crosses the primary shear zone and a chip is formed. As it progresses from the cutting edge, along the rake face until it curves away from the tool, the chip experiences a second shear force due to friction between the chip and rake face. Strain rates and temperatures are very high. Moreover, the interface between the rake face of a cutting tool and the newly formed chip is unique. The real and apparent areas of contact are indistinguishable from one another therefore Coulomb friction laws do not apply.

Research on tool and chip interfaces has been contradictory and findings are only in recent years consolidating. Initially, there were two opposing views of how the tool and workpiece interact during machining - the conclusions drawn were dependent on the method of observation chosen. One view is based on microscopy of chip-tool interfaces after rapid

separation during machining [12-14]. The rapid separation technique, or quick-stop experiment, concludes there is a sticking region close to the tool tip where the chip is atomically bonded, through intimate contact, at the interface. The velocity of the chip increases further from the tool rake face until it reaches a bulk chip velocity. As the chip progresses away from the cutting edge (along the rake face) it begins to slide.

The second, and contradictory, view was found by observing the interface in-situ using a transparent tool. It is suggested there are two zones, one of sliding near the cutting edge followed by sticking [15-18].

2.1.1. Trent, Wright and the quick-stop experiment.

Trent and Wright et al [12-14, 19] developed a theory of seizure at the rake face and chip interface based on quick-stop experiments and metallographic analysis of machining of metals at low rake angles. The quick-stop technique is the rapid deceleration of the cutting tool during metal cutting. The workpiece, tool and chip are then examined using optical and electron microscopy. The cutting tool has been observed with parts of the chip material atomically bonded to the rake face indicating *seizure* – complete and intimate contact. Cross-sectional observations show massive deformation of the chip, particularly in the secondary shear zone. This is caused by seizure of the chip and no movement at the rake face, but a gradually increasing chip velocity further from the interface due to deformation (see Figure 2.2). Scanning electron microscope (SEM) images of the tool side of the chip after a quick-stop experiment show no sliding marks, rather a detailed image of groove marks from the tool. This indicates no movement of the chip at the interface. This behaviour was even displayed when a low bonding strength TiN coating existed between chip and tool.

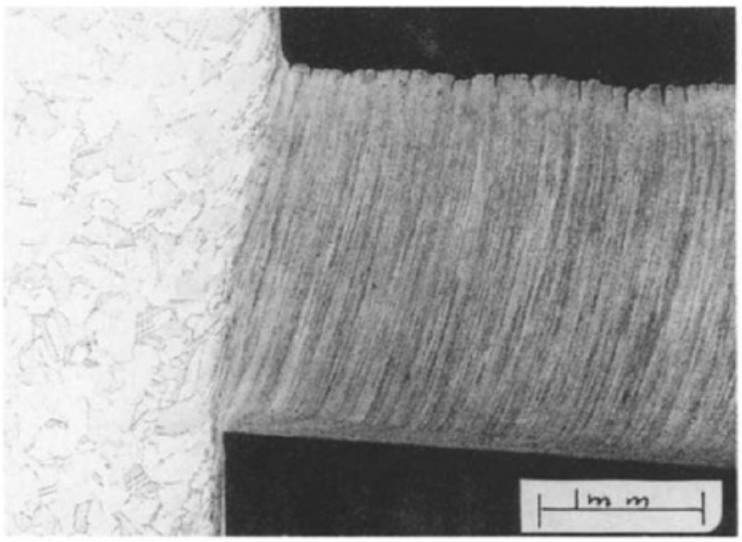

Figure 2.2: Cross-section image of a quick-stop sample prepared during orthogonal cutting of Cu at 122 m/min, showing seizure and massive deformation at the tool interface. Taken from [13]

2.1.2. The transparent tool.

In the work by Doyle *et al* [15], a transparent sapphire cutting tool was used to provide an image of the rake face and chip interface. The tool, and its application, is shown in Figure 2.3. A planing machine with a stroke of 250 mm was capable of forcing the tool over a workpiece at speeds of 0.3 to 30 m/min in a controlled gas environment (max vacuum of < 10^{-4} Pa). This apparatus enabled the *in-situ* observation of the metal cutting process. Some controversial evidence was discovered that questioned the theory of seizure.

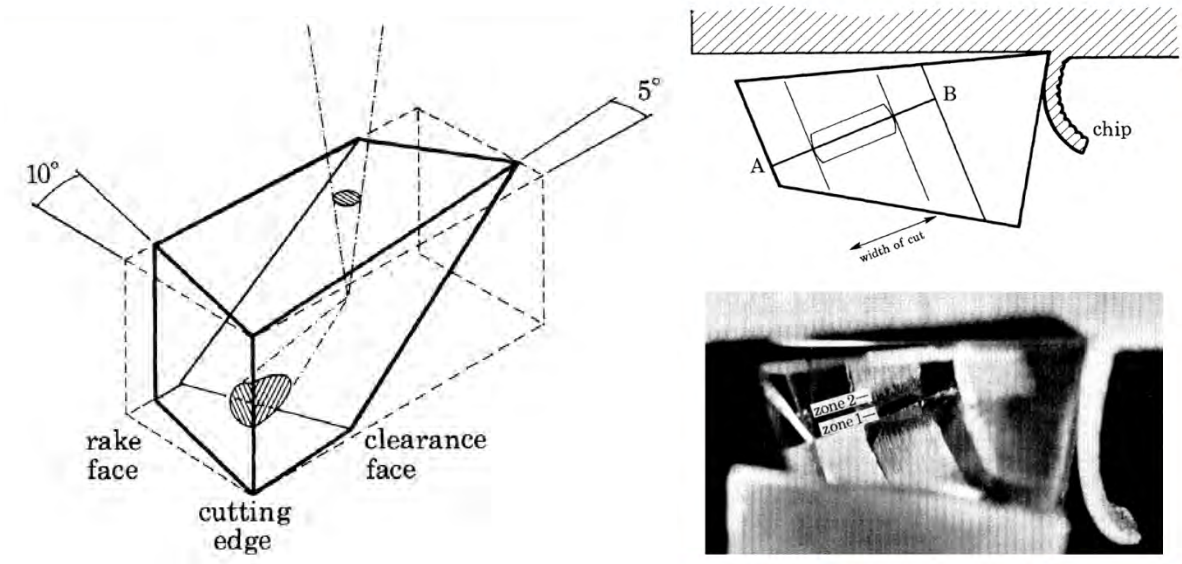

Figure 2.3: Transparent cutting tool, showing internal reflection of the chip-rake interface. Taken from [15].

Two zones were identified and are illustrated in Figure 2.4 and are described below.

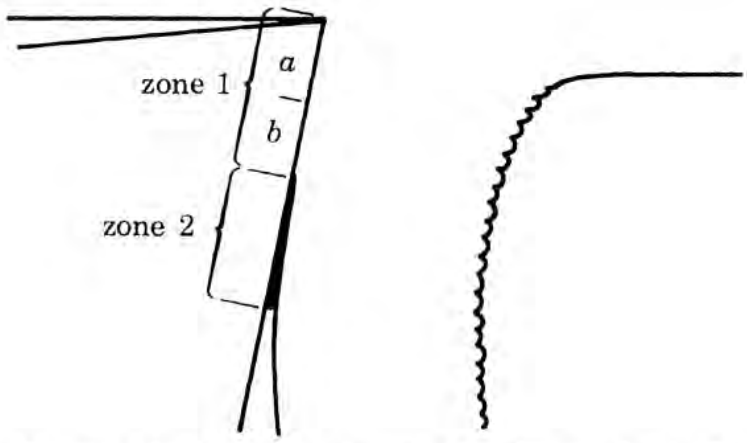

Figure 2.4: Zones 1 and 2 defined by Doyle et al [15].

Zone 1: Sliding

Zone 1a – High normal force (to the rake face) provides contact between the workpiece and tool. No abrasive wear was evident in this region when the sapphire tool is coated with a 50 µm Cu film that remained after use. Relative movement at the interface was observed.
Zone 1b – The reduced normal force in this region allows for sliding to occur and subsequent wear (commonly referred to as crater wear) of the Cu film was evident.

Zone 2: Sticking

Exposure to the atmosphere brings increased adhesion of the chip to the tool due to rapid oxidation of the newly created surface and hence increases friction, accelerating the sticking process. Sticking in this zone was non-existent when machining in vacuum, N or Ar atmospheres. This indicates the reactions at Zone 2 rely on the presence of oxygen. Furthermore, these reactions were dependent on the partial pressure of oxygen when cutting Al (Figure 2.5).

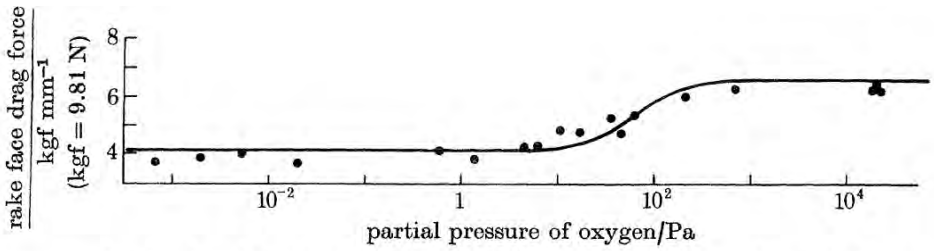

Figure 2.5: Variation in rake face drag force with changes to oxygen partial pressure when machining Al. Taken from [15].

Madhaven *et al* [17] used a transparent sapphire and glass tool to cut pure Pb, Al and Cu at speeds between 0.1 and 5 mm/second in another experiment. The tools used had rake angles between +20 and -30 degrees. With the use of high-speed cameras and optical microscopes the cutting process was captured at 30 frames per second with a resolution greater than 2 µm. The high-speed cameras enabled the confirmation of a sliding region close to the cutting edge by the movement of asperities along the rake face between frames. No difference in velocity at the interface and velocity of the bulk of the chip was discernable.

Results strongly supported the work by Doyle *et al*, however the two zones were redefined as shown in Figure 2.6 (c). Madhavan *et al* found it was more suitable to define Zone 1b as Zone 2a because this point indicates the beginning of the 'sticking' region. Zone 2b was differentiated from Zone 2a by the deposition of gross particles on the rake face. Madhavan *et al* believed it more appropriate to separate Zone 1 and 2 by the conditions of contact of the chip to the tool whereby Zone 1 is intimate contact and Zone 2 is separation of the tool and chip and exposure to the atmosphere.

Madhavan *et al* summarises chip tool interactions. If the shear strength of the interface is smaller than the bulk shear strength of the chip then sliding will occur. When the environment influences and increases the shear strength of the interface, sticking will result. This can be seen at the edges of orthogonal cuts where sticking occurs due to atmospheric exposure of the chip. Doyle *et al* had difficulty explaining the wear in their Zone 1b because of a lack of atmospheric interactions, however with Madhavan *et al's* reclassification to Zone 2 (access to atmosphere) this uncertainty is clarified. There is access to oxygen and the chip begins to have increase adhesion to the rake face.

Madhavan *et al* used intermittent cutting experiments, exposing the newly formed rake face to the atmosphere and allowing temperature to reduce, to see if access to atmosphere played any role in sticking. Zone 1 sticking was however not observed. This leads to the conclusion that perhaps something else causes sticking to occur. Perhaps deformation in the secondary shear zone causes work hardening, increasing its potential for brittle failure of the chip near the interface and subsequent shifting of the shear zone to this area, away from the interface. Leaving behind the work hardened material at the interface as a deposit.

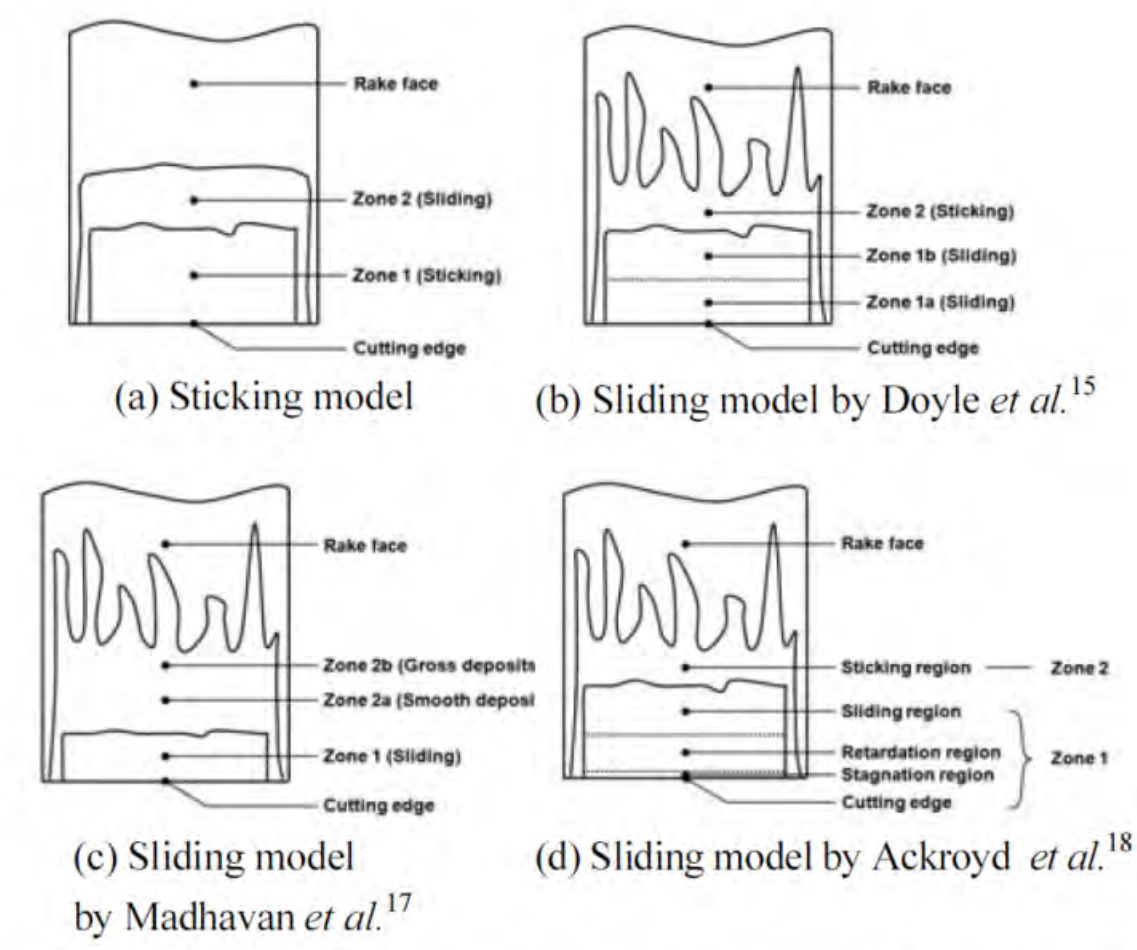

Figure 2.6: Four different zone models proposed. Taken from [20]

Ackroyd *et al* provided an additional sliding model as shown in Figure 2.6 (d). During negative rake observations (-5 degrees) during the cutting of Pb, Ackroyd *et al* noticed asperities moving along the rake face with increasing velocity as the cutting tool progressed away from the cutting edge [16]. Also a stagnation region was observed close to the cutting edge. In initial stages of cutting, some of the workpiece material was transferred to the tool

and remained there for the duration of the test. The deposit was believed to be the source of asperities seen to accelerate as the cutting tool moved away from the cutting edge. Another model of the chip-tool contact conditions was derived that compliments the theory of seizure (Figure 2.7). This adds to the confusion of findings of chip-tool interactions, but Ackroyd *et al* were capable of clarifying one ongoing justification for seizure.

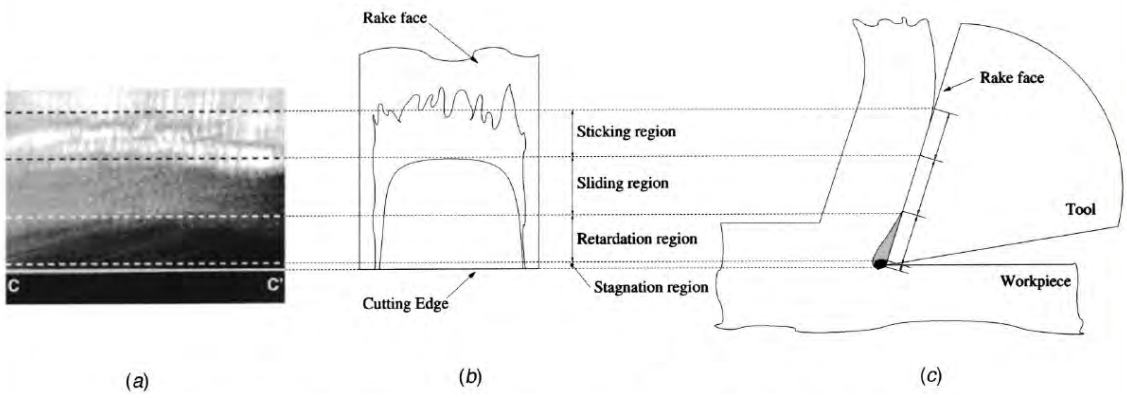

Figure 2.7: Chip-tool contact model proposed. Taken from [16].

Ackroyd *et al* contrasted scarring of the rake face of sapphire and Al tools at cutting speeds of 1 and 10 mm/second (Figure 2.8) and found the intimate contact region and region of metal deposition are almost identical for both tools. This was observed to counter Trent's argument that rake face wear will be different for sapphire and Al tools. It was insisted that seizure is less likely to occur when the tool and chip are so dissimilar in composition; steel and carbide tools are more likely to bond with Pb, Al and Cu workpieces than sapphire. This suggests that mechanisms seen on sapphire tools are a good representation of what is occurring during metal cutting on non-transparent tools, however a comparison with tool steels, carbide tools, and coated tools is not made.

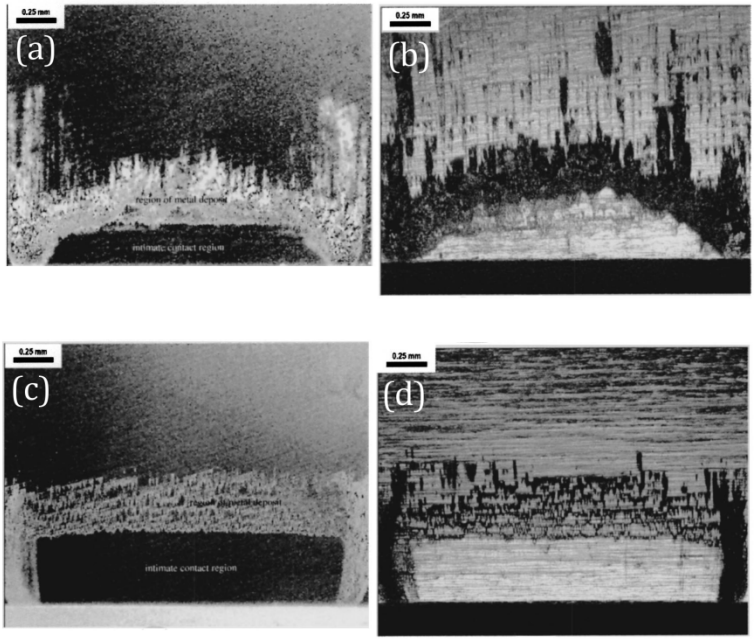

Figure 2.8: Rake face of cutting tools after 50 mm of cutting pure Pb. (a) and (c) are sapphire tools cut at 0.06 and 0.6 m/min respectively. (b) and (d) are Al tools cut at 0.06 and 0.6 m/min respectively. Figures show similarities in rake face and chip interactions despite very different tool materials. Images taken from [16]

More recently, and somewhat more conclusively, Hwang and Chandrasekar [20] performed orthogonal cutting with a sapphire tool and a high-speed photographic imaging system. They concluded that sticking, sliding and stagnation were dependent on workpiece material. Contact conditions were classified into three types (see Figure 2.9);

- Type 1 (sliding-sticking) – seen when cutting Cu and brass;
- Type 2 (stagnant material-sliding-sticking) – observed when cutting Pb and Al-1100 and;
- Type 3 (expanding zone of stagnant material) – found when cutting Al-6060-T6 and Al-Si alloys.

Figure 2.10 shows the observed chip velocities as a distance from the cutting edge, along the rake face, for different materials.

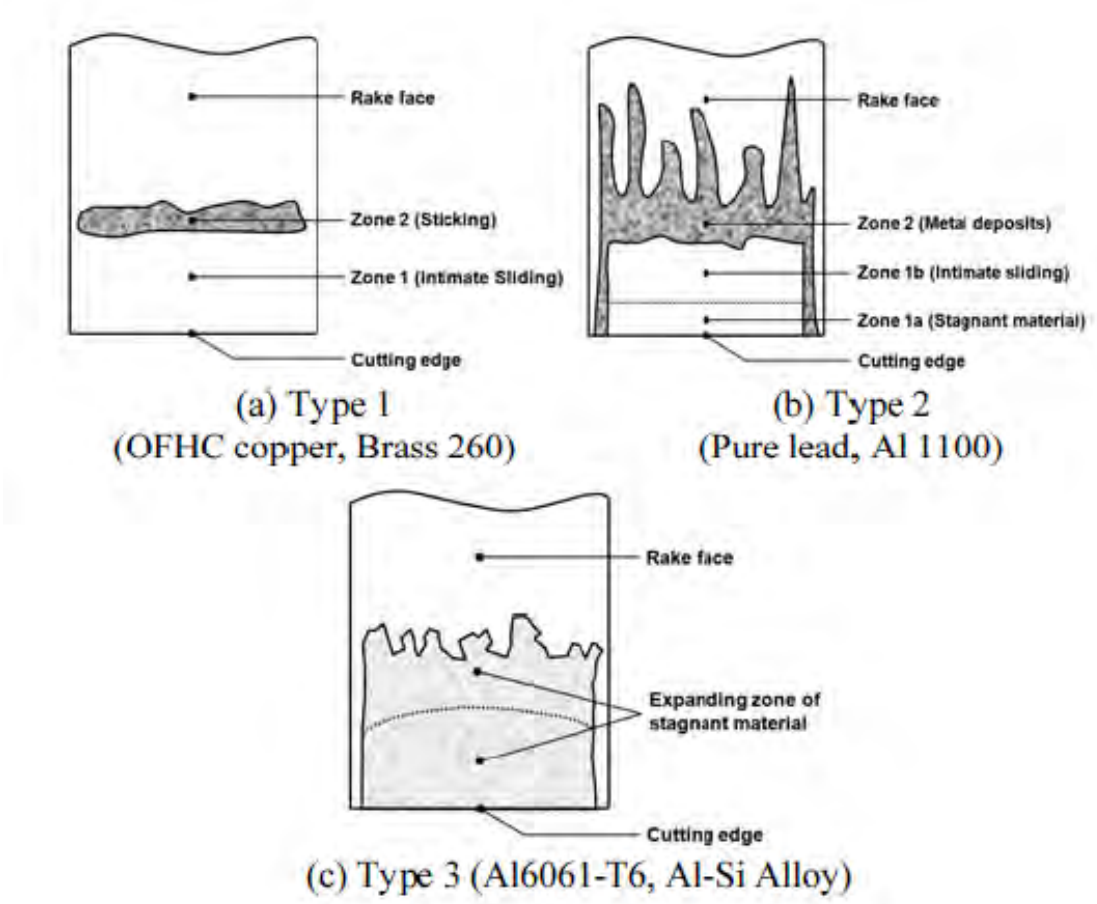

Figure 2.9: Classification of chip-tool contact conditions by workpiece materials. Taken from [20]

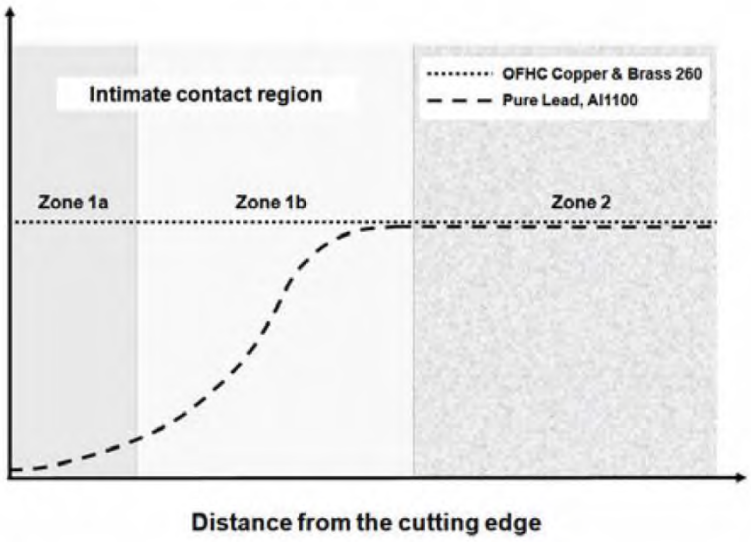

Figure 2.10: Chip velocity profile as it varies with workpiece material. Taken from [20]

The growing stagnant region of Type 3 conditions is linked to work hardening of Al6061 and Al-Si chips. Measurements of hardness showed a maximum at the edge of the chip where it

meets the rake face and deforms due to friction. As indentations were made further away from the edge, the hardness decreased until reaching the bulk chip hardness. Repeating this indentation experiment with oxygen-free high conductivity (OFHC) Cu, the hardness was uniform throughout the chip cross-section. Hwang and Chandrasekar discuss that the work-hardened chip will stick to the tool, and cause build-up if there is significant adhesion between the work-hardened chip and the flowing chip.

2.1.3. Atmospheric interactions at the chip and tool interface.

The influence of atmospheric gasses was addressed by Doyle *et al [15]*. As mentioned previously and displayed in Figure 2.5, the drag force increased with an increase in oxygen partial pressures. Madhavan *et al* [17] made observations that show Zone 1 sliding does not transfer to sticking when exposed to the atmosphere. This led to conclusions that work hardening of the chip as it slides along the rake face causes sticking to occur. The deformation becomes easier further away from the chip and rake interface and material is left deposited.

Ezugwu *et al* [21] experimented with the idea of changing atmospheres in cutting: Ar gas was compared with conventional lubricants in machining Ti6Al4V and was found to reduce tool life. The reduced performance was linked with the poor heat transfer capabilities of Ar gas when compared to lubricants. No observations comparing Ar to atmosphere were made.

It is of interest to explore the effects of Ar gas on machining, focussing on oxidation effects in Zone 2. The reduction in oxygen could influence sticking and deformation mechanisms, especially for workpiece materials that have a high affinity with oxygen. The access to oxygen will also influence the performance of alloy coatings that experience a beneficial oxidation reaction, for example TiAlN [22].

2.2. Chip formation – generally and for Ti6Al4V.

Chip formation during cutting is a highly complex process. Interactions happen with high strain rates, temperatures above 1000 °C and friction conditions that are in a state of full contact with a highly reactive newly formed surface. These conditions are all combined in a process that is almost unobservable *in-situ*.

2.2.1. Chip formation types.

Chip formation occurs as the cutting tool tip is forced into the workpiece which deforms via shear. As the tool continues, a chip is formed which progresses along the rake face of the cutting tool until it separates completely.

Chip formation can occur in two ways (Figure 2.11):

1. By continuous deformation through active slip systems; and
2. By a discontinuous mode whereby deformation is localised and the chip forms in small relatively undeformed sections separated by highly deformed bands, although there is no unified conclusion as to the cause.

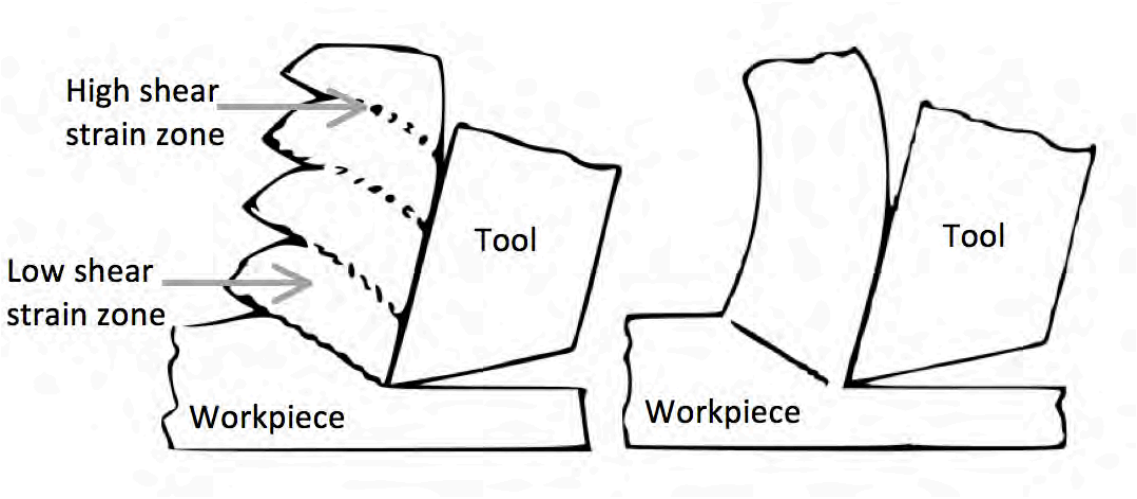

Figure 2.11: Schematic showing segmental chip formation (left) and continous chip formation (right). Adapted from [23]

The likelihood of discontinuous or rather segmental chip formation occurring can depend on the cutting conditions and the workpiece material. Materials with a propensity to work harden are more prone to segmental chip formation. Faster cutting speeds exacerbate the mechanism as slip systems have less time to become active and temperature is higher.

The cause of segmental chip formation can be separated into two opinions: dislocation build up and eventual crack propagation along the primary shear plane [24-27], or via localised heat build up, thermoplastic instability, and eventual deformation (adiabatic shear) [28-32]. This is caused by high strain rate and higher temperature cutting, and exacerbated by low workpiece thermal conductivity.

Nakayama *et* al [24] cut heavily cold worked brass and cracking was noticed. This material, because of its highly deformed state, has little to no propensity for dislocations to move, it has already saturated its ability to accommodate dislocations during cold working. The high thermal conductivity of brass will dissipate heat throughout the chip and hinder adiabatic shear mechanisms. In this case, cracks will form very quickly, leaving no opportunity for heat to concentrate – reducing thermoplastic instability and eliminating adiabatic shear.

Ueda *et al* [33] cut single crystal brass and observed that the orientation of the crystal had a huge influence on whether chip formation occurred via a continuous or segmental mode. This effect can be linked to the number of slip systems available at different orientations relative to cutting forces. Less slip systems will lead to segmental formation and, with more, a continuous mode will be active.

In other materials, the dislocation saturation and work hardening will take time and their build up will generate heat, causing adiabatic shear to occur rather than brittle failure. Barry *et al* [34] observed a short period of continuous chip formation was observed before steady state temperatures were reached and a transition to segmental formation occurred once temperatures increased, providing evidence to support adiabatic shear. Further support was found during cutting of Ti6Al4V, deformed hcp-Ti was observed and, as cutting speed was increased, localised shear regions also included martensitic-Ti [35]. This indicates high temperatures occurred in shear bands which drove the chip near or above the beta transus temperature of just under 1000 °C, from where it cooled quickly and formed martensitic-Ti.

The major characteristic of Ti6Al4V leading to the difficulty in its machinability is the predominant phase being a hexagonal crystal structure. The number of primary slip systems available in hexagonal structures is only three, whereas fcc and bcc materials can deform across a total of 12 and 48 systems respectively. This restrictive structure leads to

work hardening due to an inability to accommodate strain through dislocations, leading to higher forces required for plastic deformation and a propensity for brittle failure due to the resultant higher resolved shear stresses.

2.2.2. Observations of chip formation.

Many observations of chip formation have been made, some aim to characterise the crystallography where others focus on chip shape and colour. Electron backscatter diffraction (EBSD) is a technique developed and used in more recent years for the purpose of displaying location specific crystallographic information and has proved to be very effective in deformation analysis [36, 37]. The technique has been utilised in assessment of machined chips of some stainless steels, however difficulties were found in the indexation of Kikuchi patterns in highly deformed areas typically found in continuously deformed chips. M'Saoubi & Ryde [38] found EBSD useful for assessing segmental chip formation.

2.3. Coatings for cutting tools – current methods for wear resistance.

Coatings have a unique ability to combat the harsh conditions of metal cutting. The processes by which films are grown allow for the synthesis of non-equilibrium metastable phases of alloys that have a high defect density due to their nanometer grain sizes. The defect density leaves alloys with a hardness much greater than their bulk equivalent [2].

Inspektor & Salvador [39] provide an up up-to-date review of coatings for machining tools, addressing industry relevant research. This article covers the need for coatings in metal cutting: to expand safe operating conditions of cutting tools and increase productivity for all applications and to increase tool life within current safe conditions. Another useful article by Mayrhofer *et al* [2] focussing on the microstructure of hard coating is highly recommended for further reading.

The most effective method of raising productivity is to increase cutting speed, but in cases where high cutting speeds are unnecessary or not preferred there are still improvements to be made. The dilemma with increased cutting speed is the dramatic increase in temperature of the interaction. Then, high frequency impact, oxidation and thermal softening of the tool all become huge problems for the toolmaker. Different avenues for improvement of coatings have stemmed from these needs. Multilayered structures allow for added flexibility of application and increased toughness; nanostructures which increase coating hardness and toughness cope with high frequency loading, as well as offer super-hardness to battle abrasive wear. The addition of elements that form stable oxides battle oxidation, and ternary or quaternary coatings that decompose at higher temperatures to form harder multi phase structures overcome thermal softening. Combinations of these approaches are used to enhance coating capabilities.

2.3.1. Monolithic coatings.

Single layered architectures were the first to be utilised for metal cutting. The source of their high hardness is through high defect densities caused by the nanometer range grain sizes [2]. Early coatings included TiC, TiN, TiCN and CrN. The limitation in operation of these films is their instability at high temperatures; they begin to oxidise during higher temperature application, obstructing the use of faster cutting speeds. Other elements were added to these systems to provide higher temperature stability and oxidation resistance –

commonly Al. TiAlN films were deposited which provided higher hardness and enabled much higher cutting speeds. TiAlN was predicted to form a protective oxide during high temperature application [22] and later shown to form a protective alumina layer on the rake face of nanocrystalline films during high speed machining [40], and in ball-on-disk tests [41]. Interestingly, TiAlN was also found by Mayrhofer *et al* [42] to exhibit an increase in hardness when subjected to temperatures between ~700 °C and ~950 °C. This is attributed to the spinodal decomposition of the TiAlN system into fcc-TiN and metastable fcc-AlN (see section 2.3.3 for more details on spinodal decomposition). Temperatures above 950 °C lead to the formation of hcp-AlN and a reduced hardness is measured. Many exotic elements have been added to nitride, oxide and carbide based films targeting oxidation resistance to improve cutting tool performance.

2.3.2. Layered coatings.

A well explored avenue for coating improvement is the layered design [43, 44]. There are multilayered films, and nanolayered or superlattice coatings. Multilayer designs combine of a number of different materials which, when layered together, create a coating that performs better than the sum of the individual parts. Multilayered films can also provide flexibility in application, the alloy of each layer is carefully chosen to resist certain wear mechanisms. An example is the use of a TiCN, Al_2O_3 and TiN whereby the initial TiCN layer provides abrasive wear resistance and support for the following Al_2O_3 layer which combats oxidation on the rake face. Finally, the TiN layer on top provides a low friction surface [39].

Toughness and hardness have been shown to increase with multilayered designs [45-47]. The increase in toughness is attributed to deformation occurring in layers with lower elastic modulus, deformation in the softer layer allows the harder layers to remain intact. A simple yet effective explanation of this effect is provided when bending a single layer of brass and comparing with a multilayered brass and Pb beam [48]. The softer Pb deforms instead of the higher modulus brass and accommodates deformation without cracking. This is used as a basic example for how coatings with high and low modulus layered structures can survive heavily loaded tribological contacts. A hardness improvement in layered coatings is linked to dislocation glide limitation to within individual layers.

As the number of layers increases and the thickness of these layers decreases, films tend to be referred to as nanolayered or superlattice films. This method of coating improvement stems from the reduced dislocation glide concept and increases the number of interfaces which act as barriers to dislocation motion, increasing hardness and toughness [44, 49].

2.3.3. Nanocomposite coatings.

More recently, PVD and CVD techniques have been used to deposit nanocomposite coatings. The design of these coatings is a 3-dimensional structure, rather than the 2-dimensional cross-sections of layered designs. Nanocomposite structures are systems of two or more elements that have decomposed during deposition cycles or through post process heat treatments. They have also been observed to work harden through decomposition during high temperature operation [42, 50]. These restrict deformation and enhance hardness with the inclusion of additional defects and segregated phases, which cause localised strain fields. The interfaces between phases also provide additional strengthening due to disrupted dislocation motion.

Nanocomposites have been used to hinder intergranular deformation with a one atom thick lining of an amorphous phase around a nanometre sized grain [51] and various methods of producing superhardness are now used [52]. The two phases have been shown to form via spinodal decomposition during deposition [53]. These coatings have measured hardness of around 40 GPa, which is achieved through extremely small grain sizes and restricted dislocation motion. Other nanocomposites have been developed with more oxidation resistant elements [54-56]. The growth of nanocomposites occurs due to a decomposition of the metastable phases that are deposited with high-energy methods like CAPD, PACVD and magnetron sputtering. Under certain conditions, decomposition of a single phase can occur and segregation of two or more phases is possible. The process has been analysed for a mixed TiSiN system by Zhang and Veprek [53] and the thermodynamics that drive the segregation were carefully explained. The same calculations are repeated below to reproduce a Gibbs free energy curve, and to better understand the findings and assist in explaining the formation of nanocomposites. Introducing these calculations is important when later (Section **Error! Reference source not found.**), the same calculations will be made for the fcc-TiN and bcc-Fe system observed in experiments.

In Zhang and Veprek's calculations [53], the TiSiN system is considered a pseudo binary system of TiN and Si_3N_4. The enthalpy of formation, at the deposition temperature of 900 K, of TiSiN with a 1:1 composition of TiN and Si_3N_4 is approximated according to the following. [1]

$$\Delta H^0_{TiSi:N} = \Delta H^0_{TiSi} - \Delta H^0_{TiN} - \frac{\Delta H^0_{Si_3N_4}}{3}$$

$$= -129.225 - (-335.383 - \frac{746.994}{3})\ kJ/mol$$

$$= 455.156\ kJ/mol$$

This value is then used to calculate an approximate interaction parameter for an equal composition $x_{\mathrm{TiN}} = x_{Si_3N_4} = 0.5$

$$I^0_{TiFe:N} = \frac{\Delta H^0_{TiSi:N}}{x_{TiN} \times x_{Fe}}$$

$$= \frac{455.156}{0.5 \times 0.5}$$

$$= 1820.624\ kJ/mol$$

Then to calculate the interaction parameter, incorporating temperature and N pressure, the gas constant (R), the temperature (T) and the nitrogen gas pressure $\left(p_{N_2}\right)$ are all known, but the value of α is not. Zhang and Veprek [53] are capable of defining this value as 7.024 because a value of Gibbs free energy of $Ti_5Si_3N_y$ is provided by Sambasivan *et al* [57], where the TiN and Si_3N_4 phases coexist. They assume their TiSiN system will share the same Gibbs energy, therefore enabling the calculation of α.

$$I_{TiSi:N} \cong I^0_{TiSi:N} + \alpha RT \ln p_{N_2}$$

[1] For an unknown reason, in reference [53] the Gibbs energy values were used instead of the enthalpy values in the calculations in the above formula. Also, the values used for calculations were for a temperature of 0 K, it seemed more appropriate to use those for 900 K, closer to the 873 K examples shown in the figures of the article. This is not an issue as the outcome of the calculations does not change the conclusions drawn from the article.

$$= 1820.624\ kJ/mol + (7.024 \times 8.314 \times 10^{-3}\ kJ/Kmol \times 900\ K \times 0.00101325\ MPa)$$

$$= 1458.24\ kJ/mol$$

The interaction parameter is then used in the following equation to determine the Gibbs free energy with differing concentrations (x) of Si_3N_4.

$$G_m^{\psi} = \frac{1-x}{1+2x}\ {}^0G_{TiN}^{fcc} + \frac{x}{1+2x}\ {}^0G_{Si_3N_4}^{hex} + RT\left(\frac{1-x}{1+2x}\ln\frac{1-x}{1+2x} + \frac{3x}{1+2x}ln\frac{3x}{1+2x}\right) + \frac{3x(1-x)}{(1+2x)^2}I_{TiSi:N}$$

Plotting the results of this equation for concentrations of Si_3N_4 ranging from 0 to 1 (Figure 2.12) reveals the second derivative of the Gibbs energy with concentration of Si_3N_4 is less than zero $\left(\frac{\delta^2 G_f^0(x)}{\delta x^2} < 0\right)$ for all concentrations of Si_3N_4 in TiN. This indicates the more stable state for a TiSiN system is a separation into TiN and Si_3N_4, which occurs by spinodal decomposition.

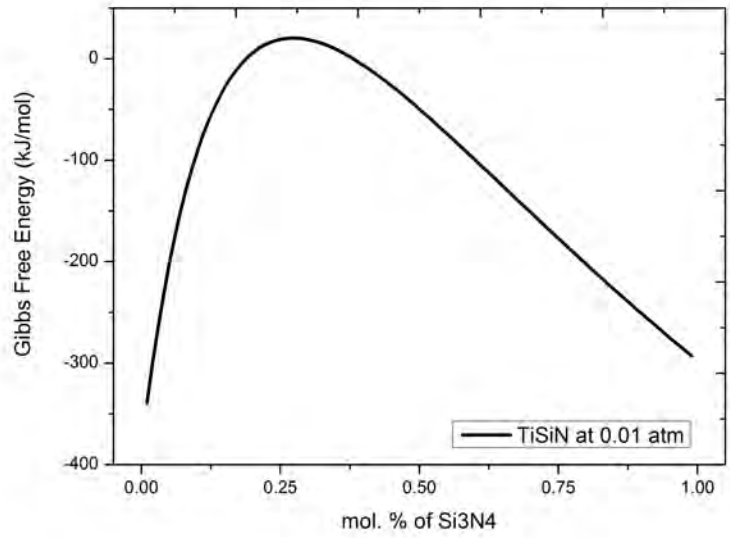

Figure 2.12: Gibbs free energy curve for pseudo binary TiN and Si_3N_4 system, calculated using the above formulas.

There are some other requirements for this segregation to occur. The reduction in Gibbs free energy from the mixed phase to the segregated state must be greater than the strain energy required to form an interface between the two resultant phases – the interface must be either coherent or semi-coherent. The thermodynamic driving force can be increased with higher N pressures and lower temperatures. However, temperature must also be high

enough to enable the diffusion process to occur during a relatively short deposition cycle (when compared to some heat treatments). In some cases this balance is not possible for cost effective production and further heat treatment is used to decompose the metastable phase, or the decomposition can occur during film application [39, 53].

2.3.4. Industrialising research.

Mayrhofer *et al* [2] summarises the field of hard coating research into two aspects: for scientists and for industry. For scientists, focus is guided towards:

- Schemes for secondary phase transformations in metastable systems. Either in-deposition or during application.
- Thermal stability and oxidation resistance.
- Improvement of materials selection for coating and workpiece combinations through an understanding of application specific friction and wear mechanisms.
- Using modelling to explain observations and predict outcomes of cutting processes.

For industry:

- Further control of sample rotation in production deposition systems for the deposition of nanostructured coatings.
- Expanding the functionality and flexibility of coatings through new layer combinations.

There are many research articles showing novel coating designs that increase hardness and oxidation resistance for improved tool life. These findings show great potential for commercialisation. There is however difficulty in turning research findings into a functional, properly priced product in a niche market. There are restrictions: perfecting deposition parameters, sourcing quality affordable target materials, the implementation of occupational health and safety issues with reactive gasses (especially in boride coatings and CVD systems).

For a complete coating and tool system, an holistic approach to all aspects is essential. For example, applying a TiN coating on forming tools did not significantly improve tool life [58, 59], unless tools were nose polished as well as coated with TiN. This pre-treatment and

coating was shown to increase tool life when compared with tools that were nose ground and coated. This is most likely due to the improvement of coating wear [60], adhesion and mechanical performance [61] observed with a lower substrate surface roughness. Also it is necessary to learn at what tool parameters (cutting speed and feed) and with what workpiece materials the tool and coating system works best. The improvements discussed in the Mayrhofer *et al*, and Inspektor & Salvador papers are promising outcomes, but as Inspektor & Salvador explain: for industry, these findings are secondary and many of them still require much effort before they can be sold to a customer.

Industry targeted research needs to take into consideration implementation timeframes. Existing tool and coating systems have a lot of potential for improvement and must be further understood. It is not always necessary to develop, for example, a new architecture. Current coating systems can still provide successful outcomes for researchers and tool manufacturers. In turn, streamlining the implementation of research can provide more for the tool manufacturer than novel coating architectures. Inspektor & Salvador explain that the role of research in the area of coatings for cutting tools is the expansion of a coating and tool system's safe operating conditions. Not only increasing cutting speed potential, but also improving performance in the low speed region. Humble coatings like TiN (which operate well with the very common HSS tool) and TiAlN (which is a high performance all-round coating for the subtractive manufacturer) have a lot of potential that requires utilisation. These coatings can provide some bridge between scientific research and profitable industrial outcomes.

2.4. Deposition technologies.

Coatings provide a barrier to tribological and thermal interactions of a cutting tool's surface, when interfaced with a workpiece during cutting, and reduce wear. There are numerous techniques for producing films. CVD techniques use temperatures and/or a plasma to promote chemical reactions on the surface of substrates to transport coating species from a gaseous reactant. PVD systems utilise numerous methods for producing plasma that is then drawn to a substrate, by taking advantage of the negative polarity of ions produced, through the application of a positive potential to a sample, where ions (and atoms) deposit. Methods include: evaporation PVD; sputtering; and CAPD. Film densities and adhesion are improved with an higher energy species or plasma.

Evaporative PVD can be achieved through different methods. In a most basic form the technique uses heat to produce a gas of the source material (thermal evaporation PVD) and another evaporation technique heats the source material with an electron beam (electron-beam PVD). In both methods, the species travels through a vacuum and deposits on a substrate to produce a film.

Sputtering techniques use strong electromagnetic fields near a target source material to produce a plasma; encouraging particle collisions that ionise inert gasses (typically Ar) which then strike a target material with significant momentum and effectively etch the target. This produces an high-energy plasma of negatively charged target material ions that is then drawn to a positively charged substrate for deposition. The use of magnetrons to encourage higher sputtering rates and increased ionisation is referred to as magnetron sputtering, and high-power impulse magnetron sputtering, which utilises a pulsed high output power source, achieves further ionisation. These techniques (and others) have developed alongside improvements in vacuum pumps and power sources.

Often referred to as vacuum arcs, cathodic arc deposition, or cathodic arc evaporation - CAPD, from early stages and due to the nature of the plasma production, has produced an highly ionised plasma. This technique is utilised in this report and the physics behind the production of plasma are detailed below.

2.4.1. Cathodic Arc Plasma Deposition (CAPD): from solid to plasma.

CAPD is widely used in the area of hard coatings for machining tools. It offers efficient production of highly ionised plasma that can be manipulated and deposited onto a wide variety of substrates allowing the growth of fully dense and highly adhesive films [62-64].

The commonly discussed detrimental side effect to coating performance is macroparticles. This side effect is often outweighed by the improved adhesion provided by such highly activated plasma, negating the need for complete macroparticle filtering in cutting tools. However in the more precise applications of optics, microelectronics and for biomedical appications, filtered arcs are essential.

Anders [65] explains the process in *Cathodic Arcs*. When plasma is present in a vacuum between a cathode and anode, the majority of current is carried by electrons due to their smaller mass and hence greater mobility, when compared to ions. Electrons in a solid material require a certain amount of energy to escape - the work function. At the anode, electrons will flow into the conduction band and eliminate the work function allowing current to flow easily. However, in the cathode a much higher voltage is required to overcome the work function and allow electrons to vacate the solid. This potential difference at the cathode is called the cathode fall, see Figure 2.13. This voltage drop in the cathode sheath, or Child sheath, creates interesting phenomena allowing the emission of electrons to produce plasma.

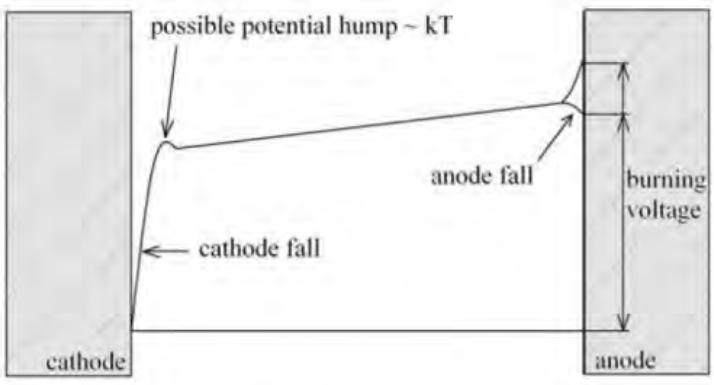

Figure 2.13: Voltage behaviours at cathode and anode surfaces under vacuum. Taken from [65].

Cathodic arc plasmas are generated due to a collective mechanism. Both thermionic and quantum-mechanical field emissions of electrons from a cathode in vacuum produce an

energised plasma. In the presence of a moderate electric field the cathode temperature increases and sufficient energy is provided for electrons to vacate the solid. Thermionic emission dominates in this low range. However with an increase in the applied electric field, field emission begins to participate.

The presence of free electrons near the surface of the cathode imposes a Coulomb force on electrons in the solid. At high field strengths, the shape of this potential barrier is changed and the cathode sheath is reduced compared to the work function. This allows electrons to escape the cathode material through a phenomenon known as quantum tunnelling – the movement of particles across apparently insurmountable barriers. The subsequent heating of the cathode due to field emission increases thermionic emission and in turn the two processes reinforce each other. A higher emission current is then experienced, this is known as the Schottky effect [65].

The Child sheath thickness is described in the following formula.

$$s_{Child} = \frac{\sqrt{2}}{3} \lambda_{De} \left(\frac{2e\,|\Delta V|}{kT_e}\right)^{\frac{3}{4}}$$

$$\text{Where: } \lambda_{De} = \left(\frac{\varepsilon_0 kT_e}{n_e e^2}\right)^{\frac{1}{2}}$$

Here: s_{Child} is the Child sheath thickness, ΔV the voltage drop, k the Boltzman constant ($1.38\text{x}10^{-23}$ J/K), T_e the electron temperature, ε_0 the permittivity of free space ($8.854\text{x}10^{-12}$ F/m) and n_e is the electron density. λ_{De}, the Debye length, is the characteristic shielding length of the long range coulomb potential of a charged particle, due to the presence of nearby charged particles. Therefore the Child sheath thickness depends on the voltage drop, local electron density and to a lesser degree electron temperature.

With the ever-present roughness of the cathode causing variations in electron densities near the surface different locations on the surface will have different sheath thicknesses (Figure 2.14). The thinner the sheath, the higher the plasma current density (for a given voltage drop).

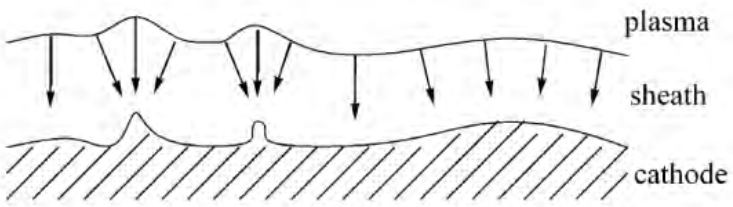

Figure 2.14: Schematic showing the concentration of electrons on a cathode surface, caused by non-uniformities. Taken from [65].

This plasma does two things: further increases the electric field due to a reduction of the sheath thickness and increases ion bombardment and its associated heating. The ion is only effective at deforming the potential barrier at a distance of around 1 nm from the cathode surface. Too far (> 5 nm) from the surface, the force is too small, too close (< 0.4 nm) and the ion will absorb electrons and lose its positive charge. This form of emission is more dominant at higher gas pressures.

The process of increased electric field, electron emission and ion bombardment leads to a micro explosion in the emission centres if the local heat input exceeds heat dissipation. The extreme current flow is evident on the cathode surface as highly concentrated, rapidly shifting spots. Current densities in the 1 to 10 µm sized spots range from 10^6 to 10^8 A cm^{-2} [66, 67]. Mesyats [68, 69] developed the Ecton model to explain what occurs in cathode spots. At these locations the cathode material explosively evaporates and produces approximately 10^{11} electrons (for an explosion lasting 10 ns), positively charged ions, neutral particles, and droplets commonly referred to as macro- and nanoparticles [65]. The electrons and ions remain in a quasi-neutral state near the cathode to form a plasma. A plasma can be thought of as a fluid that allows for conductivity between an anode and cathode. The plasma ion current is a fraction of the arc current and indicates the concentration of ions in the flux. See equation below. Typically, $\in$ ranges from 0.06 – 0.12 [70]. The circuit between anode and cathode is then completed due to the flow of electrons and charged particles, mediated by the plasma.

$$I_{\text{ion}} = \in I_{arc}$$

There are two types of cathode spots. Type 1 spots exist on non-metallic cathode surfaces. The higher impedance of non-metallic materials causes charge build-up under ion bombardment which leads to a reduced work function, increased electron emission and

thermal runaway. This leads to multiple emission centres that are electrically in parallel, sharing the current so there is less at each centre. The end result is emission centres that do not fully develop and so leave smaller craters and less macroparticles. Type 2 spots on metallic surfaces, with less impedance, cause larger electron explosion sites due to higher current densities and hence more macroparticles [65].

'Evaporation' is useful in explaining the above process but strictly speaking the majority of the cathode material is transitioned to dense plasma as opposed to a neutral vapour, hence the use of the term 'Cathodic Arc Plasma Deposition' [67].

2.5. Condensation.

2.5.1. Growth mechanisms.

An understanding of growth mechanisms during condensation on of a gaseous species on a free solid surface is critical to surface engineering. It enables control of the microstructure and performance of the film during application. Petrov *et al* [71], Mayrhofer *et al* [2] and Martin *et al* [72] provide a good explanation of this. A summary of the major factors controlling Volmer-Weber or 3D film growth is briefly addressed here.

As ions from a plasma flux and land on a substrate, they move across the surface as adatoms until they find a thermodynamically favourable location to settle and condense. The freedom for adatoms to move is dictated by the amount of energy they possess. This can be encouraged by: high energy plasma production (as in CAPD), higher substrate temperatures, and the existence of a plasma sheath on the substrate (provided by a bias voltage – ions accelerate and gain energy as they pass through it).

Adatoms saturate together on the surface and form islands. These islands grow in size as islands with lower energy and, due to their lower surface energy, absorb others. Coarsening during this phase of coalescence leads to the selection of preferred crystallographic orientations. Islands with dense planes are most commonly selected: (111) for fcc, (110) for bcc, and (0002) for hcp. Eventually the islands coalesce to form a continuous film. From this point, localised epitaxy (continuation of the crystal structure of a single grain) occurs as the arriving flux condenses on the newly formed film.

Grains of preferred growth orientation grow in height, gradually increase in width and shadow less preferred (and slower growing) grains. Alternatively, at high homologous temperature, recrystallisation may occur and will cause massive grain growth in the already deposited film. The outcome depends on temperature. Movchan and Demchishin [73] first simplified film growth as being dependent on temperature, specifically the ratio between film growth temperature (T or T_s – the 's' meaning 'substrate' as the real film temperature is unknown) and the melting temperature (T_m) of the film material. Thornton [74] developed a structure-zone model, detailing the relationship between coating morphology, deposition temperature and pressure. A structure zone diagram and has been updated by various researchers to explain behaviours relevant to their work [75]. A basic version can be seen in

.

The three zones occur because of changes to diffusion. In zone I: the normalised temperature is low and islands do not coalesce. Grains continue to grow in height from the islands and remain isolated, leaving a low-density porous film. As the temperature increases, surface diffusion can occur. Islands coalesce and grains coarsen gradually as they increase in height. Densely packed planes grow faster and cover slower grains. Grain boundary migration can occur and Zone T forms, further increasing the temperature leads to recrystallisation of the deposited film and bulk diffusion can occur. The larger grain sizes of Zone II result. The films in this work are deposited in Zone T.

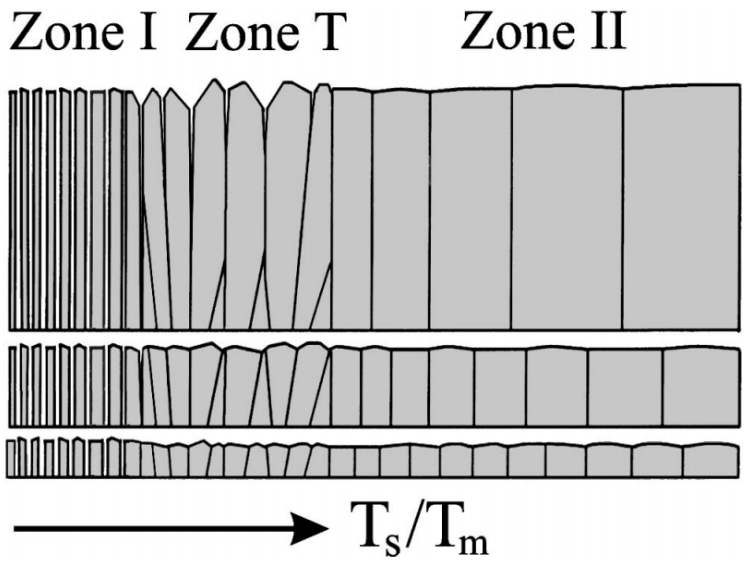

Figure 2.15: Simplified structure zone model showing a change in microstructure with a change in the temperature ratio. Taken from [71].

2.5.2. Titanium nitride and titanium aluminium nitride.

TiN is grown with PVD techniques by the deposition of a Ti plasma in a reactive gas environment of N. The newly formed Ti surface reacts with the N gas due to the elevated temperature and their affinity. TiN has a range of nitrogen solubility and the 'gold' coloured TiN typically found on cutting tools has an atom ratio of approximately Ti_xN_{1-x} (where x is around 0.1); and an fcc-NaCl structure with a lattice parameter of 4.24 Å. N atoms occupy interstitial sites in the cubic unit cell. In most CAPD processes, the deposited TiN film will form a (111) fibre texture, oriented normal to the substrate surface.

To deposit TiAlN the cathode is changed to a Ti_xAl_{1-x} which is arced in a similar N reactive gas environment. The structure remains similar to that of TiN, however Al occupies Ti sites and reduces the unit cell lattice parameter to 4.17 Å. The film also grows with a fibre texture of (111) orientation with the sample surface.

2.5.3. Stress generation and interruptions.

Residual stresses of films are of constant concern for the life expectancy of coatings. Selecting the correct application method for coatings is vital as stresses can cause adhesion failure, especially in highly stressed situations. This can bend thin substrates but if used appropriately, stresses can increase hardness and improve wear resistance [76].

An understanding of how these stresses develop is vital to controlling them and is also useful to explain coating microstructure and performance. In the literature, the technique of interrupting growth is used to assist in explaining stress generation but here the effect of interruptions themselves is the focus.

There are two types of residual stress in films, intrinsic and extrinsic. Extrinsic stresses are due to the thermal expansion mismatch between film and substrate. Intrinsic stresses are, broadly, all other stresses in the film. Sources of intrinsic stress include defects in the coating lattice for example dislocations, impurities and vacancies. Intrinsic stresses can be controlled to a certain extent by choosing the appropriate deposition conditions [77].

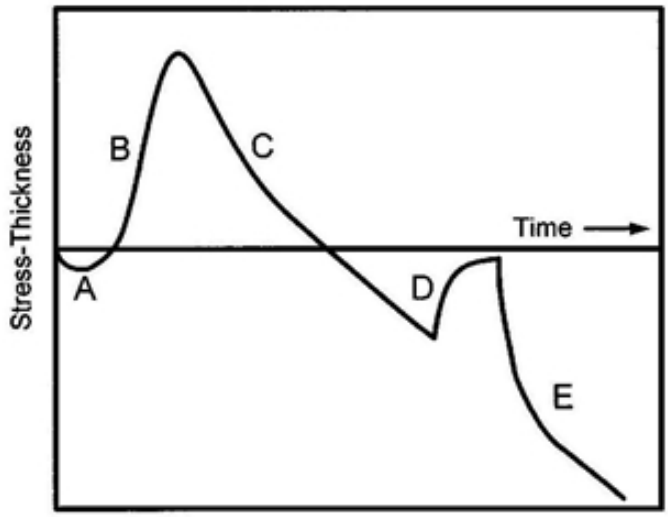

Figure 2.16: The evolution of the stress as thickness increases during depostion. Below the line represents compressive stress, above – tensile. (A) Pre-coalescence stage, (B) coalescence, (C) continuous film, (D) growth interruption, and (E) a return to pre-interruption stress state. Taken from [78].

There is some speculation on the actual mechanisms involved in stress development but a unified understanding of the stress behaviour is accepted throughout the literature on this topic [4, 5, 7, 8, 78-82].

During the precoalescence stage, adatoms form islands across the surface of the substrate. In this stage, stresses are compressive and capillary forces (surface tension) are speculated to be the cause (see Figure 2.16 - A). At the point of percolation, grain boundaries form between islands and a tensile stress develops as boundaries zip and strain together to form a single, lower energy state (Figure 2.16 - B). The resulting tensile stress depends on the grain size or total grain boundary area. Here, the smaller the grain size, the larger the tensile stress component [4].

The further development of compressive stress in post coalescence and film thickening stages (Figure 2.16 - C) are not so well understood. Chason *et al* [7] developed a model to explain post coalescence compressive stress evolution and its subsequent relaxation upon interruption of arriving flux (Figure 2.16 - D). They surmise that surface adatoms increase chemical potential at the surface of a growing film and this potential forces atoms between grain boundaries. During an interruption, this potential is removed and atoms flow out of the grain boundaries, relaxing the compressive stress.

Frieson and Thompson [8] observed interruptions in pre-coalesced Cu films. They noticed a relaxation of compressive stresses similar in magnitude to post coalescence cases. Koch *et al* [5, 9, 10] also supported this decision by finding that with subsequent interruptions, there was an increase in the tensile force that develops immediately after interruption – alongside an increase in grain size. In Chason *et al*'s model [7], stress depends inversely on grain size, so the tensile force should decrease.

Kohn and Lau [6] explains a relationship between the dipole moment of an adatom on a metal surface, and stress. Compressive stress is linked with a high population of adatoms. Frieson & Thompson [78] took this relationship and deposited Ag on Ag (111) and found that a reversible stress change is not from a relaxation of film stress, it is proportional to adatom population. During an interruption the adatom population is drastically reduced, hence the compressive stress is relaxed.

Scanning tunnelling microscopy analysis of Fe deposited on Si (001) by Koch *et al* [5] revealed that a change in the adatom density did not coincide with the changes in stress upon interruption. In fact the change in force increased with future interruptions, adatom population induced stress does not follow this trend.

Furthermore, Koch *et al* [5] found some close correlation in their experiments with work completed by Abermann [3] and Koch [4]. They proposed that the compressive stress in the film at the point of percolation of islands remains 'Locked-In' for the remainder of film growth. This stress is named the 'Laplace Stress', due to capillary forces on island droplets. The magnitude of this stress is thought to decrease as the film thickens due to the loss of strain information as defects are incorporated into the lattice.

This reduction in stress is supported by Koch *et al* experiments [5]. Their results show that compressive stress is independent of grain size and the reversible tensile rise during interruption increases with thickness. Capillary effects can explain the compressive stresses however cannot explain the increased tensile recovery change. The authors speculate that, post growth, adatoms will move via rapid diffusion from compressively strained grain centres to tensile grain boundaries, leading to tensile force. This reverses when growth is resumed. The magnitude of this effect will increase with grain size, as evidenced.

In the previous findings, some research is supportive and some contradictory – an attempt has been made by Chason [83] to simplify the work and develop a model that accommodates most of these findings. Chason [83] proposed a model which focuses on the post-coalescence stress during growth with low mobility adatoms and specifically on the grain boundary insertion mechanism, discussed previously. The basic concept is that, during an arriving flux, the chemical potential of adatoms on the surface forces adatoms into grain boundaries. This leads to the stress in films being dependent on the growth rate: the faster the film grows and the grain boundary height increases (as understood from a cross-sectional point of view), the more tensile the stress. Slower growth rates transfer the tensile stress into a compressive one as the boundaries are filled-in with surface adatoms. At the island stage of film growth, grains are round in cross-section. At the point of coalescence, grain boundaries will form at the edges where the islands meet. During this early stage, the grain boundary height will increase quickly as the grains grow due to the geometry of two circles meeting (see Figure 2.17).

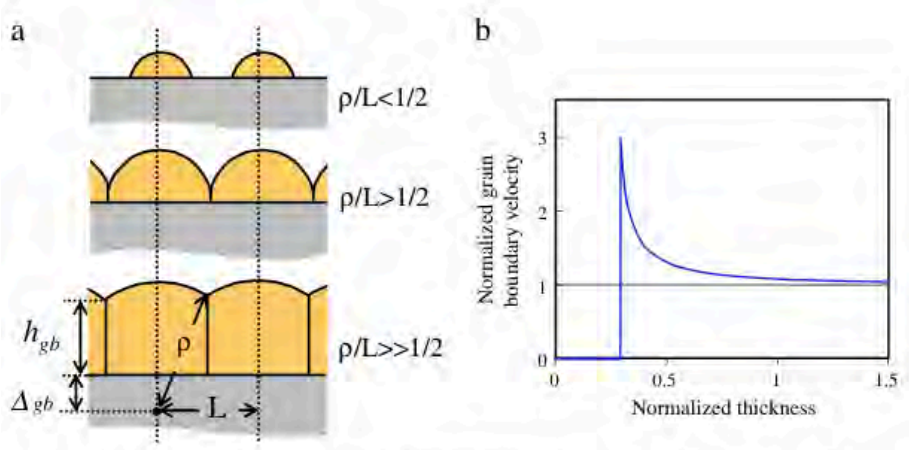

Figure 2.17: The geometric model for grain boundary height velocity during coalescence of films proposed by Chason. Taken from [83].

Because this boundary grows in height quickly, a tensile stress eventuates. As the grain height increases, the circular shape no longer exists and the speed of the growth of grain boundary height slows. Now adatoms will have time to force themselves into the attractive, lower energy, triple junction at the surface where two grains meet – the tensile stress is relaxed and a compressive stress develops. The slower the growth rate, the longer the layer remains exposed (before it is filled by more atoms and the next layer), the more compressive stress can develop as more atoms are forced into the lower energy sub surface.

Chason [83] found a lack of understanding in growth with high mobility adatoms, making it difficult to relate these findings with CAPD. However other work has given evidence to suggest the material and ultimately adatom mobility dictates the development of stress.

Low mobility metals develop tensile stress and high mobility metals initially form tensile stress that later develops into compressive stress [84] although there are some exceptions. At room temperature thermal evaporated deposition of Fe a low mobility pattern occurs, and in the same conditions Ag, Al, Au and Cu exhibit high-mobility behaviour [84]. This effect can be differentiated by the lower melting temperatures of Ag, Al, Au and Cu, where Fe has a higher comparative melting temperature. Deposition temperature can be increased for metals to display high mobility stress behaviour; for example Fe and Cu were observed to transfer to high-mobility a behaviour when heated above 520K and 300K respectively [84, 85]. In low mobility cases, adatoms will only have the required energy to condense into the first few layers, whereas in high mobility cases the adatoms can flow freely along the entire grain boundary. This leads to a potentially varying through-thickness stress state in low mobility growth and a uniform stress state in high mobility situations. CAPD for production of cutting tools is commonly performed at elevated temperatures (substrate temperatures in the experiments conducted in this work are in excess of 400 °C) therefore it is safe to assume high mobility behaviour is commonplace.

The above mentioned experiments are relevant to understanding growth mechanisms, stress development, and adatom behaviour during interruption - but in CAPD and magnetron sputtering, stress can also be controlled with adjustment of the sample bias voltage (see figure 4 in [76]). In-situ measurements of stress during magnetron sputtering of TiN also show a compressive stress develops [11] but observations of the effect of interruptions during CAPD of TiN, on *in-situ* or residual stress, have not been conducted to date.

3. Methodology.

This chapter details the deposition system and process used for the preparation of all samples in this work. It also briefly outlines; statistical techniques used for data analysis; materials analysis techniques used to test samples; and the design of a quick-stop device to allow the collection of *in-situ* formed chip cross-sections.

3.1. Sample preparation.

The device used for the deposition of films is the Innova system from Oerlikon Balzers (Figure 3.1). It is a six target CAPD system that operates in a factory environment, producing hundreds of coated products daily. A large number of substrates can be placed in the vacuum chamber and samples are rotated in planetary motion on a carousel. Prior to insertion into the chamber, substrates are put through a process of ultrasonic cleaning in ethanol, distilled water, acetone and are then dried. Flat samples used for tests such as nanoindentation and XRD are polished prior to cleaning in a four stage process of 320 grit SiC paper, 9 µm, 3 µm and then 1 µm diamond lapping. Each stage is repeated whenever necessary in order to achieve a mirror finish.

Once inside the chamber, samples are heated to deposition temperatures with radiant heaters and an Ar etching process (to further clean substrates before deposition) at a chamber pressure of 0.21 Pa, temperature of 450 °C and a substrate bias of -170 V for 25 minutes.

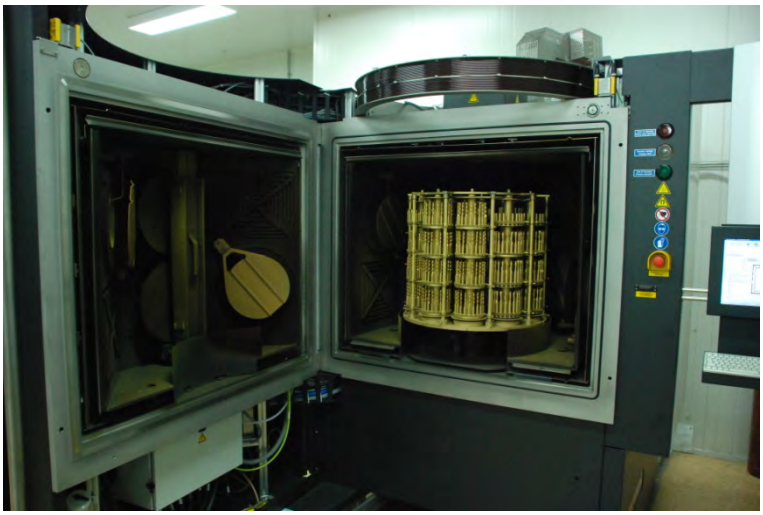

Figure 3.1: : Innova deposition system showing the interior of the chamber. The carousel on the right side of the image shows some samples just coated with TiN.

For the deposition of TiN, six grade 2 commercially pure Ti targets are arced in an Ar and N atmosphere which is introduced to the chamber at constant flow rates of 400 and 800 standard cubic centimetres per minute (or sccm). A bias voltage of -150 V is applied to the substrate carousel which has a measured temperature of 420 °C during deposition. The current density, although not directly measured, was controlled by ensuring the same load size for each cycle, providing a consistent current density for each of the samples grown here. The current density is estimated to be 8 A/m^2. The time taken to grow the film depends on the required thickness: 16, 49 and 130 mins for 1.5, 3.5 and 6.5 µm thick coatings respectively. These parameters are what is used for commercially sold TiN coated tools produced in the Innova and throughout experiments conducted, are referred to as standard (STD) TiN.

Interrupted (INT) samples were grown at the same conditions, although interruptions of various number and duration were introduced during deposition. During interruptions, spread evenly throughout the coating time, arc current and bias voltage were set to 0 A and 0 V respectively. This stops arcing of the six targets leaving a chamber with no plasma, and samples simply rest in the chamber.

Interruptions influence the vacuum environment. When depositing TiN, the system operates in a flow control mode. This keeps the flow rate of Ar and N_2 gas constant throughout the growth stage. With constant flow rates and pumping speed the total pressure, measured with a Pirani vacuum gauge, increases during interruptions due to less N being consumed in deposition (Figure 3.2 and Figure 3.3).

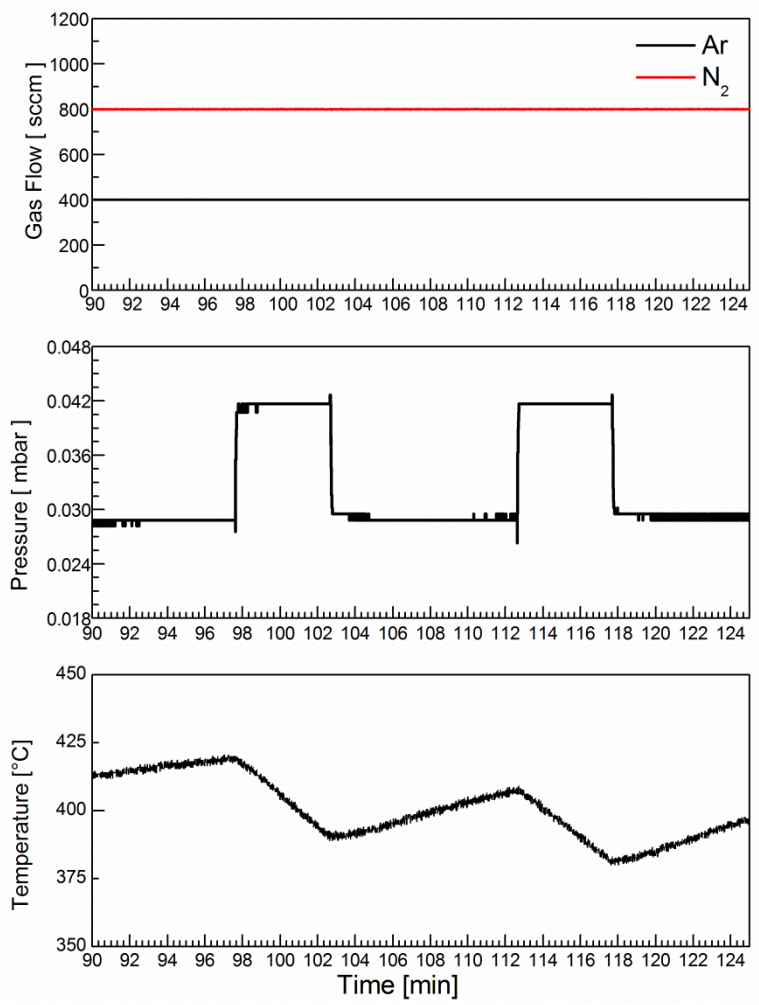

Figure 3.2: Gas flow, absolute pressure and thermocouple temperature measurements during two 5 minute long interruptions when depositing TiN in the Innova. Note the increase in pressure and decrease in temperature.

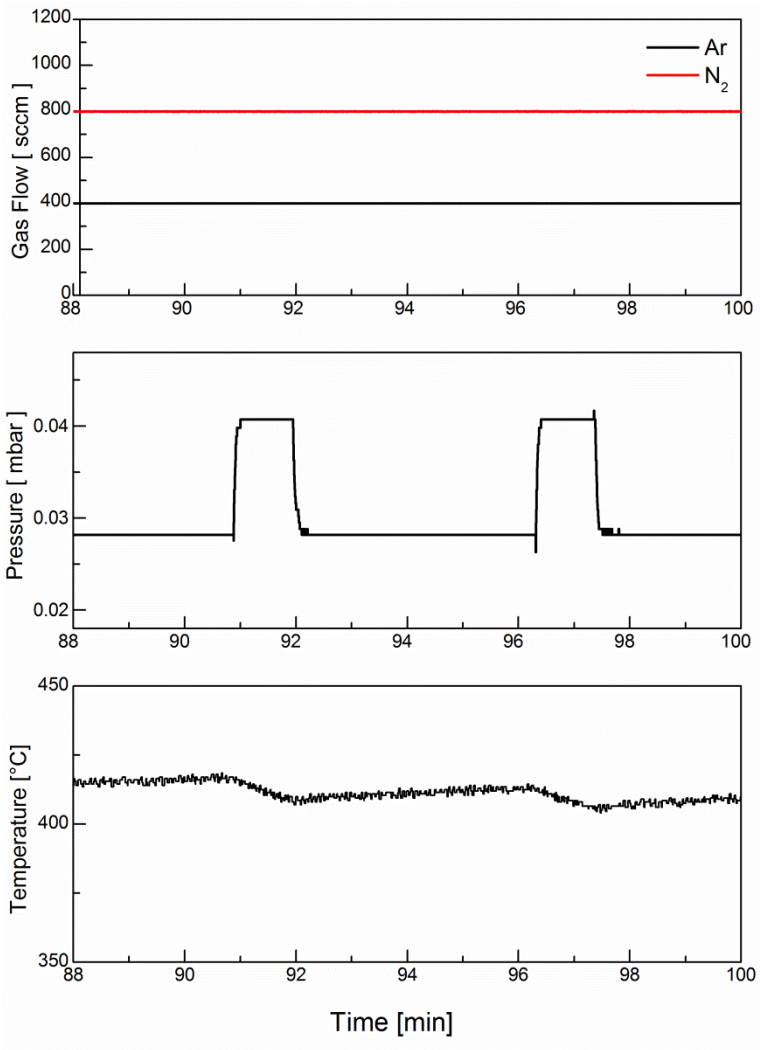

Figure 3.3: Gas flow, absolute pressure and thermocouple temperature measurements during two 1 minute long interruptions when depositing TiN in the Innova. Note the increase in pressure and decrease in temperature.

The temperature was measured with a thermocouple mounted 100 mm from samples, and recorded temperatures are displayed in Figure 3.2 and Figure 3.3. During TiN deposition, no radiant heading is provided to maintain substrate temperature and a decrease occurs during interruption. This decrease is greater in longer 5 minute interruptions than in 1 minute interruptions. Over the full deposition cycle, consecutive interruptions do not decrease the measured temperature significantly.

Films deposited for this report are as detailed in Table 3.1 along with sample nomenclature. In each of these sample runs, ten drills and two flat HSS substrates were coated to provide adequate samples for testing.

Table 3.1: Sample nomenclature.

Sample name	Number of interruptions	Duration of interruption
TiN STD	0	N/A
TiN 4-INT 5 min	4	5 minutes
TiN 9-INT 5 min	9	5 minutes
TiN 9-INT 1 min	9	1 minute

3.2. Statistical techniques.

To provide confidence in comparative analysis of experimental results, Analysis of Variance (ANOVA) and Weibull analysis techniques are used.

The ANOVA test is used to compare the mean values of three or more sample groups, taking into account the variance within a group as well as between groups. In basic terms, if the sum of variance between groups is larger than the sum of variance within groups – the difference in the mean values of is significant. There are three assumptions made when using the ANOVA test; observations must be independent, have a normal distribution, and variance must be homogenous. More information about the ANOVA test can be found in Box *et al*[86]. In this work, these three assumptions are all confirmed as true before using the ANOVA test in data analysis.

A 3 parameter Weibull analysis is used in drill testing to provide a failure time estimate of coated drills. This technique uses the sample data to calculate a Weibull distribution with a reasonable goodness of fit, another form of a probability density function. In other words, a tool life distribution function is generated to fit sample data. This distribution then allows for an estimated lower confidence interval of tool life (below which there is a 5% chance of tool failure), a mean time to failure, and an upper confidence interval (above which there is a 5% chance of tool failure). More information on Weibull analysis can be found in Box *et al* [86].

3.3. Materials analysis techniques.

Various materials analysis techniques are used in experimentation to observe and analyse coating properties (see Chapter 4). Mechanical testing encompasses nanoindentation for hardness, scratch testing for coating adhesion and cohesive strength, and drill testing for tool performance. The microstructure of films is analysed using the following techniques: Scanning Electron Microscopy (SEM), Electron Backscatter Diffraction (EBSD), Transmission Electron Microscopy (TEM), Energy Dispersive X-ray Spectroscopy (EDS), Selected Area Diffraction (SAD), Electron Energy Loss Spectroscopy (EELS),
X-ray Photoelectron Spectroscopy (XPS), and X-ray Diffraction (XRD). In Chapter 5, coated tool samples and formed chips are examined using optical microscopy, infrared cameras, SEM and EBSD.

Basic understanding of nanoindentation, scratch testing, drill testing, SEM, TEM, SAD, XPS, and XRD is assumed. However, explanations of EBSD, EDS, and EELS will be outlined below as some specifics assist in understanding results that are explained in Chapters 4 and 5. The operating parameters for these techniques are provided in the relevant section to avoid confusion as the settings vary depending on the experiment..

3.3.1. Scanning Electron Microscopy.

The SEM is a versatile instrument that can be used to observe sample surfaces at high magnification as well as provide chemical information with X-ray spectroscopy, and crystallographic information through backscattered electron diffraction [87]. An electron beam is focussed at the surface of a sample and scanned across it. When an electron beam interacts with a sample surface, many signals are produced (Figure 3.4). Depending on the detectors used, different information about the sample is collected and processed. The primary signals used in this work are:

- Secondary electrons are used to provide sample surface topographical information for imagery;
- Backscattered electrons are used to deliver a signal that offers a contrast that is sensitive to sample atomic number as well as crystallographic information if backscattered electrons satisfy the Bragg equation;
- Characteristic X-rays are analysed with a spectrometer to offer chemical information.

Most importantly for later experimentation, when analysing microstructures with nanometre range features, the interaction volume of an electron beam and sample surface is different for different signals. Notice in Figure 3.4 the various depths at which secondary electrons, backscattered electrons and characteristic X-rays are produced, as well as the corresponding spatial resolution available for each signal.

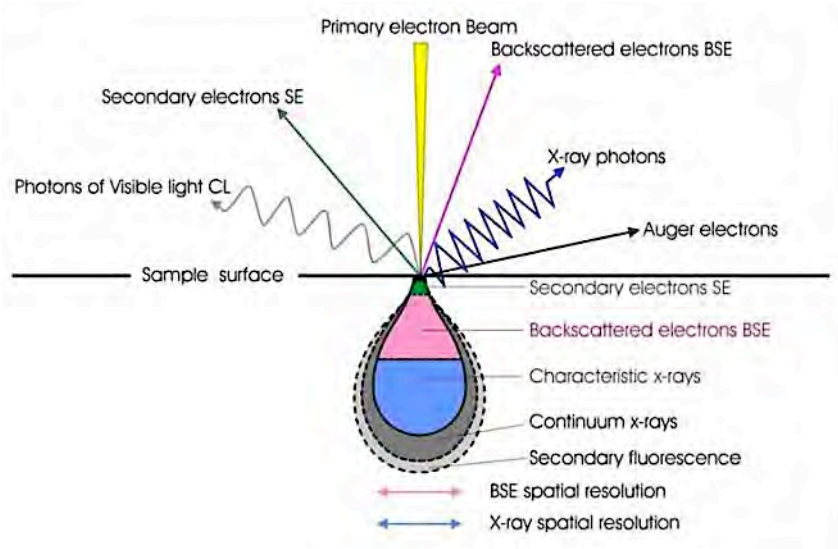

Figure 3.4: Signals produced by electron beam and sample surface interaction [88].

3.3.1.1. Electron Backscatter Diffraction.

Frequently utilised within a SEM, EBSD is a technique to identify a phase location and orientation, which is then mapped to provide detailed microstructural information over a selected area.

When an electron beam interacts with a sample, some backscattered electrons will satisfy the Bragg equation and when they escape the sample surface, Kikuchi patterns can be observed. These patterns are characteristic to the lattice spacing, crystal structure and space group of the sample and also identify the orientation of the crystal. Kikuchi patterns are detected on a phosphor screen and can be captured for analysis or, as in this work, processed with software and matched to a known phase. As the electron beam rasters across the surface of a sample the detected Kikuchi pattern is characterised at each step and mapped, recording phase and crystallographic orientation.

When conducting EBSD measurements in the SEM, the sample surface is tilted to an angle of 70° relative to the electron beam. This is done to bring the interaction volume that emits

backscattered electrons closer to the sample surface. This enhances signal intensity and contrast on the phosphor screen. In this orientation, when compared to a perpendicular beam/sample surface angle typically used in imaging and EDS chemical analysis, the interaction volume will be significantly different and can offer different signals if sample features are in the nanometre range.

3.3.1.2. Energy-Dispersive X-ray Spectroscopy.

Characteristic X-rays emitted from a sample when interacting with an electron beam can be detected with an energy-dispersive spectrometer to provide chemical information. This information is accurate for elements with atomic numbers greater than 3, and even more accurate with higher atomic number elements [89]. Again notice the different interaction volume for characteristic X-rays compared with secondary electron and backscattered electron emission. This change in interaction volume can mean significant differences in the measured signal when observing sample features with a size in the nanometre range.

3.3.2. Transmission Electron Microscopy.

Using an electron beam with a much higher acceleration voltage compared to the SEM (~15keV in SEM and ~300 keV in TEM) allows an electron beam to transmit through thin samples (typically < 1 μm) and produce images in a TEM [90, 91]. The electron beam can also be used to produce diffraction patterns in SAD; characteristic X-rays for EDS; as well as monitor energy loss through inelastic scattering of electrons that transmit through the sample –EELS.

SAD produces small volume diffraction patterns (especially with thin samples) that can be used to characterise small features in a sample, and this analysis can be combined with EDS to allow for accurate characterisation. EDS in TEM has an advantage over EDS in SEM as the interaction volume is much smaller enabling higher acceleration voltages to be used and allowing measurement of a higher electron voltage spectral range. Even with this benefit, EDS in TEM is not ideal for detection of low atomic number elements.

EELS is the technique best suited to detection of low atomic number elements (see [91] for details). With the addition of an EELS in a TEM, it is possible to measure the inelastic scattering of the transmitted electron beam and obtain high spatial resolution sample

chemical information. A method for providing semi-quantitative imagery of elemental distribution is through the division of intensity loss due to inelastic scattering during transmission by the background signal to produce a jump-ratio image [91].

3.4. Quick-stop device.

For a better understanding of cutting, it is beneficial to observe chip formation *in-situ*. Here the selection and design of a quick-stop device is explained. This device is later used in Chapter 5 to collect Ti6Al4V chip cross-sections for crystallographic analysis of chip formation.

A quick-stop device allows for the collection of an *in-situ* formed chip which can then be prepared for analysis. Although there is no stated acceleration of the cutting tool required to achieve an *in-situ* chip, the basic requirement of a quick-stop device is that it is capable of moving the cutting tool away from the work piece at a rate faster than the cutting speed. This leaves the chip partially formed as it would appear if observed during formation. The faster the separation the more likely a real semi-formed chip can be obtained.

There are a number of methods used to achieve this result and each approaches the problem in a different way. Some designs aim to achieve perfect tool and chip separation, and others aim to reach steady state cutting [92-94]. The two attributes are difficult to achieve at the same time, so a sacrifice is made depending on what outcome is desired from the experiment.

In the experiments detailed in Chapter 5, the effect of atmospheric conditions during cutting on two tool coatings was examined. To allow for oxide development, steady state tool/chip interactions and an increase in temperature was required. A device that allows for longer cutting distances was vital. This meant the speed at which the tool retracts from the cut would have been less than ideal.

A quick-stop device for this situation had to be designed and manufactured. The device was built with the following requirements:

- Must be able to cut for a desired cutting distance.
- The tool can be retracted at any time during the cut.
- The tool must be held stationary during testing to allow cutting in a lathe.

Detailed diagrams and explanation of the device's parts can be found in Appendix A.

The tool is held in place by the swing plate (off-coloured part in the bottom right of Figure 3.5). This holder is spring loaded and will rotate around the pivot pin whenever the draw pin that runs through the central axis of the device is retracted with the pneumatic actuator (top left of Figure 3.5). The pneumatic actuator can be activated at any point during operation.

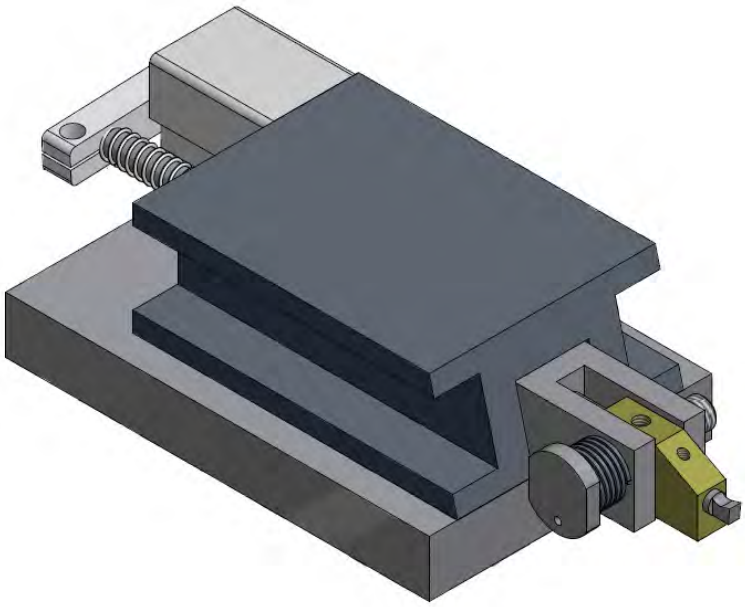

Figure 3.5: Quick-stop device mounted into a tool holder. See Appendix A for detailed diagrams.

The acceleration of the tool after activation of the device was measured, with a high-speed camera, to understand the devices limitations (see Figure 3.6). The tangential velocity of the tool after 0.0005 sec was 130 m/min, rising to 450 m/min at 0.005 sec. Testing is conducted at 50 m/min in the experiments where this device used, and without any standardised acceleration requirement for a quick-stop device, it was deemed sufficient that the cutting tool reach a velocity of 50 m/min after approximately 0.2 milliseconds, so the chip root should remain undisturbed by the cutting tool during retraction and an accurate observation of *in-situ* chip formation be obtained in collected chips.

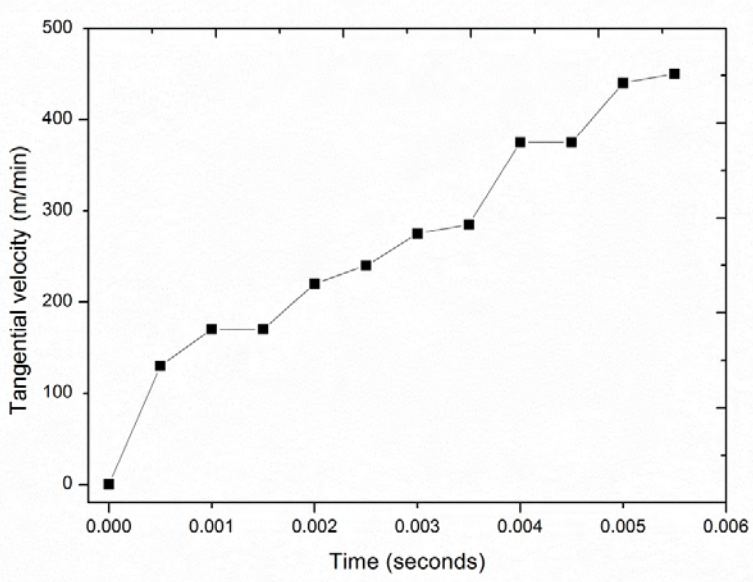

Figure 3.6: Tangential velocity of cutting tool after triggering the device, measured to confirm adequate tool/chip separation for an *in-situ* chip to be collected. Image captured every 0.0005 sec with high-speed camera and angular displacement used to calculate cutting edge velocity.

4. Interrupted deposition of titanium nitride films.

This chapter follows an investigative approach to answering the question: What is the effect of repeatedly interrupting the electric current supply to cathodic arcs during deposition of TiN films on microstructure and mechanical properties?

4.1. Film mechanical properties.

Interrupted deposition of TiN is being examined for use in cutting tools for its wear resistance. Firstly, attempts are made to characterise the material. Mechanical properties important to cutting tools are tested using laboratory techniques. After being convinced a significant difference has been made, the coating is tested in a machining process for which it is optimally used. Changes to mechanical performance are then linked to microstructural change.

4.1.1. The effect of introducing interruptions.

This section observes the effect of 4 and 9 interruptions, lasting 5 minutes each, on the properties of TiN films. The hypothesis was to create a structure that benefited from a layered design. These layers might be created by the inclusion of impurities as the sample surface is left to rest inside a hot chamber during an interruption. The exposed and newly formed hot surface may collect impurity gasses in the chamber, for example oxygen.

Questions to be answered: *Do interruptions create a layered structure or disrupt continuous though-thickness grain growth? What influence does the number of interruptions have on TiN film properties?*

4.1.1.1. Nanoindentation hardness.

Hardness is a key factor in resisting wear and is a quick way to monitor possible changes to film microstructure and wear resistance with introduced interruptions. In the test 25 indentations were made, onto the surface of samples with a Berkovich indenter at a normal load of 40 mN. This load provided an indentation depth of no more than 0.35 µm or 10 % of the film thickness to eliminate any substrate influence [95]. A box and whisker plot of the results is shown in Figure 4.1. The plot displays average values (dot within the box), median values (line within the box), upper and lower quartiles (bottom and top of the box),

maximum and minimum values (whiskers). It can be seen that the average values of hardness increases with 4 and 9 interruptions from the standard value of 18 GPa to 24 GPa and 29 GPa respectively. The whiskers show quite a large range of values here, so an analysis of variance (ANOVA) is useful to see whether the variance within the samples can account for variance between the samples (see Table 4.1). In other words, it can tell us if a significant difference has been made.

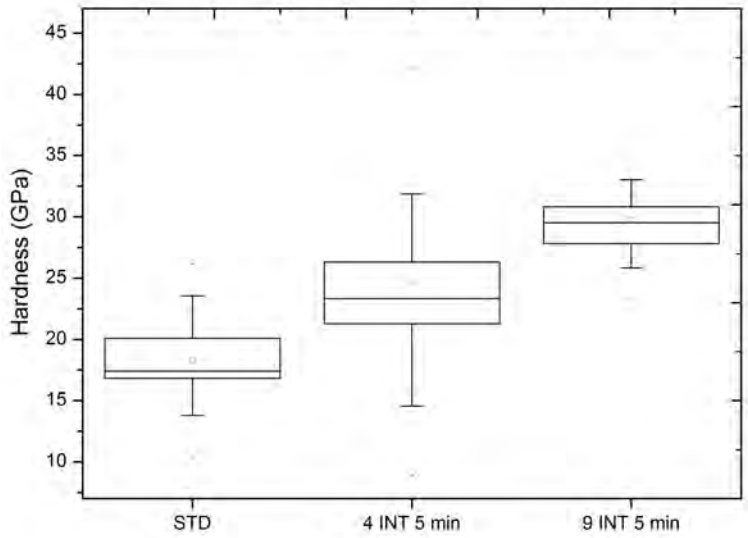

Figure 4.1: Box and whisker plot of indentation hardness measured for TiN STD, 4 INT 5 min and 9 INT 5 min.

Table 4.1: Single factor ANOVA of indentation hardness results displayed in Figure 4.1.

Summary of Hardness Data (GPa)

Groups	*Count*	*Sum*	*Average*	*Variance*
TiN STD	21	385.4465	18.35459	12.23372
TiN 4-INT 5 min	25	615.894	24.63576	52.54802
TiN 9-INT 5 min	25	743.8237	29.75295	14.85488

ANOVA

Source of Variation	*SS*	*Df*	*MS*	*F*	*P-value*	*F crit*
Between Groups	1482.932	2	741.4659	27.07324	2.25E-09	3.131672
Within Groups	1862.344	68	27.38741			
Alpha	0.05					

In the results of an ANOVA test shown in Table 4.1, SS is the Sum of Squares of the difference in each group's mean with the mean of all groups (a grand mean). This is then separated into two: Between Groups variation and Within Groups variation. The ANOVA looks for significance by comparing Between Group variation to Within Group variation,

taking into account the degrees of freedom (Df). The mean square (MS) is calculated by dividing the SS by the Df. This is then used in an F-test to calculate the value of F, which is a ratio of MS for Between Groups and Within Groups. If the ratio is above the critical F value (F crit), then the variation within groups is smaller than the variation between groups, and any differences in each group's mean are statistically significant.

In this case, the probability (P-value) that the difference in means can be from variance within the results is $P = 2.25 \times 10^{-9}$, i.e. a very low probability. The F value is larger than the F-crit, meaning there is a significant difference between measured STD, 4-INT 5 min and 9-INT 5 min TiN hardness. Therefore, a reliable conclusion can be drawn: Four 5 minute interruptions during growth of TiN films increases hardness from 18.4 GPa to 24.6 GPa; and nine 5 minute interruptions further increase hardness to 29.8 GPa.

4.1.1.2. Scratch testing.

Scratch testing is a laboratory experimental technique used to measure adhesive and cohesive strength of a coating, and can reveal differences in standard and interrupted TiN films.

Adhesion of a coating is affected by a combination of factors including (but not limited to) the substrate surface roughness, cleanliness, in-chamber etching processes, the deposition method itself, microstructure, differences in film and substrate thermal expansion coefficients, and residual stress.

The adhesion of a coating can be reliably evaluated with a scratch test, whereby a spherical diamond stylus is passed across the coating surface with a normal load (F_n). At loads where changes to deformation mechanisms occur, critical loads (L_c) are recorded.

In this case a linearly increasing normal load is used to define two points of failure of the coating. Eventually, applying enough normal load exposes the substrate. L_{c1} corresponds to the normal load at which the cohesive strength of coating is examined. This is identified as a spike in acoustic emissions and the initiation of continuous cracking of the coating. L_{c1} is linked to the coating and substrate interfacial adhesive strength. It is defined as the point where a change in the friction force (Ft) occurs along with acoustic emissions and continuous substrate exposure [1, 96].

TiN STD and 4-INT 5 min and 9-INT 5min samples were analysed with a Revetest Xpress from CSM instruments, using a diamond stylus with a radius of 200 µm at a load of 1 to 200 N over a length of 8 mm at a velocity of 8 mm/min, two scratches per sample. The two results were averaged and the range of values is displayed as an error. The results of this test can be seen in Figure 4.2, Figure 4.3 and Figure 4.4. A summary of L_{c1} and L_{c2} for the three samples is provided in Table 4.2.

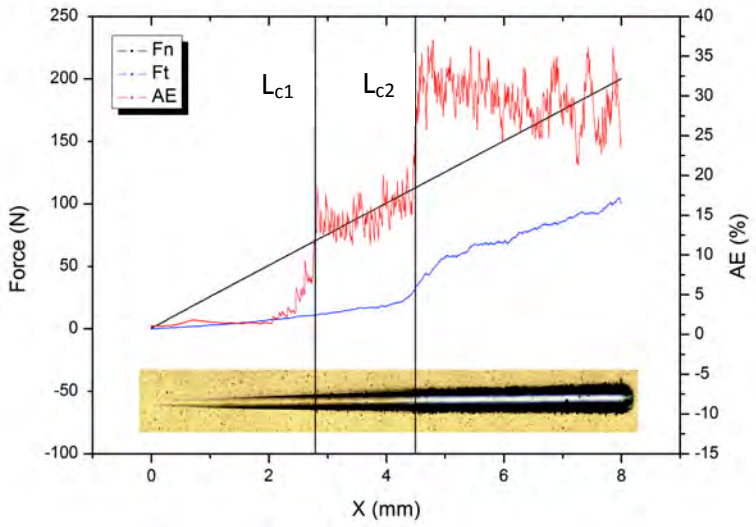

Figure 4.2: Scratch test for TiN STD film on HSS substrate. Graph displays the normal load (Fn), friction force (Ft), acoustic emissions (AE) along with an optical micrograph of the associated scratch.

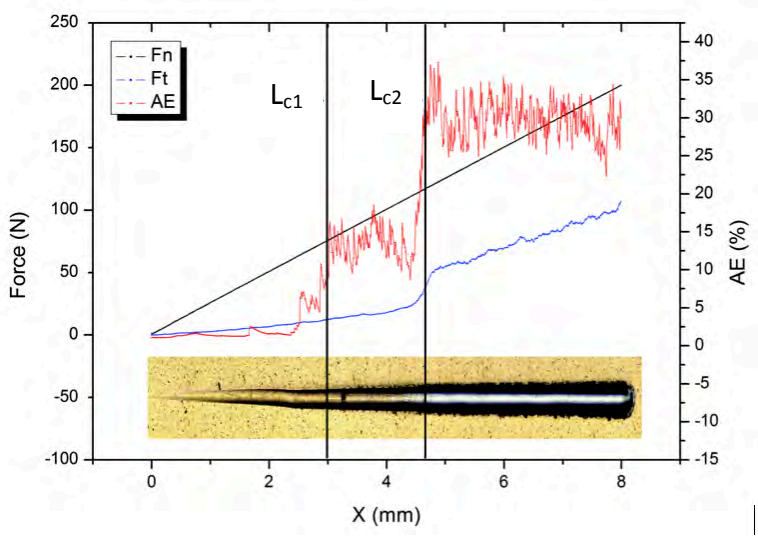

Figure 4.3: Scratch test for TiN 4-INT 5 min film on HSS substrate. Graph displays the normal load (Fn), friction force (Ft), acoustic emissions (AE) along with an optical micrograph of the associated scratch.

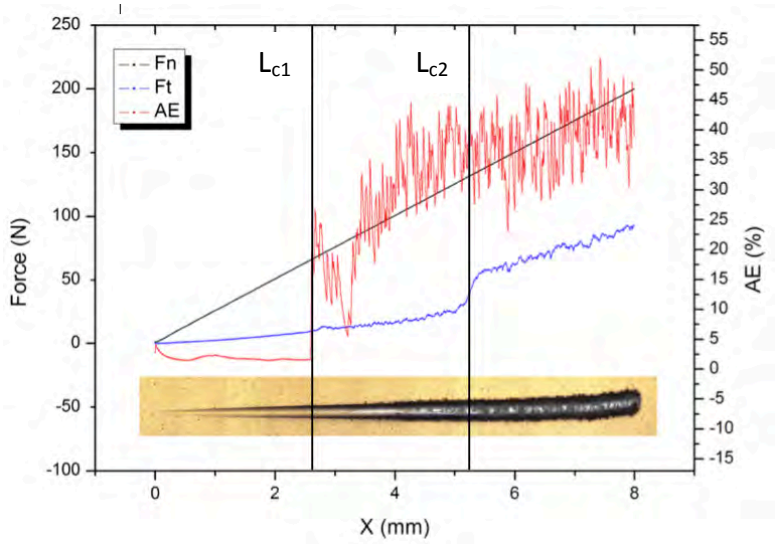

Figure 4.4: Scratch test for TiN 9-INT 5 min film on HSS substrate. Graph displays the normal load (Fn), friction force (Ft), acoustic emissions (AE) along with an optical micrograph of the associated scratch.

Table 4.2: Scratch test results for L_{c1} and L_{c2}.

Sample	L_{c1} (N)	L_{c2} (N)
TiN STD	70 ± 1	110 ± 1
TiN 4-INT 5 min	73 ± 1	111 ± 1
TiN 9-INT 5 min	70 ± 1	120 ± 10

The TiN 9-INT 5 min sample displayed a higher L_{c2} than the TiN STD and TiN 4-INT 5 min films. L_{c1} of TiN 4-INT 5 min slightly increases comparing to that of TiN STD but remains the same in the TiN 9-INT 5 min film. The changes to L_{c1} are minor and not significant. The increase in L_{c2} with the TiN 9-INT 5 min sample is more substantial, however 120 N is an average of two measurements: 110 N and 130 N. It is not valid to claim an increase in adhesive strength of this coating with one value exceeding the adhesive strength of the standard film. From this assessment alone it is difficult to make strong conclusions about the effect of interruptions on TiN film adhesion: effects remain inconclusive.

4.1.1.3. Drill testing.

With increases in coating hardness it is likely that an increase in machining performance is observable with interrupted TiN samples. Drill testing has been selected as the cutting process for testing this material as TiN is most commonly used with continuous cutting (not

interrupted cutting processes like milling). The substrate is chosen to be HSS as these cutting speeds, feeds and workpiece material suit a combination of TiN and HSS well. Applying a TiN coating to a carbide drill would limit operating speeds because TiN cannot perform at the typical cutting speeds that carbide tools can. Higher operating speeds, such as with carbide tools, require coatings that are stable up to higher temperatures (TiN is only stable up to ~500°C [22] – above which TiN will experience oxidation wear, particularly in dry or minimally lubricated cutting).

The parameters selected for this test are for accelerated conditions (to reduce the total testing time and workpiece consumption) and are outlined in Table 4.3. The test material is a tool steel in the fully annealed state, which is regarded as difficult to machine. The TiN coating thicknesses are within a narrow range of 3.6 µm to 4.3 µm - as listed in Table 4.4. Drill tests conducted at near identical conditions (in other words: 35 m/min instead of the 45 m/min used in this work) showed that a coating thickness difference of less than 10% is insignificant due to variability in results [97].

The definition of wear has been identified as 'audible screech'. This point of drill life is very clear to the machine operator and sounds immediately prior to catastrophic failure of the cutting edge. The design of this test method has been detailed in [97].

Table 4.3: Drill test conditions.

Cutting tool	HSS jobber drill – 6.35 mm diameter - deburred
Cutting speed	45 m/min
Feed rate	0.125 mm/rev
Hole depth	2x Diameter (12.7 mm)
Test material (Hardness)	D2 tool steel from Bohler (438 Leeb hardness D [HL-D][DIN 50156/ ASTM A956] = ~167 HV [1kg])
Number of samples	9 per condition (27 drills total)
Definition of wear	Audible screech

Table 4.4: Drill coating thickness.

Sample	Thickness
TiN STD	4.0 µm
TiN 4-INT 5 min	4.2 µm
TiN 9-INT 5 min	3.6 µm

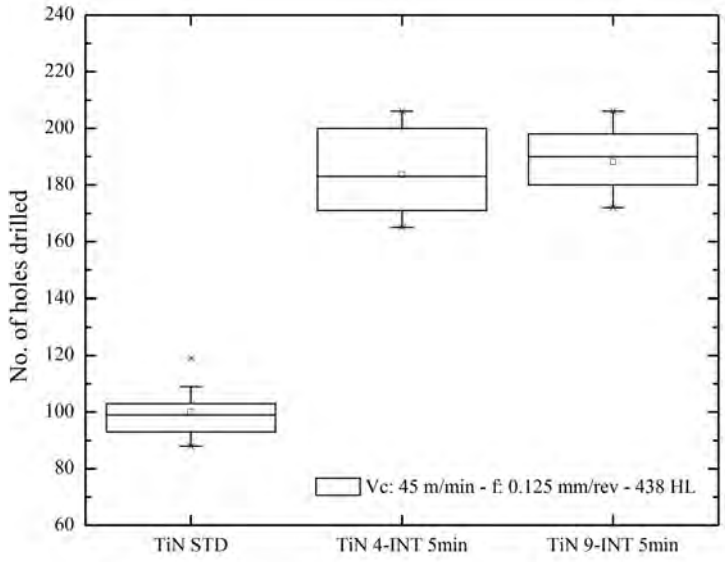

Figure 4.5: Box and whisker plot of drill test of TiN STD, TiN 4-INT 5 min, TiN 9-INT 5 min.

From the results in Figure 4.5, an improvement in drill performance is clear with the introduction of 4 and 9 interruptions (each lasting 5 minutes) during TiN deposition. There is an increase of ~90% in the number of holes cut. Results of a 3 parameter Weibull analysis (calculated using Minitab 16) are shown in Table 4.5. The mean time to failure of the TiN STD coated drill is 100.5 holes and with interruptions, an improvement of an additional 85.3 and 88 holes for 5 and 10 interruptions respectively. It is worth noting the upper confidence interval of the TiN STD sample does not exceed the lower confidence interval of both interrupted architectures. This indicates that a statistically significant improvement has been made.

Additionally, there is an improvement between TiN 4-INT 5 min and TiN 9-INT 5 min samples despite the similarities in the mean time to failure. The TiN 9-INT 5 min sample is 0.6 µm

thinner than the 4-INT 5 min sample and hence the number of holes cut per micron[3] is increased from 44 to 52 with an increase in the number of interruptions over the 25 holes per micron cut by the standard TiN coated drill. Also, the standard deviation is smaller in the 9-INT 5 min sample.

Table 4.5: Weibull analysis (3 parameter) of drill test.

Sample	Mean Time to Failure (holes)	Standard Deviation	Lower confidence interval (holes)	Upper confidence interval (holes)
TiN STD	100.5	3.5	93.7	107.6
TiN 4-INT 5 min	185.8	8.6	169.7	203.4
TiN 9-INT 5 min	188.5	4.4	180.2	197.3

4.1.1.4. X-ray Diffraction and Transmission Electron Microscopy characterisation.

In this section, XRD is utilised to observe the crystallography of coatings, enabling phase identification and potential changes to film microstructure with interruptions during deposition. Cu Kα radiation was used to scan films between 20° and 80° 2-theta at a step size of 0.02°. From scans completed (Figure 4.6), the (111), (220), (311) and (222) peaks of fcc-TiN are observed. The large relative intensity of the (111) plane indicates a (111) texture exists normal to the sample surface, as expected for TiN deposited with CAPD [76]. Other peaks observed in 2-theta scans belong to the bcc-Fe phase and numerous other W and V carbides present in the HSS substrate. With the introduction of interruptions during deposition of TiN, no clear difference in crystallography observed with XRD is noticed.

[3] Holes cut per micron of coating thickness assumes the wear rate scales linearly with thickness. Pilkington *et al* [98] used this method of comparing drill life with inconsistent coating thicknesses.

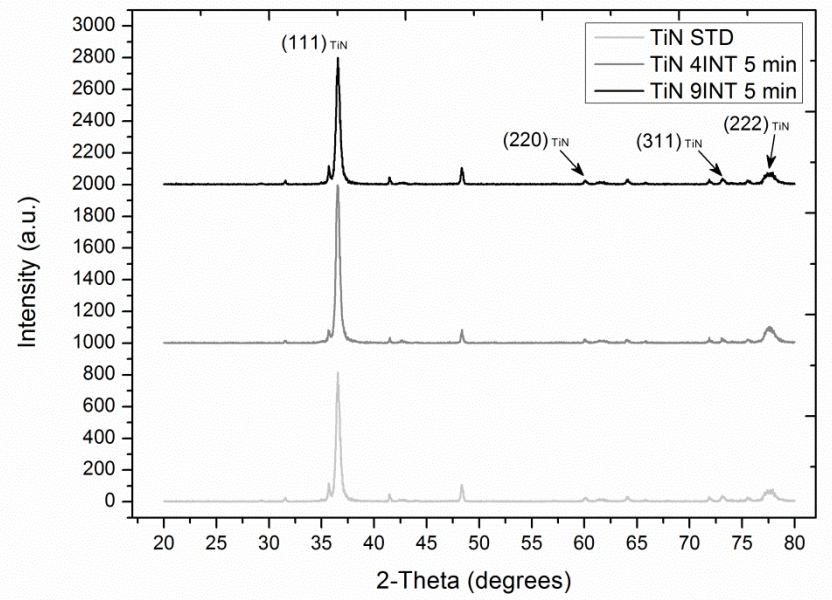

Figure 4.6: XRD 2-theta characterisation scans of standard and interrupted TiN films on HSS. Unlabeled peaks belong to the numerous Fe, W and V carbides of HSS.

To observe cross-sectional film structure, TEM and SAD were carried out using a JEOL 2011 TEM operating at 200 kV on film cross-sections prepared with a dual beam FEI Nova 600 focussed ion beam (FIB) miller, equipped with a Ga ion source (Figure 4.7). The film has a polycrystalline morphology and there are no unambiguous changes to grain structure or size. Interruptions are not observed to disrupt continuous grain growth or have any layering effect. SAD shows intensities from a number of planes with a more intense (111) peak oriented parallel to the growth direction.

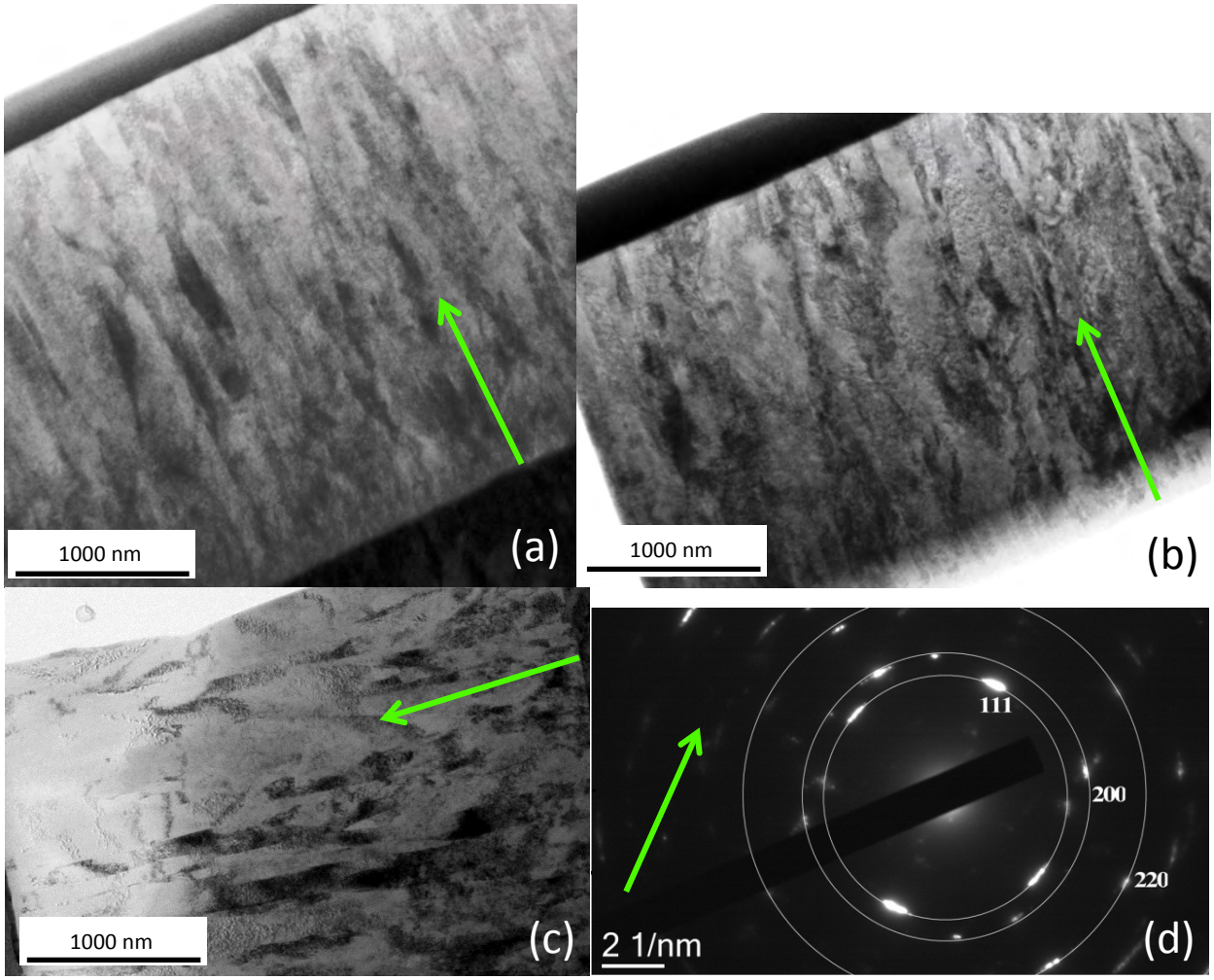

Figure 4.7: TEM micrographs of FIB cross-sections of (a) TiN STD, (b) TiN 4-INT 5min, (c) TiN 9-INT 5min. The green arrow in all images displays the film growth direction, from substrate to coating surface. Images show that no disruption of continuous grain growth is observable. (d) examples a SAD pattern for these samples showing a more intense (111) peak in the growth direction.

4.1.1.5. Cross-section observations.

A fracture cross-section is prepared through the process of sectioning a sample by cutting from the substrate side of a coating and not fully completing the cut, with approximately 1 mm of material remaining. The sample is then placed in liquid N until cooled. After striking the sample, a brittle fracture leaves a fracture cross-section in the 1 mm of uncut material. Fracture cross-sections of coatings are imaged in electron microscopy to give an idea of fracture mechanics. Layered coatings are revealed in the SEM using this method because of contrast changes due to different elements (and their electron back scattering rates) or by changes to topography provided by fracture mechanics of the film. Topography

changes can be seen when grains do not continuously grow through the thickness of films, as in some layered architectures.

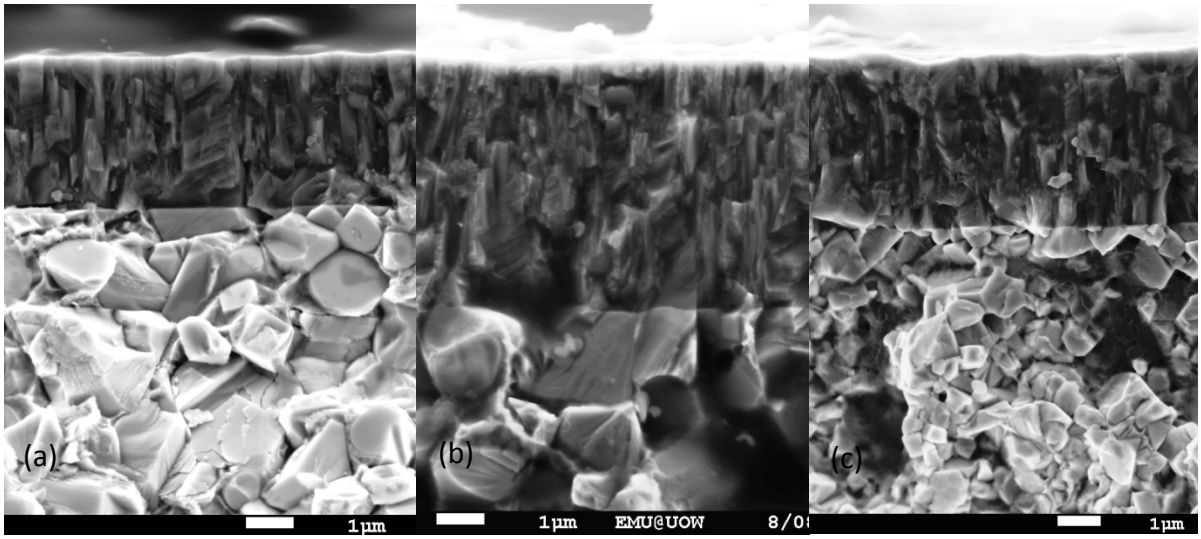

Figure 4.8: Fracture cross-section micrographs of (a) TiN STD, (b) TiN 4-INT 5 min and (c) TiN 9-INT 5 min.

In Figure 4.8 the effect of interruptions on fracture cross-sections is observed in SEM. The film thickness shown in these micrographs vary from previous measurements in Table 4.4. This could be for a number of reasons: samples are flat and mounted differently in the chamber to drills; preparation of the fractured cross section could be imperfect (in other words the cut is likely to not be perfectly normal to the sample surface; and the image could be distorted due to the close proximity of the microscope's electron beam to a large step edge. Hence these cross-sections should not be used for thickness measurements.

Topographically, no difference is noticeable in Figure 4.8. No layering effect is visible, meaning grain growth is unchanged with interruptions. Changes in contrast are not expected as alloying percentage will remain constant throughout the thickness. These conclusions are supported by the TEM micrographs of FIB prepared cross-sections in Figure 4.7 where grains sometimes grow through the entire thickness of the film. There is no observable layering in these images. The high-resolution image of an interrupted sample in Figure 4.9 also supports this finding.

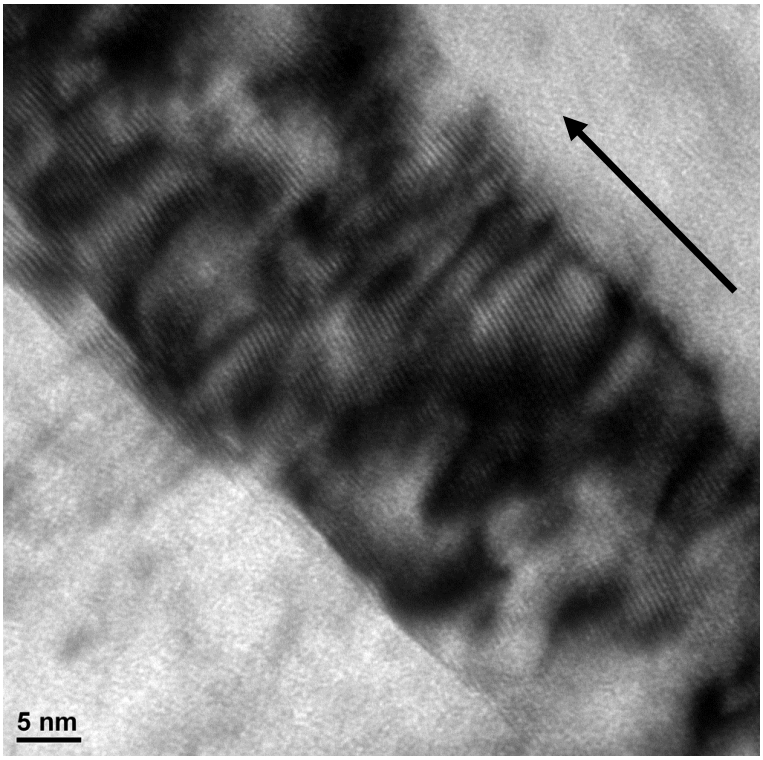

Figure 4.9: High-resolution micrograph of FIB prepared TiN 9-INT 5 min sample from TEM. Image shows continuous grain growth through an interrupted section, however the exact location of an interruption through the thickness shown is difficult to locate. In this micrograph at least one interrupted section is present, but any layering or distinct interruptions in grain growth are not observable. Arrow indicates growth direction.

To confirm no chemical changes have been made within the film, energy-dispersive X-ray spectroscopy (EDS) of a FIB cross-section are included in Figure 4.10. The analysis shows the TiN 9-INT 5 min sample deposited on a WC-Co substrate. The levels of Ti and N are unchanged through the thickness of the sample and no other elements were detected.

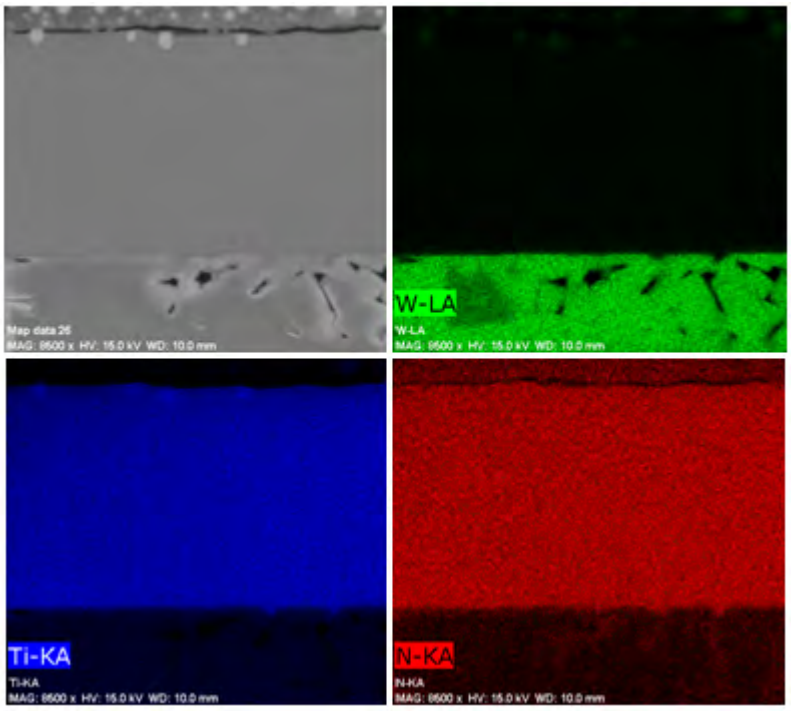

Figure 4.10: EDS of FIB cross-section of TiN 9-INT 5 min sample on a tungsten carbide substrate. No changes in chemistry noticeable.

4.1.2. The effect of reducing interruption time.

With the introduction of interruptions during deposition of TiN, there is an increase in total deposition cycle time (45 min with 9 interruptions lasting 5 min each). This added time is undesirable in a production environment, hence there is considerable need to reduce total cycle time. The reduction in deposition time can also give some understanding of the possible mechanisms involved in increasing hardness and drill performance. In the longer 5 min interruptions, a reduction in measured substrate temperature is noticed – a linear decrease of approximately 25°C over the 5 min, and a total decrease in temperature of 60°C (from 430°C to 370°C) over the duration of the deposition cycle. This decrease in temperature could lead to a change in the stress state of the film. With lower deposition temperatures an increase in compressive stress could be due to less stress being annealed out (which correlates with the aforementioned increase in hardness). With shorter interruption times, this effect would be reduced leading to a decrease in drill life.

A TiN sample was deposited with an interruption time of 1 min and it was decided to apply 9 interruptions, the optimal number based on the observations made previously in Section 4.1.1. The TiN 9-INT 1 min coating was deposited on HSS and measurements of hardness,

adhesion and drill life were made in an effort to answer the question: *Does interruption time have an effect on film mechanical properties?*

4.1.2.1. Nanoindentation hardness

Hardness tests we completed on the surface of coated HSS samples. A Berkovich indenter was used to indent samples 100 times with a normal load of 40 mN. Results of measured hardness are plotted in Figure 4.11. Changes to hardness are not obvious so an ANOVA is completed and summarised in Table 4.6. The average values of hardness remain the same for the TiN STD and TiN 9-INT 1 min samples, within experimental error. The ANOVA test shows us that a statistically significant change in hardness has occurred, and this difference comes from the increase in hardness measured for the TiN 9-INT 5 min sample only. This small change in hardness is likely to increase drill life, but unlikely to be the sole cause of the 90% increase in coated drill life observed in Section 4.1.1.3.

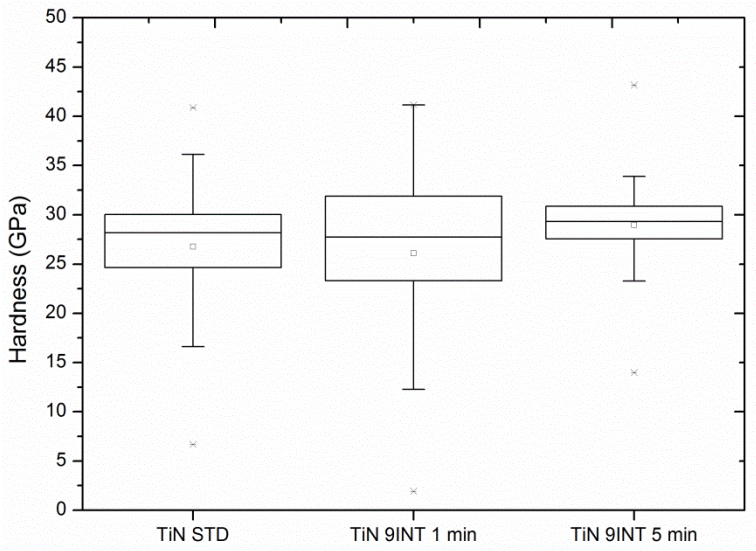

Figure 4.11: Box and whisker plot of nanoindentation hardness results.

Table 4.6: Single factor ANOVA of hardness measurements in Figure 4.11.

Summary of Hardness Data (GPa)

Groups	Count	Sum	Average	Variance
TiN STD	84	2248.0781	26.762835	38.184658
TiN 9-INT 1 min	94	2452.4026	26.08939	80.200849
TiN 9-INT 5 min	89	2577.8884	28.965038	17.815198

ANOVA

Source of Variation	SS	df	MS	F	P-value	F crit
Between Groups	408.3	2	204.155	4.419	0.0129	3.029
Within Groups	12195.7	264	46.196			
Alpha	0.05					

4.1.2.2. Drill testing.

A drill test was conducted with the test conditions outlined in Table 4.7, it is worth noting the significant increase in plate hardness when compared with the drill test in Section 4.1.1.2. Because of this, a decrease in the cutting speed is necessary to allow tools to cut without prematurely failing. The reason for this change in workpiece is due to difficulties in the supply of D2 tool steel from Bohler. Drills coated with TiN 9-INT 5 min films are tested alongside to allow comparison with previous results.

Table 4.7: Drill test conditions.

Cutting tool	HSS jobber drill – 6.35 mm diameter - deburred
Cutting speed	30 m/min
Feed rate	0.125 mm/rev
Hole depth	2.5 x Diameter (15.875 mm)
Test material (Hardness)	D2 tool steel (495 HL-D = ~215 HV [1kg])
Number of samples	10
Definition of wear	Audible screech

From Figure 4.12 we can see a decrease in drill performance with the introduction of 9 interruptions with a duration of 1 min. To check this change is significant, the results of a t-test are displayed in Table 4.8.

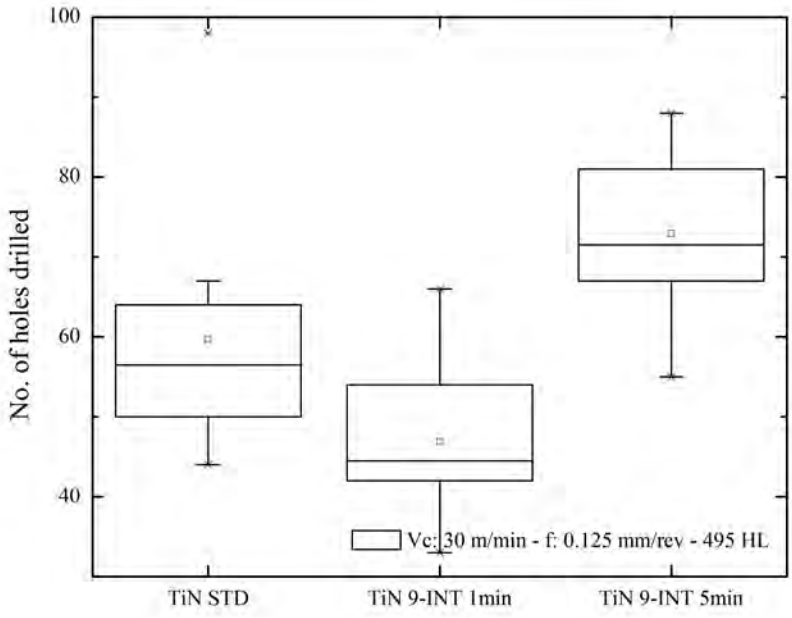

Figure 4.12: Box and whisker plot of drill test. Note plate material hardness and cutting speed.

Table 4.8: Two-sample, two-tailed t-test of drill test data (assuming unequal variances).

	TiN STD	TiN 9-INT 1 min
Mean number of holes cut	59.7	46.9
Variance	231.7	103.2
Observations	10	10
df	16	
t Stat	2.21	
P	0.0419	
t Critical	2.12	
Alpha	0.05	

The analysis shows the probability (P) that the difference between the two means can be explained by the variation in each sample is 4.19%. This is below the set confidence interval of 95% so we can say there is a difference between the means. Additionally, with a t-

statistic larger than the t-critical value, we can say a difference has been made. The result is close, but there has in fact been a significant decrease in the mean drill life with the introduction of 9 interruptions lasting 1 min – from 59.7 to 46.9 mean holes cut. The performance of the TiN 9-INT 5 min drills was tested alongside to allow comparison and it is clear that the performance of longer interruption times is greater than the TiN STD coating and a TiN coating with 1 min interruptions

4.1.2.3. Scratch testing.

TiN STD and 9-INT 1 min and 9-INT 5 min samples were analysed with the same conditions described in Section 4.1.1.2. The results for TiN STD and TiN 9-INT 5 min were already displayed in Section 4.1.1.2 (shown again here in Table 4.9). Results of the TiN 9-INT 1 min sample can be seen in Figure 4.16.

L_{c1} and L_{c2} remained consistent for the 1 minute interrupted and the standard sample. The effect of interruption time on this experiment is therefore insignificant or not detectable with this test and its selected parameters.

Table 4.9: Scratch test results for L_{c1} and L_{c2}.

Sample	L_{c1} (N)	L_{c2} (N)
TiN STD	70 ± 1	110 ± 1
TiN 9-INT 1 min	70 ± 1	110 ± 1
TiN 9-INT 5 min	70 ± 1	120 ± 10

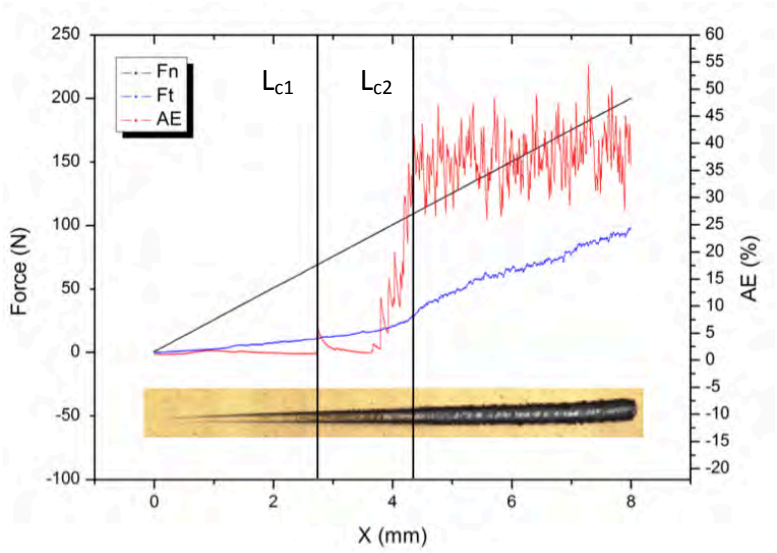

Figure 4.13: Scratch test for TiN 9-INT 1 min film on HSS substrate. Graph displays the normal load (Fn), friction force (Ft), acoustic emissions (AE) along with an optical micrograph of the associated scratch.

4.1.3. Material properties: a summary and remaining questions.

What is the effect of repeatedly interrupting the electric current supply to cathodic arcs during deposition of TiN films on microstructure and mechanical properties? What influence does the number of interruptions have on TiN film properties?

Statistical techniques have been utilised to state, with confidence, that increases in nanoindentation hardness and drill performance are evident with interrupted deposition of TiN coatings. The optimal number of interruptions for an increase in hardness and drill performance, when cutting D2 steel, was found to be 9 with an interruption time of 5 min. Decreasing interruption time decreased performance. Scratch testing showed some increase in the adhesive strength of the TiN 9-INT 5 min sample. However after consideration of variability in results, any differences in coating cohesive or adhesive strength remain inconclusive.

Do interruptions create a layered structure or disrupt continuous though-thickness grain growth?

Based on XRD characterisation and SAD in TEM, no change to the crystallography of interrupted TiN coatings is observed. Analysis of film cross-sections with SEM, TEM and high-resolution TEM show interruptions do not cause any layering effect. EDS conducted with SEM show no changes to film chemistry.

Does interruption time have an effect on film mechanical properties?

Longer interruption times have a significant influence on improving TiN film hardness and drill life. The cause of this effect is unknown. An increase in N pressure during an interruption could lead to a thin layer of a N rich TiN phase or some change to the phase stoichiometry, however these effects have not been noticed in XRD characterisation, TEM examinations or EDS analysis with SEM. Testing more samples with different interruption time and number of interruptions to give a more detailed trend would be ideal, however due to time constraints this is not completed in the following work, instead a thorough examination of the affect of interruptions on microstructure is investigated.

Another difference in deposition conditions for longer (5 min) interrupted samples is a linear decrease of ~25 °C over the 5 min. For 1 min interruptions a smaller decrease of ~10 °C occurs. Over the full deposition cycle, consecutive interruptions do not decrease the measured temperature significantly. Differences in thermal history could cause a reduction in annealing effects, and changes to N pressures could drive changes to the equilibrium phase. Although no changes in peak shape or position is noticed with XRD characterisation, an important material property to examine closely in solving these questions is residual stress. It can dictate performance and provide a window into film microstructure.

4.2. Residual stress analysis.

After measuring a significant increase in hardness in Section 4.1.1.1, interrupted samples are expected have an increased compressive residual stress [76]. In preliminary analysis of XRD residual stress, some questionable results were found (not shown here). Tests measured a decrease in compressive stress with an increase in hardness for the same three samples examined in Section 4.1.1 – hardness should increase with compressive residual stress in TiN films [76] This led to the use of an alternative XRD method for stress analysis. One ambiguity in the results was the effect of film thickness on stress, so an experiment that incorporated changes in coating thickness was also necessary.

In this section the use of combining two XRD stress analysis methods to elucidate the effect of interruptions during growth on the residual stress of TiN films is discussed. The $\sin^2\psi$ and crystallite group method (CGM), scanning the (220) peaks from all grains in the film and only (111) oriented crystallites respectively, were used to analyse residual stress. A complexity with residual stress is that it can change with coating thickness. It is necessary to explore the effect of thickness on residual stress in CAPD TiN, as well as interruptions and interruption time. TiN STD and TiN 9-INT 1 min samples 1.5, 3.5, and 6.5 µm thick, grown on HSS substrates, were examined in the ambition of understanding: *What is the effect of interruptions on residual stress of TiN films and is there any correlation between stress, thickness and 1 minute interruptions?*

Another experiment was later conducted with 1 min and 5 min interruptions for a 3.5 µm thick film using the CGM to measure residual stress after trends had been identified in the TiN 9-INT 1 experiments. The absence of 5 min interrupted samples in the first experiment was decided based on the need to gather an understanding of the effect of increased N pressures caused by interruptions, with minimal effects from the temperature change due to longer interruptions. The later experiment comparing stress for short and long interruption times was conducted to observe the effect of both the N pressure increase and temperature decrease experienced by films during interruptions. This detailed exploration of shorter interruption times also suits the demand from industry for an examination of reduced interruption times. The later experiment questions: *What is the difference in*

residual stress of TiN films with 1 and 5 minute interruptions; and attempts to understand*: how is any difference related to further reduced temperatures in 5 minute interruptions?*

4.2.1. Stress analysis: $\sin^2\psi$ and CGM

Usually, for both methods, the ψ angle is in-plane or parallel to the incident beam, here the ψ angle is perpendicular (see Figure 4.14), enabling the use of higher ψ angles without the incident beam impacting the sample edge due to goniometer geometry.

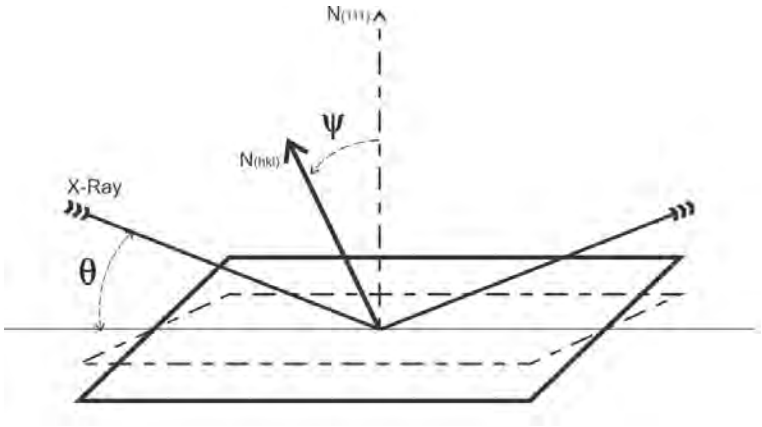

Figure 4.14: Perpendicular shift of ψ to detect various hkl planes.

The $\sin^2\psi$ method measures the d-spacing of a chosen plane at different ψ angles. Using the equation below, assuming biaxial strain, and known x-ray elastic constants the stress can be calculated from the slope of the line when d-spacing is plotted versus $\sin^2\psi$.

$$\frac{d_\psi - d_0}{d_0} = \sigma \frac{(1 + v_{hkl})}{E_{hkl}} sin^2\psi - \frac{v_{hkl}}{Y_{hkl}} (\sigma_1 + \sigma_2)$$

In the CGM [99], multiple planes from (111) crystallites with reflection normals at different ψ angles are chosen using:

$$\psi = cos^{-1} \frac{h_1h_2 + k_1k_2 + l_1l_2}{\left[\left({h_1}^2 + {k_1}^2 + {l_1}^2\right)\left({h_2}^2 + {k_2}^2 + {l_2}^2\right)\right]^{\frac{1}{2}}}$$

Then the corresponding 2θ position of the plane reflection can be calculated with:

$$n\lambda = 2d_{hkl} \sin\theta$$

CGM requires the conversion of measured d-spacings (of each selected plane) to values of stressed lattice parameter (a_ψ). Assuming the sample is cubic, the lattice parameter can be calculated:

$$a_\psi = d_\psi(h^2 + k^2 + l^2)$$

Residual stress is then calculated using the appropriate x-ray elastic constants for each plane (see

or values - tensors are used to provide directionally accurate elastic constants for each plane normal).

$$a_\psi = \sigma a_0 f(\psi) + a_0$$

$$\text{Where: } f(\psi) = \frac{(1+\nu_{hkl})}{E_{hkl}} sin^2\psi - 2\frac{\nu_{hkl}}{E_{hkl}}$$

4.2.2. X-ray Diffraction measurements.

Stress analysis scans were completed with a PANalytical X'Pert Pro materials research diffractometer using a Cu Kα source. Before each scan the goniometer is calibrated with the sample surface to ensure an accurate zero degrees position and hence a sample that is in precisely the same plane as the goniometer, ensuring accurate θ and ψ angles. The $\sin^2\psi$ method was performed on all samples at a 2θ angle of 61.8 ° within a 3.5 ° range to scan the (220) peak of TiN, with a step size of 0.02 ° and scan time of 50 sec/step. The ψ angle was changed from 0-90 ° in increments of 9 °. For the CGM, selected planes, each plane's ψ ° reflection normals relative to the sample surface oriented (111) and 2θ angles are shown in Table 4.10 along with their associated tensor values from [100]. These planes were scanned with a step size of 0.02 ° at 10 sec/step. Tensors are a vector form of an x-ray elastic constant used to explain a different plane's resistance to strain; the values of S_1 and ½ S_2 are components of a tensor.

Table 4.10: Lattice planes scanned in CGM - associated ψ ° and 2θ reflection angles and tensors.

h	k	l	Ψ(°)	2θ(°)	S_1	$1/2S_2$
1	1	1	0.00	36.41	-0.49	2.89
2	0	0	54.70	42.68	-0.42	2.67
2	2	0	35.00	61.71	-0.47	2.83
3	1	1	29.47	73.90	-0.45	2.77
3	3	1	21.97	104.14	-0.48	2.85
4	2	0	39.17	108.64	-0.45	2.77
4	2	2	19.46	124.87	-0.47	2.83

4.2.3. Thickness vs. stress.

A simple examination of stress changes with increased thickness (Figure 4.15 and Figure 4.16) shows the stress becoming less compressive as the thickness of TiN films deposited on HSS change from 1.5 µm to 6.5 µm. Previous studies have found changes in stress with thickness to plateau around -1 to -1.5 GPa at 2 µm for sputter deposited TiN films [101, 102] and 1.5 µm for ZrN [103] on Si substrates. Köstenbauer et al [101] found the compressive stress of sputtered TiN films deposited on (100) Si substrates reduces with an increase in coating thickness up to 2.9 µm, Kamminga et al [104] observed the compressive stress of sputtered TiN deposited on tool steel substrates reduced with an increase in coating thickness up to 6.2 µm, and Machunze & Janssen [102] show the compressive stress of unbalanced magnetron sputtered TiN deposited on (001) Si substrates reduces with an increase inciting thickness up to 1.9 µm. These findings match observations made here where compressive stress reduces up to a coating thickness of 6.5 µm. Interruptions during growth seem to have no effect on this trend. The absolute change to stress with interruptions is unchanged by thickness. It is possible that stress gradients exist in these films and the differences measured simply come from a change in the diffraction volume [102]. Typically in PVD films grown at similar conditions to these films, grains will grow larger in diameter as the thickness increases and we see this in 3.5 µm thick films in TEM (Figure 4.17) and although not observed it is expected to be more pronounced in the thicker 6.5 µm film. Larger grain sizes lead to less grain boundaries and a lower defect density - an

eventual decrease in compressive residual stress results [2]. Thicker films will then have a reduced compressive strain, which is as observed here.

The effect of 9 interruptions (1 min) on biaxial stress change should be most visible in the thinnest coating with 6 interruptions per micron of coating, and almost invisible in the 6.5 μm coating - only 0.722 interruptions per 1 um of coating. Surprisingly, this is not the case. Notice that the absolute change in stress due to interruptions is independent of film thickness and associated grain size. The effect of interruptions on residual stress does not appear to be influenced by grain size – a very different finding to in-situ stress measurements found in the literature where interruptions and grain size correlate (stress changes are more pronounced with a smaller grain size). Furthermore: previous findings, in Section 4.1.1.4, show that interruptions do not influence grain size; the number of interruptions and total interruption time had no effect on grain size from film cross-section observations in the TEM. In these samples, it is therefore unlikely for interruptions to influence grain size, there will only be a difference in grain size at different film thickness. Interestingly, when grain size is small (as in the 1.5 um samples), the absolute change in stress due to interruptions is the same as with the larger grain size at thicknesses of 3.5 um and 6.5 um. Therefore, grain size has no influence on the mechanism by which interruptions change the residual stress state of TiN films. This correlates with Chason's model [83], discussed in Section 2.5.1, which proposes a dependence of intrinsic stress on growth rate. With a faster growth rate, less compressive stress will develop post-coalescence. Interruptions are increasing the total time taken to grow a film, but not strictly changing a growth rate during arcing, hence it is possible that the total interruption time, more so than the number of interruptions, is causing an increase in compressive stress.

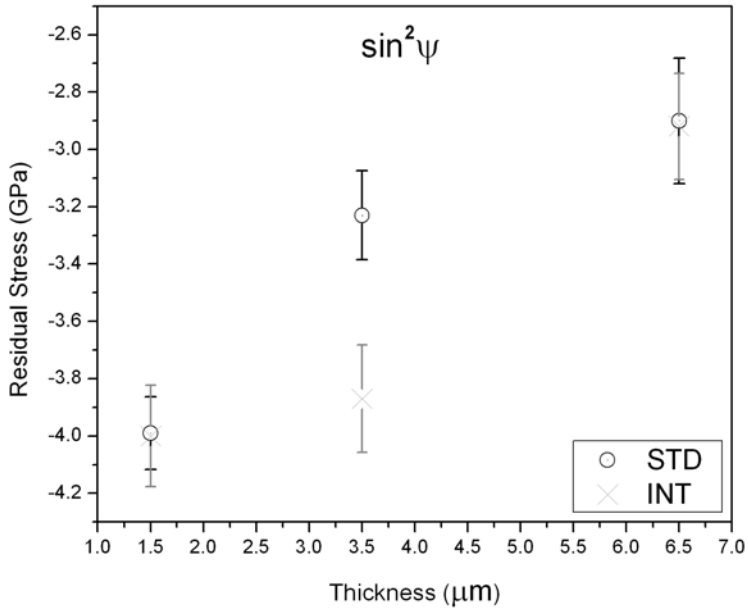

Figure 4.15: $\sin^2\psi$ residual stress of TiN STD and TiN 9-INT 1 min samples at different thicknesses.

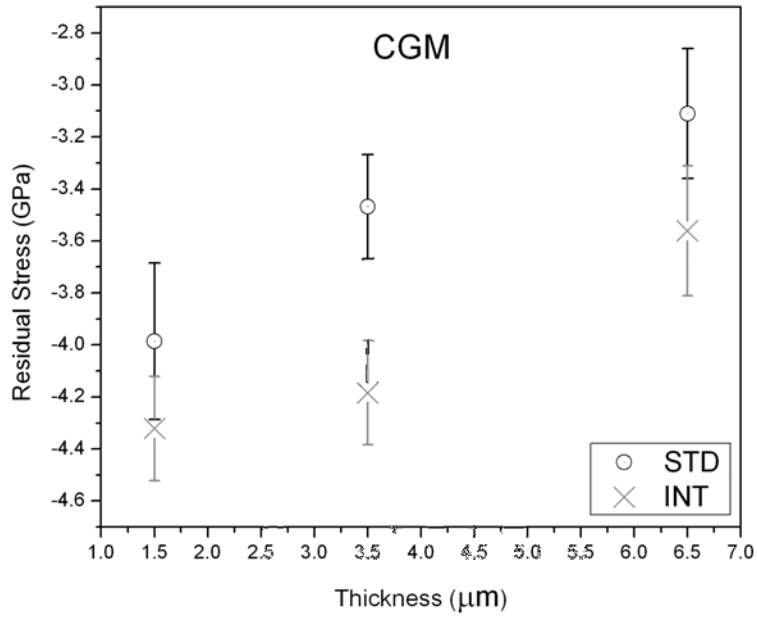

Figure 4.16: CGM residual stress of TIN STD and TiN 9-INT 1 min samples at different thicknesses.

4.2.4. $\sin^2\psi$ vs. CGM.

Comparing these two methods of stress analysis can help to draw some useful conclusions about the state of films and textured materials. As we can see in Figure 4.17, during early stages of film growth many random orientations of TiN crystals will form, where (220), (200) and (111) are seen. Later, (111) is the preferred orientation of TiN with these deposition conditions. If we consider $\sin^2\psi$ first, the method scans the (220) plane peak of TiN at

various ψ angles between 0-90 °. The films examined in this study are highly (111) oriented polycrystalline grains of TiN, hence the (220) plane reflections are very weak, except at Ψ = 35 ° where this plane reflects in the (111) oriented crystallites. So the majority of detected X-rays in the $\sin^2\psi$ method scanning the (220) peak of TiN, are from early stages of the film where (220) crystallites remain.

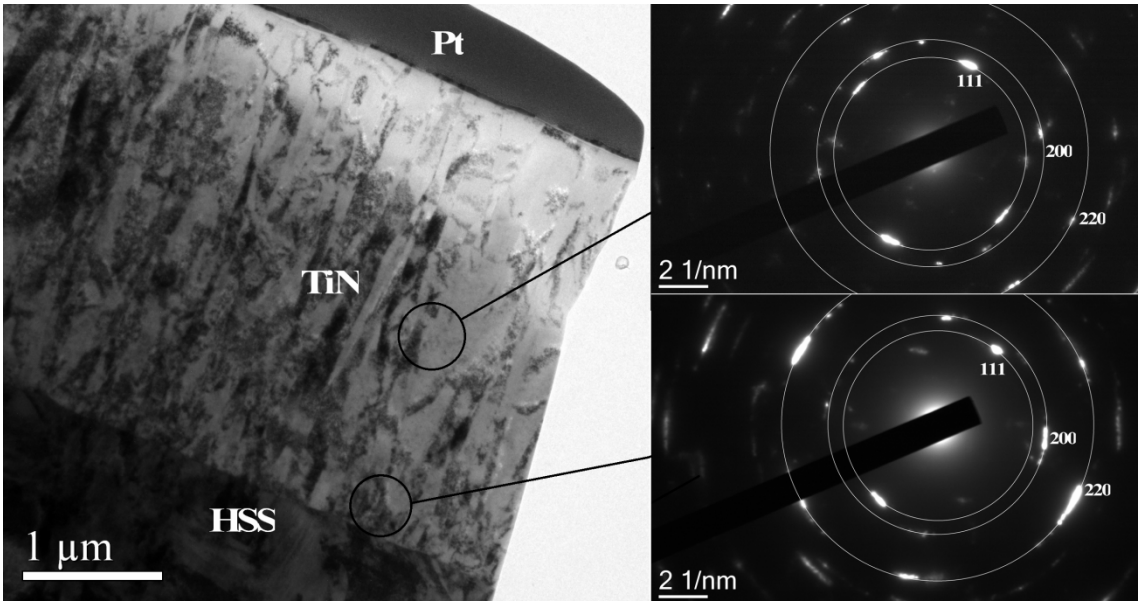

Figure 4.17: TEM micrograph and SAD patterns of FIB prepared 3.5 µm TiN 9-INT 1 min sample, showing (111) oriented film, also randomly and (220) oriented early stage film.

The CGM is designed to scan reflections of (111) oriented (normal to the coating surface) grains of fibre textured films at various ψ angles to detect changes in d-spacing due to strain. CGM shows differences in stress between STD and INT films, but $\sin^2\psi$ does not, with the exception of the 3.5 µm sample (compare Figure 4.15 and Figure 4.16). This indicates that stress in (111) crystallites is more dependent on interruptions than in (220) crystallites. A crystallite is defined as a group of crystals that satisfy the Bragg equation, adding intensity to reflections and peaks observed in XRD. Crystallites are differentiated from grains because an entire grain will not satisfy the Bragg equation and produce a peak, some of the grain within a diffraction volume will not perfectly align and provide intensity, only crystallites will. Eshelby states in his continuum theory of lattice defects, that the [111] direction has a lower defect interaction energy than the [110] direction [105]. Consequently (111) planes will appear more highly stressed than (220) planes if defects are present in the lattice, due to the higher level of strain experienced in the (111) direction. Abadias [106] has

shown that (111) grains are more sensitive to point defect related strain than (001) grains, and based on Eshelby's work, (220) will behave in a similar manner. If interruptions are causing an increase in the number of defects in the lattice, stress in interrupted samples measured with CGM should increase, as evident. Only when combining these two methods are we able to extract this information.

4.2.5. Lattice parameter.

A change in unstressed lattice parameter (a_0) calculated with the CGM for 1.5 µm, 3.5 µm and 6.5 µm TiN films can be seen in Figure 4.18 (a), (b), (c) as the y-intercept. In all interrupted samples, the lattice has expanded compared to the standard TiN film. Kamminga *et al* [107] state that growth defects create lattice distortions associated with a hydrostatic stress component and explains that these defects could be Ar atoms on N sites, Ti atoms on N sites and N atoms on tetrahedral sites, and concludes that growth stress is caused by Ti on N sites and, depending on the concentration of Ar in the film, Ar on N sites. Oxygen too is a commonly found impurity in deposition chambers. It is notoriously difficult to remove from internal components of chambers and can be found in target materials, hence it is a potential impurity detected with this analysis. The detected expansion of the lattice, evident as an increase in a_0 in interrupted samples, supports a higher concentration of defects in (111) oriented grains, as discussed in Section 4.2.5.

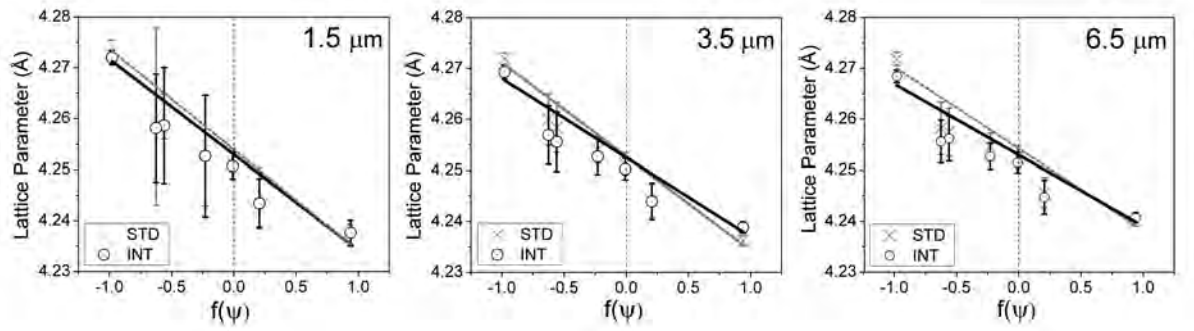

Figure 4.18: CGM plots of a_ψ vs. f(ψ) showing a_0 at y-intercept: (a) 1.5 µm, (b) 3.5 µm and (c) 6.5 µm TiN films. The black linear fit is for TiN STD films and the grey linear fit is for TiN 9-INT 1 min samples.

4.2.6. Stress vs. interruption time.

The effect of longer interruption times on residual stress was observed with XRD using the CGM. These scans were conducted at a later date to the previous scans so were repeated for the TiN STD and TiN 9-INT 1 min samples to ensure an accurate comparison with a TiN 9-

INT 5 min sample. All samples were 3.5 µm in thickness. The results of this experiment are shown in Figure 4.19. In this case, the differences in stress calculated for TiN STD and TiN 9-INT 1 min are less obvious, however the stress for the longer interruption times of the TiN 9-INT 5 min sample is considerably more compressive. This result follows a similar trend to hardness data collected for the same samples in Section 4.1.2.10. However, it is still unknown as to what effect of the change in temperature with 5 min interruptions has on residual stress and TiN films. Reduced annealing effects (and more defects) could be responsible for the additional compressive strain measured in longer 5 min interrupted samples.

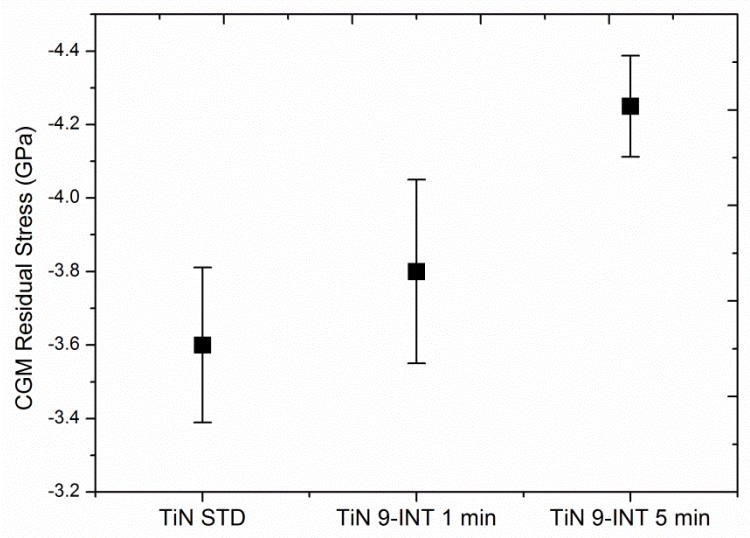

Figure 4.19: The effect of longer interruption times on XRD residual stress, measured with the CGM.

4.2.7. Residual stress analysis: a summary and remaining questions.

What is the effect of interruptions on residual stress of TiN films and is there any correlation between stress, thickness and 1 minute interruptions?

The $\sin^2\psi$ method does not reveal any changes in stress with interruptions however, measurements using the CGM show increased compressive stress and an increased a_0 in the resultant TiN films. A comparison of results from both XRD methods indicates that an increased compressive stress from interruptions could be due to an increased number of defects in (111) oriented grains, which would also affect a_0 as evident.

In both methods, compressive stresses are found to decrease with increased thickness of films. This is linked to the larger grain sizes of thicker coatings and associated reduction in

grain boundary density. Because 1 min interruptions cause a consistent absolute increase in compressive residual stress with changing thickness and associated grain size, it is sensible to state that the effect of interruptions on residual stress is not influenced by grain size. This is not to say that interruptions do not influence grain size, but grain size does not appear have an influence on the effect of interruptions. The total interruption time then becomes a more sensible correlation, and this finding is supported by the larger increase in compressive residual stress observed with longer 5 min interruptions.

What is the difference in residual stress of TiN films with 1 and 5 minute interruptions, and how is any difference related to further reduced temperatures in 5 minute interruptions?

The effect of 9 interruptions (1 min) during growth of TiN films on residual stress is an increase in the compressive residual stress of (111) oriented grains. This change in stress is believed to be caused by defects being incorporated into or not annealed out of (111) oriented crystallites during interruptions. An increased interruption time of 5 min appears to further increase compressive stress of TiN films, a result corroborated by previous hardness measurements and trends observed in drill test results. Further reduced substrate temperatures experienced by samples during longer interruption times hint towards an annealing effect whereby films are annealed less, leaving more defects, and higher compressive stress. Increased compressive stress in the TiN 9-INT 5 min sample could also be a similar response of residual stress to grain size discussed in Section 4.2.3. Perhaps the grain size is being reduced by interruptions and a corresponding increase in residual stress is noticed.

An additional finding from these experiments is that the combination of residual stress results from $\sin^2\psi$ and CGM can be readily applied to the detection of residual stress in randomly oriented grains and fibre textured grains and can be compared to assist in linking stress to sample microstructure.

4.3. A search for defects: the effect of interruptions on microstructure.

Interruptions during growth in CAPD have caused measurable changes to TiN films. These include an increase in hardness and drill life; no layering effects or discontinuous through-thickness grain growth are observed; and residual stress is more compressive.

Although they have not been directly observed in microscopy, defects are suspected to be the cause of additional compressive stress in (111) oriented grains. These defects were not discovered in TEM FIB cross-sections. This could be due to the difficulties in the TEM technique at discovering unknowns. When changes to a sample are not obvious or fully understood, the technique is challenging. It requires almost exact knowledge about what to investigate before it is able to identify and characterise a finding. Later, in Section 4.3.5, cross-sections are carefully analysed in the TEM; and even with a targeted approach, findings are not unambiguous.

The noticeable trend between changes to compressive stress in (111) oriented grains and interruptions is: as the number of interruptions and the duration of each interruption increases, there is an increase in compressive stress. It still remains unknown as to whether lower temperatures or higher N pressures caused by interruptions are responsible however, the total time spent in an interruption state is likely to be an important factor. Because of this trend and observations made so far, only TiN STD, TiN 9-INT 1 min and TiN 9-INT 5 min samples will be analysed further. In some cases only the TiN 9-INT 5 min sample is examined against the TiN STD sample, as it will provide the most contrast against the TiN STD film.

Some questions that remain from the previous analysis are apparent: Is the suspected increase in defects related to reduced grain size, or are impurities being included in the lattice? If grain size is consistent with and without interruptions, what are the impurities?

4.3.1. X-ray diffraction characterisation: Rietveld analysis

Defects can manifest in a number of ways: the simplest being a reduction in grain size and an associated increase in the volume fraction of grain boundaries in the film. Observations in TEM, of small cross-sections, have not indicated a change in grain size with an introduction of interruptions, however this only provides a microscopic view of the total

grain size. XRD Rietveld analysis allows for a macroscopic view and can deliver a more accurate grain size for each sample. Rietveld analysis is a modelling technique used to provide detailed crystallographic information from a diffraction pattern. A line is made to fit the measured diffraction pattern based on physical crystallography of declared phases. Once the calculated pattern is made to fit the observed pattern, information about crystallite size, microstrain and texture can be extracted.

Characterisation of TiN STD, TiN 9-INT 1 min and TiN 9-INT 5 min samples was conducted with slow scan rates using the aforementioned PANalytical diffractometer, and scans were analysed with MAUD software [108-111]. For line broadening and size-strain models, Popa rules were used to fit the diffraction pattern of each sample [110]. An harmonic function was used to account for a fibre texture. Four phases were included in the analysis: TiN, Fe, VC and Fe_3W_3C. These phases were chosen after careful analysis and matching of the diffraction pattern to known peak positions; Fe, VC and Fe_3W_3C are prominent phases of HSS that are have observed in XRD [112].

The diffraction patterns, Rietveld fit and residuals plot can be seen in Figure 4.20, Figure 4.21, and Figure 4.22.

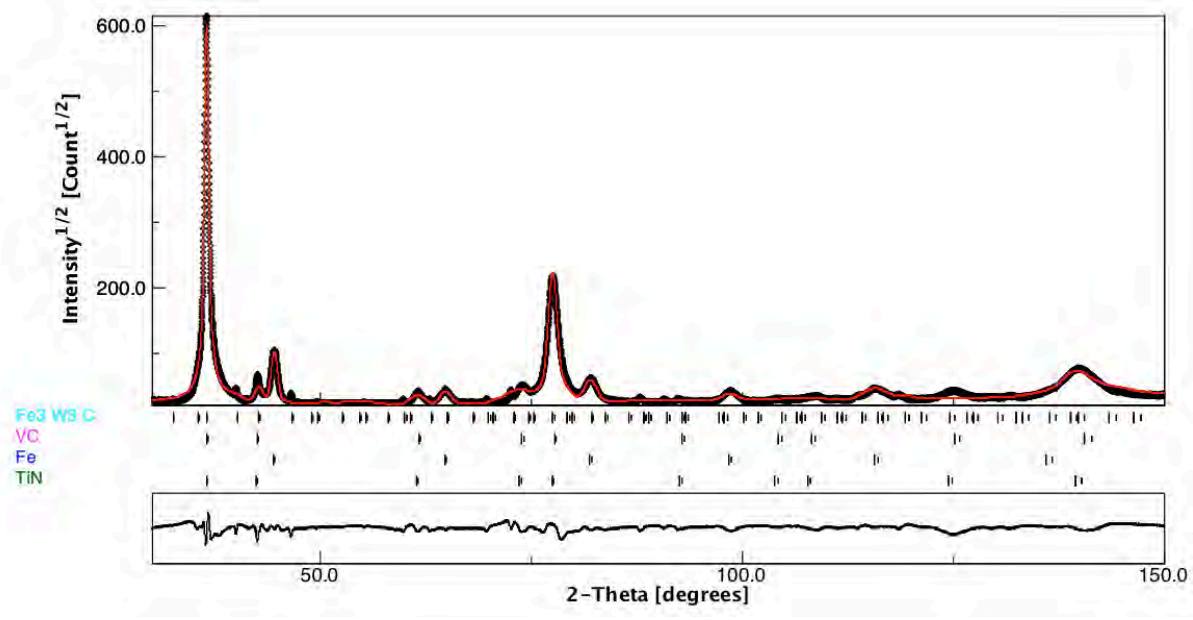

Figure 4.20: XRD 2theta diffraction pattern (black) and MAUD Rietveld line analysis (red) of TiN STD coating on HSS. Peak positions for TiN, Fe, VC and Fe_3W_3C labelled. Residuals plot below.

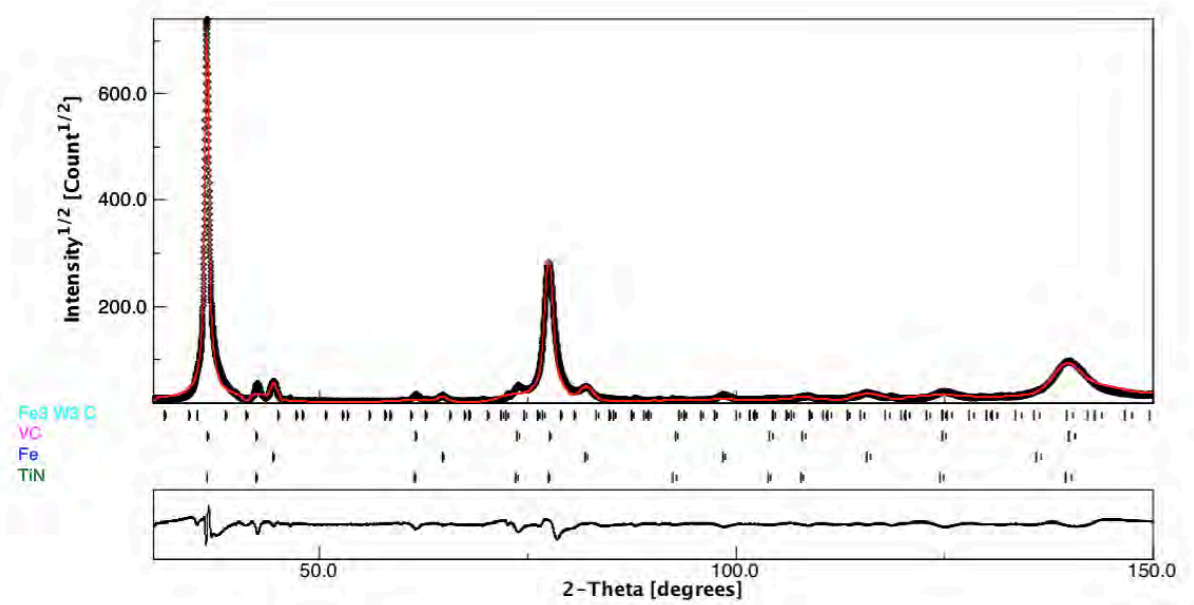

Figure 4.21: XRD 2theta diffraction pattern (black) and MAUD Rietveld line analysis (red) of TiN 9-INT 1 min coating on HSS. Peak positions for TiN, Fe, VC and Fe_3W_3C labelled. Residuals plot below.

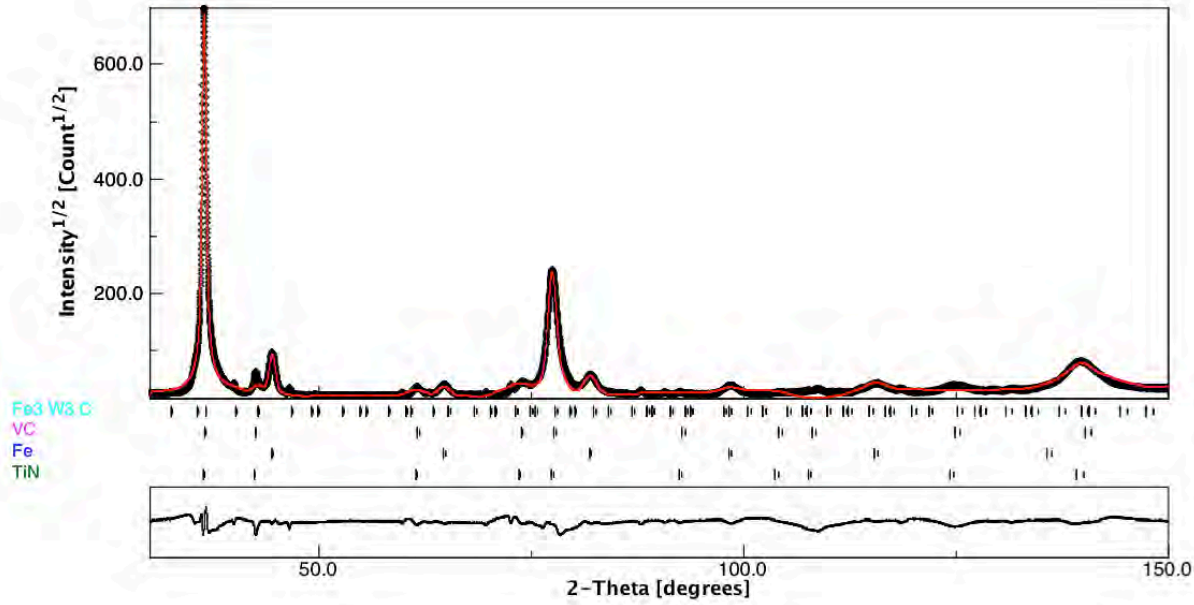

Figure 4.22: XRD 2theta diffraction pattern (black) and MAUD Rietveld line analysis (red) of TiN 9-INT 5 min coating on HSS. Peak positions for TiN, Fe, VC and Fe_3W_3C labelled. Residuals plot below.

Crystallite size and microstrain values acquired from these diffraction patterns are summarised in Table 4.11. The crystallite size is not consistent for different plane normal directions; they are smallest in the (111) direction and largest in the (200) direction. This can be ascribed to the columnar structure of films; in these samples, with (111) fibre textured high aspect ratio grains, (111) crystallites will be the smallest as they are normal to

the sample surface, and as the plane normal directions possess a higher angle (closer to being in-plane with the sample surface), the crystallite size will increase – as seen with (200) planes in Table 4.11. The variation in results, comparing the same plane directions, between all samples is minor. There is a minor measured increase in crystallite size for the TiN 9-INT 1 min sample, and the differences between TiN STD and TiN 9-INT 5 min are insignificant. Trends for microstrain are similar, showing a slight decrease in microstrain with the TiN 9-INT 1 min sample.

Table 4.11: Crystallite size and microstrain values of various plane reflections of each sample, as calculated with Rietveld analysis.

Crystallite Size (Å)	TiN STD	TiN 9-INT 1 min	TiN 9-INT 5 min
(111)	502	536	523
(200)	4125	4240	4172
(220)	689	704	690
(311)	985	1009	982

Microstrain	TiN STD	TiN 9-INT 1 min	TiN 9-INT 5 min
(111)	0.0037	0.0034	0.0036
(200)	0.0025	0.0027	0.0025
(220)	0.012	0.014	0.012
(311)	0.018	0.020	0.018

The film texture calculated with this analysis is displayed in pole figures for each sample, see Figure 4.23, Figure 4.24 and Figure 4.25. The results show a strong (111) fibre texture for all three samples, fitting with literature for TiN films deposited with CAPD using a bias voltage [76]. No changes in texture are observed for interrupted samples.

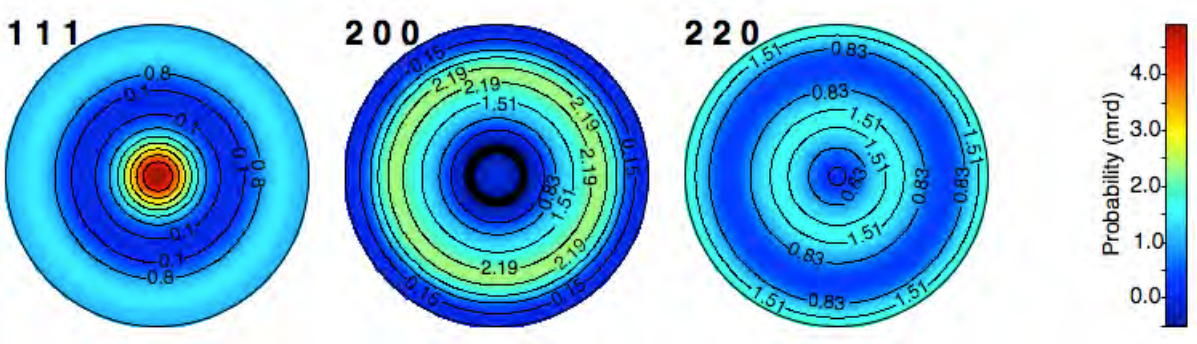

Figure 4.23: Pole figure plots for TiN STD film on HSS. Generated with MAUD from Rietveld analysis.

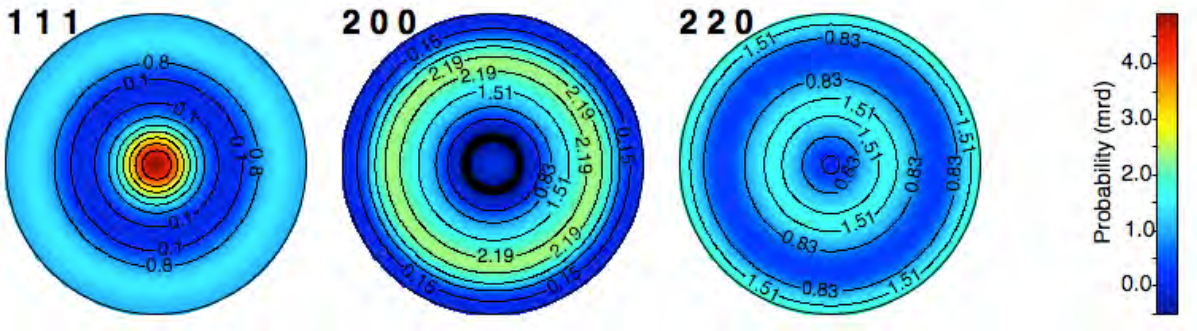

Figure 4.24: Pole figure plots for TiN 9-INT 1 min film on HSS. Generated with MAUD from Rietveld analysis.

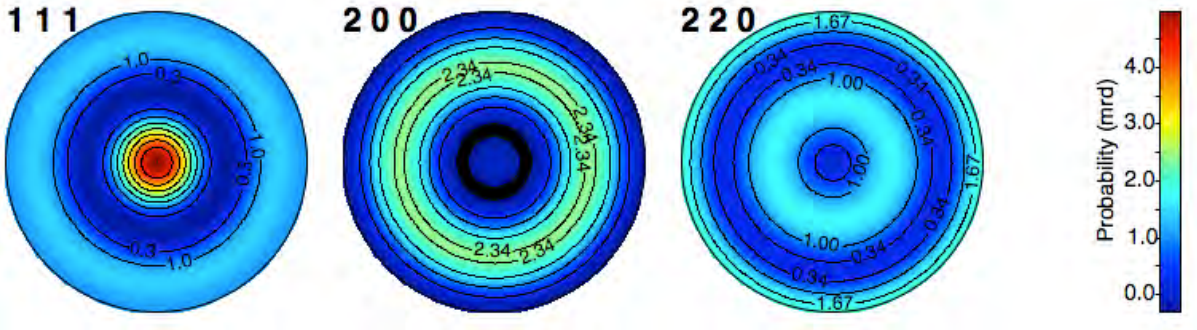

Figure 4.25: Pole figure plots for TiN 9-INT 5 min film on HSS. Generated with MAUD from Rietveld analysis

4.3.2. X-ray Photoelectron Spectroscopy.

With the lack of any correlation between interruptions, their duration, and grain size measured with Rietveld analysis, the suspected increase in defects due to increased grain boundary volume fraction is unlikely. This leaves the possibility that the inclusion of impurities is responsible for the increase in defect density in interrupted TiN films.

Impurity defects can include a number of things: misplaced atoms in the TiN lattice structure - which could be oxygen from inside the chamber atmosphere; unexpected elements from the chamber walls, fixtures or targets; Ti or N in incorrect locations; and trapped Ar from the gas environment.

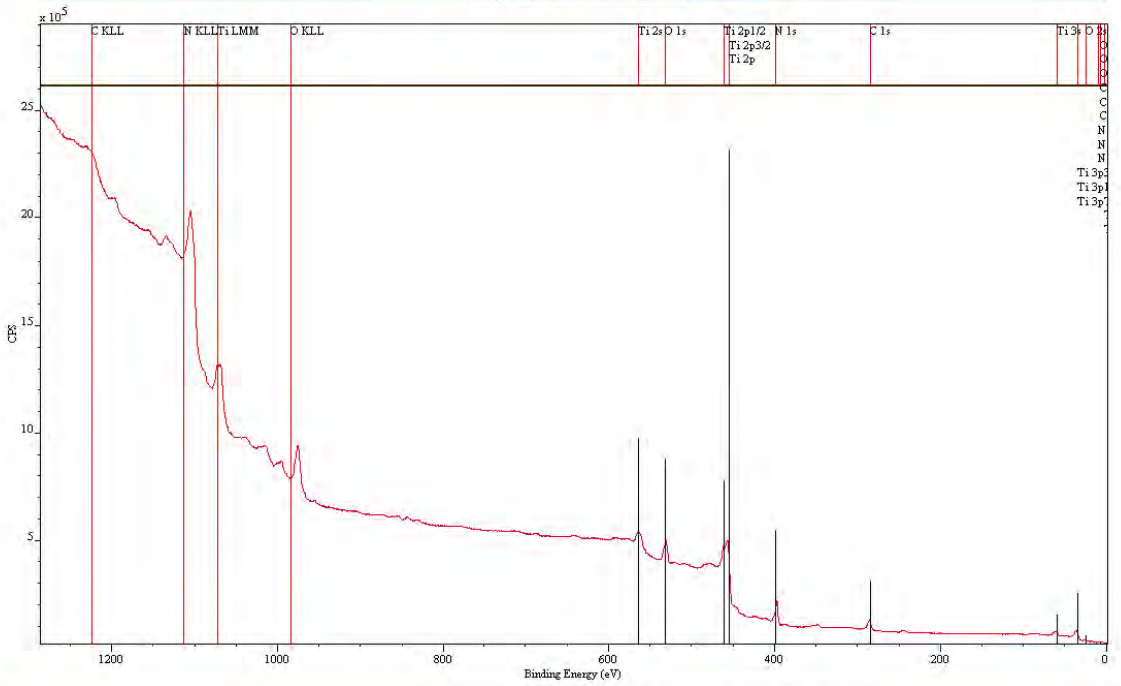

Figure 4.26: Exploratory XPS scan of near surface of TiN 9-INT 5 min sample.

Exploratory X-ray photoelectron spectroscopy (XPS) was conducted on the TiN 9-INT 5 min sample to survey film elements. The sample surface was cleaned with an ion etch to remove any oxidation layer caused by atmospheric exposure. The survey found no unexpected elements in the binding energy scan.

Immediately after triggering vacuum arcs, the composition of the plasma is likely to include water vapour from the chamber walls, even in high vacuum [65]. This could mean that when cathodic arcs are initiated after an interruption, oxygen and hydrogen impurities can be included in the film. Detecting hydrogen in a film is more difficult, but oxides can be detected in XPS. Hence, it was deemed essential to conduct a depth profile analysis of oxygen concentrations in XPS of an interrupted sample to find a point where an interruption occurred.

Table 4.12: XPS instrument parameters.

Instrument	ESCALAB 250 Xi
Manufacturer	Thermo Scientific, UK
Background vacuum	better than 2E-9 mbar
X-ray source	mono-chromated Al K alpha (energy 1486.68 eV)
Power	150 W (13 kV x 12 mA)
Spot size	500 µm
Photoelectron takeoff angle	90 degrees
Pass energy	100 eV for survey scans, or 50 eV for depth profiling region scans
Software	Avantage
Spectrometer calibration	Au 4f7 = 83.96 eV, Ag 3d5 = 368.21 eV, Cu2p3 = 932.62 eV
Binding energy reference	C 1s = 285.0 eV for adventitious hydrocarbon
Ar ion beam	3 KeV
Ion beam current	10 µA
Etched area	2 mm x 2 mm
Reference etching rate	0.66 nm/s

A depth profile analysis of an interrupted TiN coated HSS sample was conducted to observe any changes in the concentration of Ti, N and O throughout the 3.5 µm thickness. The coating examined was TiN 9-INT 5 min. Detailed scan parameters are specified in Table 4.12. Binding energy surveys were completed for O1s, Ti2p and N1s peaks at more than 570 steps through the thickness of the film to ensure an interrupted section was encountered. Results of the scan can be seen in Figure 4.27, also labelled are the approximate depths at which an interruption was programmed during deposition.

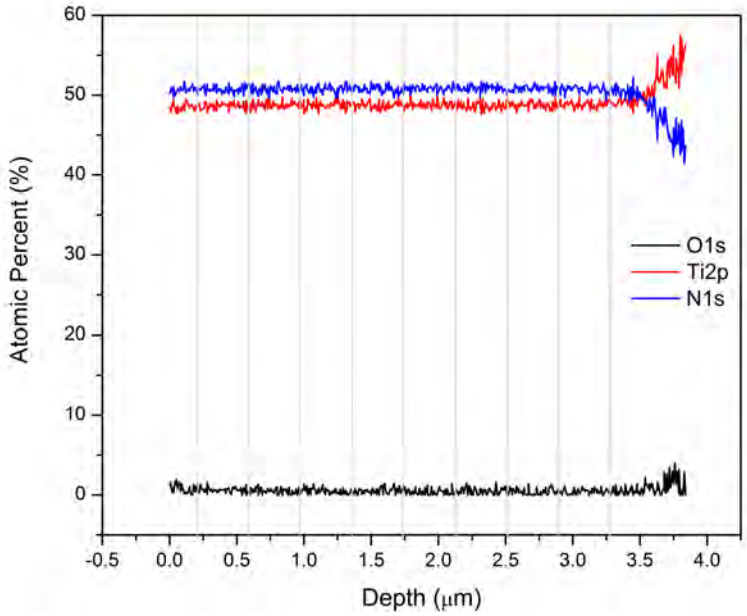

Figure 4.27: XPS atomic percentage depth profile or TiN 9-INT 5 min sample on HSS. Atomic percentages of Ti, N and O shown. Vertical grey lines indicate the approximate location of interruptions, according to the deposition process recipe.

Ti and N percentages remain constant throughout the thickness of the film, the Ti atomic percentage was just less than 50% and N just above 50%. A higher concentration of oxygen was noticed in the first few layers of the film, this is likely to be due to oxidation of the sample surface from atmospheric exposure. Thereafter oxygen was close to non-existent and no pattern was noticed to give evidence that interruptions during film growth cause oxygen impurities in CAPD TiN films.

The Ti, N and oxygen levels change at a depth of ~3.5 µm. This is the interface of coating and substrate. To confirm the finish point was in fact the substrate, a survey of elements was conducted and can be seen in Figure 4.28. Fe and alloying elements typical for M2 HSS can be seen (e.g. Cr, Mo, W and V), indicating the coating was penetrated.

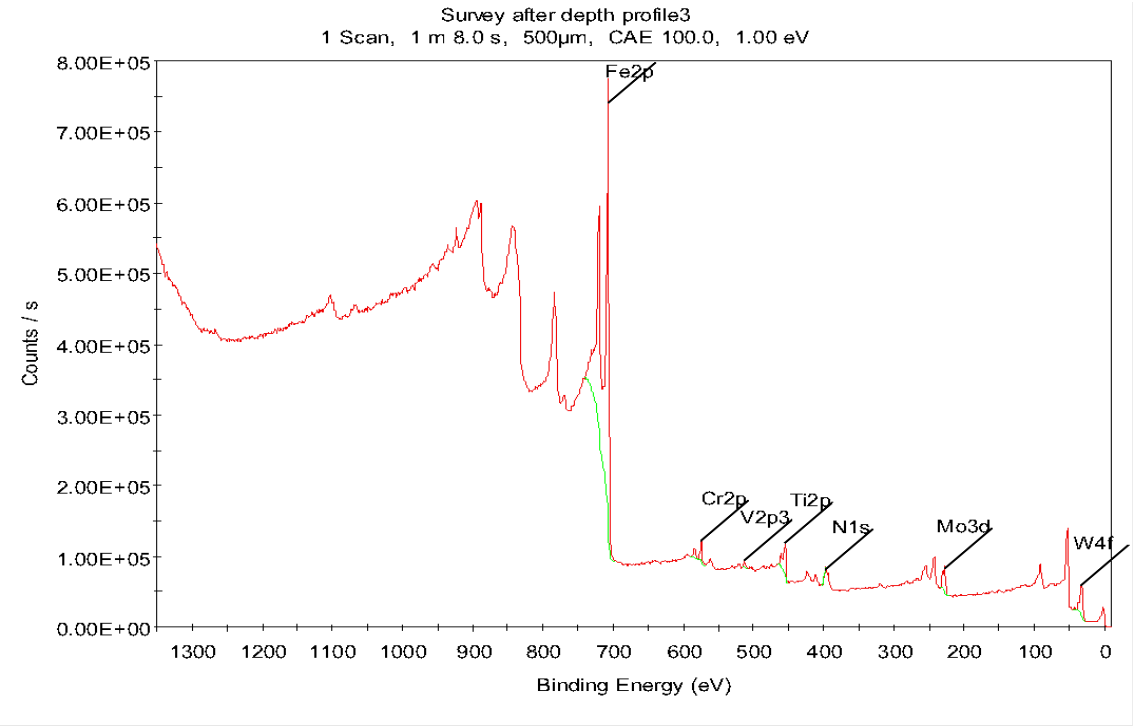

Figure 4.28: Survey of sample after 40 000 seconds etch time.

4.3.3. Electron Backscatter Diffraction.

The search for defects has thus far been unsuccessful in finding an impurity element. No unexpected elements are detected in a near surface survey and no oxides are outstanding throughout the thickness of the TiN 9-INT 5 min sample. Another possibility is some abnormality in the crystallography of interrupted TiN films. EBSD can provide location specific, through-thickness crystallography (from a cross-section) with conventional mechanical polishing preparation methods. The following EBSD scans provide phase analysis, grain dimension information and crystallographic texture. Mapping used a JEOL 7001 field-emission gun SEM equipped with an Oxford Instruments Nordlys-II(S) EBSD detector and post processing was completed with the Channel 5™ software package. Scan settings: acceleration voltage of 15 kV, probe current of 3.5 nA, working distance of 12 mm, tilt angle of 70° and a step size of 0.05 µm.

Figure 4.29 shows the Kikuchi band contrast of the measured area, brighter regions indicate where diffraction was intense and darker regions where diffraction is less intense or non-existent. This image provides some clue as to the quality of the map, and in this case the diffraction is adequate for the majority of the film cross-section, except for areas closer to

the substrate interface where grain size is so small that the 0.05 µm step size is too large or the interaction volume of the electron beam too large to resolve the crystal structure.

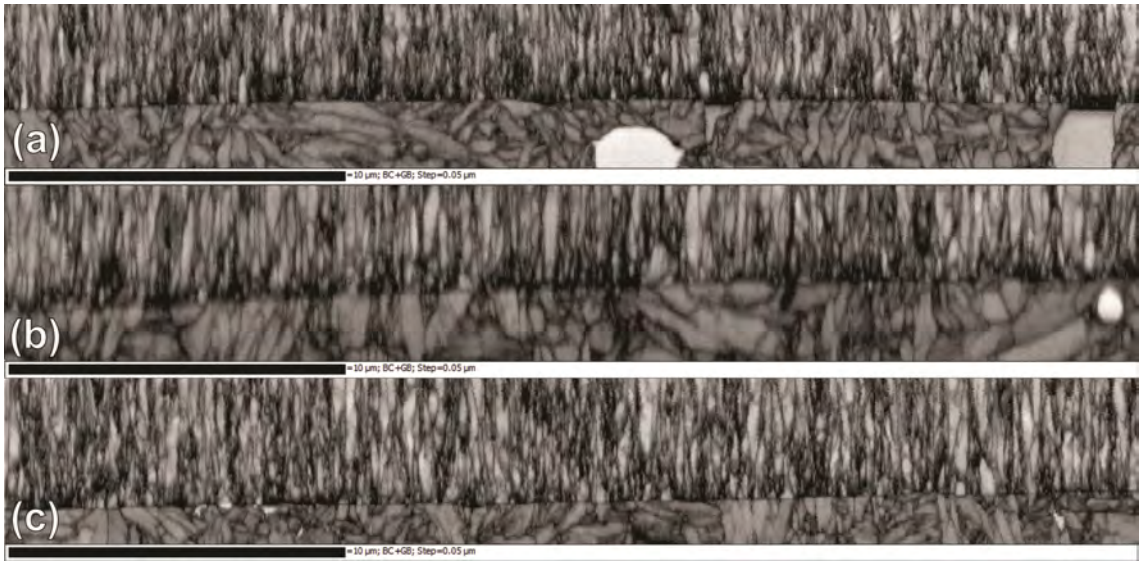

Figure 4.29: EBSD band contrast map - (a) TiN STD, (b) Tin 9-INT 1min, (c) TiN 9-INT 5min. The black micron bar in the bottom left of each image is 10 µm in length. Darker areas indicate where diffraction was minimal and less Kikuchi patterns were resolved.

Channel 5™ provides grain boundary statistics through a grain boundary line intercept function (Table 4.13). Grain boundaries are defined as an orientation mismatch of greater than 15 degrees. Values indicate some change to the mean grain size, however standard deviations are far too large to allow for any significant differentiation. The minimum grain size is limited by the mapping step size and not representative of the real minimum grain size. Regardless, the trends are similar to grain size measurements with Rietveld analysis (Section 4.3.1) – the absolute values are different as this technique measures grains whereas XRD takes measurements from crystallites.

Table 4.13: Grain size statistics from EBSD maps. Values are distances measured from grain boundary intercepts with many horizontal lines drawn on maps. HKL Tango software used to produce data.

	TiN STD	TiN 9-INT 1 min	TiN 9-INT 5 min
Mean Grain Size (μm)	0.21	0.26	0.20
Standard Deviation	0.13	0.17	0.13
Minimum Grain Size (μm)	0.05	0.05	0.05
Maximum Grain Size (μm)	1.28	1.95	1.55

Figure 4.30 is a phase map of the three TiN films on HSS substrates. The red colour corresponds to bcc-Fe and the yellow colour indicates fcc-TiN. The grey lines are grain boundaries (excluding any orientation mismatch below 2 degrees). The raw maps are displayed to show the before and after effects of post-processing. This is done to provide evidence of precisely what the EBSD detector and software have identified.

It is again clear that interruptions have no effect on through-thickness crystal growth. Interestingly and surprisingly, the bcc-Fe phase is indexed within the TiN coating. This phase appears in small islands, typically at triple junctions of TiN grains. After completing area analysis of these maps, there is an observed increase in the percentage of this phase within the coating as interruptions are introduced: 2% Fe in the TiN STD film and the area percentage increases from 3% to 5% for TiN 9-INT 1 min and TiN 9-INT 5 min samples respectively.

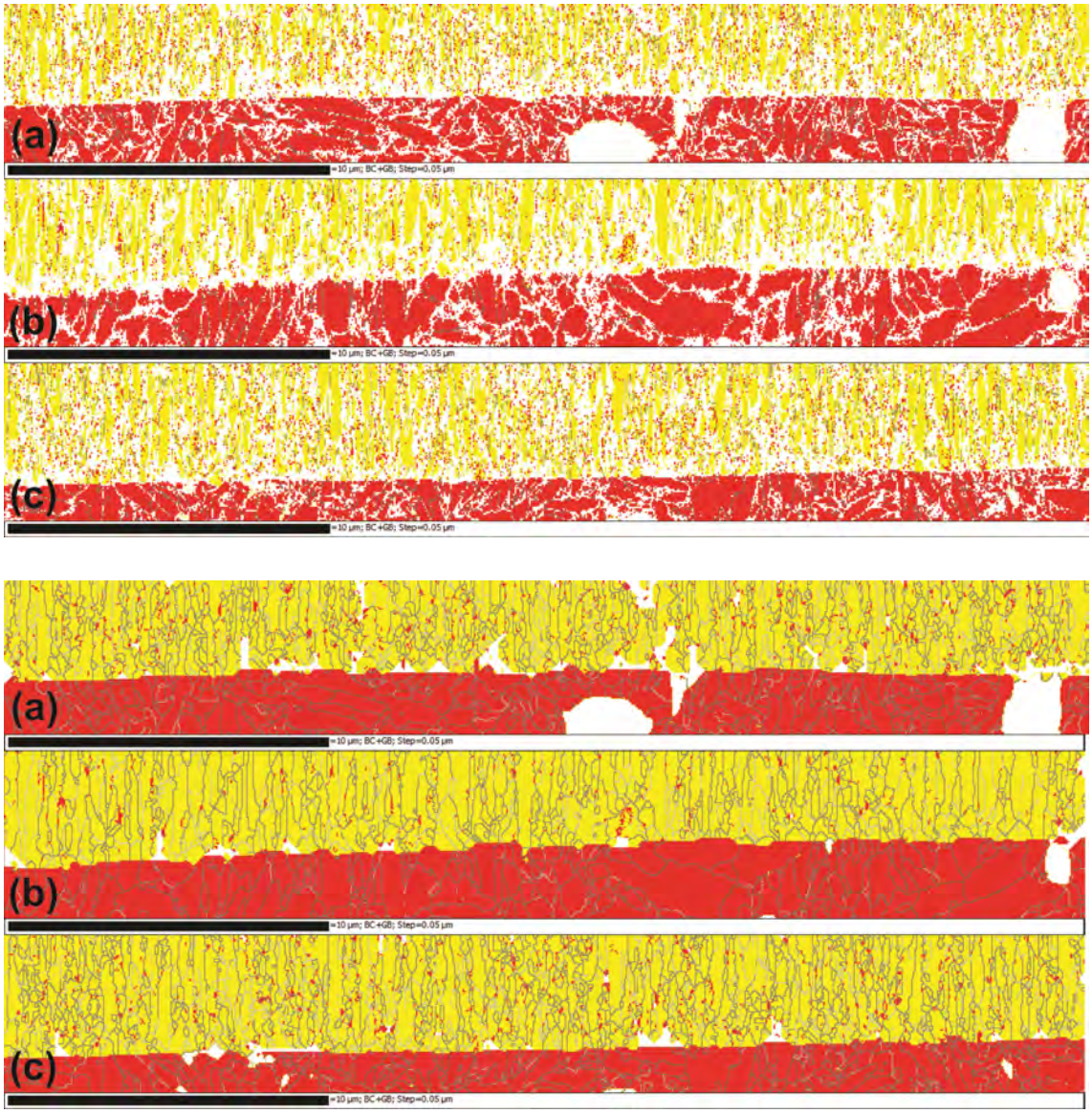

Figure 4.30: Raw (top three images) and post-processed (bottom three images) EBSD phase maps showing fcc-TiN (yellow) and bcc-Fe (red). (a) TiN STD, (b) Tin 9-INT 1min, and (c) TiN 9-INT 5min. White areas are unresolved Kikuchi patterns, except the large white areas within the HSS substrate, which are VC and are not indexed here. The black micron bar in the bottom left of each map is 10 µm in length.

There are some ambiguities with this second phase in the coating. The Oxford Instruments software used for mapping will identify a Kikuchi pattern that matches the crystal structure and lattice parameter of whatever material card is input. If the software cannot identify either of these two Kikuchi patterns, it will leave an unresolved pixel. In this case, two phase cards were input to the system: TiN, an fcc structure with a lattice parameter of 4.25 Å and; Fe, a bcc structure with a lattice parameter of 2.87 Å. The crystal structure and orientation are well indexed from Kikuchi patterns, but there is a general rule of 10% error in the lattice parameter measurement. If a phase with the same structure but only slightly

different lattice parameter exists, this experiment could not differentiate the two. This allows the possibility that the indexing of bcc-Fe in the TiN coating is false.

Another possibility for the existence of indexed bcc-Fe in the TiN coating could be from mechanical polishing during preparation. The iron could be transferred from the substrate and then remain on the surface of the sample where it is indexed during EBSD. To eliminate this possibility of sample preparation contamination, an ion beam polishing method is used whereby polishing of a cross-section of the sample, from the coating side only, reveals a clean surface for Kikuchi patterns to form from. If the bcc-Fe phase is still indexed in this experiment, its existence is less ambiguous.

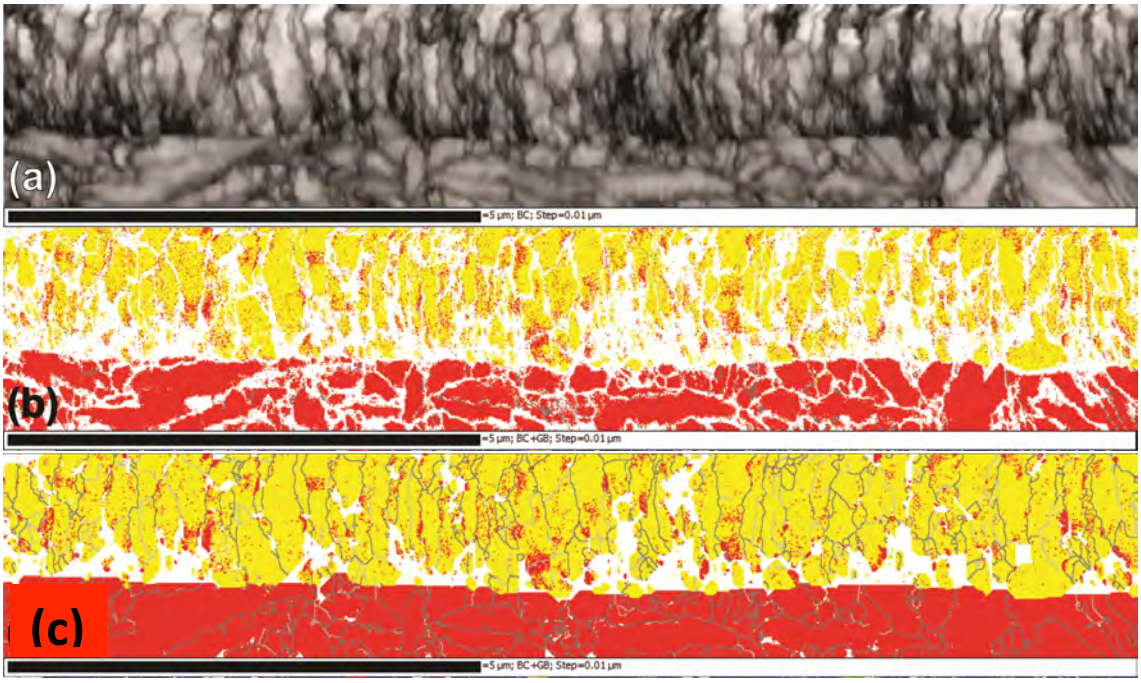

Figure 4.31: EBSD maps of an ion beam polished cross section of the TiN 9-INT 5min sample on a HSS substrate. Showing; (a) the band contrast image, (b) the raw phase map showing fcc-TiN (yellow) and bcc-Fe (red), and (c) the post-processed phase map. This indicates the presence of a secondary phase of Fe is not the cause of any remaining particles due to mechanical polishing. The black micron bar in the bottom left of each map is 10 µm in length.

The secondary phase of bcc-Fe is again indexed, despite the use of a second sample preparation method. In this map, the fraction of bcc-Fe resolved has increased and groups are larger than previously observed (Figure 4.30).

To further explore this finding, EDS in the SEM was completed on the same samples to find chemical evidence of Fe. The diameter of the identified bcc-Fe phase within the coating is approximately 50 nm and below, so providing contrast between TiN and Fe in spectroscopy

with an electron beam and a thick sample is challenging. Hence, acceleration voltages were kept very low (5 kV) to reduce the electron beam interaction volume. The area scanned with EDS was carefully selected from EBSD maps to be an area that included a large bcc-Fe grouping. The EDS map is shown in Figure 4.32 and shows no concentration of Fe.

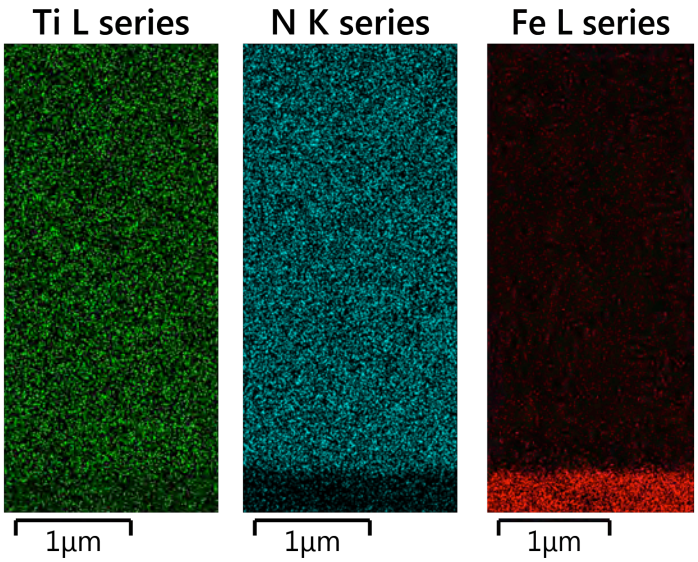

Figure 4.32: Maps of Ti, N and Fe from low accelerating voltage EDS scans.

The conflicting findings between EBSD and EDS can be explained. EDS does not provide the spatial sensitivity required. The reason is because of the interaction volume of the electron beam. In EBSD the Kikuchi patterns diffract from an interaction volume at a very shallow depth whereas in EDS, the X-ray signal is collected from a much larger volume at a greater depth. Effectively, the scanned volumes are different. The two methods will not provide the contrast required to identify a localised phase of Fe so small.

4.3.4. Electron Backscatter Diffraction: texture.

Texture information is also gathered from the mapped area in EBSD. The inverse pole figure (IPF) map shows a (111) texture is parallel to the growth direction, as supported by XRD characterisation in Section 4.3.1 and other orientations are present at the interface between coating and substrate, as shown in TEM (Figure 4.7). Pole figures of the three scans are shown in Figure 4.34 and indicate interruptions have no effect on the texture of TiN films produced by CAPD, except for the TiN 9-INT 5min sample in (c): the minor components visible as a ring in the (111) pole figures of (a) and (b) are more textured into

three directions in the (111) pole figure in (c). This indicates some changes to texture in the area measured from these EBSD maps, however this only shows a change in a small portion of the film. In pole figures from Rietveld analysis, where a macro observation is made, no change in texture is observed (see Figure 4.25), hence this change is deemed insignificant.

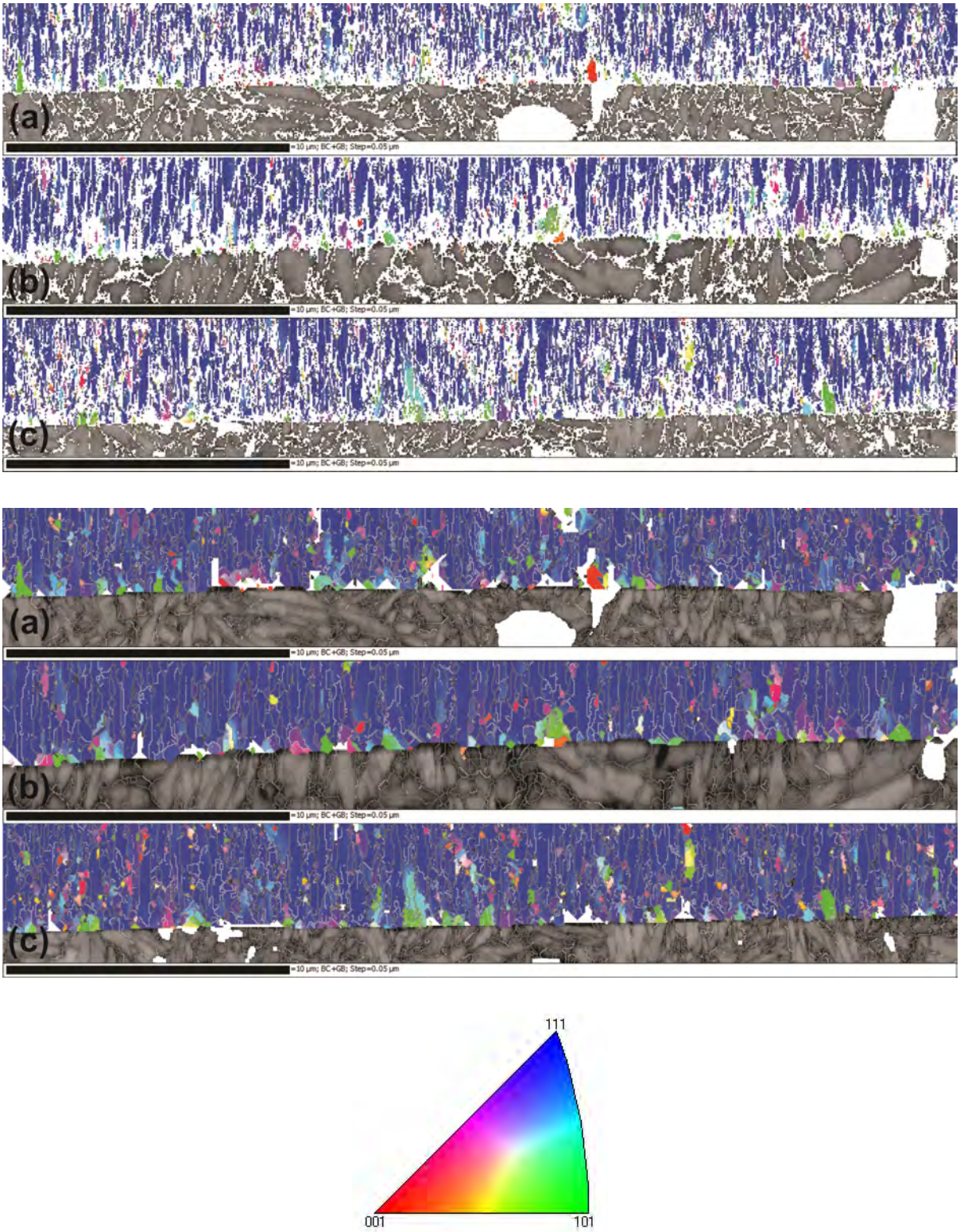

Figure 4.33: Raw (top image) and cleaned (bottom image) EBSD IPF map of TiN phase - (a) TiN STD, (b) Tin 9-INT 1min, (c) TiN 9-INT 5min. Below: the IPF colour key. Sample direction is set to z-axis, parallel to growth direction - up. A (111) texture is evident in the growth direction. The black micron bar in the bottom left of each map is 10 µm in length.

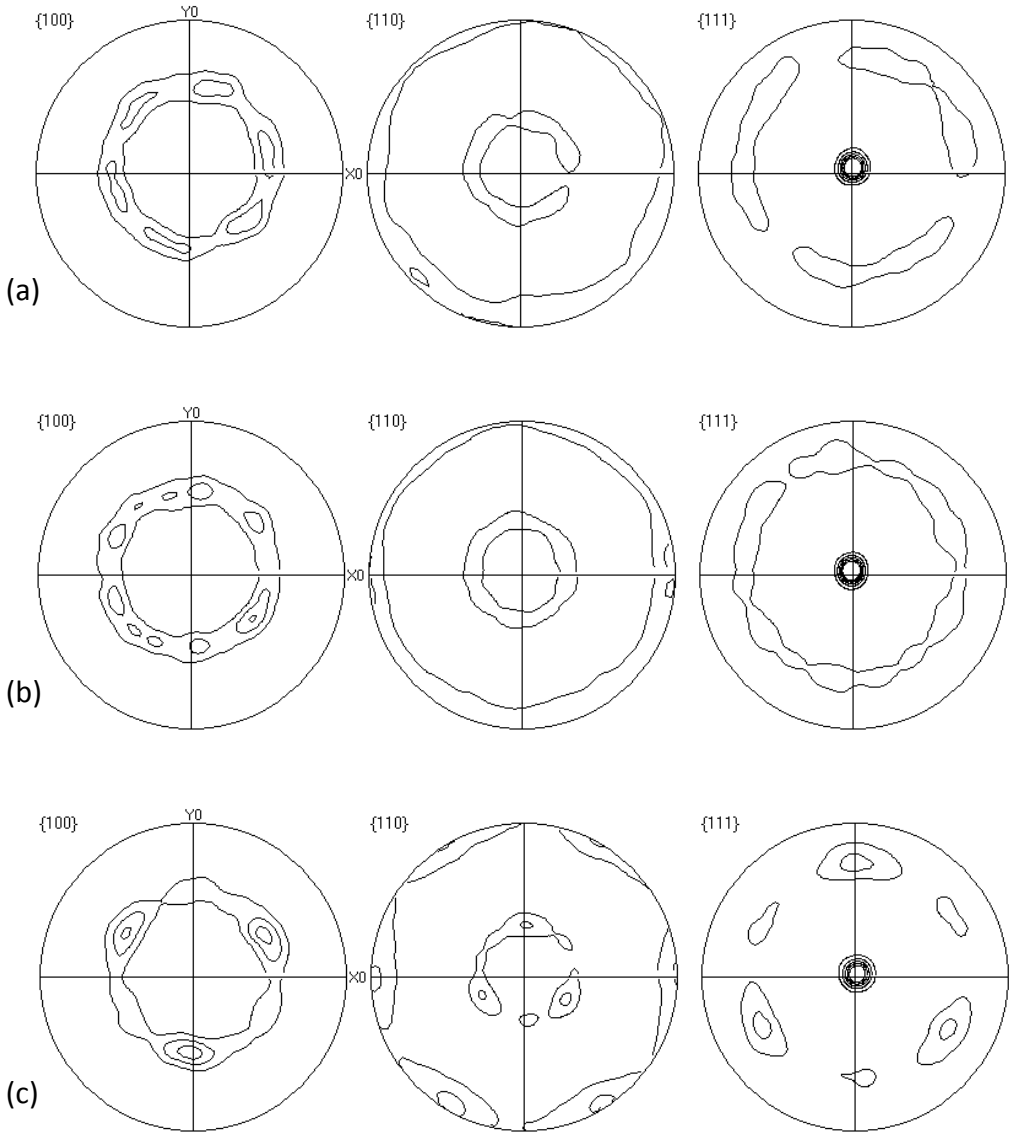

Figure 4.34: {100}, {110} and {111} pole figures of (a) TiN STD, (b) Tin 9-INT 1min, (c) TiN 9-INT 5min from EBSD cross-section maps. The [111] is parallel with the sample surface normal in this case, indicating a strong (111) fibre texture in all films

4.3.5. Transmission Electron Microscopy: a close-up investigation of impurity phases.

4.3.5.1. Diffraction and Dark Field imaging.

An investigation into the identified secondary phase within the TiN coating using EBSD was carried out and requires additional evidence to support the finding. A cross-section observed in TEM is shown in Figure 4.35 and Figure 4.7, displaying a bright field image in the top left, with the substrate in the bottom left of that micrograph. A selected area diffraction pattern is taken of this same area and the typical diffraction pattern of the fcc-TiN phase is visible. There is some diffraction within the first ring and between the second and third that

appear out of place (see circles and arrows). The bright crystals in the two dark field images on the right of the figure show the location of these diffraction spots within the film. Their locations are similar to what is shown in EBSD, at grain boundaries and triple junctions.

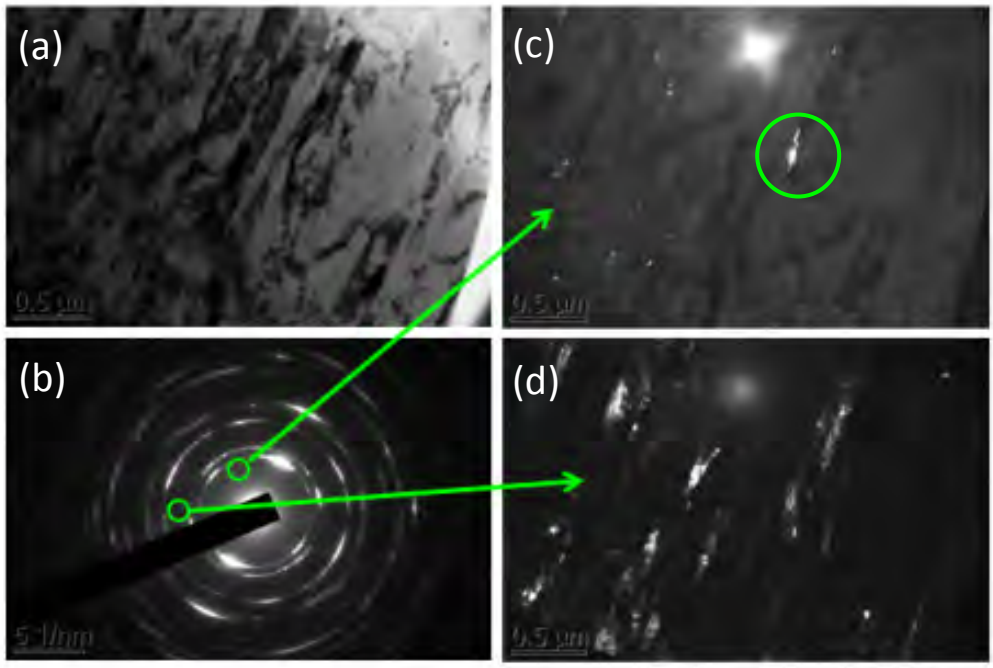

Figure 4.35: TEM micrographs: dark field imaging (a) and selected area diffraction (b) and of TiN 9-INT 5min sample. The two dark field images (c) and (d) come from the two diffraction spots within the circles in (b). The circle in (c) shows the area observed using EDS in Section 4.3.5.2.

4.3.5.2. Energy-Dispersive X-ray Spectroscopy.

EDS spectra of the area within the circle in (c) of Figure 4.35 were collected and Figure 4.36 shows the elemental composition of a spot adjacent to the unknown phase (bright grain). Figure 4.37 shows the composition of the unknown phase, and from careful comparison of the two, no significant difference is observable. The Fe peak at 4.6 keV is convoluted with the nearby Ti peak and the Fe peak intensity at 6.4 keV appears the same in both spectrums. Other impurity elements such as oxygen are unseen and fluctuations in N levels are indistinguishable, a common issue with low atomic number element identification using EDS. Oxygen is also not likely to exist as XPS experiments in Section 4.3.2 show. It could be possible that these impurities seen here and in EBSD are another phase of Ti or a non-stoichiometric TiN, however fluctuations in N levels will be impossible to observe with EDS in the TEM.

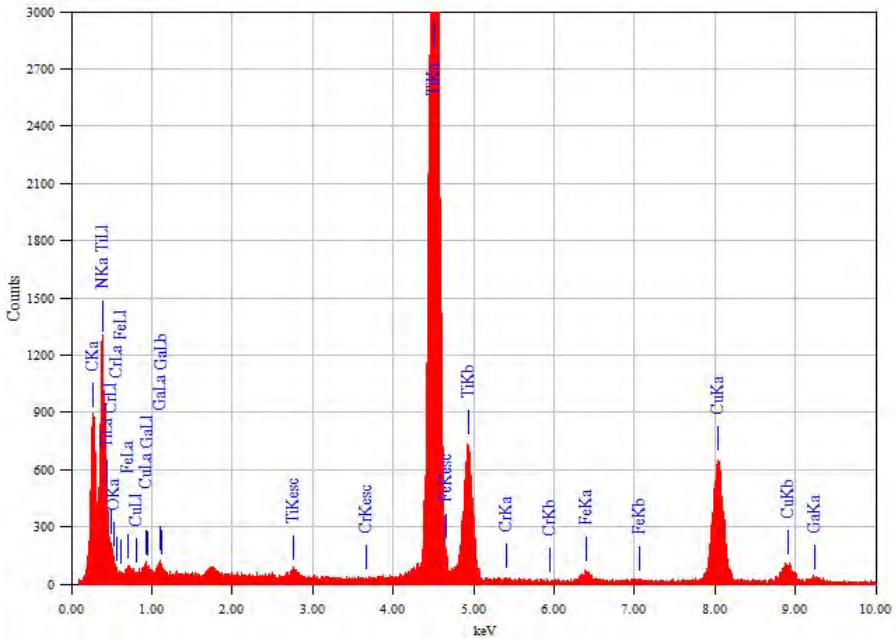

Figure 4.36: EDS Spectrum of an area adjacent to the encircled area in the top right image of Figure 4.35.

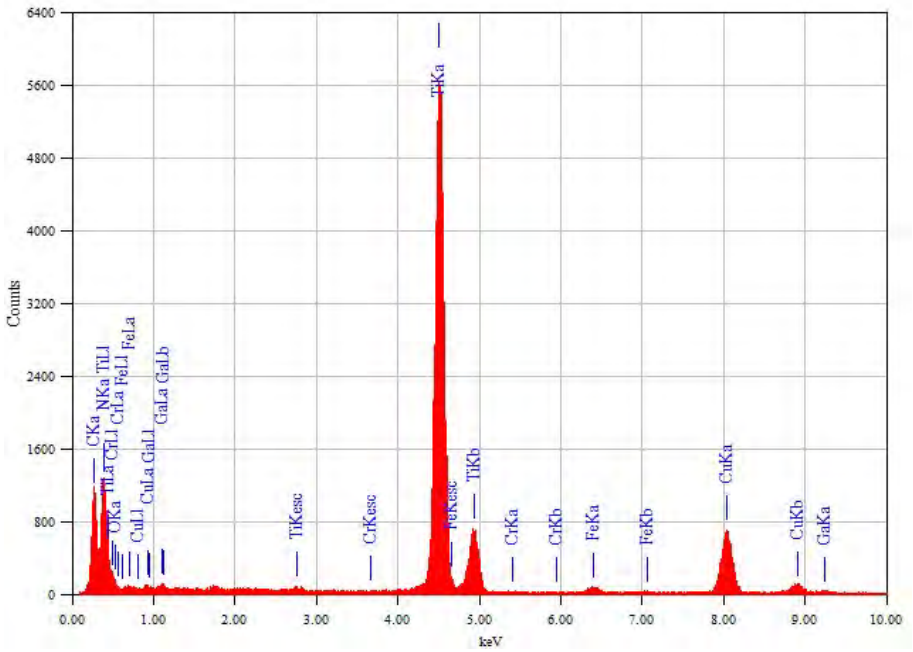

Figure 4.37: EDS spectrum of the bright section within the encircled area in the top right image of Figure 4.35.

4.3.5.3. Electron Energy Loss Spectroscopy.

A technique more suited to detecting low atomic number elements is EELS. Jump ratio images for Ti and N are displayed in Figure 4.38, (b) and (c) respectively. There appear to be minor fluctuations in the concentrations, however no distinct abnormalities emerge.

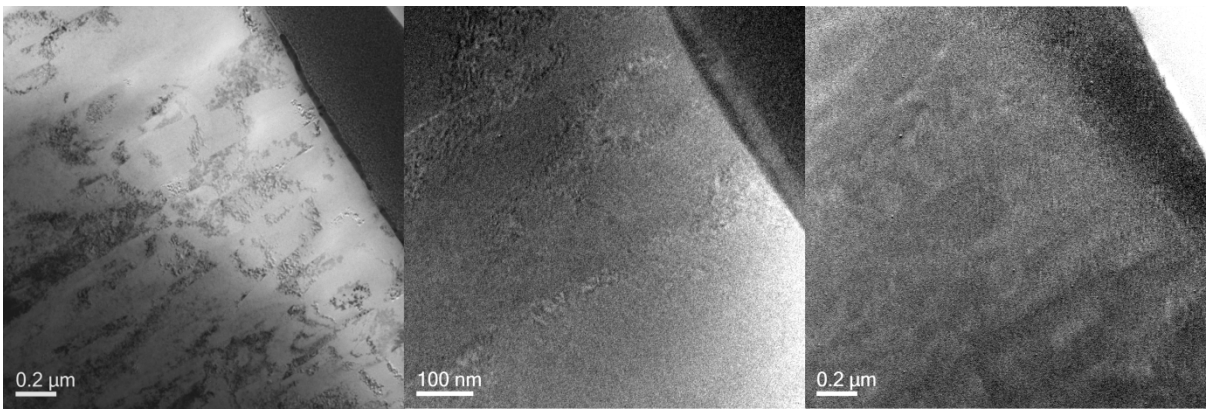

Figure 4.38: TEM micrographs and EELS jump ratio images - (a) bright field image, (b) Ti jump ratio image, (c) N jump ratio image.

4.3.6. Glancing Angle X-ray Diffraction: a macroscopic view.

The characterisation of a secondary phase in TiN samples has been attempted by using a number of techniques, however the only clear identification of a secondary phase is provided by EBSD. The mapped area in EBSD measurements is very small and does not provide macroscopic evidence that an increase in a secondary phase occurs with interruptions. To provide this evidence it is necessary to use XRD, however the typical theta-2theta scanning modes will not differentiate Fe from the substrate and Fe from within the film. A diffractometer in a glancing angle set up will allow for diffraction of the coating and not from the substrate.

Scans were completed using Cu Kα radiation at a range of 30 to 85 degrees 2theta with a fixed incident angle of 4 degrees. The incident angle was tested at 2 degrees however the diffracted signal was extremely weak, even long 25 hour scans were unable to provide adequate signal to noise ratios. The incident angle was then increased to 4 degrees to increase the diffracted volume and achieve an acceptable peak. The penetration depth at this angle is calculated from the trend shown in [113] and is expected to be at best 2 µm, which means the penetration depth will not exceed the coating thickness of the samples tested; any Fe peak detected will be from within the coating. Scans lasted almost 30 hours

for each sample and were conducted on the aforementioned PANalytical diffractometer. Results are shown in Figure 4.39: for TiN STD and TiN 9 INT 1 min samples, the $(110)_{Fe}$ peak is not detected. The TiN 9 INT 5 min sample, with diffraction pattern on the top of the figure, shows a peak at ~44.5 degrees 2theta which represents the (110) plane reflection of the bcc-Fe phase with a lattice parameter of 2.87 Å.

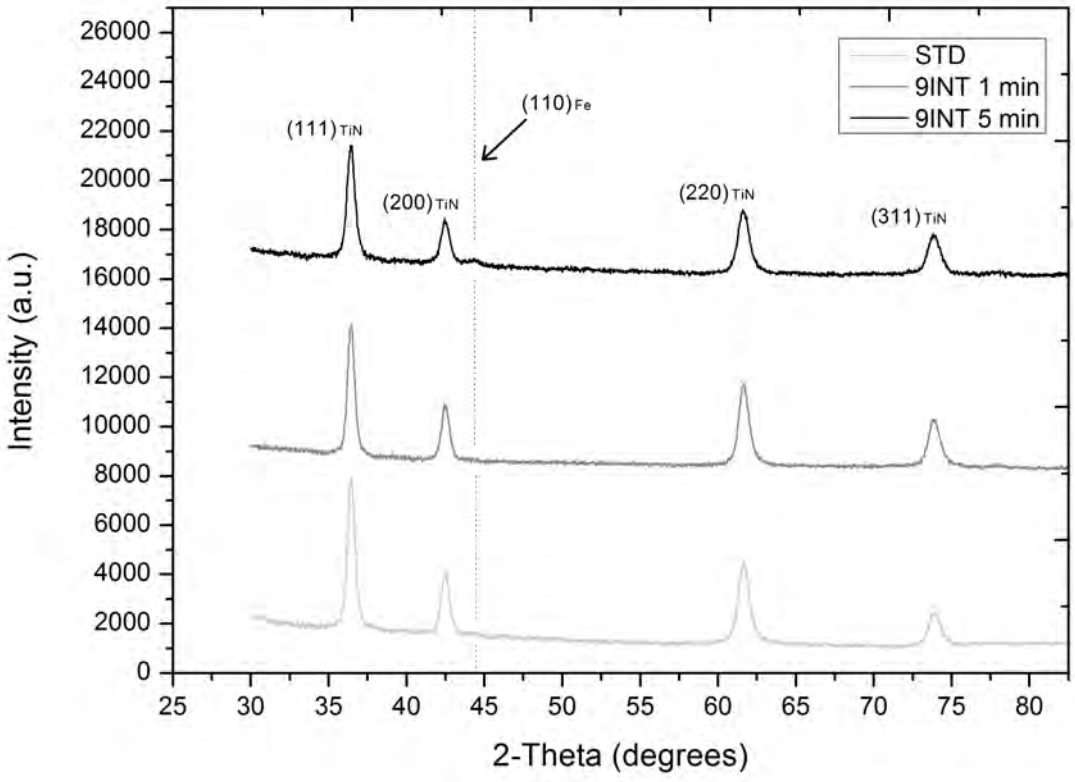

Figure 4.39: Intensity peaks for glancing angle scans of STD and INT TiN films. The small $(110)_{Fe}$ peak is only significant in the TiN 9 INT 5 min sample indicating the secondary phase volume fraction increases on a macroscopic scale with the introduction of longer interruptions.

4.4. Discussion: Where are the differences coming from?

Interruptions during CAPD of TiN has been shown to have significant influences on mechanical properties of the coating. Hardness increases by 8 %, the film cohesive strength shows improvements in scratch testing, and the number of holes cut by TiN coated HSS jobber drills has increased by 90 % when machining D2 steel with a hardness of 438 HL at 45 m/min and by 22 % when cutting D2 steel with a hardness of 486 HL at a cutting speed of 30 m/min. These increases were observed over TiN STD for TiN coatings that experienced 9 interruptions lasting 5 minutes each. A reduction in interruption time (to 1 min) significantly reduced drill performance, compared to both TiN 9-INT 5min and TiN STD. This is discussed later in this section.

The source of improvements in mechanical testing of interrupted TiN CAPD coatings is more difficult to identify. An increase in compressive stress is observed with two XRD stress analysis techniques and with a combination of both results, a conclusion is drawn explaining the source of additional strain is impurities in (111) oriented TiN grains. The impurity driven compressive stress was further increased with longer (5 min) interruption times compared to 1 min interruption samples. A lengthily search for impurities using various spectroscopy, diffraction and microscopy techniques had difficulty in characterising any impurity elements or secondary phases. Texture was also shown to remain consistent between standard and interrupted films. However, EBSD was able to show a secondary phase of bcc-Fe with a lattice parameter of 2.87 Å at grain boundaries and triple junctions of TiN grains that increased in percentage as 9 interruptions were introduced and further increased with longer interruption times. Glancing angle XRD was then able to identify a (110) peak at 44.5 degrees 2theta, corresponding to the same bcc-Fe phase.

Initially, Fe was considered to be a very unlikely impurity element. The sources of Fe in a deposition chamber are very limited unless sample bias voltages are high enough to sputter away substrate or chamber material. In this case the voltages are too low to allow sputtering to occur and this gives no explanation as to why the percentage would increase with interruptions. The main suspect for a source of Fe in TiN films is the targets. It was assumed that targets used in the Innova deposition system were high purity as other systems used by the author have always used high purity targets. This assumption was false

and in fact, commercial purity (Grade 2) Ti targets were used. Grade 2 Ti has a short list of impurity elements, see Table 4.14 – Grade 1 Ti is included for comparison.

Table 4.14: Titanium grade 1 and 2 impurity elements.

Impurity Element	Grade 1 Ti (max. wt.%)	Grade 2 Ti (max. wt.%)
C	0.1	0.1
N	0.03	0.03
O	0.18	0.25
H	0.01	0.01
Fe	0.2	0.3

With iron impurities at a maximum of 0.30% in the target, it is possible that this element is present in the deposited TiN coating. It is expected that Fe remains a solid solution within the TiN lattice, so how are much larger percentages of 2-4 % observed in the film as a segregated phase and why do interruptions encourage a higher percentage of the second phase?

The segregation of Fe as a second phase depends on the Gibbs free energy. This can be calculated by closely following the calculations made by Zhang and Veprek [53] and using thermochemical data of pure substances found in Barin's book [114]. In Zhang and Veprek's paper, the system examined is TiSiN and is considered as a pseudo binary system of TiN and Si_3N_4. The same consideration will be made in this case but for a TiFeN system consisting of the two phases fcc-TiN and bcc-Fe.

The enthalpy of formation, at the deposition temperature of 400 °C, of TiFeN with a 1:1 composition of TiN and Fe is approximated according to

$$\Delta H^0_{TiFe:N} = \Delta H^0_{TiFe} - \Delta H^0_{TiN} - \Delta H^0_{Fe}$$

$$= -41.724 - (-336.539 - 0)\ kJ/mol$$

$$= 294.814\ kJ/mol$$

This value can then be used to calculate an approximate interaction parameter for an equal composition $x_{\mathrm{TiN}} = x_{\mathrm{Fe}} = 0.5$

$$I^0_{TiFe:N} = \frac{\Delta H^0_{TiFe:N}}{x_{TiN} \times x_{Fe}}$$

$$= \frac{294.814}{0.5 \times 0.5}$$

$$= 1179.257\ kJ/mol$$

Then, to calculate the interaction parameter, incorporating temperature and N pressure. The gas constant (R), the temperature (T) and the N pressure $\left(p_{N_2}\right)$ are all known, but the value of α is not. Zhang and Veprek are capable of defining this value as 7.024 because a value of Gibbs free energy of $Ti_5Si_3N_y$ is provided by [57], where the TiN and Si_3N_4 phases coexist. They assume their TiSiN system will share the same Gibbs energy, thereby enabling the calculation of α. This same luxury is unavailable in our case as no evidence of a coexistence temperature and pressure of TiFeN has been found in the literature. So here it is assumed to be 7.024 as well, and it is found that changing this value in the range of 1 to 15 makes little difference to the conclusions made here. In other cases, where different conclusions must be made, the significance of three decimal places would be necessary.

$$I_{TiFe:N} \cong I^0_{TiFe:N} + \alpha RT \ln p_{N_2}$$

$$= 1179.257\ kJ/mol + (7.024 \times 8.314{\times}10^{-3}\ kJ/Kmol \times 673.15\ K \times 2.67{\times}10^{-6}\ MPa)$$

$$= 674.7\ kJ/mol$$

The interaction parameter is then used in the following equation to determine the Gibbs free energy with differing concentrations (*x*) of Fe.

$$G_m^{\psi} = \frac{1-x}{1+2x}\ {}^0G_{TiN}^{fcc} + \frac{x}{1+2x}\ {}^0G_{Fe}^{bcc} + RT\left(\frac{1-x}{1+2x}\ln\frac{1-x}{1+2x} + \frac{3x}{1+2x}ln\frac{3x}{1+2x}\right) + \frac{3x(1-x)}{(1+2x)^2}I_{TiFe:N}$$

Plotting the results of this equation for concentrations of Fe ranging from 0 to 1 yields Figure 4.40. The slope of the curve indicates the more stable situation for a TiFeN system is a dual phase separation into TiN and Fe, especially at low Fe concentrations. The ternary phase diagram displayed in Figure 4.41 also supports this phase segregation. In the diagram, at any concentration of Fe in TiN, the two phases are immiscible. The diagram is calculated for a temperature of 800 °C, a temperature higher than this case, but solubility will only be reduced with a lower temperature.

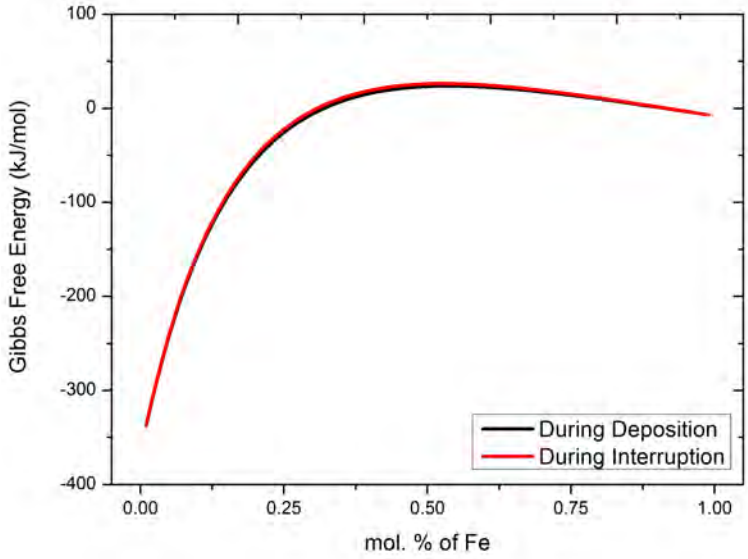

Figure 4.40: Gibbs energy curves during deposition and during interruption for a pseudo binary TiN and Fe system.

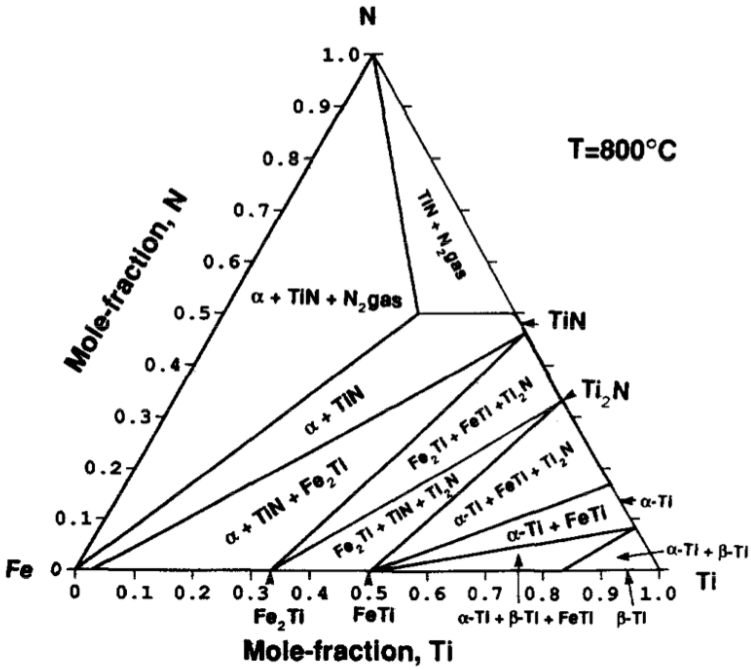

Figure 4.41: Ternary phase diagram for TiFeN system at 800 °C. Taken from [115].

There is however a condition that must be met in order for the decomposition of TiFeN into fcc-TiN and bcc-Fe. The two phases must be coherent, or the Gibbs free energy term must be large enough to overcome an incoherency. A coherent interface is considered to be one with an interfacial strain energy ≤ 200 mJ/m^2, a semi-coherent up to 500 mJ/m^2 and up to 1000 mJ/m^2 for an incoherent interface [53, 116]. A coherent interface exists between fcc-TiN and bcc-Fe with the Baker-Nutting orientation relationship shown below [117].

$$\{001\}_{TiN} \,||\, \{001\}_{Fe},\ \langle 110\rangle_{TiN} \,||\, \langle 100\rangle_{Fe}$$

Within this orientation relationship, there are some options for where the Fe atoms are positioned on the TiN lattice (see Figure 4.42) and based on the modified embedded-atom method calculations made by Kim *et al* [118], the interfacial energy for (a) is 175 mJ/m^2, (b) is unstable, and (c) 484 mJ/m^2. Hence, the most likely interface to occur, due to the lowest interfacial energy, is the positioning of Fe on top of N in the fcc-TiN lattice. Because of this low energy interface, the segregation of TiN and Fe in these films will not be hindered. By comparison, the decomposition of TiN and Si_3N_4 in Zhang and Veprek's work [53] occurs with a semi-coherent interface. The Gibbs energy term is large enough in their case to overcome the incoherency, and therefore a larger interfacial strain component is required to accommodate the dual phase system. The result of this increase in strain is an increase in hardness, for similar reasons to those described for precipitation hardening [119], or age hardening, in bulk material alloys (for example: Al-Cu alloys), and more specifically due to a coherency hardening effect. A dislocation pinning effect is also likely to have a minor effect. In the TiN and Si_3N_4 system, coherency hardening leads to superhardness - values of around 50 GPa [52].

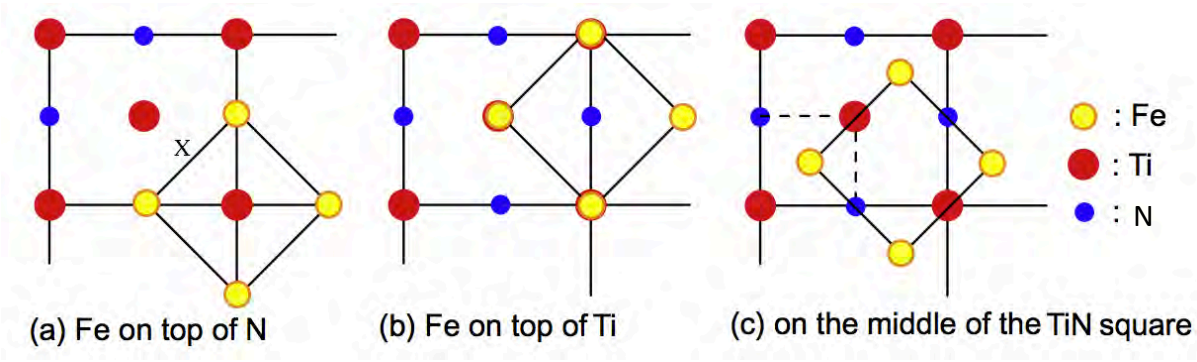

Figure 4.42: Schematic of Fe positioning on TiN lattice. Taken from [118]

In our case, indentation hardness is measured to increase by a maximum of 52% with the TiN 9-INT 5 min sample and the mechanism for this increase is partially due to an added interfacial strain component, and less so by a dislocation pinning effect. The added strain is also noticed in XRD strain measurements and stress calculations addressed in Section 4.2, and the conclusion that added defects are the cause of an increase in compressive stress from those experiments can be linked to the existence of the secondary Fe phase in the TiN film. As shown in Figure 4.43, the secondary phase will cause a strain field at the location of

compositional modulation. With the positioning of Fe on top of N sites in the TiN lattice, there is a mismatch in the distance marked 'X' in Figure 4.42 (a). For TiN this distance is calculated to be 3.0 Å, based on a lattice parameter of 4.252 Å. The lattice parameter of the iron phase, as measured with XRD, is 2.88 Å meaning the Fe phase will add a compressive strain to the TiN lattice and the Fe will experience a tensile strain as the two structures accommodate each other.

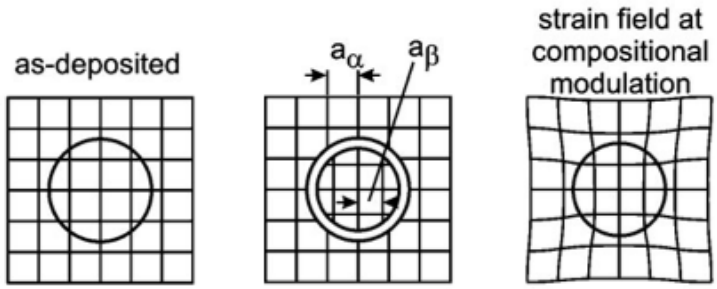

Figure 4.43: Schematic displaying the effect of a secondary phase on the surrounding lattice. Taken from [42].

Drill performance in the TiN 9-INT 1min sample was reduced. This is a difficult observation to explain; the coherency strain effect could be too small to have a significant influence on mechanical properties tested, and the dislocation pinning component could be too small to provide an assistive strain field. Precipitates could be too finely spaced, therefore aiding dislocations instead of hindering them. The increase in precipitates, when compared with the TiN STD film, could be just the right to ease dislocation motion, but not enough to hinder it, and in the TiN STD film there are fewer precipitates, spaced far enough away from each other, they hinder dislocation motion – leading to better TiN STD mechanical performance.

Based on the calculations from Kim *et al* [117], the interface should have the Baker-Nutting relationship [117]. This can be checked using EBSD maps and building pole figures, for the two phases, from a reduced section where only few pixels are selected. The (100) and (110) pole figures should be opposites for the TiN and Fe phases. Figure 4.44 shows the pole figures from reduced sections and the Baker-Nutting relationship is not seen. The two phases remain in a cube-on-cube relationship with some distortion in the orientation at the interface: notice the slight clockwise rotation of the Fe (100) pole figure compared to the TiN equivalent (see arrows), and the shift in the orientation of the (110) axis (see how the

normal to the ring of intensities shifts from being normal to the (110) plane to being oriented in the negative Y0 direction), and the (111) axis. This relationship is somewhat irrational, but as Zhang and Weatherly explain – an interface is often irrational and not simple to explain based on cohesive interface energies and a habit plane [120]. Other information on an interface between these two phases has not been found in the literature.

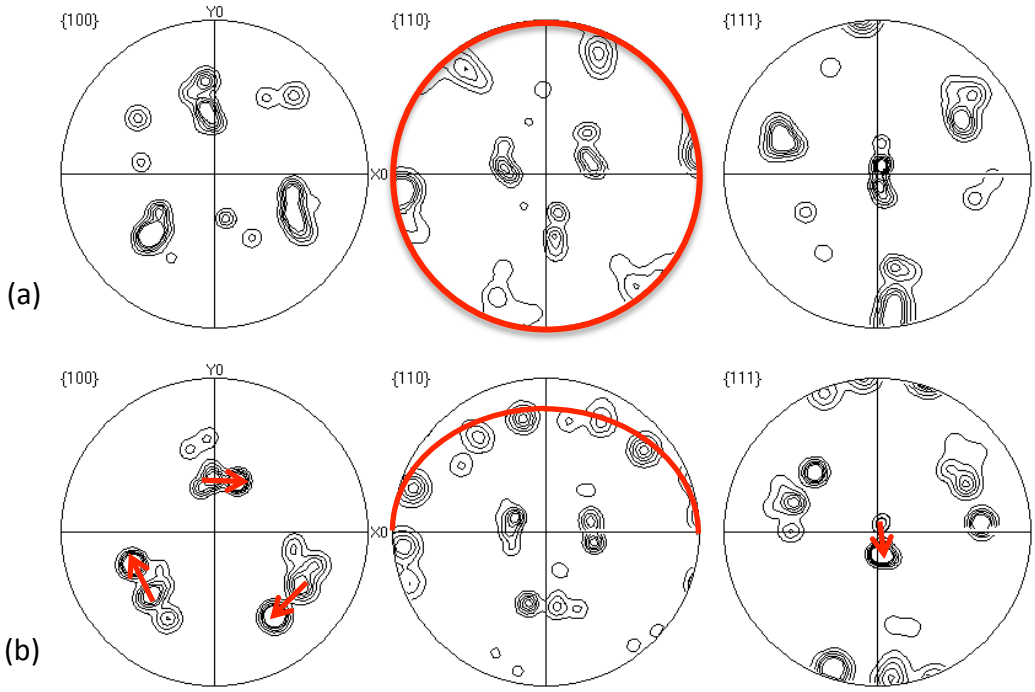

Figure 4.44: {100, {110 and {111 Pole figures (from EBSD) for (a) TiN and (b) Fe, drawn from a very small area where an interface between the two phases exists. Reflections are taken from less than 20 pixels.

Besides the hardness increase due to interfacial strains, there are other beneficial effects of a dual phase coating, again similar to bulk material alloys, that could be participating in improvements identified here. For example, cohesive strength is increased due to hindering of dislocation motion by the segregated phase, and some toughness enhancement could occur from strain being accommodated in the lower elastic modulus Fe phase. Also the TiN lattice is purified through the removal of solid solution Fe atoms in regions nearby the segregated phase.

So the next question to address is: why do interruptions encourage the decomposition of Fe and TiN? Again, there are a few probable causes. During an interruption, there is a decrease in substrate temperature of ~25 °C for longer 5 min interruptions. In the TiFeN system, a decrease in temperature increases the slope of the Gibbs free energy curve and therefore

provides additional thermodynamic driving force for segregation. On top of this, the partial pressure of N during an interruption increases due to less N being consumed as the film grows. This also influences the slope of the Gibbs free energy curve, increasing the driving force for decomposition. Despite these findings, the changes in N pressure and temperature caused by interrupting film growth are indeed minor and the energy curves fluctuate only slightly, so the most likely factor to increase the percentage of the secondary Fe phase is time. With longer interruption times and more of them, the total time of the deposition cycle is substantially increased, allowing the film to remain at the right conditions for more diffusion and segregation of Fe to occur. This could be achieved through post coating heat treatment, however the time required to achieve the same result would increase dramatically and necessitate higher temperatures. Interruptions during deposition are effectively a heat treatment step within the cycle, but more efficient. Recall in Section 2.5.1 covering growth mechanisms, in the zone T temperature range diffusion only occurs on the surface, and in between grain boundaries, of a growing film. Interruptions will allow the film time to diffuse and segregate on the surface, leaving more efficient diffusion and segregation of TiN and Fe – at lower temperatures than regular heat treatment.

4.5. Summary.

In conclusion the effect of interruptions on CAPD, arcing Grade 2 Ti targets in the Innova deposition system has an effect on the microstructure and the mechanical properties of TiN films grown on HSS. Using Ti grades as targets, which contain controlled amounts of Fe or other elements that encourage a beneficial segregated phase, could further increase the performance of TiN films. In the process of identifying the effect of interruptions during CAPD of TiN, useful techniques and methodologies for coating analysis were identified.

During growth of TiN with Grade 2 Ti targets using standard cycle conditions, the deposited film contains a segregated bcc-Fe phase – a previously unknown occurrence to Sutton Tools Pty Ltd, and probably to most other PVD practitioners. This occurs due to a lower free energy state when the two phases are unmixed. The two phases are immiscible at the deposition temperatures used here (~425 °C). The additional time provided by repeated 5 minute interruptions is found to encourage further segregation of this second phase, and is thought to be encouraged by diffusion that occurs on the surface of the film during an interruption.

Based on Gibbs energy calculations of a binary fcc-TiN and bcc-Fe system, the increase in N pressure and the decrease in sample temperature experienced during interruptions increase the slope of the Gibbs energy curve for the two phases, providing a driving force for a lower energy unmixed film of fcc-TiN and bcc-Fe.

The secondary phase has no influence on grain size measured with Rietveld analysis or EBSD. This supports the idea of an age hardening coherency precipitation of Fe within TiN grains, rather than segregation to grain boundaries (as tends to happen with small mobile elements such as Si and B). The secondary phase is believed to provide two beneficial changes to the TiN film: the strain at interfaces between the phases adds compressive stress to the TiN lattice that increases measured film hardness; and the small dispersed Fe phase may hinder deformation through dislocation pinning effects. A combination of these two factors increases the performance of coated HSS drills.

The hardness was measured with a nanoindentation test and results show significant increases in hardness with four and nine 5 minute interruptions when compared with a

standard TiN film. The introduction of four 5 minute interruptions increase hardness from the standard TiN film hardness of 18.3 GPa to 24.6 GPa and nine interruptions increased hardness to 29.7 GPa. In another nanoindentation test the standard hardness was measured at 26.7 GPa and with four 5 minute interruptions this increased to 29.0 GPa. The same measurement on a TiN sample with nine 1 minute interruptions displayed no increase in hardness (26.8 GPa).

Drill tests, cutting D2 equivalent tool steels with a range of hardness from 438 to 496 HL, at 30 and 45 m/min showed a significant increase in drill life between standard and longer interruption time TiN films. Shorter 1 min interruptions displayed a decrease in tool life. Drills coated with a TiN film which had four and nine 5 min interruptions in the deposition cycle cut 44 and 52 holes at 45 m/min. An improvement over the 25 holes per micron cut from the standard TiN coated drill. In another drill test at 30 m/min in a harder D2 plate, the standard TiN coated drill cut 59.7 holes and an increase to 73.5 was observed with nine interruptions (5 min). The use of nine 1 min interruptions reduced tool life to 46.9 holes.

These improvements in drill life are real and valuable to the cutting tool manufacturer. More importantly the implementation of interruptions in the deposition cycle is very simple, streamlining the application of this research into the production environment.

Using the technique of interrupting film growth is readily applicable to other coating recipes to encourage and hasten segregation. As addressed by Mayrhofer [2] hard coating researchers should focus on schemes for secondary phase transformations in metastable systems in-deposition. The use of interruptions during growth targets this demand.

Combined stress analysis with the $\sin^2\psi$ method and the CGM was utilised to suggest defect concentration had increased in interrupted samples. The combined technique is readily applicable to the detection of residual stress in randomly oriented grains and fibre textured grains. Fibre textured grains can be compared to assist in linking stress to sample microstructure.

Finally, this chapter offers a useful test methodology for the comparison of very similar films. The most valuable tests identified through this report are nanoindentation hardness, controlled drill tests and the use of EBSD for microstructural evaluation. XPS, EDS in the

SEM, and EDS in TEM had difficulty in providing necessary resolution for small defects. Microstructural evaluation with TEM offers little as an exploratory method for identifying unknowns in these small grain size microstructures. TEM is more aptly suited to proving a known rather than finding an unknown. Finally, sample preparation for fracture cross-sections are more difficult and offer less information than EBSD mapping.

4.6. Recommendations for future work

Continuing research on the use of interruptions for improving hard coatings for cutting applications is highly recommended. The technique is a scheme for providing secondary phase transformations in metastable systems in-deposition. There is currently much research into nanocomposite films and further improving them is possible with the use of interruptions during deposition.

Interruptions would suit the improvement of films that are known to experience segregation and could be utilised to decompose coating architectures that do not segregate within reasonable cycle times.

Some experiments were conducted with other coating architectures during this project, however are not reported here. Interruptions were introduced during deposition of TiAlN and testing has shown considerable improvements in tool life during side milling of medium carbon steel. Continuing to test the effect of interruptions on CAPD growth of TiAlN and its performance when applied to cutting tools for high speed machining.

From an investigative point of view, there are a number of observations that are required to fully analyse and understand the secondary phase of Fe in TiN films deposited with Grade 2 Ti targets. It is recommended that TEM be utilised to explain the interface adequately, following methods outlined in [120]. If sample preparation is adequate, transmission Kikuchi diffraction and mapping would also provide useful information on the small sized Fe phases in these TiN films that supports TEM analysis.

Analysis of interrupted TiN films during deformation is also recommended. The scratch test offers controlled deformation of films and analysing cross-sections of scratches, combining EBSD and TEM, is of high interest. This could offer more information as to how this secondary phase influences deformation of TiN.

XRD with sample temperature and atmospheric control offers an interesting opportunity for comparing thermochemical calculations with observation.

There are many pathways for research or engineering with this technique that could benefit both research institutions and industry.

5. Developing controllable machining tests.

Due to the highly complex process of cutting, predicting tool and coating performance is a difficult task. Tool manufacturers test coating and tool systems in their intended processes. Drill tests and milling tests are standardised to have consistency, providing tests with a certain amount of control to reduce variability. The definition of a worn tool is chosen to determine tool life. Then, statistical analysis is used to identify changes to tool performance. This level of control is adequate when using a large sample size to accommodate variability.

For in-depth materials analysis of cutting tools, coatings and corresponding chip formation, it is preferable to establish a controlled cutting system. One that is not only able to evaluate tool performance, but also helpful in understanding the mechanisms involved, and single out individual contributing factors. This chapter aims to develop a test that balances between real application and simplicity for materials analysis.

TiN and TiAlN, two coatings with very different characteristics and wear behaviours, are tested. These films were chosen to provide contrast during development of a test method. Examining and understanding the mechanisms by which these films protect cutting tools is also beneficial to allow improved cutting parameter selection and tool design.

TiN was developed into TiAlN by Münz [22] and Holleck [121] to increase achievable operating speeds due to higher hardness, hot hardness, and improved oxidation resistance. The formation of an high hardness Al_xO_{1-x} layer on the surface of TiAlN films acts as a passivation layer, improving oxidation resistance. The mechanisms responsible for oxidation resistance and hot hardness only begin to have an effect at elevated temperatures (discussed in Section 2.1.3). TiAlN will begin to gain mass due to oxidation between 800-900 °C [122] and reach a maximum hardness at 900 °C [42]. TiN will begin to oxidise at 550 °C [1]. This indicates that at higher cutting temperatures TiAlN performance will increase and TiN will decrease.

Machining operations generate temperature in a number of ways; deformation of workpiece material as a chip forms, and friction between the chip and rake face of the cutting tool (Figure 5.1).

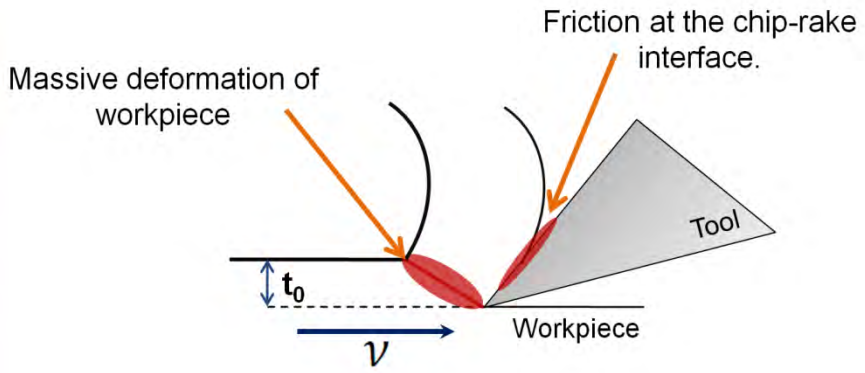

Figure 5.1: Where heat (red) is generated in a simplified, orthogonal cutting operation.

Section 0 aims to change cutting temperature by modifying cutting process parameters. Attempts are then made to link the effect of cutting parameters to tool life (more specifically coating performance) and temperature changes. With higher cutting temperatures, the beneficial oxidation and phase segregation of TiAlN should improve wear resistance and coated tools will begin to outperform TiN tools.

Later, some control of oxidation is provided with the use of inert gasses. This is done to reduce the beneficial oxidation of TiAlN, and the detrimental effect of TiN oxidation. The influence of reduced oxygen on coated tool wear is observed.

Section 5.2 furthers the development of this test by simplifying the process to a 2-dimensional cut. The focus of this section is the influence of oxidation on TiN and TiAlN coated tool wear, and Ti6Al4V chip formation.

5.1. Face Milling: TiN vs. TiAlN.

Face milling is used here to observe changes to tool wear under different cutting conditions with TiN and TiAlN coated carbide (sintered WC) inserts. The process of face milling was chosen due to its simplicity in executing tests. The workpiece material can be easily mounted and efficiently consumed with repeated passes of the cutting tool. Using a simple shaped cutting tool allows for less complicated microscopy and analysis of wear.

This section covers the effect of cutting parameters and atmospheric conditions on the tool life of coated tools. The aim is to develop a test which can answer the question: *What is the effect of changing feed rate and cutting speed, on TiN and TiAlN coated carbide tool life during face milling of K1045 steel?* During the development process, another question is added: *Does supplying Ar to the cutting atmosphere change oxidation reactions and hence tool life behaviour of TiN and TiAlN coated carbide inserts?*

5.1.1. The effect of feed rate.

A basic experiment changing feed rate in face milling is conducted which allows us to initiate testing and assess a capability to identify changes to machining parameters by evaluating tool wear. Test parameters are outlined in Table 5.1, and Figure 5.2 displays milling cutter orientation with the workpiece during operation.

Table 5.1: Milling test conditions.

Cutting tool (substrate)	Iscar F90-D100-32 (Carbide)
Cutting speed	200 m/min
Feed rate	0.1 mm/tooth and 0.2 mm/tooth
Axial depth of cut (a_a)	1 mm
Radial depth of cut (a_r)	50 mm
Milling direction	Down milling
Cutting length – one pass	300 mm
Test material	K 1045 low carbon steel
Cutting fluid	None
Number of samples	2 diametrically opposed - see Figure 5.2(b)]
Definition of wear	Crater reaches tool edge

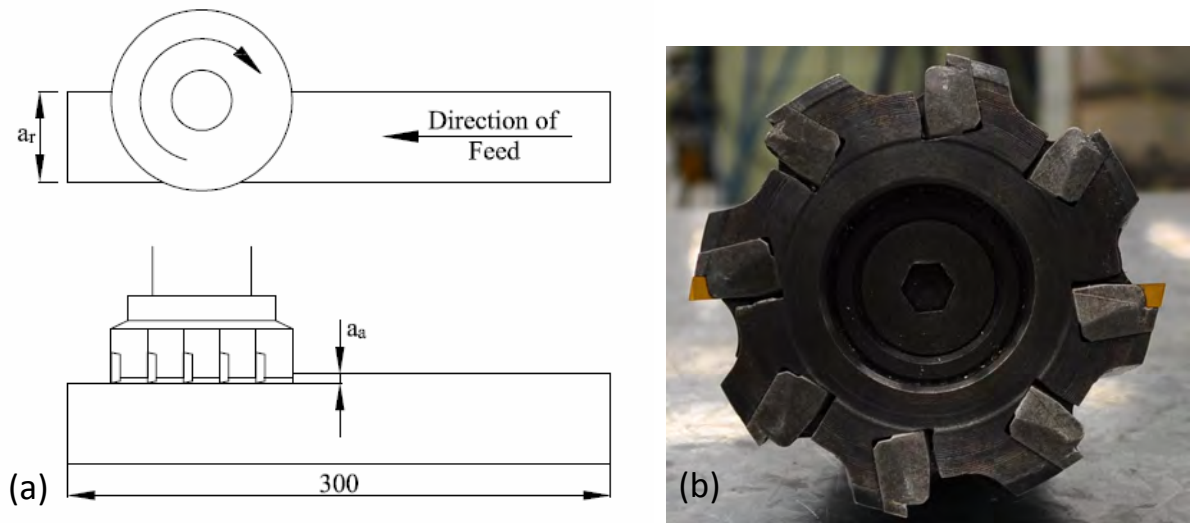

Figure 5.2: (a) Milling cutter orientation and (b) two cutting tips mounted in cutter (left and right).

Coating cross-sections were observed using fracture cross section imaging in the SEM. Micrographs of TiN and TiAlN coatings can be seen in Figure 5.3.

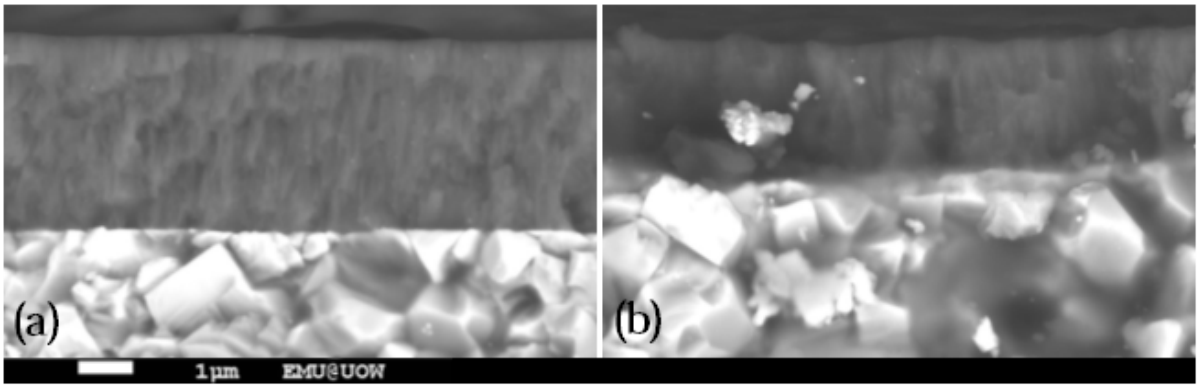

Figure 5.3: Fracture cross-section micrographs of (a) TiN and (b) TiAlN coatings, 3.5 µm and 2.3 µm thick respectively.

5.1.1.1. Feed rate of 0.1 mm/tooth.

Rake wear of both samples was observed in the SEM and from micrographs in Figure 5.4. Craters have formed on both tools. A comparison of the crater size indicates the TiN coated carbide insert has a smaller crater and therefore outperforms the TiAlN coated tool.

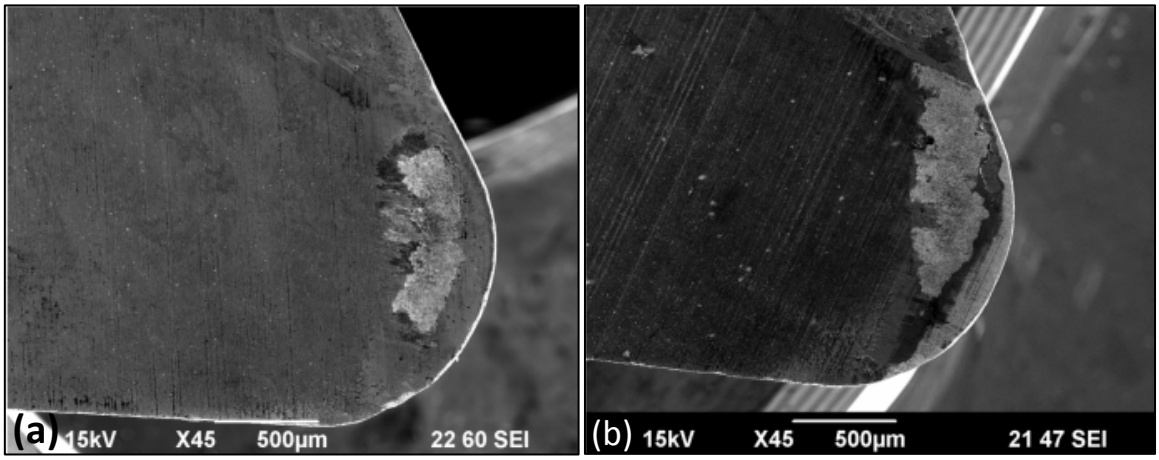

Figure 5.4: Electron micrograph of the rake face of (a) TiN and (b) TiAlN coated inserts after cutting distance of 3 m at a feed rate of 0.1 mm/tooth. TiAlN has larger crater wear and the crater has reached the cutting edge.

Measured cutting forces (Figure 5.5) also support this finding as TiAlN cutting forces are greater than TiN tools at a feed rate of 0.1 mm/tooth and a cutting distance of 3 m.

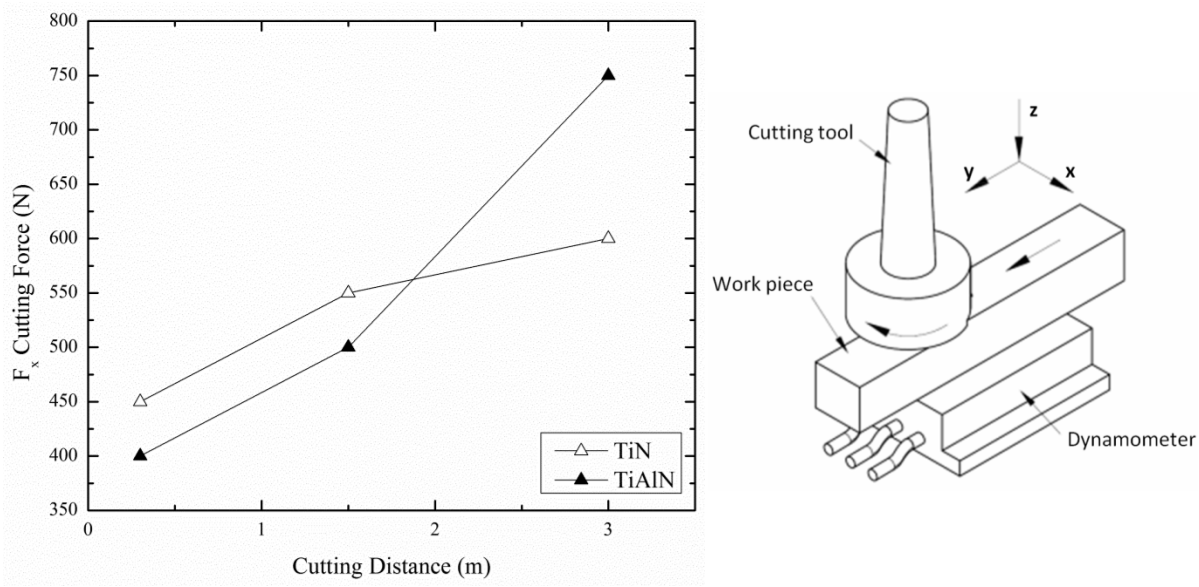

Figure 5.5: Progression of x-direction cutting force during milling test at 0.1 mm/tooth. Force axis key shown on right.

5.1.1.2. Feed rate of 0.2 mm/tooth.

The test in Section 5.1.1.1 was repeated with identical conditions, except with an increased feed rate of 0.2 mm/tooth. From Figure 5.6 the progression of crater wear on the TiAlN coated milling insert is shown for a cutting distance up to 15 m and the cutting forces are shown in Figure 5.8 for a cutting distance greater than 35 m. The performance of the TiAlN coating has dramatically increased when compared with the previous test at a feed rate of 0.1 mm/tooth, and the TiN coated tool is observed to have a reduced tool life. It catastrophically fails after 3 m of milling – see Figure 5.7.

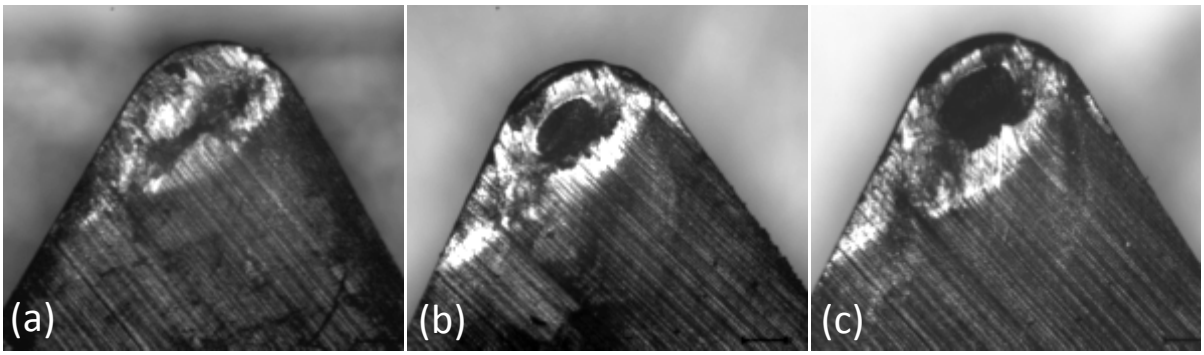

Figure 5.6: Crater wear optical micrographs of TiAlN coated insert after a cutting distance of (a) 3 m, (b) 10 m and (c) 15 m. The tool was capable of continuing to cut.

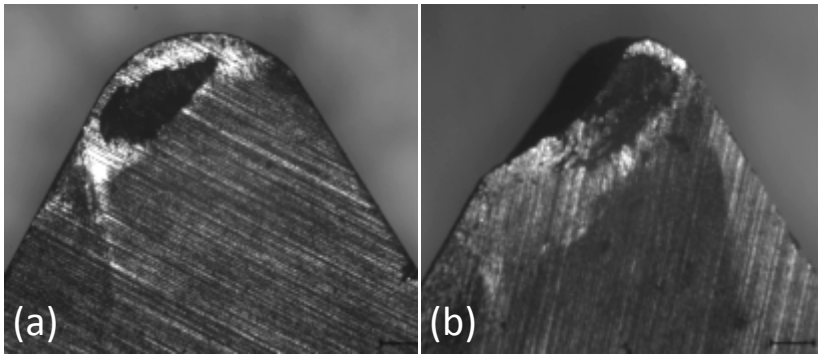

Figure 5.7: Crater wear optical micrographs of TiN coated insert after a cutting distance of (a) 1.5m and (b) 3 m. The insert has catastrophically failed.

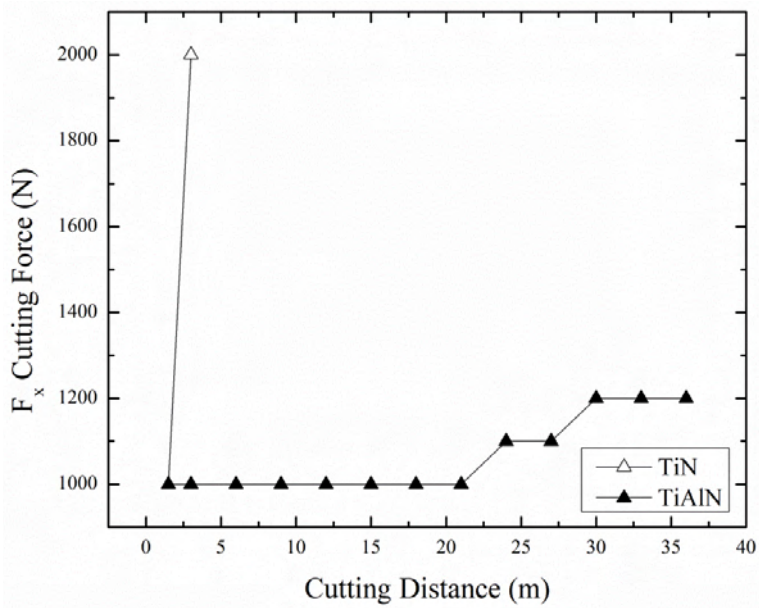

Figure 5.8: Progression of x-direction cutting force during milling test at 0.2 mm/tooth.

5.1.1.3. In summary.

From this examination of the effect of feed rate on the performance of TiN and TiAlN coatings during face milling of K1045 steel at a cutting speed of 200 m/min, significant differences in tool wear are observable. The test indicated that TiAlN coatings, when operating at a higher feed rate of to 0.2 mm/tooth, offer improved wear protection of carbide inserts in face milling than when operating at lower 0.1 mm/tooth feed rate.

This change in the performance of TiAlN coated tools is expected to be due to the higher temperatures that would be experienced with a higher feed rate. Higher temperatures will

cause beneficial oxidation reactions to occur on the rake face; and phase segregation, which will increase film hardness.

This higher temperature will cause the oxidation of TiN films, and as observed the TiN test - performance reduces with a higher feed rate. Interestingly, TiN coated inserts perform better than TiAlN coated tools at a feed rate of 0.1 mm/tooth. This is most likely due to the lower friction coefficient of TiN when sliding against steel at these speeds. TiN shows a friction coefficient of ~0.23 at 200 m/min when cutting K1045 steel [123], and TiAlN exhibits a higher coefficient of friction at 0.58 when cutting the same material at 180 m/min [124] (the trend displayed in [124] indicates a slightly lower friction coefficient will occur at 200 m/min for TiAlN, however it will remain higher than TiN operating at the same conditions).

5.1.2. Cutting speed and feed: their effect on temperature and coating performance.

The feed rate during face milling of K1045 steel at 200 m/min has been shown to have an effect on the performance of TiN and TiAlN coatings. The cause of these changes has been linked to the increased temperatures generated at higher feed rates, which in turn cause the oxidation and degradation of TiN films, and the beneficial oxidation and phase segregation of TiAlN coatings. How then does cutting speed fit into this problem? Will increasing speed also improve the comparative performance of TiAlN coatings in face milling operations, leading it to outperform TiN?

The equation in Figure 5.9 attempts to formulate how temperature is generated in cutting. The specific energy, volumetric specific heat of the workpiece and thermal diffusivity are all conditions that remain unchanged if workpiece material and the machining operation are consistent.

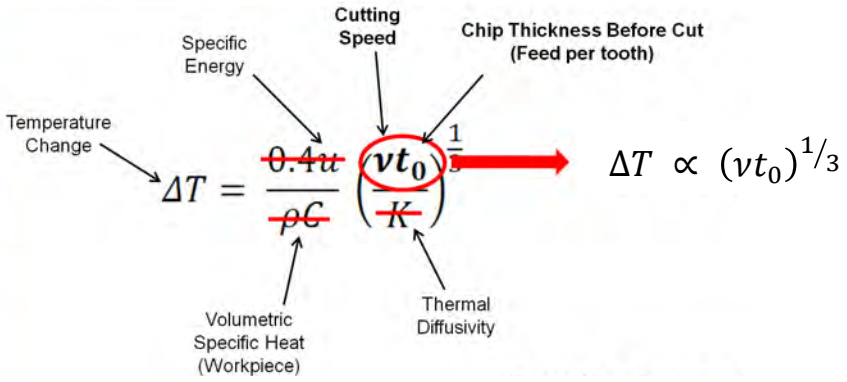

Figure 5.9: Cutting temperature and its relationship with speed and feed rates in a machining operation. Formula taken from [23] and conditions under which formula were developed are not specified.

If they remain constant, the only influences on temperature change are cutting speed and feed (or chip thickness before cut), according to this formula. This is an oversimplification of a complex process, and further examination is necessary; experimentation can allow for real observations.

Figure 5.10 speculates the likely differences between heat generated with changes to cutting speed and feed. Changes to the cutting speed are likely to change heat generated in the primary shear zone and at the tool/rake interface. Differences in feed rate are most likely to have an effect only on the heat generated at the tool/rake interface. Extra heat generated in the primary shear zone during higher feeds could transfer through the extra chip thickness available and have less of an effect on temperature at the cutting tool surface.

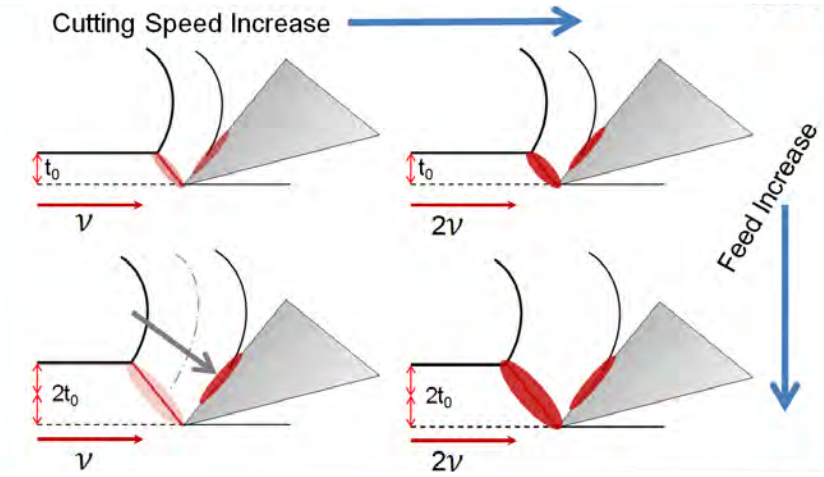

Figure 5.10: Hypothesized changes to heat generated with changes to cutting speed and feed. Cutting speed is likely to have larger impact on temperature and feed will most likely increase temperature generated by friction of the chip with the rake face.

An experiment is designed to observe the hypothesis proposed in Figure 5.10 in a face milling operation much like in Section 5.1.1. Two cutting speeds, 200 and 300 m/min are tested with two feed rates of 0.1 and 0.2 mm/tooth.

5.1.2.1. Temperature measurements.

Temperature was measured using a Raytek Raynger 3i series pyrometer, set to return a maximum temperature in a given area of vision. Table 5.2 shows temperatures and cutting conditions measured during tests. It is important to realise these temperatures are much lower than the 'flash' temperatures at the interface, which are more likely to reach 800 °C.

Table 5.2: Recorded pyrometer cutting temperatures of four tests and their cutting speed and feed parameters for face milling operation.

	Cutting speed (m/min)	Cutting speed (m/min)
Feed rate (mm/tooth)	200	300
0.1	TiN: **255** °C TiAlN: **360** °C	TiN: **370** °C TiAlN: **365** °C
0.2	TiN: **295** °C TiAlN: **335** °C	TiN: **278** °C TiAlN: **308** °C

The two highest recorded temperatures are at conditions of 300 m/min and 0.1 mm/tooth - 370 °C for the TiN sample and 365 °C for TiAlN. The trends do not match the hypothesised situation in Figure 5.10 and no real trend is observable.

The absolute values of temperature appear too low for this operation at these cutting speeds. The pyrometer is measuring infrared wavelengths radiating from the cutting tool and chip. The temperature at the interface between the chip and tool rake face during cutting must be higher than what is recorded with the pyrometer, but the infrared light is shielded by the chip and tool. The temperatures measured can also be erroneous due to the speed at which the tool moves through the area detected by the pyrometer. An high velocity tool poses complications as perhaps the tool itself does not remain in the pyrometer field of view for long enough to allow accurate temperature measurement.

5.1.2.2. Tool life.

Tool failure is defined as the point when the crater on the rake face of tools reaches the edge of the tool or catastrophic failure occurs. Flank wear was found to be minimal for all samples (not shown). Tool life (displayed as cutting distance) results from this test are shown in the column chart in Figure 5.11.

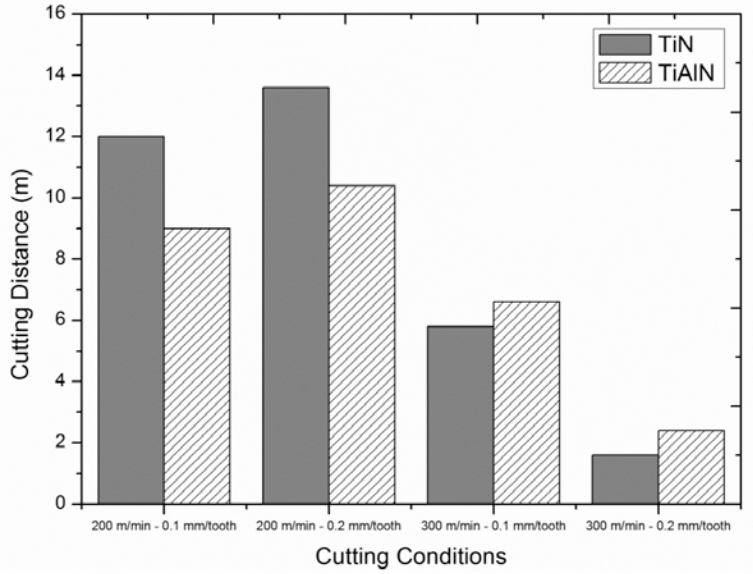

Figure 5.11: Milling test for TiN and TiAlN at various cutting conditions. TiN performs best at 200 m/min, TiAlN performs better at 300 m/min.

A trend is noticeable whereby TiN coated tools perform better than TiAlN tools at 200 m/min cutting speeds. As cutting speed is increased to 300 m/min, TiAlN begins to surpass the performance of TiN at the same cutting conditions. This can be explained by the activation of an Al_xO_{1-x} passivation layer in the TiAlN films, which would only form at elevated chip-tool interface temperatures that occur at higher cutting speeds. Where TiAlN will have better milling performance at higher speeds, TiN will oxidise at higher speeds and temperatures and exhibit a comparative decrease tool life. A significant reduction in tool life is observed for both samples with an increase in cutting speed; an effect almost always observed due to drastic increases in temperature and cutting force.

Tools operating at 200 m/min and a feed rate of 0.2 mm/tooth offer longer life than those operating at 0.1 mm/tooth. Rather than a temperature related effect, a likely reason for this effect is because the cutting force is applied further away from the cutting edge with a 0.2 mm/tooth cut, to a section of the tool that is better shaped to deal with an applied load: close to the edge (in the 0.1 mm/tooth case), there is more of a cantilever effect – further away, a better supported 'beam' and improved tool life.

The definition for a worn tool was decided as the point when the crater on the rake face connects with the cutting edge. However, the point became difficult to define because all 0.1 mm/tooth tools had craters that were so small and close to the cutting edge. This is due to the small depth of cut. Additionally, some cutting edges failed due to a brittle fracture, before the crater developed fully. See the tools on the bottom right of Figure 5.12. These complexities do not degrade the results obtained, however they restrict an ability to convincingly conclude findings.

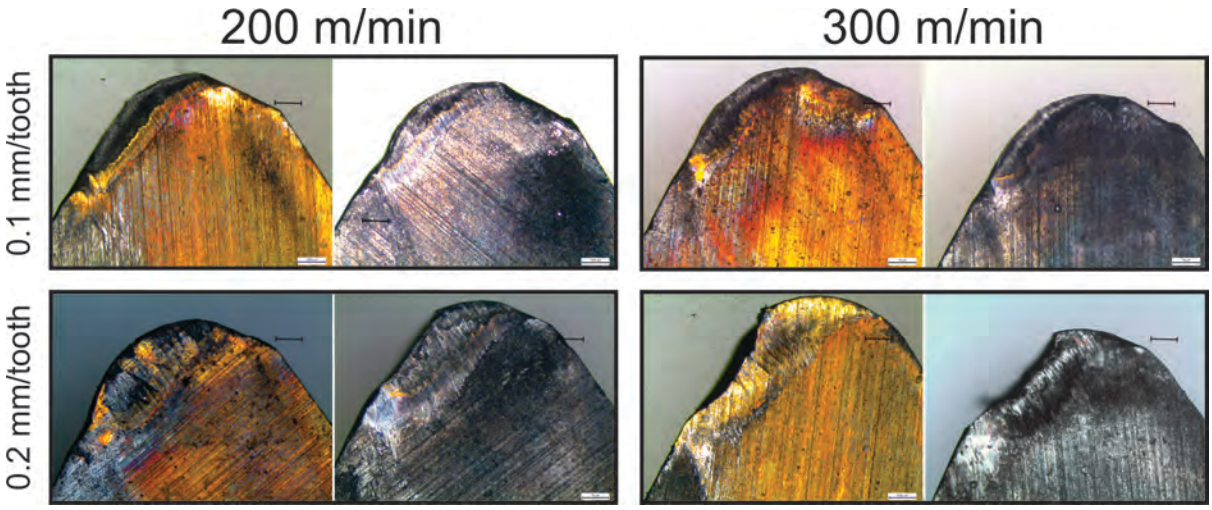

Figure 5.12: Optical micrographs of crater wear at failure of each tool. TiN is always on the left in the pairs and the micron bars read 200 µm.

The same effect of increased TiAlN performance with a change in feed rate from 0.1 to 0.2 mm/tooth as in previous experiment (Section 5.1.1) is not observed in this case. Reasons for this could be numerous: changes to workpiece hardness and abrasives content, tool engagement issues (entry and exit of the tool into and out of the workpiece can sometimes be dangerous for cutting tools).

5.1.2.3. Summary.

From measurements made using an infrared pyrometer, temperature follows no trend with changes to speed and feed. This could be due to a few reasons. The pyrometer may be incapable of accurately measuring temperature from a fast moving cutting tool. The real temperature at the rake/chip interface is definitely higher than the measured temperature. This is due to the shielding of the interface by the chip or workpiece material. This was understood when measurements were made, but a trend between temperatures and cutting parameters was expected regardless.

The performance of TiN and TiAlN coated inserts in face milling applications of K1045 steel is dependent on cutting speed and feed. TiN coated tools perform better than TiAlN tools at 200 m/min., and TiAlN coated tools perform better than TiN tools at 300 m/min. All tools exhibited a longer tool life at 200 m/min, and the optimum cutting conditions for tool life were at 200 m/min and a feed rate of 0.2 mm/tooth.

5.1.3. How does the presence of oxygen affect coating performance?

The same cutting test as in Section 5.1.2 was repeated with the addition of a box surrounding the workpiece and milling cutter, flooded with high purity Ar gas. Ar was chosen due to it being low-cost as well as inert. The box was metal on three sides with a Perspex side facing towards the user – as pictured in Figure 5.13. The gas is supplied through a hole in the bottom right of the image, with the bottom of the box sealed the flow should continue to the top and escape through gaps that remain where the lid connects with the walls of the box. The design is not meant to leave an atmosphere of pure Ar, this is very difficult to achieve without a vacuum system, but will reduce the oxygen content as Ar gas flows into the chamber. The oxygen levels were measured inside the box using a Cambridge Sensotec Rapidox 2100 O_2 transducer and atmospheric levels of 21 % were reduced to 13-15 % and - with higher flow rates of Ar - 4-6 % oxygen.

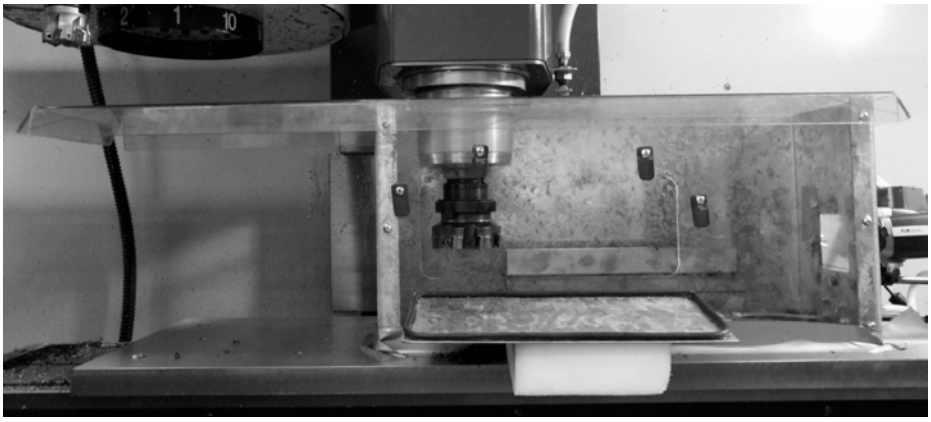

Figure 5.13: Box surrounding workpiece and milling cutter. Box is mounted to the machine table, moving with the workpiece. A lid is loosely secured to the miller head and will move independently of the box.

The purpose of displacing oxygen in the cutting region is to observe its influence on the performance of TiN and TiAlN coated tools during face milling by monitoring crater wear. Ideally, this experiment will allow for some control of the beneficial oxidation reaction that TiAlN coatings utilise for added performance. A change in TiAlN tool life might then be observable. Additionally the performance of TiN films could increase due to reduced oxidation and associated wear.

Results show the cutting distance achieved for each coated tool in each condition (Figure 5.14). The performance of TiN coated tools is relatively close to observations made when

cutting at normal atmospheric conditions. The distance cut for TiN at cutting speeds of 300 m/min is greater than the distance cut by TiAlN coated tools at both feed rates. This trend is expected with reduced oxygen in the atmosphere in the cutting region and supports the beneficial oxidation explanation for TiAlN performance.

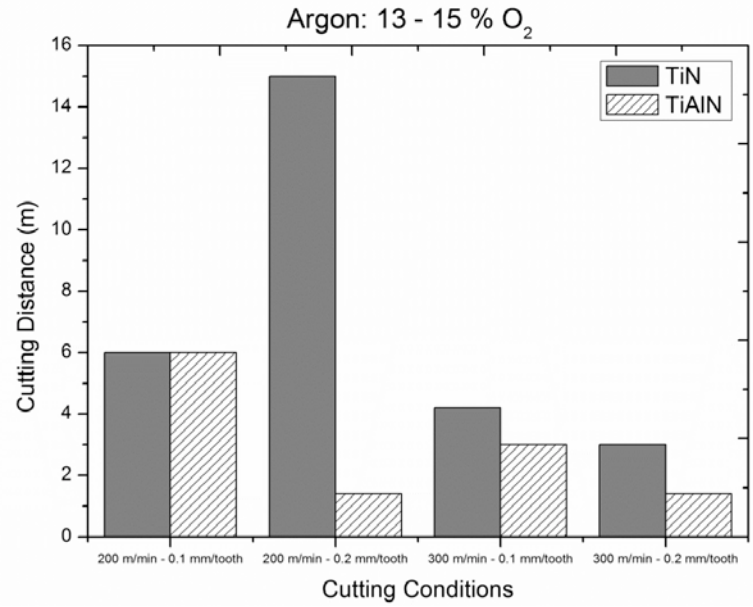

Figure 5.14: Milling test for TiN and TiAlN in a 13 – 15 % oxygen atmosphere at various cutting conditions. TiN cut distance is either the same or greater than TiAlN in all cases.

The two tests at 200 m/min have some issues: firstly, the TiAlN tool at a feed of 0.1 mm/tooth appears to have failed prematurely (see the fractured area in black on the rake face of the TiAlN tool in the top right of Figure 5.15). The TiN test at 0.1 mm/tooth could continue to cut, depending on how strictly one adheres to the definition of wear. It has been stated that when the crater on the rake face reaches the cutting edge, the tool is regarded as worn. Technically, the TiN tool cut at 200 m/min and 0.1 mm/tooth is worn, but it is still very capable of removing additional material effectively. The TiAlN tool at 200 m/min and 0.2 mm/tooth has also prematurely failed with chipping of the edge. This was more noticeable when observing the tool during operation. An irregular audible noise and spark ejection were obvious. This complication causes difficulties in making conclusions about the real effect of reducing oxygen levels during face milling with TiN and TiAlN tools, however from the results obtained it can be stated that a reduction in oxygen levels leads to a reduction in the performance of both coating architectures. A TiAlN film's reliance on the presence of oxygen to form protective oxide layers is anticipated, however a reduction in

TiN performance is an unexpected observation. From this experiment, we can see TiN benefits from the presence of oxygen in its surrounding atmosphere in face milling operations. Further experimentation to better explore and understand this finding is recommended as premature tool failures and definitions of tool wear have potential to generate erroneous results.

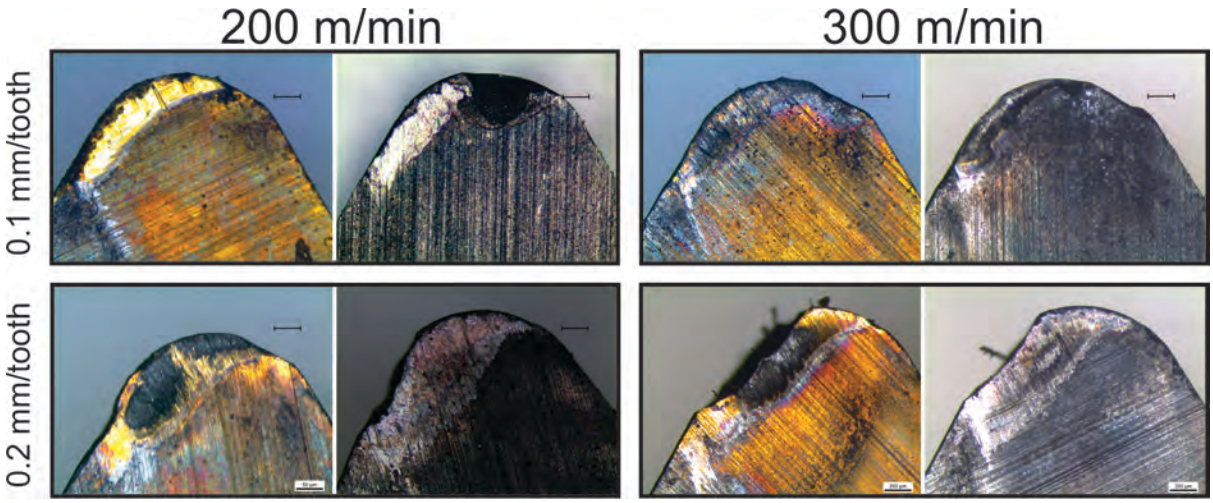

Figure 5.15: Optical micrographs of crater wear at failure of each tool that operated under reduced oxygen atmospheres of 14-15% O_2. TiN is always on the left in the pairs and the micron bars read 200 µm.

Another test was completed at a higher flow rate of Ar gas into the chamber, achieving an oxygen percentage of 4-6 %. Operating at this higher flow rate used large quantities of Ar gas so the cutting distance for TiN and TiAlN were only recorded for one cutting condition. The condition here was chosen due to reliability, higher speeds seem to cause edge chipping and lower feed rates have the issue of difficult to characterise crater wear.

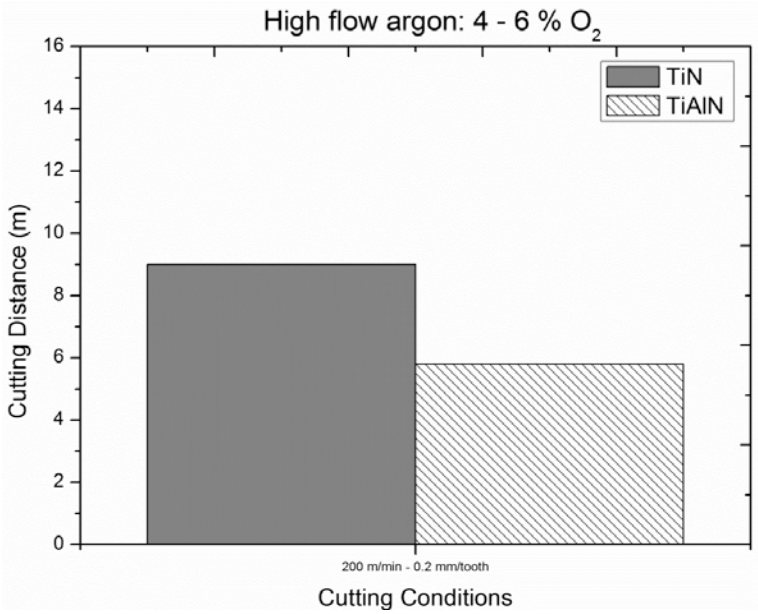

Figure 5.16: Milling test for TiN and TiAlN in a 4 – 6 % oxygen at 200 m/min and 0.2 mm/tooth.

As hypothesised, the performance of TiN is superior to that of TiAlN when oxygen is reduced; further supporting the reliance of TiAlN performance on the presence of oxygen. However, comparing the 13-15% O_2 and 4-6% O_2 tests for TiAlN tools operating at 200 m/min and 0.2 mm/tooth, tool life has in fact increased from 1.5 m to 5.5 m respectively, with a decrease in oxygen levels. This can be justified by noting the premature failure of the TiAlN coated cutting tool at 13-15% O_2 conditions. Without premature failure, it is likely that the higher oxygen levels would promote longer tool life than the tool operating at further reduced oxygen conditions.

As in the previous test with 13-15% O_2 in the cutting atmosphere, the performance of TiN coatings operating at these conditions has reduced. Focusing on TiN tools operating at 200 m/min and 0.2 mm/tooth (mainly due to their gradual and comparative wear); the tool life is 13.5 m in atmosphere, 15 m in 13-15% O_2, and 9 m at 4-6% O_2. Under atmosphere and O_2 levels of 13-15%, the results are similar and can be thought of as approximately equal when considering experimental and observational errors. However, at the two extremes of O_2 levels, there is a reduction in tool life of 4.5 m with a reduction in O_2. This is an unexpected observation and it would appear that oxidation has some beneficial effects for TiN coatings as well as for TiAlN films. Perhaps the formation of rutile-TiO_2 provides a protective layer to TiN coated cutting tools in a similar way to the mechanism of $Al_xO_{1-}x$ formation on the rake face of TiAlN coated cutting tools.

5.1.4. Face milling of TiN and TiAlN: a summary.

There are benefits to conducting research at conditions where coatings and tools will be used in industry practice, it enables the gathering of observations to include as evidence towards building statistical significance, but can be difficult for scientists to unambiguously state mechanisms for a result. Having said that, there are some conclusions that can be made from these experiments.

The feed rate during face milling of K1045 steel at 200 m/min was observed to influence the tool life of TiN and TiAlN coated carbide inserts. At a feed of 0.1 mm/tooth TiN coated samples performed marginally better than TiAlN tools. At a feed of 0.2 mm/tooth a change in this trend occurred and TiAlN tools performance substantially better than TiN inserts. This change in tool life is linked to the mechanisms of segregation hardening and tribo-oxidation for the TiAlN architecture. The activation of these mechanisms occurs at higher temperatures and only with a higher feed rate are they likely to operate.

Combining the effects of speed and feed, another test was completed to examine the tool life of TiN and TiAlN coated carbide inserts in face milling. This test was designed to measure temperature behaviours with changes to feed and speed. Either the concepts hypothesised were incorrect or the pyrometer used was incapable of accurately measuring temperature of a fast moving tool. As well as this potential problem, the temperature measured from any infrared device will never capture the real temperature at the chip and tool interface (in this process) as it is hidden from line of sight.

The tool life observed for this test was a maximum for TiN coated inserts at 200 m/min at a feed rate of 0.2 mm/tooth. Higher speeds of 300 m/min are where TiAlN films performed better than TiN. The higher speeds were seen to reduce performance of all tools significantly when compared with results at 200 m/min. Rake wear was the prominent wear mechanism for all samples.

The presence of oxygen in the cutting region was then checked for an influence on the performance of TiN and TiAlN tools by running a comparative test in an Ar enriched environment. TiN performance was shown to also reduce with lower levels of O_2, an unanticipated finding that may be linked to a protective layer of rutile-TiO_2. The

performance of TiAlN decreases in all reduced oxygen cases. This effect is linked to the beneficial tribo-oxidation of the TiAlN coated tool rake face and its reduction in Ar flooded environments.

The phase segregation hardening effect does not appear to influence TiAlN performance under these cutting conditions. TiAlN will only begin to segregate and increase hardness above 700 °C [42]. Hence, it is possible that this mechanism is not active at the cutting temperatures in this case and TiAlN performance is more reliant on oxidation at these cutting parameters.

The optimal cutting conditions for predictable wear were 200 m/min and 0.2 mm/tooth. Higher speeds caused edge chipping and lower feeds leave difficulty in characterising rake wear and a worn tool.

5.2. Orthogonal cutting with a quick-stop device.

This section covers the use of an orthogonal test rig, utilising a quick-stop device, that aims maximise the control of the cutting process to enable detailed scientific analysis of coated tool wear under different atmospheric conditions, whilst also monitoring chip formation of a Ti6Al4V workpiece.

Orthogonal cutting is conducted using a lathe and a round bar workpiece, providing a significant cutting distance for each test. This allows for steady state cutting to be achieved after longer cutting distances; whereby the development of interactions between tool and workpiece can eventuate, and the effect of temperature on oxidation of TiN and TiAlN films can be observed at typical industry cutting parameters.

In this process the cutting tool will remain stationary, enabling more accurate measurements of temperature with infrared instruments, as well as gas delivery to a stationary rake and chip interface is simplified. This removes the need for a chamber to create a less reactive atmosphere.

In the experiments performed in the previous section, it would be have been useful to observe chip formation as there could be changes to chip formation that drive changes to tool and coating behaviour, but is too complex to analyse in a milling process. Understanding chip flow is troublesome when cutting occurs on two faces of a tool, so with an orthogonal cutting process, chip formation is 2-dimensional and less troublesome. A quick-stop device is used in this section to leave a semi-formed chip. This can provide information about *in-situ* chip formation under 2-dimensional force conditions.

The experiment here aims to continue an analysis of TiN and TiAlN films in dry (no lubricant/coolant) cutting. A reduction in oxygen levels, provided by Ar gas supply, is used to influence the oxidation effects of both coatings. TiAlN is of particular interest with Ar supplied in an attempt to differentiate the effects of segregation hardening and beneficial oxidation. The work aims to address the question: *What is the effect of Ar gas supplied, to the rake face of TiN and TiAlN coated tools, on tool wear during dry orthogonal cutting?*

The workpiece material cut is Ti6Al4V. This material was chosen due to the widespread interest in understanding its chip formation mechanisms. It is of significance to observe the

effect that oxygen has on chip formation. Ti6Al4V has a high affinity with oxygen, potentially leaving a more dramatic change with Ar supply. Here, another question is tackled: *What is the effect of Ar gas supplied, to the rake face of tools, on chip formation mechanisms of Ti6Al4V during dry orthogonal cutting?*

5.2.1. System design.

From previous face milling (Section 5.1) experiments there have been some problems and limitations.

- Tests are time intensive for each sample.
- Much of the workpiece material is consumed.
- Analysis of crater wear and chip formation is complex as chip flow occurs in many directions.
- Infra-red sensors are potentially ineffective when used with fast moving cutting tools.
- Tool wear, as a definition of performance, can be complex and results have variability, demanding larger sample numbers to observe a population.

There is a need to solve as many of these issues as possible, whilst maintaining the ability to test at cutting speeds and feeds typical of industry practice. The first step in solving many of these problems is to cut orthogonally. Much of the work addressed in Section 2.1 is completed with orthogonal cutting in planing operations and conducting experiments at similar conditions allows for comparison. Planing is desirable from a scientific point of view because of its simplicity, but has limitations in cutting speed, and total cutting distance which leads to non-steady state conditions.

So in the interest of industry, there is a need to make observations of tool wear and chip formation at operational cutting speeds. Cutting distance is very important for measuring interactions between chip and tool. An example is if reactions with atmospheric conditions are to be observed, adequate cutting distance and speed must be given to allow these mechanisms to develop.

To satisfy these needs this experiment achieves orthogonal cutting using a lathe and a round bar workpiece. The concept has been adapted from a test method developed by Astakhov

[125]. The quick-stop device detailed in Chapter 3 has been included to allow for careful observations of chip formation.

5.2.1.1. Orthogonal cutting with a lathe.

A round bar is used as the workpiece. It is prepared with a single lead, square thread. The crest width (the section of the thread removed for each test) is machined to 2mm, and the root width 1 mm, creating a 3 mm pitch. The thread length is cut to 250 mm, allowing for 83 revolutions of the workpiece and a total orthogonal cutting distance of 13 m at a constant cutting speed.

Other methods of cutting orthogonally on a lathe by reducing the workpiece diameter in an x-movement means the cutting speed changes as the diameter is reduced at a constant revolution velocity. Computer numerically controlled (CNC) lathes can maintain a constant cutting speed with a changing diameter, however actual speeds fluctuate as the feedback system accommodates changes.

Figure 5.17: Ti6Al4V workpiece prepared with 3mm pitch square thread. Cutting tool holder and quick-stop device shown on left, the copper pipe channelling compressed gasses can also be seen.

During tests, a 3 mm wide tool is used to remove the 2 mm crest of the thread. This provides, from the tools perspective, orthogonal cutting conditions for a large distance at any speed and feed desired, but it must be considered that CNC machines will have some limit to the possible tool linear velocity, meaning there will be a limited revolution speed of

the workpiece allowed to keep the tool synchronised with the crest of the thread. Cutting tools will also have a limitation on speed and feed that they are capable of operating at.

5.2.2. Orthogonal cutting of Ti6Al4V: TiN & TiAlN, Compressed air & Argon.

During tests, a 3mm wide tool was used to remove the 2 mm crest of the thread at a cutting depth of 0.08 mm at 50m/min. Compressed gas, from a cylindrical bottle source (i.e. dry), was applied at a regulator flow rate of 10 L/min via a copper pipe to the rake and chip interface (see copper pipe in Figure 5.17).

The workpiece chosen for this experiment was Ti6Al4V in the mill-annealed state. This alloy was preferred because of its high affinity for oxygen, which should encourage a reaction on the newly formed chip and add contrast to this experiment with and without Ar gas supply.

When the tool moved towards the end of the cut, an infrared image of the tool was taken with a Flir B200 infrared camera. Shortly after, an *in-situ* chip was captured as the quick-stop device was activated. This process was repeated four times, once for each of conditions: i) TiN coated tool with compressed high purity Ar applied to the rake and chip interface, ii) TiN coated tool with compressed air applied to the rake and chip interface and iii) TiAlN with compressed high purity Ar applied to the rake and chip interface, iv) TiAlN coated tool with compressed air applied to the rake and chip interface. Cutting forces were measured during this test, but no discernable differences were noticed for all samples and results are not shown here.

5.2.2.1. SEM and EDS: rake wear behaviour.

Zone 2 (as defined in [17]) in develops due to oxidation of the chip and tool. With changes in gas applied, a change in Zone 2 wear is expected because access to oxygen is limited with Ar applied. Oxidation of the newly formed chip could influence deformation mechanisms. As a result, workpiece deposits and wear behaviour could also change. Low magnification micrographs of the cutting tools after testing are shown in Figure 5.18. The cutting edge is at the top of all four images. These images provide an overview of all worn test cutting tools and show how the wear patterns are centred on the 3 mm wide cutting edge. The

wear patterns also show similar wear patterns to the more traditional orthogonal tests discussed in Section 2.1.

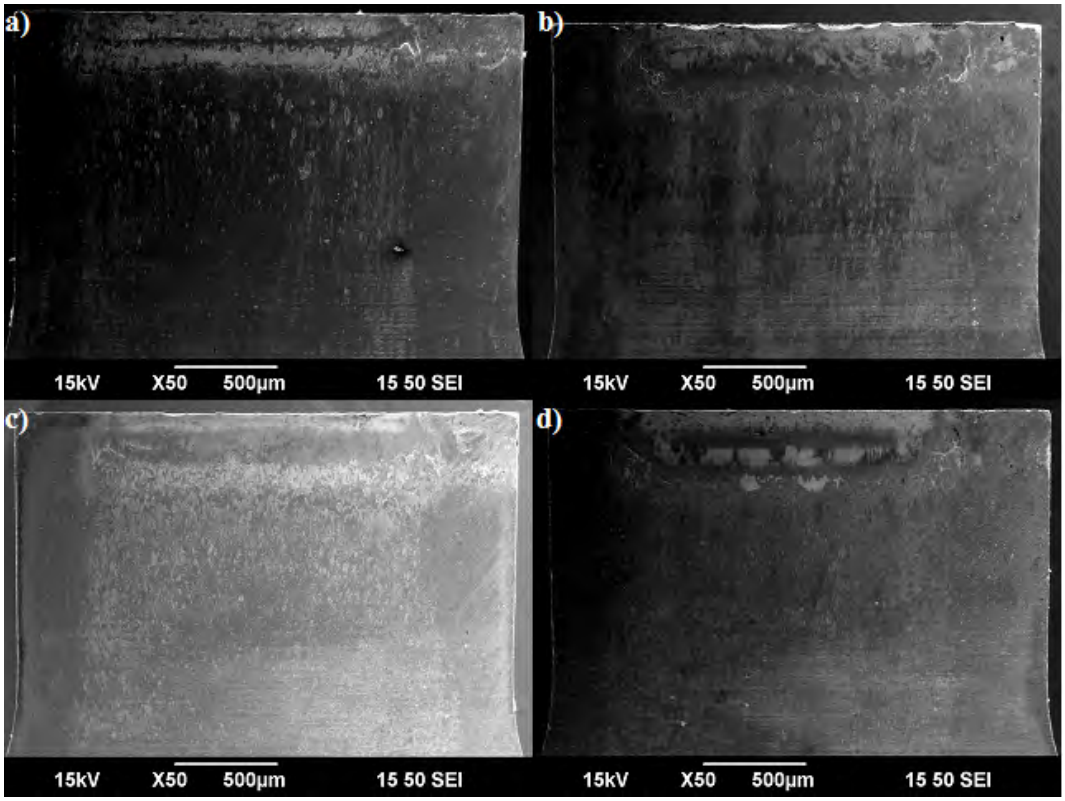

Figure 5.18: Low magnification scanning electron micrographs of the rake face of coated tools. a) TiN + Air, b) TiN + Ar, c) TiAlN + Air, d) TiAlN + Ar.

Higher magnification micrographs are displayed in Figure 5.19, the broken white line indicates the real depth of cut – as measured after testing. Variations in the depth of cut, from the programmed 0.8 mm can be attributed to movement of the tool in the tool holder, flex of the workpiece, and/or misalignment of the *x*-direction tool zero. Zones 1 and 2 can be identified in each case, the boundary between which is indicated by the broken line. This line is also the depth of cut for each respective test.

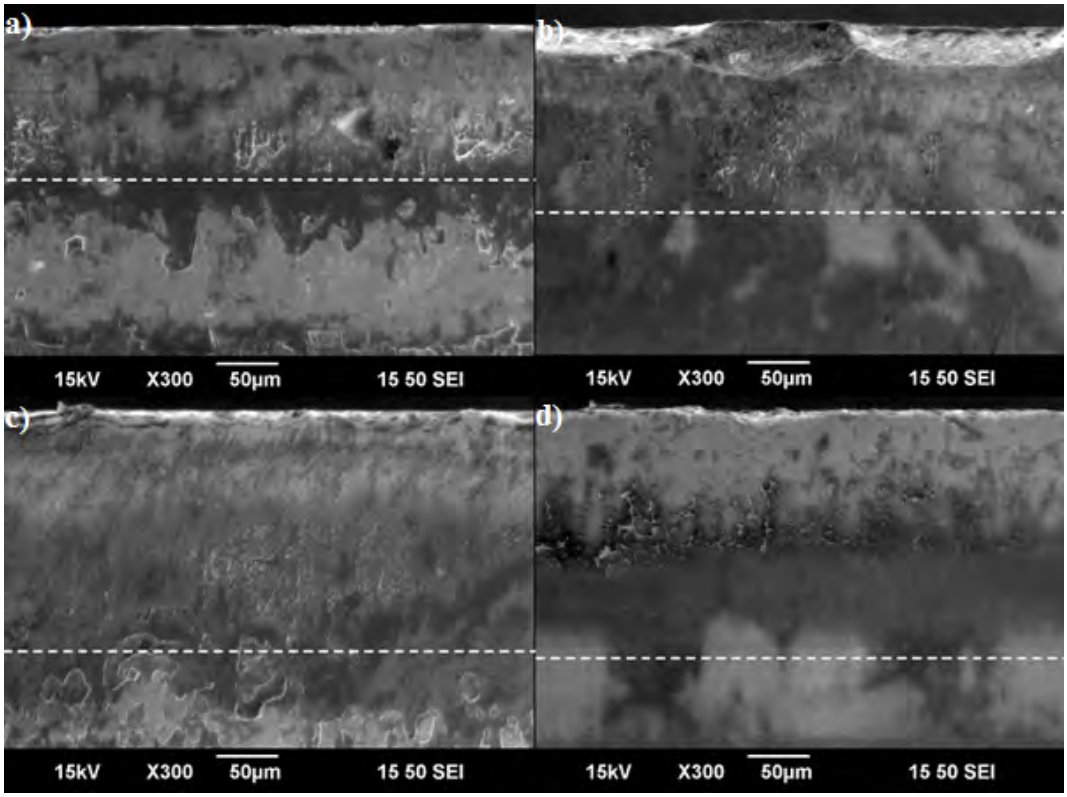

Figure 5.19: Micrographs of cutting tool rake face with the depth of cut identified. a) TiN + Air, b) TiN + Ar, c) TiAlN + Air, d) TiAlN + Ar.

Compare Zone 2 wear below the broken white line for each case. In both compressed air tests, the surface appears rough. In both cases of Ar supplied, wear below the line is smooth. With secondary electron images alone, it is not possible to determine if coating remains or workpiece material deposits exist.

EDS analysis of the rake face of tools allows for better characterisation of rake wear. EDS of the TiN sample tested with compressed air is shown in Figure 5.20. The W image provides similar information to the secondary electron image in Figure 5.19 – the coating is worn away and the substrate revealed in Zone 2. However in Zone 1, according to the secondary electron image, the coating remains. From EDS, we can see Al is detected in the same zone. Al must be from the Ti6Al4V workpiece and it has deposited on the surface of the tool in Zone 1, however it is possible that coating remains underneath and workpiece material is covering the coating, hiding the N signal.

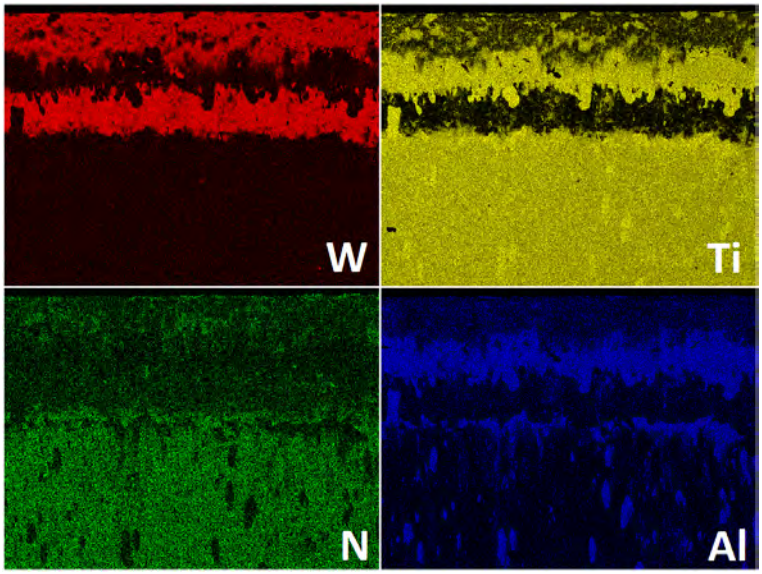

Figure 5.20: TiN with applied compressed air - EDS mapping of W, Ti, N and Al

To clarify this, a cross-section of the same sample was made and EDS analysis completed (see Figure 5.21). Below Zone 2, a layer of Ti (yellow) and N (green) is observed. This is the TiN coating. In Zone 1, what looks like a coating is detected. The element is Ti (yellow), but contains no N (green). An Al (blue) signal is collected here, indicating the deposit must be workpiece material - not TiN coating. This indicates that the coating is completely removed from the rake face in Zone 1, but remains in the area below Zone 2.

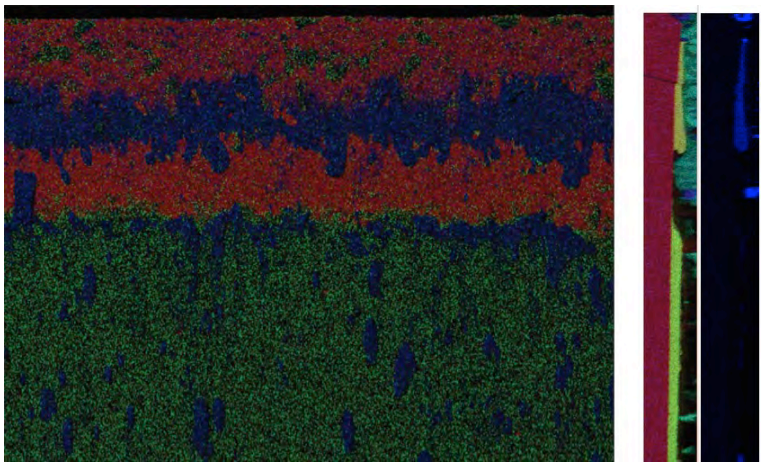

Figure 5.21: TiN sample with applied compressed air. The image on the left is a layered image of the EDS map in Figure 5.20, and on the right are two cross-sectional EDS maps of the same tool: the middle image is a layered image (Ti is mapped as yellow, all other colours are the same as in the previous EDS analysis), and the far right a map of the Al signal (in blue). The cross-sectional images provide additional information to clarify whether elements seen in the planar view EDS maps are from the coating or from deposited workpiece material.

EDS analysis of the TiN sample tested with Ar supplied to the rake face is shown in Figure 5.22. Notice the Al signal is high where the N signal is absent. Again, a cross-section must be observed to identify if coating exists underneath the detected Al.

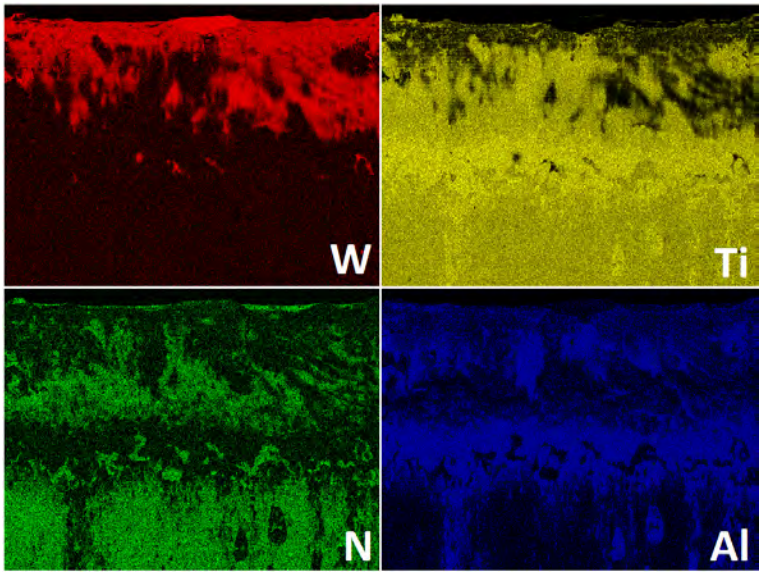

Figure 5.22: TiN sample with applied Ar - EDS mapping of W, Ti, N and Al.

Cross-sectional analysis of this sample reveals that the coating remains underneath the Ti6Al4V workpiece deposited on the tool. The coating can be identified by the presence of both Ti and N. The green colour of N differentiates coating from Ti6Al4V, as well as the Al (blue) indicates the workpiece deposited. Areas where coating is removed can be identified by exposure of the substrate W signal.

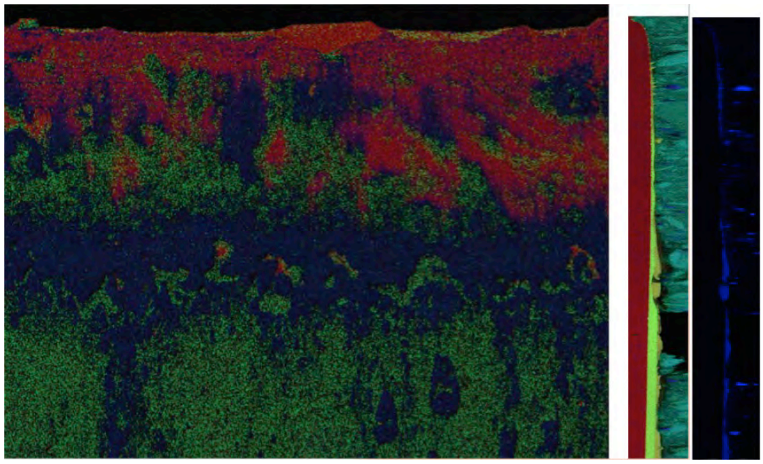

Figure 5.23: TiN sample with applied Ar. The image on the left is a layered image of the EDS map in Figure 5.22, and on the right are two cross-sectional EDS maps of the same tool: the middle image is a layered image (Ti is mapped as yellow, all other colours are the same as in the previous EDS analysis), and the far right a map of the Al signal (in blue). The cross-sectional images provide additional information to clarify whether elements seen in the planar view EDS maps are from the coating or from deposited workpiece material.

A comparison of TiN coated tools with Ar or compressed air is now possible. With compressed air, the coating is completely removed from the rake face. Only below Zone 2 does coating remain. When Ar is applied to the rake face, the TiN coating remains across Zones 1 and 2. The remaining film gradually increases in thickness from cutting edge to below Zone 2.

Workpiece material pickup is higher in Zone 1 for the compressed air sample than the Ar test. Pickup is more pronounced in Zone 2 when Ar is applied.

As with TiN samples, assessing the TiAlN coated sample with secondary electron images alone is difficult – compare c) and d) of Figure 5.19. EDS of the TiAlN coated tool tested with compressed air supply is shown in Figure 5.24. The W signal clearly reveals a worn coating and substrate exposure, and N indicates the presence of film. The Al signal is more complex in this case as there is Al in the TiAlN film as well as the Ti6Al4V workpiece.

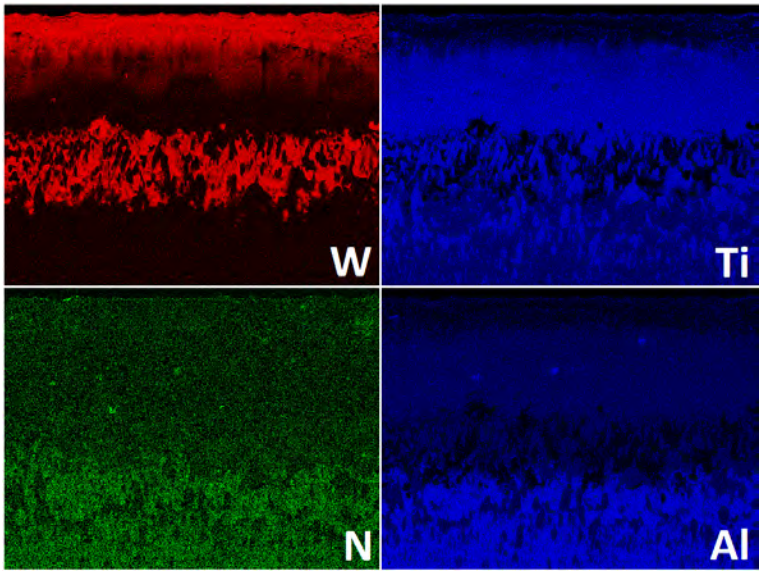

Figure 5.24: TiAlN with applied compressed air - EDS mapping of W, Ti, N and Al.

It is possible to differentiate Al from these two sources by paying attention to the intensities of Al across the rake face. The TiAlN film will have a higher atomic percentage of Al than Ti6Al4V, hence will return more signal in EDS, appearing brighter in images. This is supported by cross-sectional EDS observations of the tool in Figure 5.25.

It is clear that in Zone 1, there is a very feint Al signal and in areas below Zone 2 the Al signal is bright. In the lower region, N is shown to add a green colour to the layered image of the coating, indicating this region is deposited coating. The N signal is absent in the Zone 1 deposit, hence this area is deposited workpiece. The bright Al signal detected below Zone 2 comes from same area as the TiAlN coating.

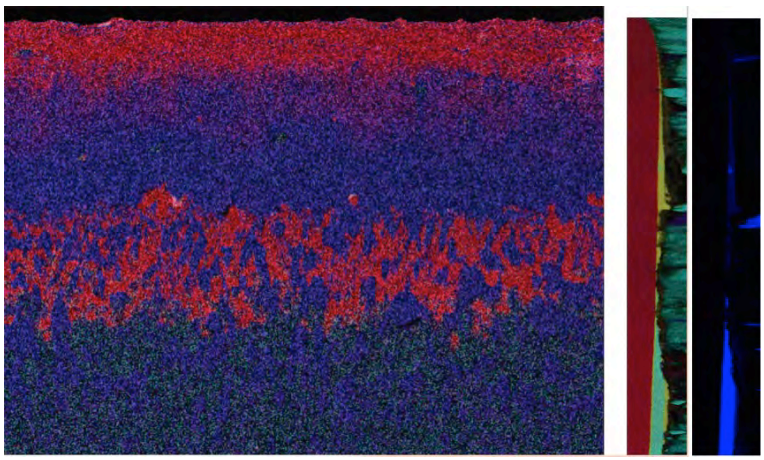

Figure 5.25: TiAlN sample with applied compressed air. The image on the left is a layered image of the EDS map in Figure 5.24, and on the right are two cross-sectional EDS maps of the same tool: the middle image is a layered image (Ti is mapped as yellow, all other colours are the same as in the previous EDS analysis), and the far right a map of the Al signal (in blue). The cross-sectional images provide additional information to clarify whether elements seen in the planar view EDS maps are from the coating or from deposited workpiece material.

For the TiAlN sample cut with Ar applied, there appears to be deposited workpiece in Zone 1 (see feint Al signal in Figure 5.26). The bright Al and the N signal indicates the location of coating and the W signal reveals the substrate. This is supported by cross-sectional EDS in Figure 5.27.

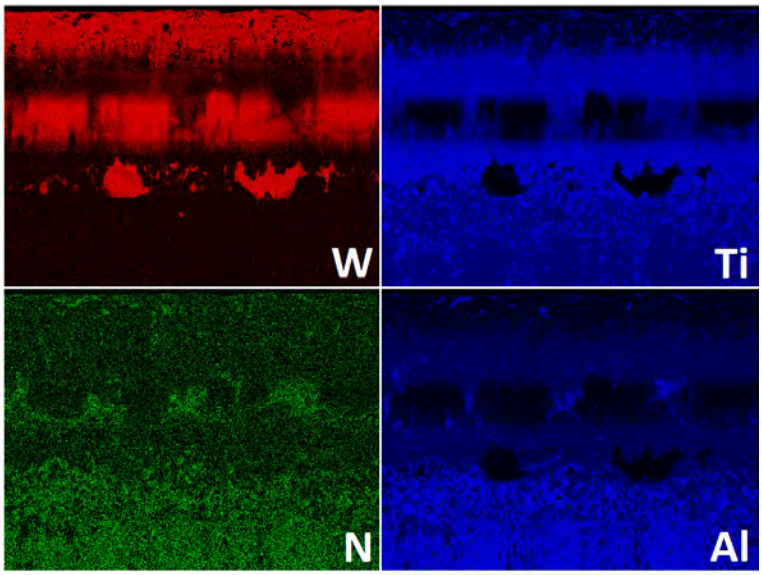

Figure 5.26: TiAlN with applied Ar - EDS mapping of W, Ti, N and Al.

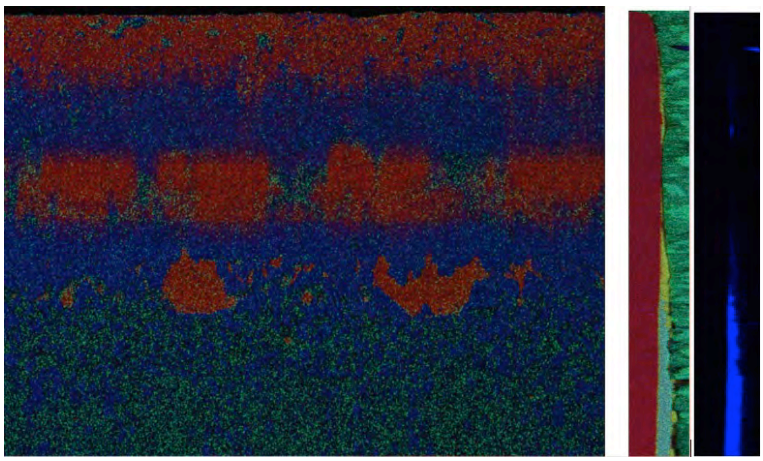

Figure 5.27: TiAlN sample with applied Ar. The image on the left is a layered image of the EDS map in Figure 5.26, and on the right are two cross-sectional EDS maps of the same tool: the middle image is a layered image (Ti is mapped as yellow, all other colours are the same as in the previous EDS analysis), and the far right a map of the Al signal (in blue). The cross-sectional images provide additional information to clarify whether elements seen in the planar view EDS maps are from the coating or from deposited workpiece material.

Comparisons of TiAlN films under two atmospheric conditions show wear of the coating is similar. The film is fully removed across both Zones 1 and 2. Although it does appear that there are some differences in the sticking behaviour of the Ti6Al4V workpiece in Zone 2.

Firstly to focus on Zone 1. In all conditions for both coatings, Zone 1 appears to have some deposit of the Ti6Al4V workpiece. This does not change with changes to gas applied to the

rake face and this should be the case as Zone 1 is defined as having no access to the atmosphere. The deposition of workpiece material in this zone could be due to the propensity for Ti6Al4V to work-harden. The secondary shear zone could further deform the chip and work-harden it. The hard chip then adheres to the rake face and remains (this is discussed in Chapter 2 and [20]).

Secondly, Zone 2 displays some differences with applied Ar and compressed air. In the samples where Ar is used, there are more deposits of workpiece material. Appreciate the small Ti (yellow) build-up of material which remains at the edge of the coating in the layered cross-sections of Figure 5.27. This does not exist in the compressed air sample in Figure 5.25. This same comparison can be made between Figure 5.21 and Figure 5.23.

The cause of this finding could be from two factors: changes to chip formation due to oxygen, or a change in coating oxidation, either or a combination could be affecting friction conditions. The friction coefficient of a coating operating in air will be higher than in vacuum [126] and perhaps under Ar conditions, with a reduction in oxygen partial pressure, a similar reduction in friction can be found. However, an increase in the adhesion of the Ti6Al4V workpiece to the rake face of tools cut under Ar conditions is observed here. One reason could be due to a change in chip formation, especially in the secondary shear zone, but if oxygen influences secondary shear deformation, this would only cause the chip to be more brittle. The reduction in ductility is linked with additional workpiece deposits on the rake face of the tool as discussed by Madhavan *et al* [17] and mentioned in Section 2.1. In this case, with less oxygen (Ar conditions), an increase in workpiece deposits found. The source of this change is unknown, and could be due to variability in tests and must be further investigated. It would be beneficial to observe any changes to secondary shear zone deformation in the Ti6Al4V chips. A detailed analysis of chip formation crystallography is provided in Section 5.2.2.3, but no changes are noticed due to difficulties in observing the secondary shear zone.

Another finding from analysis of these tools is that under Ar conditions, the wear track appears smoother than with compressed air conditions. Zone 2 wear appears less abrasive than the roughly abraded Zone 2 of the compressed air samples. Perhaps when the Ti6Al4V chip oxidises it becomes harder and more abrasive, leaving large gouges. With Ar applied,

this effect is reduced and a smoother wear track remains after a less abrasive chip flows over it. There is then a possibility that the smoother surface encourages deposits of the workpiece material noticed in Zone 2 in Ar conditions.

5.2.2.2. Temperature measurement with Infrared imaging.

A typical infrared image of the tool and chip during cutting can be seen in Figure 5.28. The maximum temperature measured with an infrared camera can help to identify friction conditions and, potentially, tool wear. Higher temperatures can be linked with increased friction, which could relate to tool wear.

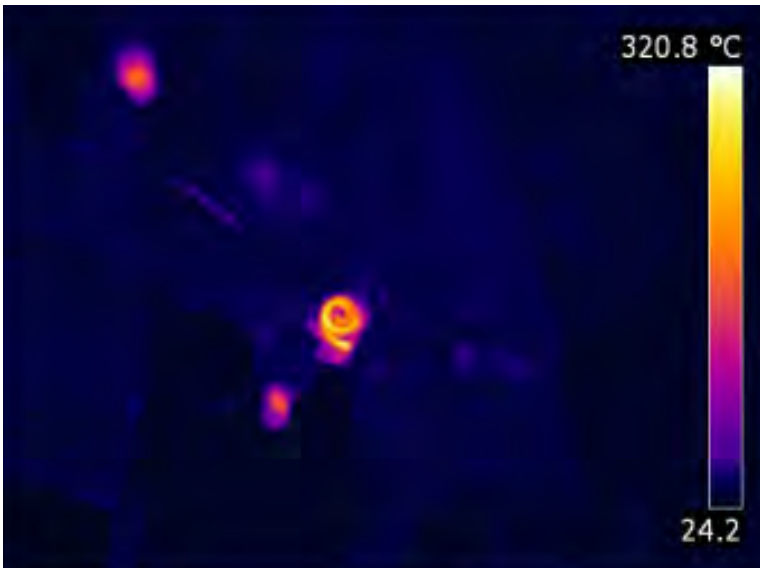

Figure 5.28: An example of a typical infra-red image. TiAlN cutting the Ti6Al4V workpiece with Ar applied to the rake face.

The temperature of the TiN cut is higher with compressed air (350 °C) than with Ar (333 °C). This reduction in measured temperature for TiN coated tools tested with Ar correlates with the apparent smoother Zone 2 wear and the reduced wear of the coating noticed in Figure 5.23 of the TiN coating in Ar conditions. The TiAlN sample maximum temperature is 310 °C with compressed air and 321 °C with Ar; a finding that suggests the TiAlN coated tool is worn to a greater degree under Ar conditions than the compressed air TiAlN coated tool. This is a less likely outcome when considering the rack face observations made in Section 5.2.2.1 - Figure 5.27 (Ar conditions) shows smoother rake face wear when compared with Figure 5.25 (compressed air). The amount of coating remaining on both TiAlN tools is similar in both compressed air and Ar conditions. The apparent smoother wear of TiAlN

under Ar conditions contradicts temperature observations: this could be due to inaccurate temperature measurements, temperatures and wear that are not significantly different to enable accurate determination of which tool is more worn, or a change in friction conditions that affects temperature but not wear. An explanation of the cause of this discrepancy requires further experimentation and these temperature measurements are not ideal for measuring wear in this experiment.

5.2.2.3. In-situ chip formation.

To observe changes in chip formation with cutting atmosphere, chip roots were collected after 13 m of cutting distance with a quick-stop device. Chip roots were carefully removed from the workpiece, mounted and polished in conductive Bakelite, then ground with 800 and 1200 grit SiC paper at a normal force of 15 N for 5 mins each. Then polishing with a 15 µm diamond lapping mat and finished using colloidal silica. Samples were etched using Kroll's reagent for optical microscopy. Figure 5.29 shows cross-sections of in-situ chips for all four samples.

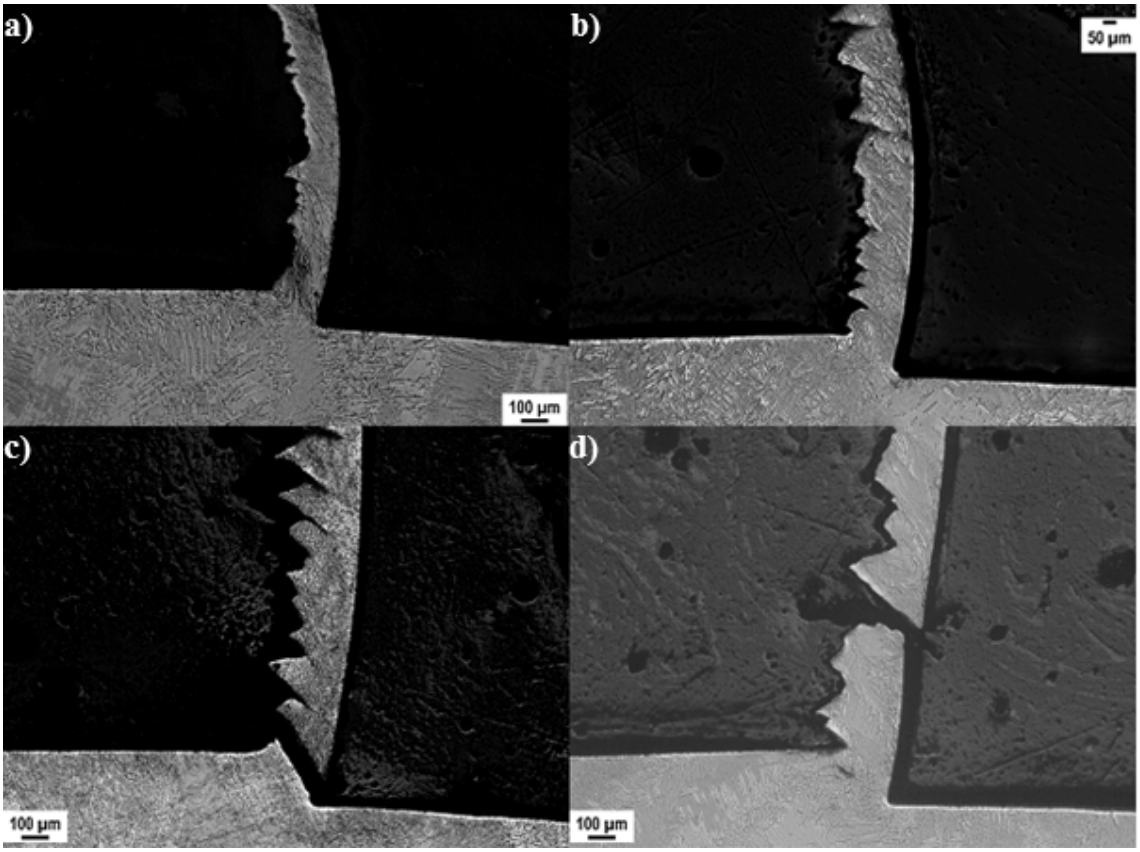

Figure 5.29: Cross section optical microscopy of in-situ chips. a) TiN + Air, b) TiN +Ar, c) TiAlN + Air, d) TiAlN + Ar. All images captured at the same magnification.

Chip formation in all four of these samples appears different. There are distinct segments in the deformed section of the TiAlN sample [Figure 5.29 (c)] cut with compressed air and a semi-continuous chip is visible in the TiN sample cut with air [Figure 5.29 (a)]. The other two chips exhibit a mixture of semi-continuous and segmental formation. Semi-continuous can be defined as irregular segmentation with some continuous chip formation.

It is not possible to differentiate the effects of coating or cutting atmosphere on segmental or continuous chip formation of Ti6Al4V in this case. The changes to chip formation are more likely to be the cause of unexpected differences in the depth of cut, or workpiece crystallography.

Table 5.3 displays chip properties measured from optical micrographs, showing that all samples were cut at greater depths of cut than the programmed 80 µm. With greater depths of cut, thicker chips will be formed and the primary shear plane angle will increase – both of which are observed (this is explained mathematically in [127]).

Table 5.3: Measured properties of in-situ chips.

	Chip thickness (µm)		Depth of cut (µm)	Primary shear angle (°)	Segment spacing (µm)
	Segmented	Semi-continuous			
TiN + Air	157	123	129	36	91
TiN + Ar	181	197	158	39	114
TiAlN + Air	216	n/a	201	44	145
TiAlN + Ar	210	198	206	53	102

Changes to chip thickness with workpiece crystal orientation have been observed in turning monocrystalline iron-aluminium [128]. This leads to another potential cause for changes in chip morphology. With polycrystalline samples, at some orientations relative to the cutting direction, undeformed material could accommodate deformation due to accessible slip systems. But at others, these systems are unavailable due to their orientation relative to the cutting force and do not have the required time to rotate into position.

Shear bands will then preferentially form. Hence, through a given cutting distance, chip formation could change between segmental (dramatic localised shear) and continuous (slip system activation) depending on the orientation of the workpiece grains. This phenomena of changing chip morphology was also observed when machining β-brass [33] and could be a cause of the variation in continuous and segmental formation seen in this experiment.

Changes to atmosphere and coating during orthogonal cutting of Ti6Al4V are most likely to be apparent at the chip and rake interface. This requires adequate characterisation of the secondary shear zone, which is difficult with optical microscopy. The edges of chips are rounded from the polishing process and light reflects at many angles here, making optical methods inadequate.

Even with SEM, observing changes to secondary shear zones is difficult (Figure 5.30). No noticeable differences were observed, but the region of deformation is difficult to measure accurately.

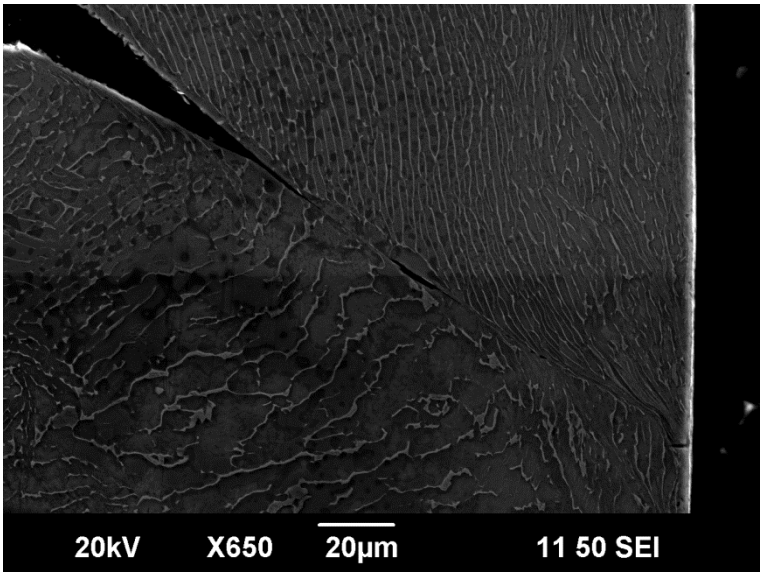

Figure 5.30: Secondary electron micrograph of TiAlN + Air chip cross section. Secondary shear zone to the right side of this image is difficult to fully characterise due to different secondary electron interaction at edges.

To further analyse these samples, and perhaps observe changes to the secondary shear with variation in experimental parameters, EBSD was conducted. Samples were repolished using colloidal silica mixed with 12 % ammonia and 8 % hydrogen peroxide until a satisfactory finish and etch was achieved, before EBSD mapping.

EBSD mapping was completed for each sample and the results can be seen in Figure 5.31 toFigure 5.34. Images show a map of the α-Ti phase (in yellow) over the top of a band contrast image. The black areas come from the band contrast image and indicate where very little signal was detected and no Kikuchi patterns were indexed. From these images, areas of greater deformation are clear – the black areas indicate a high level of deformation.

The primary shear plane can be observed to be active in an almost straight line between the tool tip and the exposed surface. The shear plane angle measured from EBSD maps appears identical to measurements made with optical microscopy (Table 5.3).

The β-Ti phase is not clear here, but only exists in small areas mostly within the undeformed area of the cross-section. No β-Ti phase is identified nearer to the primary shear plane and

in the deformed section, which is expected as this phase will deform with less stress than α-Ti. It will then become too deformed to diffract an indexable Kikuchi pattern. This is a good indication that deformation is occurring ahead of the shear plane in all samples.

Another clear example of deformation ahead of the shear plane is in the TiAlN + air chip cross-section (Figure 5.33), where indexing of α-Ti is reduced ahead of the primary shear. This observation was also made by Brömmelhoff *et al* [129] when analysing in-situ chip formation with synchrotron X-rays. They measured a decrease in diffraction intensity and an increase in full width at half maximum (direct indicators of a deformed crystal) was noticed in areas ahead of the primary shear plane, that appeared undeformed according to optical micrographs.

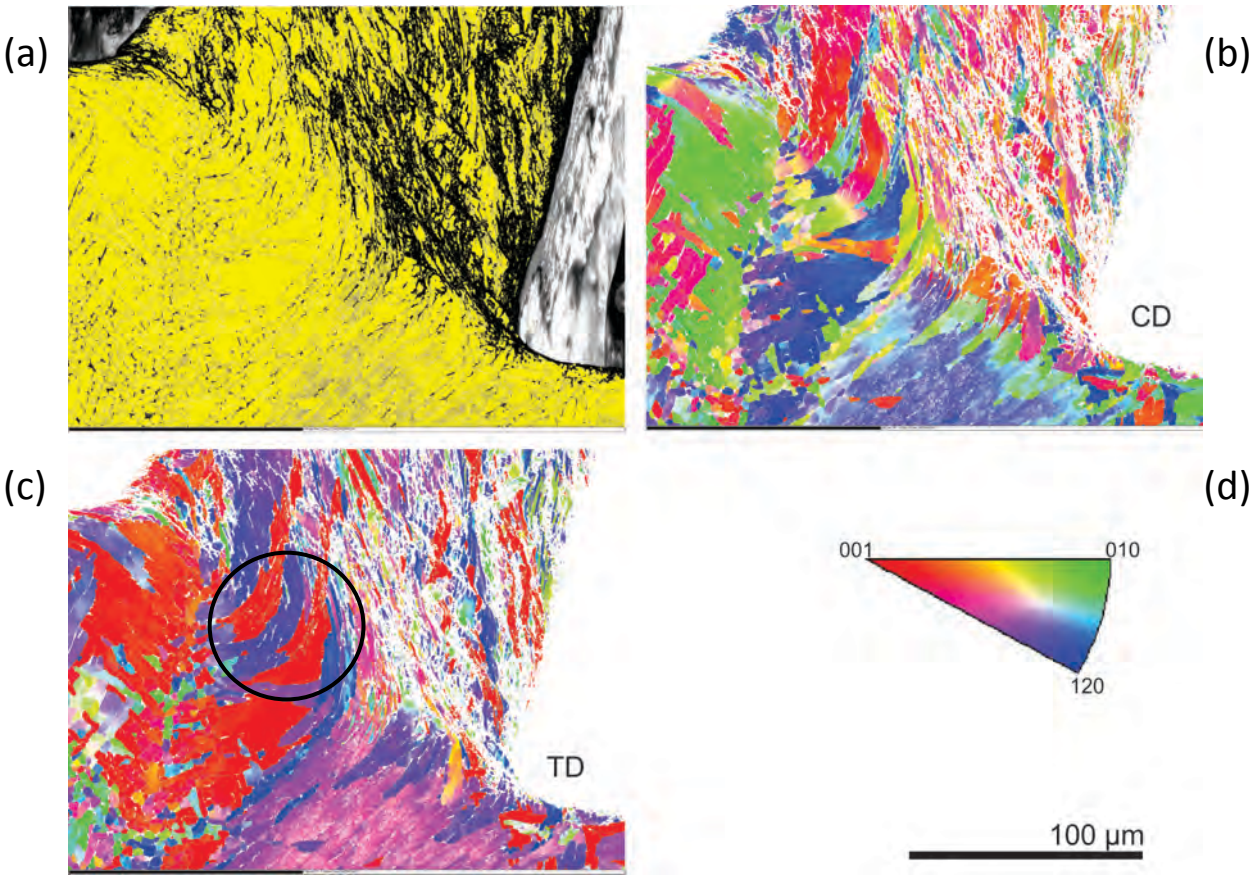

Figure 5.31: TiN + Air in-situ chip – (a) phase (Ti6Al4V identified as yellow) and band contrast (grey scale areas) image, (b) cutting direction IPF, (c) transverse direction IPF, and (d) IPF colour key.

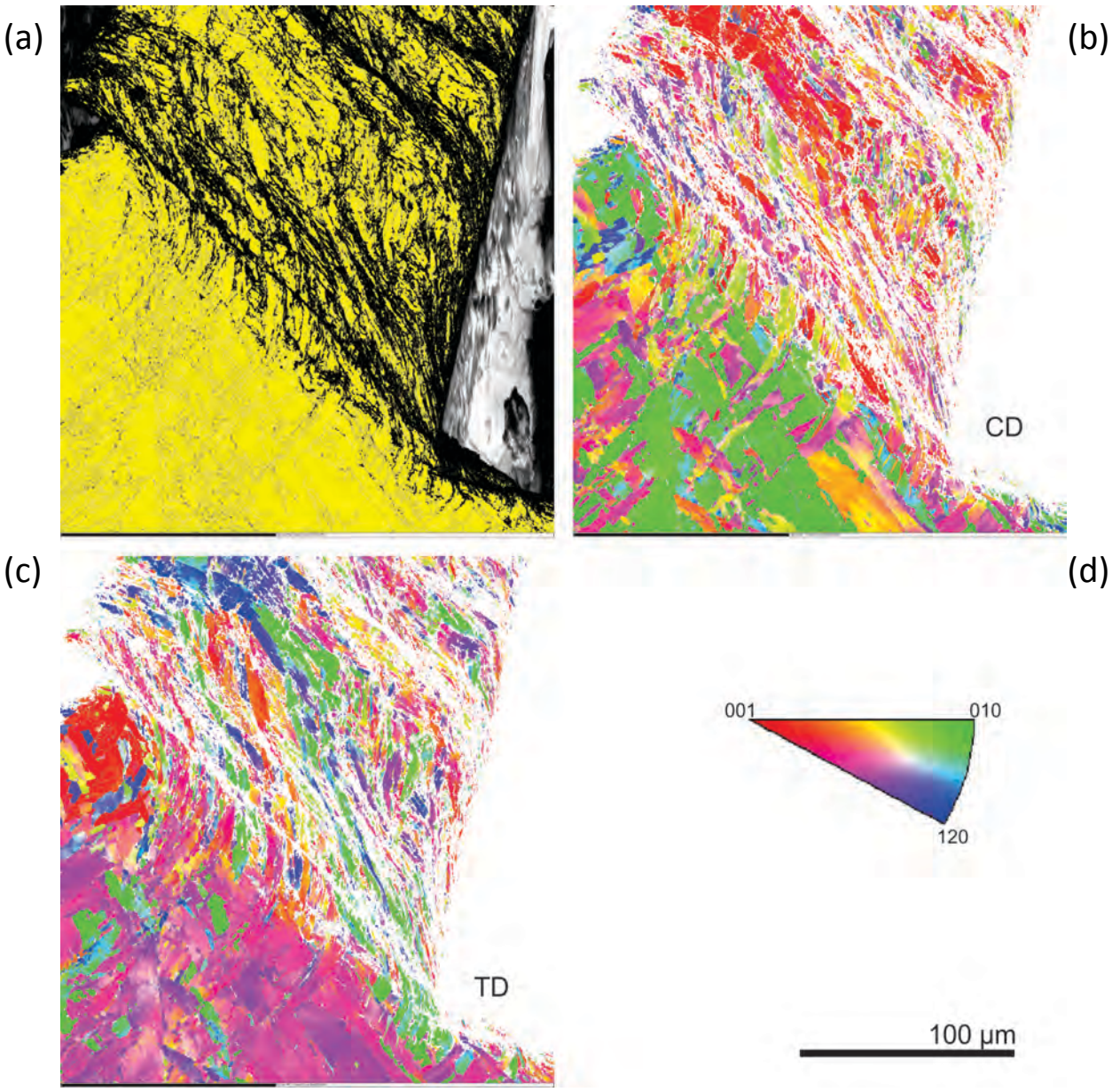

Figure 5.32: TiN + Ar in-situ chip – (a) phase (Ti6Al4V identified as yellow) and band contrast (grey scale areas) image, (b) cutting direction IPF, (c) transverse direction IPF, and (d) IPF colour key.

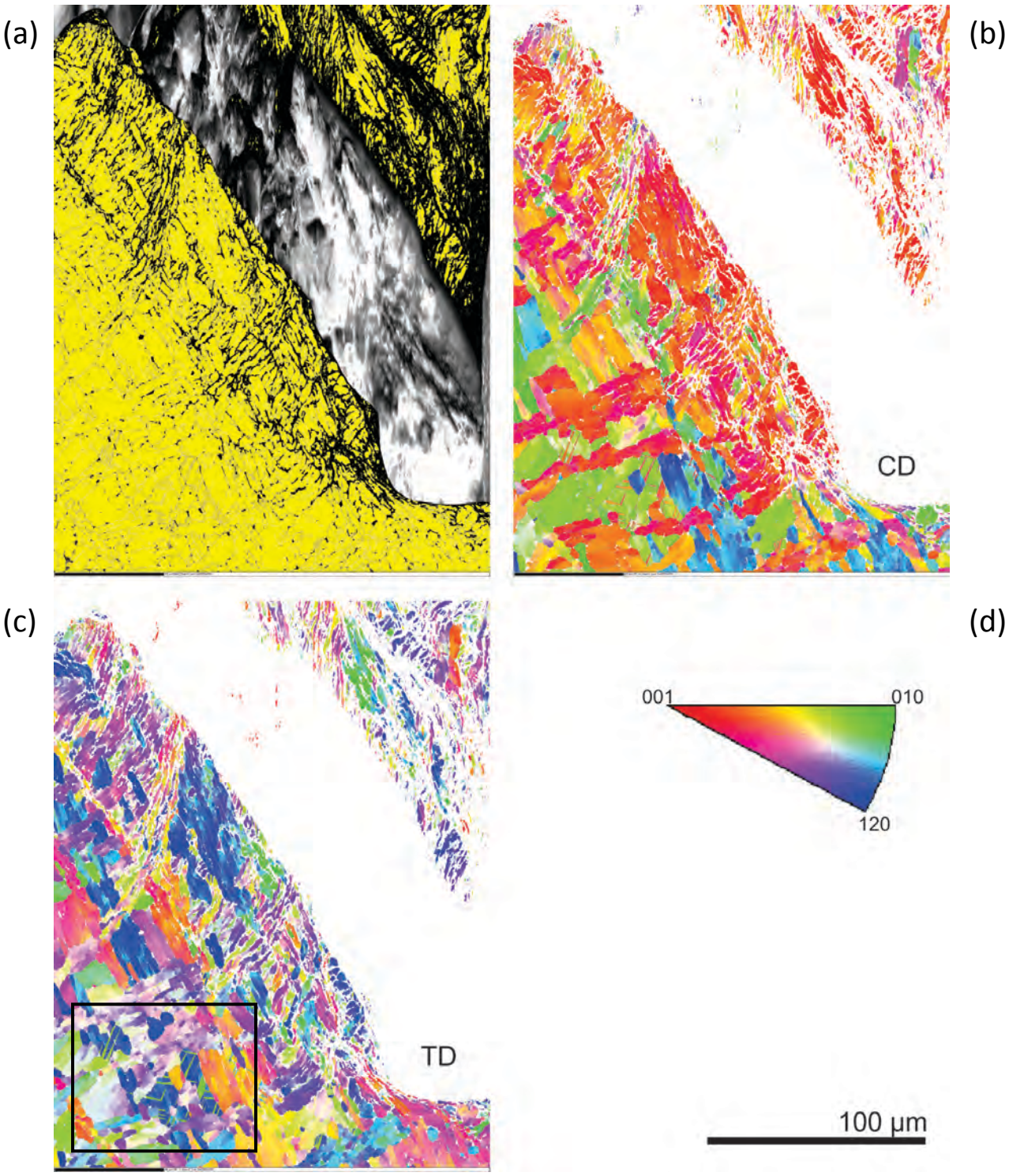

Figure 5.33: TiAlN + Air in-situ chip – (a) phase (Ti6Al4V identified as yellow) and band contrast (grey scale areas) image, (b) cutting direction IPF, (c) transverse direction IPF, and (d) IPF colour key.

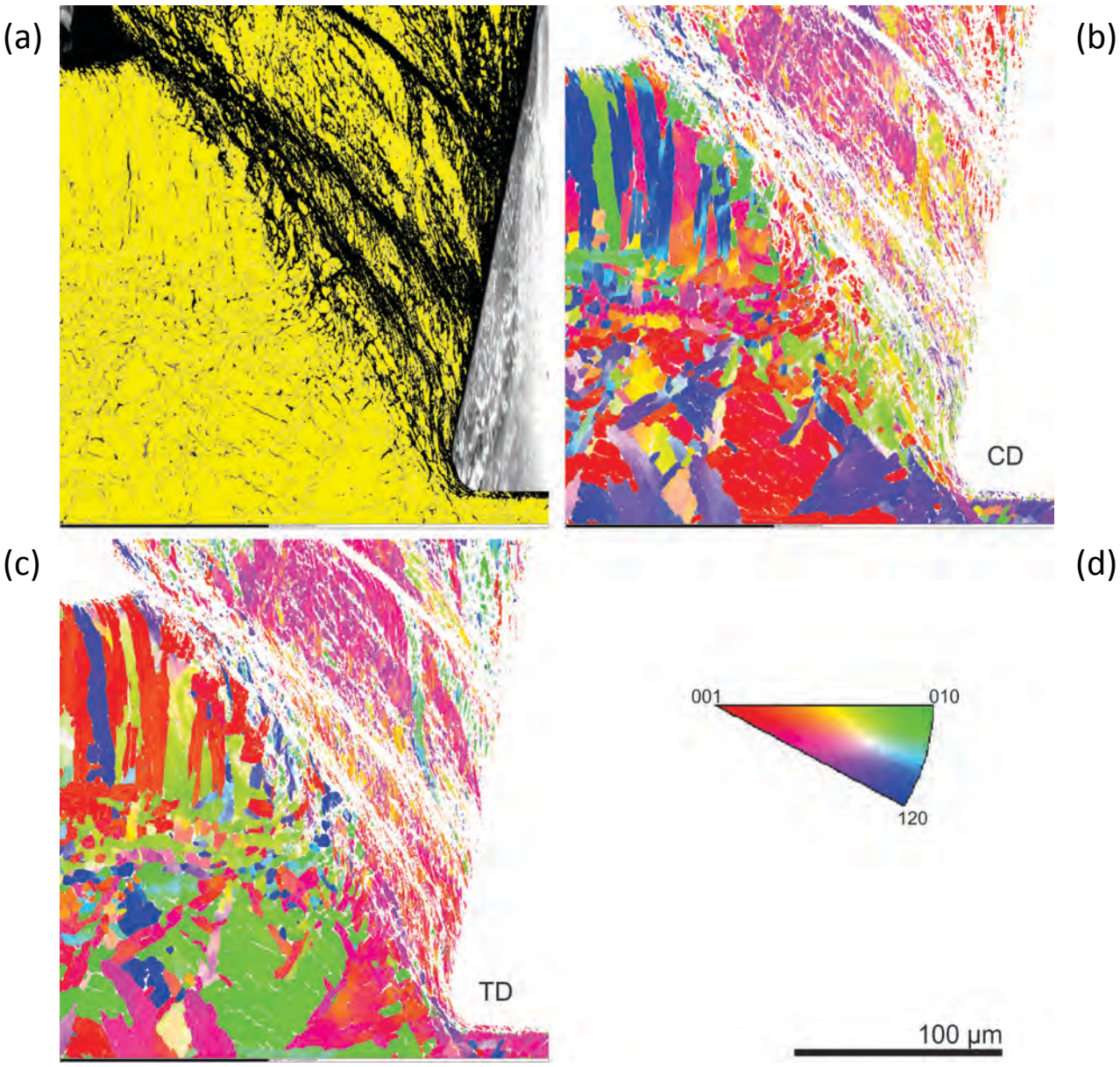

Figure 5.34: TiAlN + Ar in-situ chip – (a) phase (Ti6Al4V identified as yellow) and band contrast (grey scale areas) image, (b) cutting direction IPF, (c) transverse direction IPF, and (d) IPF colour key.

Deformation of the chip is not uniform through its thickness. There appears to be more deformation nearer the interface (right) than towards the exposed surface of the chip (left), particularly in Figure 5.31 (see (a) phase and band contrast image). This is due to friction between the chip and rake face.

The thickness of the unindexed (black) region close to the chip and tool interface is measurable, but there are no obvious discernible differences between coatings and atmospheric conditions. Comparison between secondary shear zones of all four samples is again inconclusive with this technique. The TiAlN + Air chip is disconnected, making direct

comparison with the Ar conditions difficult. This disconnected chip is likely to have been forced apart during sample preparation and mounting in conductive Bakelite.

Closely observing the secondary shear zone can give some indication of tool wear, for example in Figure 5.31 the interface between chip and rake face is not a straight line like the other three samples. This corresponds with the crater wear seen on the rake face of this cutting tool in Figure 5.18 and Figure 5.19.

In summary: to reveal unknowns about the effects of atmospheric gas and tool coating on chip formation of Ti6Al4V during orthogonal cutting, EBSD mapping of frozen chip cross-sections reveals no discernible crystallographic differences.

The secondary shear zone is thought to be the prime suspect for any differentiation, but because of high levels of deformation, electron diffraction from these areas is noisy and Kikuchi patterns are very feint or unresolved.

Regardless of these problems, the EBSD maps are of significant value. M'Saoubi & Ryde [38] experienced difficulty in resolving indexable signals from workpiece material that had passed through the primary shear. This data could provide interesting information to be used in visco-plastic self-consistent modelling of chip formation. Some observations made from this data are detailed below.

The TiN + air *in-situ* chip (Figure 5.31) was stopped at a point where part of the chip is being deformed via a rotation of the hexagonal α-Ti crystal. The middle section of the primary shear plane contains a cluster of crystals oriented with (001) or (0001), and (120) or (12-30) parallel to the transverse direction that are being rotated in the same axis as they pass through the primary shear plane (see encircled area in Figure 5.31).

The angle of rotation is approximately the same as the shear plane angle, when observed relative to the cutting direction, see point 'A' in Figure 5.35. The crystal was originally oriented with the $(12\bar{3}0)$ plane to the cutting direction and after passing through the primary shear plane, it rotated to bring the (010) or $(01\bar{1}0)$ planes into orientation with the cutting direction, a 30° rotation of the hexagonal crystals c-axis (see Figure 5.36). This angle is approximately equal to the shear plane angles measured (Table 5.3).

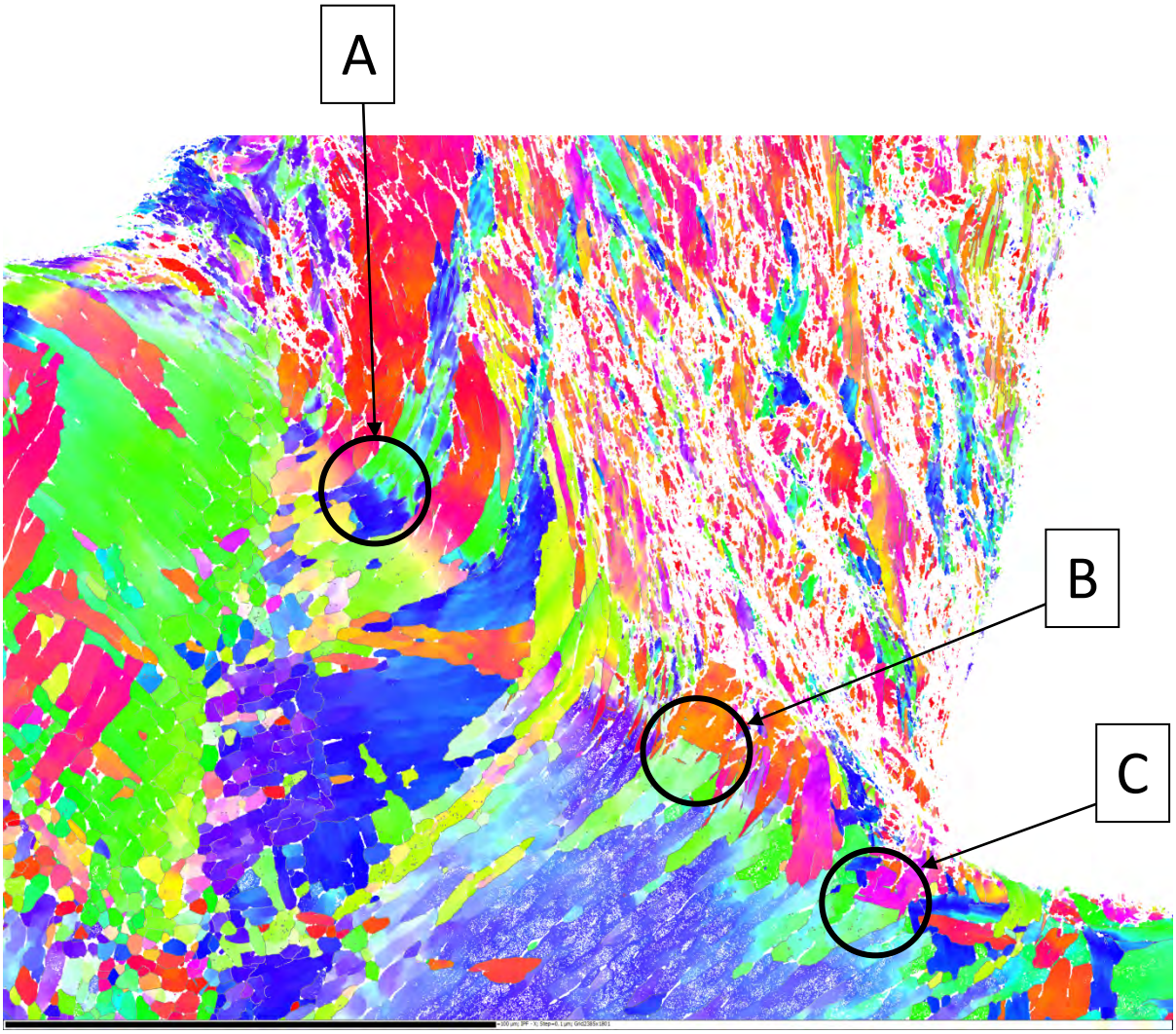

Figure 5.35: TiN + air IPF map, orientation relative to cutting direction. Various points of interest: rotation of the crystal across the primary shear plane (A), and potential deformation twinning (B) and (C).

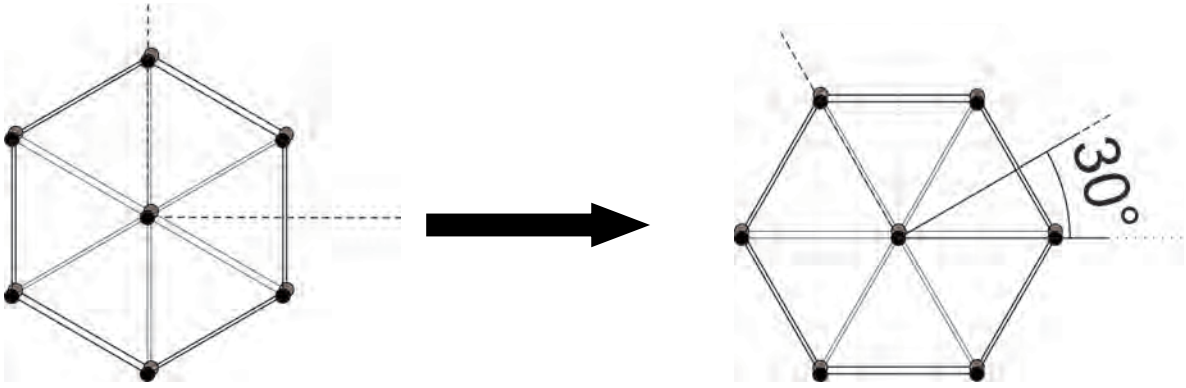

Figure 5.36: Rotation of hexagonal α-Ti grains, at point 'A' of Figure 5.35, across primary shear plane relative to the transverse direction. This perspective is from the transverse direction but the rotation is only noticeable when observing from the cutting direction in Figure 5.35 (point 'A') because the crystal changes relative to the cutting direction, not the transverse direction.

In points B and C of Figure 5.35 there is evidence of deformation twins with an 85° rotation relative to the parent crystal. This rotation is visualised best from the point of view of the transverse direction - see Figure 5.37. It is differentiated from the deformation in point 'A' because the change in crystal orientation is not gradual - compare graphs in Figure 5.38.

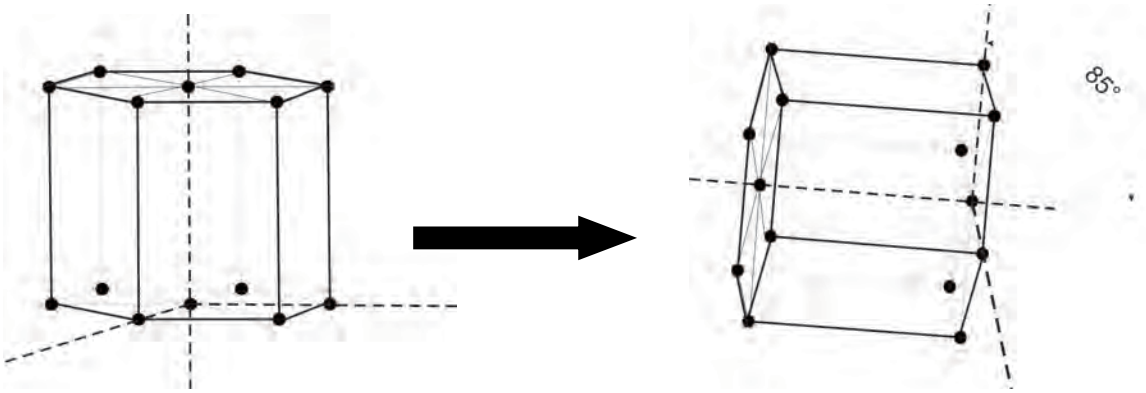

Figure 5.37: Twinning rotation of the hexagonal α-Ti grains, point 'C' (Figure 5.35), across primary shear plane as seen from the transverse direction.

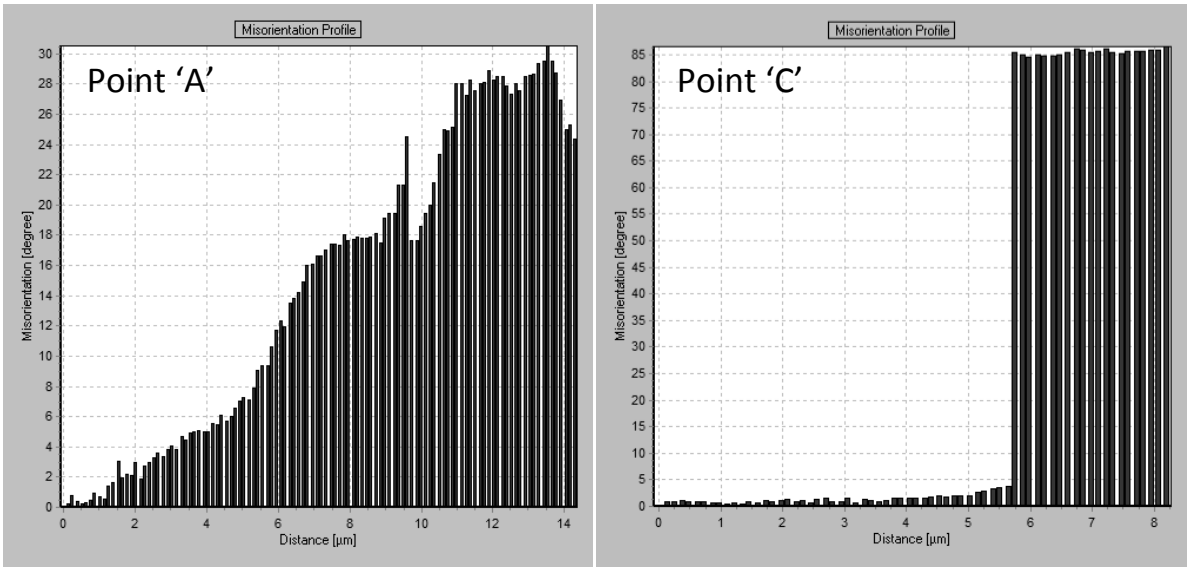

Figure 5.38: Misorientation profiles of grains in points A and C (Figure 5.35). The misorientation angle (degrees) is taken relative to the angle at the beginning of a line drawn in the undeformed section that crosses the primary shear perpendicularly. Notice the gradual change from point A and the dramatic misorientation from point C, indicating twinning deformation is active.

More evidence of deformation twins exists in the TiAlN + air sample where twins appear far ahead of the primary shear plane – see Figure 5.39. These twins exhibit a misorientation of 85-90° to the parent crystal. These can be seen far ahead of the primary shear plane,

indicating deformation is active in areas where optical and electron microscopy cannot identify.

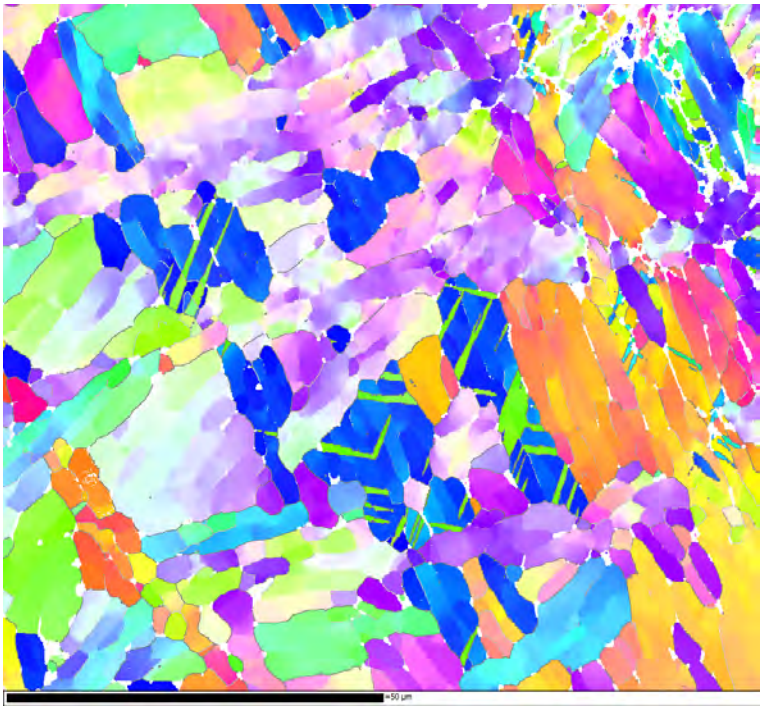

Figure 5.39: Enlarged section of TiAlN + air IPF map in Figure 5.33 (see highlighted square area) showing deformation twins far ahead of the primary shear plane.

Pole figures from the EBSD map of the TiN + air sample are shown in Figure 5.40. The grain orientation across the primary shear plane rotates by a similar angle to the 45° shear plane, this rotation is displayed in Figure 5.40 (a) undeformed grains, through to (d) deformed chip section – notice the 45° anti-clockwise rotation of the {0001} reflections in each set of pole figures. There does not appear to be any formation of texture in this case, although the low number of grains making up these pole figures means texture determination is inaccurate. The other three samples behaved in a similar manner, or no grain orientation change was visible due to shear banding effects and disconnected chips.

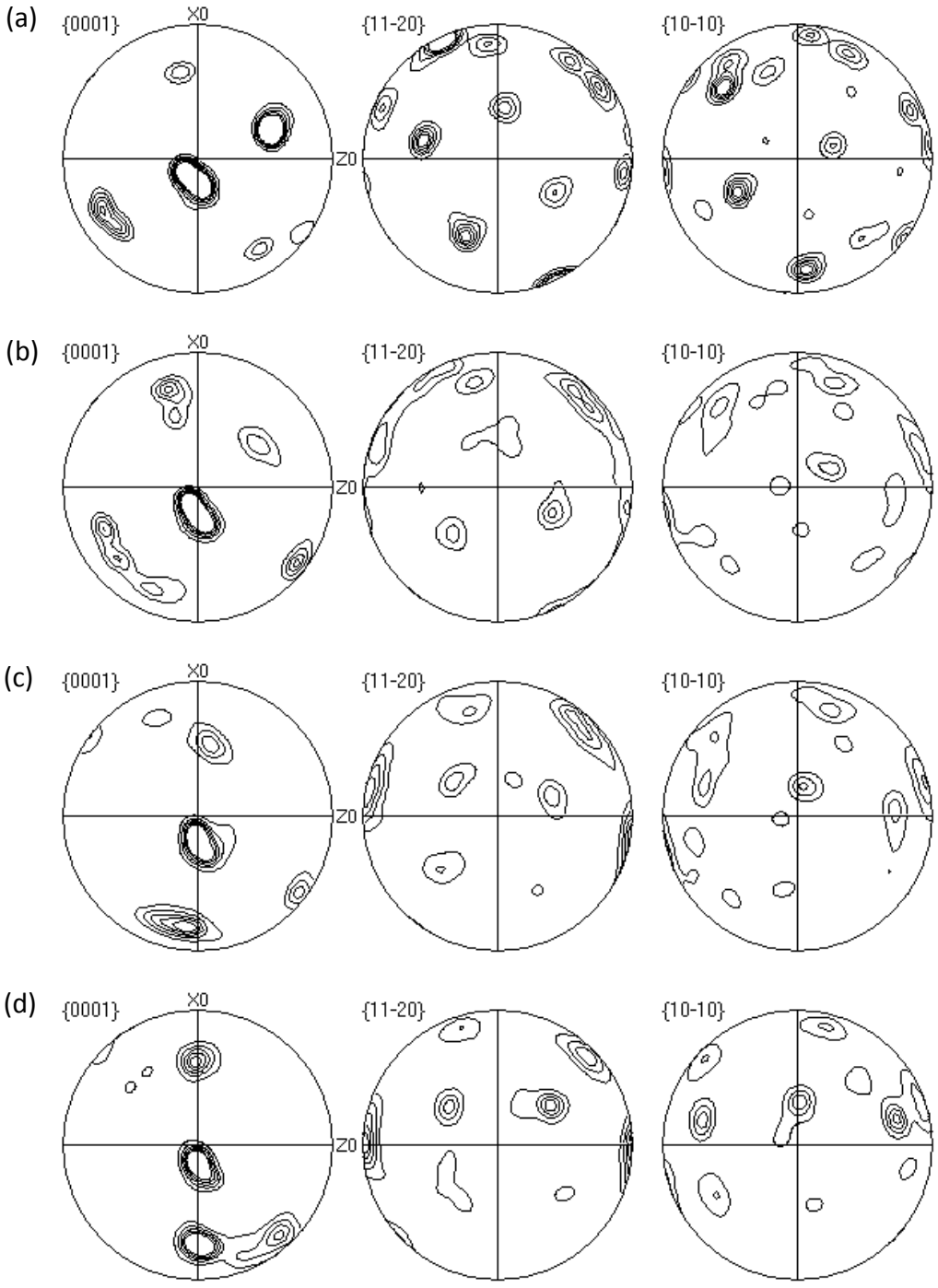

Figure 5.40: Pole figures from areas in steps across the primary shear plane of the TiN + air chip cross section. (a) undeformed grains, (b) just in front of the shear plane, (c) within the shear plane and, (d) in the fully deformed chip section. X-axis is parallel with the cutting direction, Z-axis is vertical in previous maps and the Y-axis (out of the page) is the transverse axis. The grain orientations appear to rotate in the transverse axis by approximately 30°.

5.3. Summary.

The purpose of these experiments was to gain more of an understanding of the machining process to improve coatings for machining tools. The experiments aimed to achieve this goal by simplifying a very complex process. Hence obtaining a level of control, allowing scientific research to be conducted as close to industry conditions as possible. This was achieved through the use of orthogonal cutting on a lathe, and control of oxidation conditions.

Face milling experiments were conducted with TiN and TiAlN coated carbide cutting tools at different feed rates to find optimum conditions for cutting K1045 steel. TiN was seen to perform better than TiAlN at lower cutting speeds and feed rates. A feed rate of 0.2 mm/tooth allowed tools to cut for longer distances than at 0.1 mm/tooth due to proper engagement of the tool, which reduced edge-chipping effects. Increasing cutting speeds increased wear rates dramatically for both TiN and TiAlN coatings in all cases.

Improvement of TiAlN coated tool performance, when compared to TiN, at higher speeds and feeds was anticipated. This was expected for TiAlN coated tools due to two reasons. The tribologically activated preferential oxidation of Al to form a protective layer of Al_2O_3 on the rake face, and the phase segregation hardening effect.

The tribo-oxidation mechanism was observed by reducing access to oxygen with a machining cell that was flooded with Ar gas. The cell successfully displaced oxygen and TiAlN tool life reduced. This adds evidence to tribo-oxidation being vital for TiAlN performance. A stable oxide tribofilm formation was also deemed beneficial to TiN performance under moderate feeds and speeds.

The phase segregation hardening effect will only begin to increase hardness above 700 °C [42]. Hence, it is possible that this mechanism is not active at the cutting temperatures in this case and TiAlN performance is more reliant on oxidation at these cutting parameters.

An orthogonal cutting test was designed to further experiments on TiN and TiAlN coated cutting tools with different atmospheric conditions. Tests were conducted on a lathe with long cutting distances to allow for activation of oxidation effects and tool wear mechanisms. A quick-stop device was used to observe effects of oxidation on chip formation of Ti6Al4V.

This experiment allowed for simple examination of tool wear and effects of oxygen on rake wear, which correspond with literature on chip formation in orthogonal cutting.

TiN coated tools were improved when Ar was applied to the rake and chip interface. With compressed air, the coating is completely removed from the rake face. Only below Zone 2 does coating remain. When Ar is applied to the rake face, the TiN coating remains across Zones 1 and 2. Oxidation of the coating is reduced in Ar conditions, reducing wear of the TiN coated tool.

In all conditions, Zone 1 appears to have some deposit of the Ti6Al4V workpiece. This does not change with changes to gas applied to the rake face and this should be the case as Zone 1 is defined as having no access to the atmosphere. The deposition of workpiece material in this zone could be due to the propensity for Ti6Al4V to work-harden. The secondary shear zone could further deform the chip and work-harden it, causing cracking to occur in the chip, further away from the chip-rake interface. The hard chip (at the interface) then experiences less deformation, separates from the remainder of the chip and adheres to the rake face where it remains as deposited material (this is discussed in Chapter 2 and [9]).

Zone 2 displays some differences with applied Ar and compressed air. In the samples where Ar is used, there are more deposits of workpiece material, and the wear track is smoother. This leads to the possibility that because of the smoother surface under Ar conditions, workpiece material s encouraged to deposit on the rake face.

Mapping of chip cross-sections is achieved where it has been unseen in the current literature and was helpful in identifying slip, rotational and twinning deformation. The most valuable finding is evidence of deformation of the workpiece observed far ahead of the primary shear plane. It manifests itself as twinning of the α-Ti crystals and a reduction in indexable β-Ti and α-Ti crystals.

Changes to secondary shear behaviour could not be identified for use in understanding chip formation dependencies on oxygen levels. Analysis of chip formation was complex and requires more observations and modelling to allow for additional conclusions to be made.

5.4. Recommendations for further work.

The development of more efficient and more accurate test systems is constantly required for the tool manufacturer. This chapter has detailed the refinement of a test method for TiN and TiAlN coatings at different atmospheric conditions and still requires improvement.

Two avenues suggested for development are: an improvement in crystallographic analysis of chips, and more controlled atmospheric conditions for continued analysis of coated tool wear.

For a better understanding of Ti6Al4V deformation, it would be beneficial to continue analysis of chip formation in an orthogonal cutting experiment with no changes to tool or atmosphere. Cutting parameters can be changed to provoke changes in chip formation mechanisms, and with EBSD it would be possible to shed light on the current debate on which cutting conditions encourage adiabatic shear and which cause crack propagating in segmental chip formation. In particular, changing cutting speeds to provoke a change in the chip formation mechanism of Ti6Al4V from a continuous (or semi-continuous) mechanism into fully segmental formation. This requires exploring cutting speeds from 20 m/min through to 100 m/min and above (at approximately 50 to 60 m/min a transfer from continuous to segmental chip formation will occur). Combined with a TEM study of shear bands, to adequately capture information within shear bands, to observe cracking and highly deformed areas. This matched with nanoindentation hardness measurements to monitor work hardening in shear bands and at the chip-rake interface will deliver significant findings to add to the body of knowledge surrounding Ti6Al4V chip formation.

Another avenue for understanding the crystallography of Ti6Al4V chip formation, to allow a complete appreciation and explanation of the EBSD maps similar to the ones presented in this chapter is by separating deformation into constituent loads and understanding the response of the material. Compression, tension and shear of Ti6Al4V must be isolated and analysed with EBSD, this will allow an understanding of the material's response. With this knowledge, modelling of the more complex chip formation process can be done by combining the known response of Ti6Al4V to various load types with visco-plastic self-consistent modelling. To continue assessing coated tool wear, especially of films that rely on tribo-oxidation mechanisms for performance, atmospheric conditions must be controlled

more effectively: encasing the test bed designed in this chapter in a vacuum chamber would allow for complete control of oxygen levels. Keeping consistent cutting parameters and changing oxygen levels whilst testing TiN and TiAlN coated tools, with numerous test repetitions, will deliver more confident findings about the effect of oxygen levels on wear mechanisms and chip-rake interactions.

The test system could be used to analyse any combination of tool design changes such as geometry, edge preparation, and tool coatings. These could then be examined during cutting of different workpiece materials. Cutting tool manufacturers are constantly striving to design tools with, for example, the ideal geometry to cut particular workpiece materials. Closely monitoring cutting forces during these tests would provide fast results for the tool designer to optimise geometry and generate a body of knowledge that can be used to manufacture cutting tools with known ideal and specific applications.

6. Conclusions.

The purpose of this work is to conduct research that is relevant to the cutting tool manufacturing industry. New coating architectures with impressive properties are not always required for the toolmaker. Utilising the systems and film architectures currently available and modifying them, on the factory floor, has shown to be successful for improving cutting tools. But examining coatings in metal cutting tests and being able to make conclusive statements is complex.

The effect of interruptions on CAPD TiN film properties was investigated extensively. Interruptions, which last 5 mins and repeated nine times during deposition, were found to be a method for providing in-deposition secondary phase transformations for metastable systems. TiN films grown from Grade 2 Ti targets in CAPD were discovered to be a dual phase system of fcc-TiN and bcc-Fe. A combined XRD stress analysis technique identified compressive stress in (111) oriented grains was higher than in randomly oriented grains of interrupted TiN films, a phenomenon that was likely to be a consequence of segregation of impurities in the TiN lattice. Although XPS was unable to show any impurity layers and no outstanding impurity elements could be identified, the existence of a bcc-Fe phase was discovered using EBSD and later confirmed macroscopically with glancing angle XRD techniques as a segregated phase of bcc-Fe in the fcc-TiN lattice for all interrupted and uninterrupted TiN films. For interrupted samples the segregation was further developed: the more time TiN films remained in the deposition chamber under interruption conditions, the more the bcc-Fe segregated from fcc-TiN. The segregated phase of Fe was then confirmed to occur in a ternary system of Ti, Fe and N at deposition conditions; and with Gibbs energy calculations made for a pseudo-binary system of TiN and Fe. An increased interfacial strain component imposed on the TiN lattice by the Fe phase is linked to the measured increase in indentation hardness and biaxial compressive strain measured in (111) crystallites with the CGM of XRD stress analysis. The discovered bcc-Fe inclusions are thought to hinder dislocation motion in the TiN lattice and provide a modulated strain field, allowing for the accommodation of strain in the Fe phase. The segregation effect brought on by nine 5 minute-long interruptions significantly improved TiN coated HSS drill life when cutting D2 tool steel at 30 m/min and 45 m/min, whereas scratch testing was unable to

detect any improvement in coating and substrate interfacial adhesive strength or film cohesive strength.

The greatest value of the interruption technique is its potential to offer an in-deposition scheme for secondary phase transformations in metastable systems, which is one of the points mentioned by Mayrhofer *et al* [2] as being an area in which coating scientists can add value. Other added value of the interruption technique is that it is immediately available for Sutton Tools Pty Ltd to implement in the production of TiN films; and it has also been explored for use in deposition of TiAlN, where milling tool life results are very promising.

A major difficulty in this project was staying relevant to both academic research and to industry. Cutting tests that suited industry were less useful to the materials scientist. An iterative process was followed in Chapter 5 to design a test system that satisfied both needs. Firstly a chamber was used to surround a face milling tool with Ar, to have some control of oxygen partial pressures during operation. The use of Ar gas during cutting has seen little attention in the literature, and was explored here as a method of controlling film oxidation. Supplying Ar gas provided an opportunity to better understand tribo-oxidation of coated tools. TiN and TiAlN were examined and the performance of TiAlN coated tools was shown to be dependent on the presence of oxygen in the cutting atmosphere in face milling of K1045 steel at 200 m/min – TiAlN requires oxygen to activate tribo-oxidation and hence the formation of Al_xO_{1-x} to protect the film and increase tool life. TiN tool life was also shown to have a dependency on oxygen levels in the cutting atmosphere: with a reduced partial pressure of oxygen, TiN tool life reduced when face milling K1045 steel at 200 m/min – understanding the exact mechanism to explain this finding remains a task for future work.

An orthogonal cutting test with a quick-stop device was then designed based on an understanding of the limitations operating with the complex cutting and chip formation process of face milling. An orthogonal cutting test enabled the observation of chip formation mechanisms, and with controllable atmospheres, it was used in the analysis of TiN and TiAlN coated tools. Orthogonal cutting of Ti6Al4V at 50 m/min in controlled atmosphere displayed some interesting changes to the rake-face wear of TiN and TiAlN coated tools. Changes to wear in Zone 1 were not noticeable due to the coating being removed in all samples, but Zone 2 displayed some changes in wear: the rake face surface in Zone 2 was

smoother when cutting with Ar applied to the chip-rake interface. The TiN coated tool was found to have reduced rake-face wear under Ar conditions when compared to compressed air conditions, however wear of the TiAlN coated tool was similar in both atmospheric conditions.

In the same orthogonal cutting experiment, a quick-stop device was used to collect *in-situ* chip formation of Ti6Al4V cut with TiN and TiAlN coated tools under Ar and compressed air conditions (four tests in total). Cross-sections of the chips, from the four tests, were mapped using EBSD to monitor the combined effects of oxygen levels and coating architecture on the crystallography of chip formation of Ti6Al4V at 50 m/min. No obvious changes in crystallography were noticed between the four conditions, but key areas such as the secondary shear zone (close to the chip-rake interface where oxidation effects will play a significant role in chip formation) were not resolved using the EBSD technique. Despite being unable to identify the effect of changes to atmosphere, and coating, on chip formation, EBSD maps identified some interesting mechanisms that have not yet been published in the literature. Notably: deformation of the workpiece far ahead of the primary shear plane, made evident by the presence of unresolved Kikuchi patterns, and through deformation twins in areas ahead of the primary shear plane. Also a rotation of some grains was observed as they pass through the primary shear plane, along with twinning that occurred across the primary shear plane. The EBSD maps obtained for Ti6A4V are unseen in the literature and add to the body of knowledge, especially if used to generate models of cutting processes.

References.

1. Veprek, S. and Veprek-Heijman, M.G.J., *Industrial applications of superhard nanocomposite coatings.* Surface and Coatings Technology, 2008. **202**(21): p. 5063-5073.
2. Mayrhofer, P.H., Mitterer, C., Hultman, L., and Clemens, H., *Microstructural design of hard coatings.* Progress in Materials Science, 2006. **51**(8): p. 1032-1114.
3. Abermann, R., *Measurements of the Intrinsic Stress in Thin Metal-Films.* Vacuum, 1990. **41**(4-6): p. 1279-1282.
4. Koch, R., *The Intrinsic Stress of Polycrystalline and Epitaxial Thin Metal-Films.* Journal of Physics-Condensed Matter, 1994. **6**(45): p. 9519-9550.
5. Koch, R., Hu, D.Z., and Das, A.K., *Compressive stress in polycrystalline Volmer-Weber films.* Physical Review Letters, 2005. **94**(14).
6. Kohn, W. and Lau, K.H., *Adatom Dipole-Moments on Metals and Their Interactions.* Solid State Communications, 1976. **18**(5): p. 553-555.
7. Chason, E., Sheldon, B.W., Freund, L.B., Floro, J.A., and Hearne, S.J., *Origin of Compressive Residual Stress in Polycrystalline Thin Films.* Physical Review Letters, 2002. **88**(15): p. 156103.
8. Friesen, C. and Thompson, C.V., *Reversible stress relaxation during precoalescence interruptions of Volmer-Weber thin film growth.* Physical Review Letters, 2002. **89**(12).
9. Koch, R., Hu, D.Z., and Das, A.K., *Comment on "Compressive stress in polycrystalline Volmer-Weber films" - Reply.* Physical Review Letters, 2005. **95**(22).
10. Friesen, C. and Thompson, C.V., *Comment on "Compressive stress in polycrystalline Volmer-Weber films".* Physical Review Letters, 2005. **95**(22).
11. Machunze, R., Tichelaar, F.D., and Janssen, G.C.A.M., *Co-development of stress and texture in reactive magnetron sputtered TiN films revealed by in situ film stress measurements.* Surface and Coatings Technology, 2010. **205**(5): p. 1313-1319.
12. Trent, E.M., *Metal cutting and the tribology of seizure: III. Temperatures in metal cutting.* Wear, 1988. **128**(1): p. 65-81.
13. Trent, E.M., *Metal cutting and the tribology of seizure: I. Seizure in metal cutting.* Wear, 1988. **128**(1): p. 29-45.
14. Trent, E.M., *Metal cutting and the tribology of seizure: II. Movement of work material over the tool in metal cutting.* Wear, 1988. **128**(1): p. 47-64.
15. Doyle, E.D., Horne, J.G., and Tabor, D., *Frictional interactions between chip and rake face in continuous chip formation.* Proceedings of the Royal Society London, 1979. **366**: p. 173-183.
16. Ackroyd, B., Chandrasekar, S., and Compton, W.D., *A model for the contact conditions at the chip-tool interface in machining.* Journal of Tribology, 2003. **125**(3): p. 649-660.
17. Madhavan, V., Chandrasekar, S., and Farris, T.N., *Direct Observations of the Chip-Tool Interface in the Low Speed Cutting of Pure Metals.* Journal of Tribology, 2002. **124**(3): p. 617-626.
18. Mativenga, P.T., Abukhshim, N.A., Sheikh, M.A., and Hon, B.K.K., *An investigation of tool chip contact phenomena in high-speed turning using coated tools.* Proceedings of the Institution of Mechanical Engineers, 2006. **220**(B5): p. 657-667.
19. Trent, E.M., *Metal Cutting*. Third ed ed. 1991, London: Butterworth-Heinemann.

20. Hwang, J. and Chandrasekar, S., *Contact Conditions at the Chip-Tool Interface in Machining.* International Journal of Precision Engineering and Manufacturing, 2011. **12**(2): p. 183-193.
21. Ezugwu, E.O., Da Silva, R.B., Bonney, J., and Machado, A.R., *The effect of argon-enriched environment in high-speed machining of titanium alloy.* Tribology Transactions, 2005. **48**: p. 18-23.
22. Münz, W.D., *Titanium aluminum nitride films: a new alternative to TiN coatings.* Journal of vacuum science and technology A, 1986. **4 (6)**: p. 2717-2725.
23. Groover, M.P., *Fundamentals of Modern Manufacturing: Materials, Processes and Systems*. 2007, Hoboken: John Wiley & Sons.
24. Nakayama, K., Arai, M., and Kanda, T., *Machining Characteristics of Hard Materials.* CIRP Annals - Manufacturing Technology, 1988. **37**(1): p. 89-92.
25. Vyas, A. and Shaw, M.C., *Mechanics of Saw-Tooth Chip Formation in Metal Cutting.* Journal of Manufacturing Science and Engineering, 1999. **121**(2).
26. Elbestawi, M.A., Srivastava, A.K., and El-Wardany, T.I., *A model for chip formation during machining of hardened steel.* CIRP Annals - Manufacturing Technology, 1996. **45**(1): p. 71-76.
27. Poulachon, G. and Moisan, A., *A contribution to the study of the cutting mechanisms during high speed machining of hardened steel.* CIRP Annals - Manufacturing Technology, 1998. **47**(1): p. 73-76.
28. Komanduri, R., Schroeder, T., Hazra, J., Flom, D.G., and von Turkovich, B.F., *On the catastrophic shear instability in high-speed machining of an AISI 4340 steel.* TRANS. ASME J. ENGNG. IND., 1982. **104**(2 , May 1982): p. 121-131.
29. Davies, M.A., Chou, Y., and Evans, C.J., *On chip morphology, tool wear and cutting mechanics in finish hard turning.* CIRP Ann., 1997. **45**: p. 25-30.
30. Semiatin, S.L. and Rao, S.B., *Shear localization during metal cutting.* Materials Science and Engineering, 1983. **61**(2): p. 185-192.
31. Hou, Z.B. and Komanduri, R., *Modeling of thermomechanical shear instability in machining.* International Journal of Mechanical Sciences, 1997. **39**(11): p. 1273-1314.
32. Jawahir, I.S. and van Luttervelt, C.A., *Recent Developments in Chip Control Research and Applications.* CIRP Annals - Manufacturing Technology, 1993. **42**(2): p. 659-693.
33. Ueda, K., Iwata, K., and Nakayama, K., *Chip Formation Mechanism in Single Crystal Cutting of β-Brass.* CIRP Annals - Manufacturing Technology, 1980. **29**(1): p. 41-46.
34. Barry, J., Byrne, G., and Lennon, D., *Observations on chip formation and acoustic emission in machining Ti–6Al–4V alloy.* International Journal of Machine Tools and Manufacture, 2001. **41**(7): p. 1055-1070.
35. Wan, Z.P., Zhu, Y.E., Liu, H.W., and Tang, Y., *Microstructure evolution of adiabatic shear bands and mechanisms of saw-tooth chip formation in machining Ti6Al4V.* Materials Science and Engineering: A, 2012. **531**(0): p. 155-163.
36. Chen, Y.J., Li, Y.J., Walmsley, J.C., Dumoulin, S., Skaret, P.C., and Roven, H.J., *Microstructure evolution of commercial pure titanium during equal channel angular pressing.* Materials Science and Engineering: A, 2010. **527**(3): p. 789-796.
37. Saleh, A.A., Pereloma, E.V., and Gazder, A.A., *Microstructure and texture evolution in a twinning-induced-plasticity steel during uniaxial tension.* Acta Materialia, 2013. **61**(7): p. 2671-2691.

38. M'Saoubi, R. and Ryde, L., *Application of the EBSD technique for the characterisation of deformation zones in metal cutting.* Materials Science and Engineering: A, 2005. **405**(1–2): p. 339-349.
39. Inspektor, A. and Salvador, P.A., *Architecture of PVD coatings for metalcutting applications: A review.* Surface and Coatings Technology, 2014. **257**: p. 138-153.
40. Fox-Rabinovich, G.S., Weatherly, G.C., Dodonov, A.I., Kovalev, A.I., Shuster, L.S., Veldhuis, S.C., Dosbaeva, G.K., Wainstein, D.L., and Migranov, M.S., *Nano-crystalline filtered arc deposited (FAD) TiAlN PVD coatings for high-speed machining applications.* Surface and Coatings Technology, 2004. **177–178**(0): p. 800-811.
41. Luo, Q. and Hovsepian, P.E., *Transmission electron microscopy and energy dispersive X-ray spectroscopy on the worn surface of nano-structured TiAlN/VN multilayer coating.* Thin Solid Films, 2006. **497**(1–2): p. 203-209.
42. Mayrhofer, P.H., Hörling, A., Karlsson, L., Sjölén, J., Larsson, T., Mitterer, C., and Hultman, L., *Self-organized nanostructures in the Ti-Al-N system.* Applied Physics Letters, 2003. **83**(10): p. 2049-2051.
43. Holleck, H. and Schier, V., *Multilayer PVD coatings for wear protection.* Surface and Coatings Technology, 1995. **76-77**(1 -3 pt 1): p. 328-336.
44. Stueber, M., Holleck, H., Leiste, H., Seemann, K., Ulrich, S., and Ziebert, C., *Concepts for the design of advanced nanoscale PVD multilayer protective thin films.* Journal of Alloys and Compounds, 2009. **483**(1-2): p. 321-333.
45. Wang, C., Shi, K., Gross, C., Pureza, J.M., de Mesquita Lacerda, M., and Chung, Y.W., *Toughness enhancement of nanostructured hard coatings: Design strategies and toughness measurement techniques.* Surface and Coatings Technology, 2014.
46. Helmersson, U., Todorova, S., Barnett, S.A., Sundgren, J.E., Markert, L.C., and Greene, J.E., *Growth of single-crystal TiN/VN strained-layer superlattices with extremely high mechanical hardness.* Journal of Applied Physics, 1987. **62**(2): p. 481-484.
47. Leyland, A. and Matthews, A., *Thick Ti/TiN multilayered coatings for abrasive and erosive wear resistance.* Surface and Coatings Technology, 1994. **70**(1): p. 19-25.
48. Matthews, A., Jones, R., and Dowey, S., *Modelling the deformation behaviour of multilayer coatings.* Tribology Letters, 2001. **11**(2): p. 103-106.
49. Hultman, L., Engström, C., Birch, J., Johansson, M.P., Odén, M., Karlsson, L., and Ljungcrantz, H., *Review of the thermal and mechanical stability of TiN-based thin films.* Zeitschrift fuer Metallkunde/Materials Research and Advanced Techniques, 1999. **90**(10): p. 803-813.
50. Mayrhofer, P.H., Mitterer, C., and Clemens, H., *Self-organized nanostructures in hard ceramic coatings.* Advanced Engineering Materials, 2005. **7**(12): p. 1071-1082.
51. Veprek, S., *The origin of superhardness in TiN/Si3N4 nanocomposites: The role of the interfacial monolayer.* High Pressure Research, 2006. **26**(2): p. 119-125.
52. Veprek, S., Veprek-Heijman, M.G.J., Karvankova, P., and Prochazka, J., *Different approaches to superhard coatings and nanocomposites.* Thin Solid Films, 2005. **476**(1): p. 1-29.
53. Zhang, R.F. and Veprek, S., *On the spinodal nature of the phase segregation and formation of stable nanostructure in the Ti-Si-N system.* Materials Science and Engineering A, 2006. **424**(1-2): p. 128-137.
54. Jilek, M., Cselle, T., Holubar, P., Morstein, M., Veprek-Heijman, M.G.J., and Veprek, S., *Development of novel coating technology by vacuum arc with rotating cathodes*

for industrial production of nc-(Al1− x Ti x)N/a-Si3N4 superhard nanocomposite coatings for dry, hard machining. Plasma Chemistry and Plasma Processing, 2004. **24**(4): p. 493-510.
55. Jilek, M., Holubar, P., Veprek-Heijman, M.G.J., and Veprek, S. *Towards the industrialization of superhard nanocrystalline composites for high speed and dry machining*. in *Materials Research Society Symposium - Proceedings*. 2002.
56. Männling, H.D., Patil, D.S., Moto, K., Jilek, M., and Veprek, S., *Thermal stability of superhard nanocomposite coatings consisting of immiscible nitrides.* Surface and Coatings Technology, 2001. **146-147**: p. 263-267.
57. Sambasivan, S. and Petuskey, W.T., *Phase chemistry in the Ti-Si-N system: Thermochemical review with phase stability diagrams.* Journal of Materials Research, 1994. **9**(09): p. 2362-2369.
58. Dowey, S.J., *Advanced on-line and off-line process control for surface-engineered applications*. 1999, University of Hull: Hull, England.
59. Dowey, S.J., Rähle, B., and Matthews, A., *Performance analysis of coated tools in real-life industrial experiments using statistical techniques.* Surface and Coatings Technology, 1998. **99**(1–2): p. 213-221.
60. Abusuilik, S.B., *Pre-, intermediate, and post-treatment of hard coatings to improve their performance for forming and cutting tools.* Surface and Coatings Technology.
61. Lin, S.-s., Zhou, K.-s., Dai, M.-j., Hu, F., Shi, Q., Hou, H.-j., Wei, C.-b., Li, F.-q., and Tong, X., *Effects of surface roughness of substrate on properties of Ti/TiN/Zr/ZrN multilayer coatings.* Transactions of Nonferrous Metals Society of China, 2015. **25**(2): p. 451-456.
62. Irie, M., Ohara, H., Tsujioka, M., and Nomura, T., *The production and properties of TiN-Ni nanostructure films by filtered vacuum arc deposition.* Materials Chemistry and Physics, 1998. **54**(1-3): p. 317-320.
63. Randhawa, H., *Cathodic arc plasma deposition technology.* Thin Solid Films, 1988. **167**(1-2): p. 175-186.
64. Anders, A., *Approaches to rid cathodic arc plasmas of macro- and nanoparticles: a review.* Surface and Coatings Technology, 1999. **120-121**: p. 319-330.
65. Anders, A., *Cathodic Arcs - From Fractal Spots to Energetic Condensation*. 2008, New York: Springer.
66. Martin, P.J. and Bendavid, A., *Review of the filtered vacuum arc process and materials deposition.* Thin Solid Films, 2001. **394**(Compendex): p. 1-15.
67. Sanders, D.M. and Anders, A., *Review of cathodic arc deposition technology at the start of the new millennium.* Surface and Coatings Technology, 2000. **133-134**: p. 78-90.
68. Litvinov, E.A., Mesyats, G.A., and Proskurovsky, D.I., *Field emission and explosive electron emisison processes in vacuum discharges.* Soviet Physics-USPEKHI, 1983. **26**: p. 138-159.
69. Mesyats, G.A., *Ecton mechanism of the vacuum arc cathode spot.* Plasma Science, IEEE Transactions on, 1995. **23**(6): p. 879-883.
70. Brown, I.G., *Vacuum arc ion sources.* Review of Scientific Instruments, 1994. **65**(10): p. 3061-3081.
71. Petrov, I., Barna, P.B., Hultman, L., and Greene, J.E., *Microstructural evolution during film growth.* Journal of Vacuum Science and Technology A: Vacuum, Surfaces and Films, 2003. **21**(5): p. S117-S128.
72. Martin, P.M.*e.a.*, *Handbook of deposition technologies for films and coatings*. Third Edition ed. 2009, Burlington, MA, USA: William Andrew.

73. Movchan, B.A. and Demchishin, A.V., *Study of the structure and properties of thick vacuum condensates of nickel, titanium, tungsten, aluminum oxide and zirconium dioxide.* Fiz Metallov i Metalloved, 1969. **28**(4): p. 653-660.
74. Thornton, J.A., *Influence of apparatus geometry and deposition conditions on the structure and topography of thick sputtered coatings. .* J Vac Sci Technol, 1974. **11**(4): p. 666-670.
75. Anders, A., *A structure zone diagram including plasma-based deposition and ion etching.* Thin Solid Films, 2010. **518**(15): p. 4087-4090.
76. Bendavid, A., Martin, P.J., Netterfield, R.P., and Kinder, T.J., *The properties of TiN films deposited by filtered arc evaporation.* Surface and Coatings Technology, 1994. **70**(1): p. 97-106.
77. D'Heurle, F.M. and Harper, J.M.E., *Note on the origin of intrinsic stresses in films deposited via evaporation and sputtering.* Thin Solid Films, 1989. **171**(1): p. 81-92.
78. Friesen, C., Seel, S.C., and Thompson, C.V., *Reversible stress changes at all stages of Volmer-Weber film growth.* Journal of Applied Physics, 2004. **95**(3): p. 1011-1020.
79. Abermann, R. and Koch, R., *The Internal-Stress in Thin Silver, Copper and Gold-Films.* Thin Solid Films, 1985. **129**(1-2): p. 71-78.
80. Shull, A.L. and Spaepen, F., *Measurements of stress during vapor deposition of copper and silver thin films and multilayers.* Journal of Applied Physics, 1996. **80**(11): p. 6243-6256.
81. Friesen, C. and Thompson, C.V., *Correlation of stress and atomic-scale surface roughness evolution during intermittent homoepitaxial growth of (111)-oriented Ag and Cu.* Physical Review Letters, 2004. **93**(5).
82. Abadias, G. and Guerin, P., *In situ stress evolution during magnetron sputtering of transition metal nitride thin films.* Applied Physics Letters, 2008. **93**(11).
83. Chason, E., *A kinetic analysis of residual stress evolution in polycrystalline thin films.* Thin Solid Films, 2012. **526**: p. 1-14.
84. Koch, R., *Stress in Evaporated and Sputtered Thin Films – A Comparison.* Surface and Coatings Technology, 2010. **204**(12–13): p. 1973-1982.
85. Koch, R., Winau, D., Führmann, A., and Rieder, K.H., *Growth-mode-specific intrinsic stress of thin silver films.* Physical Review B, 1991. **44**(7): p. 3369-3372.
86. Box, Hunter, and Hunter, *Statistics for Experiments*. 1st Edition ed. 1978, New York: Wiley.
87. Reimer, L., *Scanning electron microscopy : physics of image formation and microanalysis*. Springer series in optical sciences: v. 45. 1998: Berlin ; New York : Springer, c1998.
88. Glasgow, U.o. *Scanning Electron Microscopy (SEM)*. 20/11/2015]; Available from: http://www.gla.ac.uk/schools/ges/research/researchfacilities/isaac/services/scanningelectronmicroscopy/.
89. Goldstein, J., Newbury, D., Joy, D., Lyman, C., Echlin, P., Lifshin, E., Sawyer, L., and Michel, J., *Scanning electron microscopy and X-ray microanalysis*. 3rd ed. 2003, New York: Springer.
90. Reimer, L., *Transmission electron microscopy: physics of image formation and microanalysis*. 4th ed. 1997, Berlin; New York: Springer.
91. Egerton, R.F., *Electron energy-loss spectroscopy in the TEM.* Reports on Progress in Physics, 2009. **72**(1).
92. Satheesha, M., Jain, V.K., and Kumar, P., *Design and development of a quick-stop device (QSD).* Precision Engineering, 1990. **12**(4): p. 205-212.

93. Black, J.T. and James, C.R., *The Hammer QSD-Quick Stop Device for High-Speed Machining and Rubbing.* J. Eng. Ind. (Trans. ASME), 1981. **103**(1): p. 13-21.
94. Chern, G.-L., *Development of a new and simple quick-stop device for the study on chip formation.* International Journal of Machine Tools and Manufacture, 2005. **45**(7–8): p. 789-794.
95. Vepřek, S., Reiprich, S., and Shizhi, L., *Superhard nanocrystalline composite materials: The TiN/Si3N4 system.* Applied Physics Letters, 1995: p. 2640.
96. Sveen, S., Andersson, J.M., M'Saoubi, R., and Olsson, M., *Scratch adhesion characteristics of PVD TiAlN deposited on high speed steel, cemented carbide and PCBN substrates.* Wear, 2013. **308**(1-2): p. 133-141.
97. Toton, J., *The design, characterisation and application of an accelerated drill test for cutting tool development.*, in *School of Applied Science*. 2014, RMIT University: Melbourne, Australia.
98. Pilkington, A., Dowey, S.J., Toton, J.T., and Doyle, E.D., *Machining with AlCr-oxinitride PVD coated cutting tools.* Tribology International, 2013. **65**: p. 303-313.
99. Quaeyhaegens, C., Knuyt, G., and Stals, L.M., *Study of the Residual Macroscopic Stress in Tin Coatings Deposited on Various Steel Types (Tusa1).* Surface & Coatings Technology, 1995. **74-5**(1-3): p. 104-109.
100. Sloof, W.G., Kooi, B.J., Delhez, R., deKeijser, T.H., and Mittemeijer, E.J., *Diffraction analysis of nonuniform stresses in surface layers: Application to cracked TiN coatings chemically vapor deposited on Mo.* Journal of Materials Research, 1996. **11**(6): p. 1440-1457.
101. Kostenbauer, H., Fontalvo, G.A., Kapp, M., Keckes, J., and Mitterer, C., *Annealing of intrinsic stresses in sputtered TiN films: The role of thickness-dependent gradients of point defect density.* Surface & Coatings Technology, 2007. **201**(8): p. 4777-4780.
102. Machunze, R. and Janssen, G.C.A.M., *Stress and strain in titanium nitride thin films.* Thin Solid Films, 2009. **517**(Compendex): p. 5888-5893.
103. Koutsokeras, L.E. and Abadias, G., *Intrinsic stress in ZrN thin films: Evaluation of grain boundary contribution from in situ wafer curvature and ex situ x-ray diffraction techniques.* Journal of Applied Physics, 2012. **111**(9).
104. Kamminga, J.D., de Keijser, T.H., Delhez, R., and Mittemeijer, E.J., *A model for stress in thin layers induced by misfitting particles: An origin for growth stress.* Thin Solid Films, 1998. **317**(1–2): p. 169-172.
105. Eshelby, J.D., *The Continuum Theory of Lattice Defects.* Solid State Physics, 1956. **3**.
106. Abadias, G., *Stress and preferred orientation in nitride-based PVD coatings.* Surface & Coatings Technology, 2008. **202**(11): p. 2223-2235.
107. Kamminga, J.D., de Keijser, T.H., Delhez, R., and Mittemeijer, E.J., *On the origin of stress in magnetron sputtered TiN layers.* Journal of Applied Physics, 2000. **88**(11): p. 6332-6345.
108. Lutterotti, L., *Maud: a Rietveld analysis program designed for the internet and experiment integration.* Acta Crystallogr., Sect. A: Found. Crystallogr, 2000. **56**: p. S54.
109. Lutterotti, L., *Total pattern fitting for the combined size–strain–stress–texture determination in thin film diffraction.* Nuclear Instruments and Methods in Physics Research Section B: Beam Interactions with Materials and Atoms, 2010. **268**(3–4): p. 334-340.
110. Lutterotti, L. and Scardi, P., *Simultaneous structure and size-strain refinement by the Rietveld method.* Journal of Applied Crystallography, 1990. **21**: p. 246-252.

111. Lutterotti, L. *MAUD, version 2.44 (MAC OSX)*. Available from: http://maud.radiographema.com/.
112. Godec, M., Batič, B.Š., Mandrino, D., Nagode, A., Leskovšek, V., Škapin, S.D., and Jenko, M., *Characterization of the carbides and the martensite phase in powder-metallurgy high-speed steel.* Materials Characterization, 2010. **61**(4): p. 452-458.
113. Tagliente, M.A., Falcone, R., Mello, D., Esposito, C., and Tapfer, L., *On the influence of carbon implantation on the structural properties of hard TiN coatings studied by glancing incidence X-ray diffraction.* Nuclear Instruments and Methods in Physics Research Section B: Beam Interactions with Materials and Atoms, 2001. **179**(1): p. 42-54.
114. Barin, S., *Thermochemical data of pure substances*. Third Edition ed. 1995, Online: Verlagsgesellschaft mbH.
115. Ohtani, H. and Hillert, M., *A thermodynamic assessment of the Fe-N-Ti system.* Calphad, 1991. **15**(1): p. 41-52.
116. Porter, D.A. and Easterling, K.E., *Phase transformation in metals and alloys*. Second Edition ed. 2001, Cheltenham: Nelson Thorns Ltd.
117. Baker, R.G. and Nutting, J., *The Tempering of 2-1/4% Cr-1% Mo Steel After Quenching and Normalizing.* Journal of Iron and Steel Research International, 1959. **192**: p. 2570268.
118. Kim, Y.W., Moser, J., Petrov, I., Greene, J.E., and Rossnagel, S.M., *Directed Sputter-Deposition of AlCu - Film Microstructure and Microchemistry.* Journal of Vacuum Science & Technology A -Vacuum Surfaces and Films, 1994. **12**(6): p. 3169-3175.
119. Reed-Hill, R.E. and Abbaschian, R., *Physical metallurgy principles*. The PWS-KENT series in engineering. 1992: Boston : PWS-Kent Pub., c1992. 3rd ed.
120. Zhang, W.-Z. and Weatherly, G.C., *On the crystallography of precipitation.* Progress in Materials Science, 2005. **50**: p. 181-292.
121. Holleck, H., *Metastable coatings — Prediction of composition and structure.* Surface and Coatings Technology, 1988. **36**(1): p. 151-159.
122. Woo, J.H., Lee, J.K., Lee, S.R., and Lee, D.B., *High-Temperature oxidation of Ti0.3 Al0.2 N0.5 thin films deposited on a steel substrate by ion plating.* Oxidation of Metals, 2000. **53**: p. 529.
123. Ben Abdelali, H., Claudin, C., Rech, J., Ben Salem, W., Kapsa, P., and Dogui, A., *Experimental characterization of friction coefficient at the tool–chip–workpiece interface during dry cutting of AISI 1045.* Wear, 2012. **286–287**: p. 108-115.
124. Grzesik, W., *Friction behaviour of heat isolating coatings in machining: mechanical, thermal and energy-based considerations.* International Journal of Machine Tools and Manufacture, 2003. **43**(2): p. 145-150.
125. Astakhov, V., *Tribology of metal cutting*. First Edition ed. 2006, Oxford UK: Elsevier.
126. Liew, W.Y.H., Jie, J.L.L., Yan, L.Y., Dayou, J., Sipaut, C.S., and Madlan, M.F.B., *Frictional and Wear Behaviour of AlCrN, TiN, TiAlN Single-layer Coatings, and TiAlN/AlCrN, AlN/TiN Nano-multilayer Coatings in Dry Sliding.* Procedia Engineering, 2013. **68**(0): p. 512-517.
127. Cotterell, M. and Byrne, G., *Characterisation of chip formation during orthogonal cutting of titanium alloy Ti–6Al–4V.* CIRP Journal of Manufacturing Science and Technology, 2008. **1**(2): p. 81-85.
128. Denkena, B., Stiffel, J.-H., Hasselberg, E., and Breidenstein, B., *Chip formation in monocrystalline iron-aluminum.* CIRP Journal of Manufacturing Science and Technology, 2014. **7**(2): p. 71-82.

129. Brömmelhoff, K., Henze, S., Gerstenberger, R., Fischer, T., Schell, N., Uhlmann, E., and Reimers, W., *Space resolved microstructural characteristics in the chip formation zone of orthogonal cut C45E steel samples characterized by diffraction experiments.* Journal of Materials Processing Technology, 2013. **213**(12): p. 2211-2216.

Personal Achievements.

Publications:

Sinkovits, T., Zhao, Y., O'Brien, R. & Dowey, S. X-ray diffraction stress analysis of interrupted titanium nitride films. Thin Solid Films 562 (2014) 206-210.

Li, J., Zheng, H., Sinkovits, T., Hee, A.C. & Zhao, Y., Mono- and multiple TiN(/Ti) coating adhesion mechanism on a Ti-13Nb-13Zr alloy, Applied Surface Science 355 (2015) 502-508.

Doyle D., Dowey, S., Pagon, A., McCulloch, D., Pilkington, A., Sinkovits, T., Gulizia, S. & Jahedi, M. Pathways for innovation in physical vapour deposition (PVD). Materials Forum, (2011) 31-41.

Awards:

Defence Materials Technology Centre Awards for Excellence 2014: Industry Partnership Award.

Presentations:

International conference on metallurgical coatings and thin films – San Diego USA, 2011 – "*Modification of PVD TiN Coatings by Interrupting Film Growth"*.

International conference on advances in materials & processing technologies – Wollongong Australia, 2012 – "X-ray diffraction stress analysis of interrupted titanium nitride films: combining the $\sin^2\psi$ and crystallite group methods".

Beihang University of Aeronautics and Astronautics – University of Wollongong joint workshop on advanced materials – Beijing, P. R. China 2013 – *"The effect of oxidation on performance of TiN and TiAlN coated carbide tools and chip formation during orthogonal cutting of Ti6Al4V"*.

Four annual progress meeting presentations with industry partner Sutton Tools.

Four Defence Materials Technology Centre annual student conferences.

Appendix A.

The following figures are technical drawings of the quick-stop device fabricated for experiments conducted in Chapter 5.

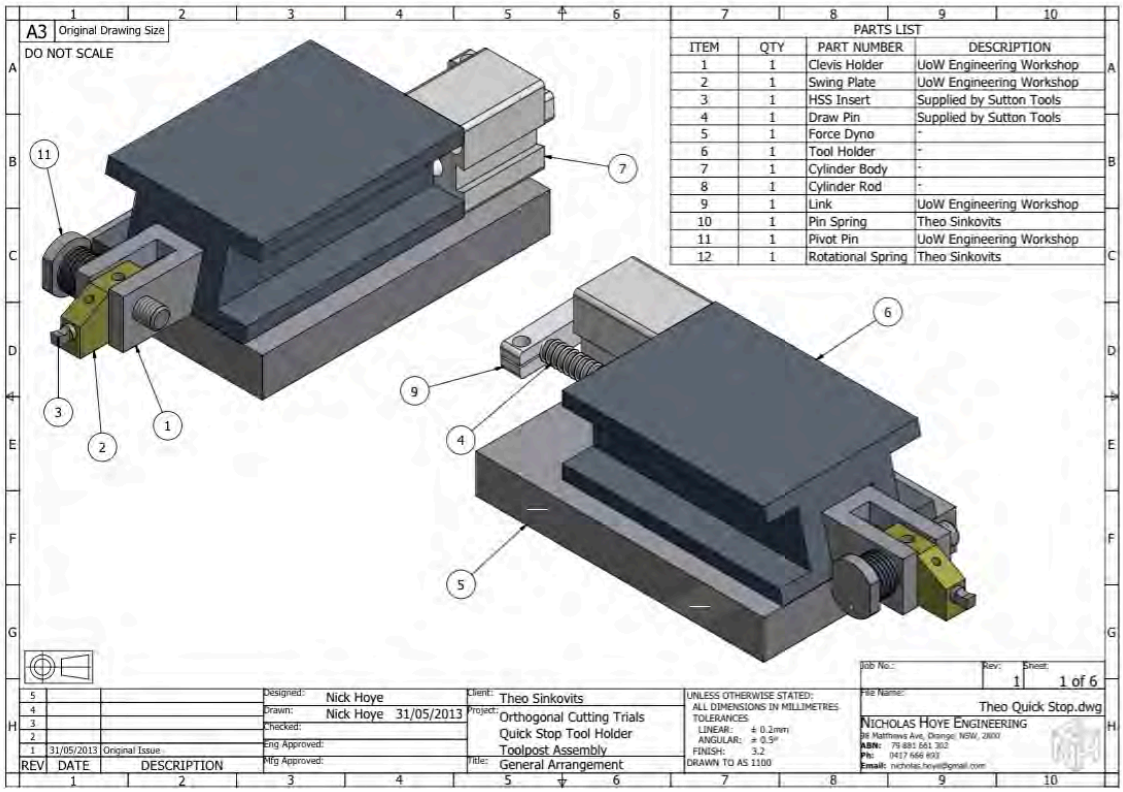

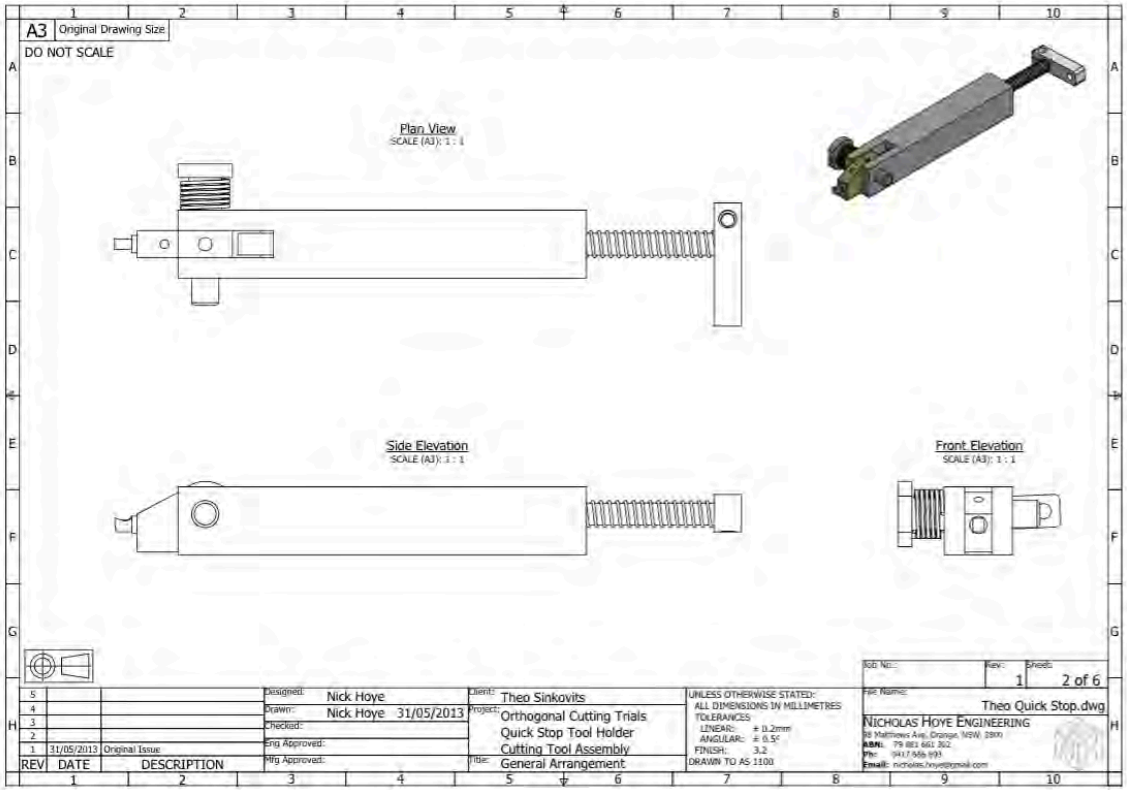
A3 Original Drawing Size
DO NOT SCALE
Plan View
SCALE (A3): 1 : 1
Side Elevation
SCALE (A3): 1 : 1
Front Elevation
SCALE (A3): 1 : 1
REV DATE DESCRIPTION
1 31/05/2013 Original Issue
Designed: Nick Hoye
Drawn: Nick Hoye 31/05/2013
Checked:
Eng Approved:
Mfg Approved:
Client: Theo Sinkovits
Project: Orthogonal Cutting Trials
Quick Stop Tool Holder
Cutting Tool Assembly
Title: General Arrangement
UNLESS OTHERWISE STATED:
ALL DIMENSIONS IN MILLIMETRES
TOLERANCES:
LINEAR: ± 0.2mm
ANGULAR: ± 0.5°
FINISH: 3.2
DRAWN TO AS 1100
Job No.:
Rev: 1
Sheet: 2 of 6
File Name: Theo Quick Stop.dwg
NICHOLAS HOYE ENGINEERING

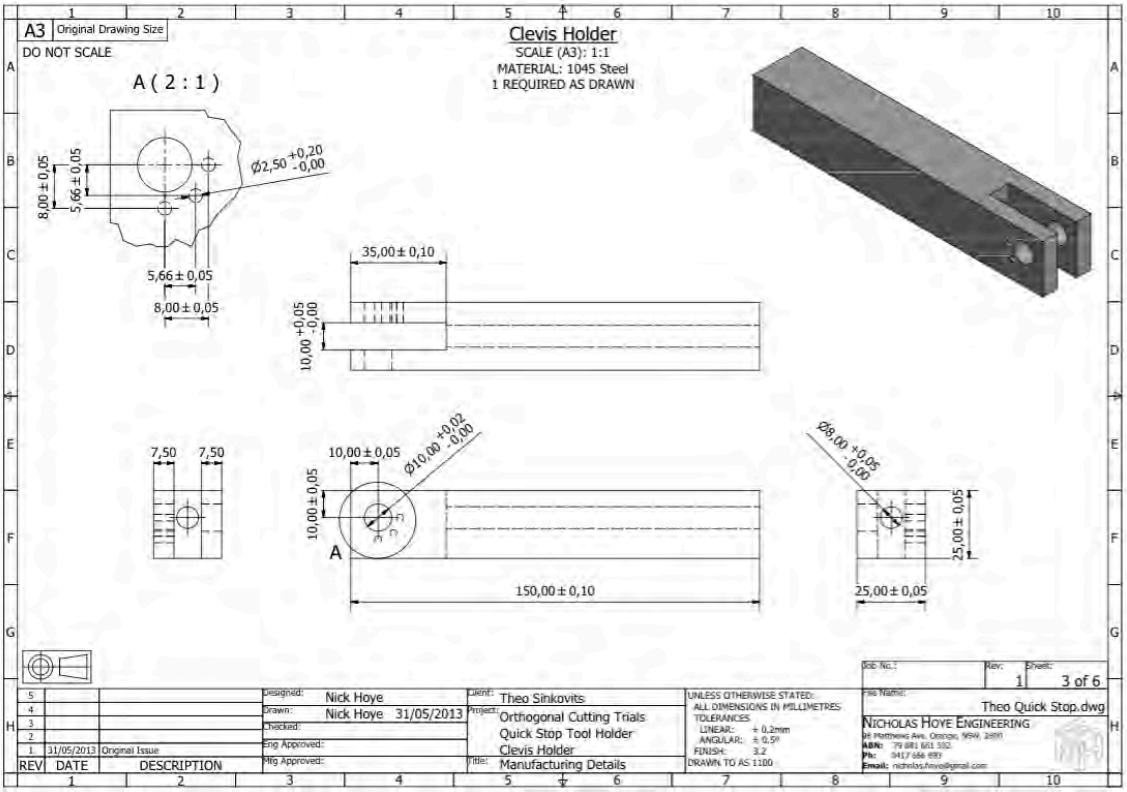
A3 Original Drawing Size
DO NOT SCALE
Clevis Holder
SCALE (A3): 1:1
MATERIAL: 1045 Steel
1 REQUIRED AS DRAWN
A (2 : 1)
8,00 ± 0,05
5,66 ± 0,05
Ø2,50 +0,20 -0,00
5,66 ± 0,05
8,00 ± 0,05
35,00 ± 0,10
10,00 +0,05 -0,00
7,50
7,50
10,00 ± 0,05
10,00 ± 0,05
Ø10,00 +0,02 -0,00
A
150,00 ± 0,10
Ø8,00 +0,05 -0,00
25,00 ± 0,05
25,00 ± 0,05
REV DATE DESCRIPTION
1 31/05/2013 Original Issue
Designed: Nick Hoye
Drawn: Nick Hoye 31/05/2013
Checked:
Eng Approved:
Mfg Approved:
Client: Theo Sinkovits
Project: Orthogonal Cutting Trials
Quick Stop Tool Holder
Clevis Holder
Title: Manufacturing Details
UNLESS OTHERWISE STATED:
ALL DIMENSIONS IN MILLIMETRES
TOLERANCES:
LINEAR: ± 0.2mm
ANGULAR: ± 0.5°
FINISH: 3.2
DRAWN TO AS 1100
Job No.:
Rev: 1
Sheet: 3 of 6
File Name: Theo Quick Stop.dwg
NICHOLAS HOYE ENGINEERING

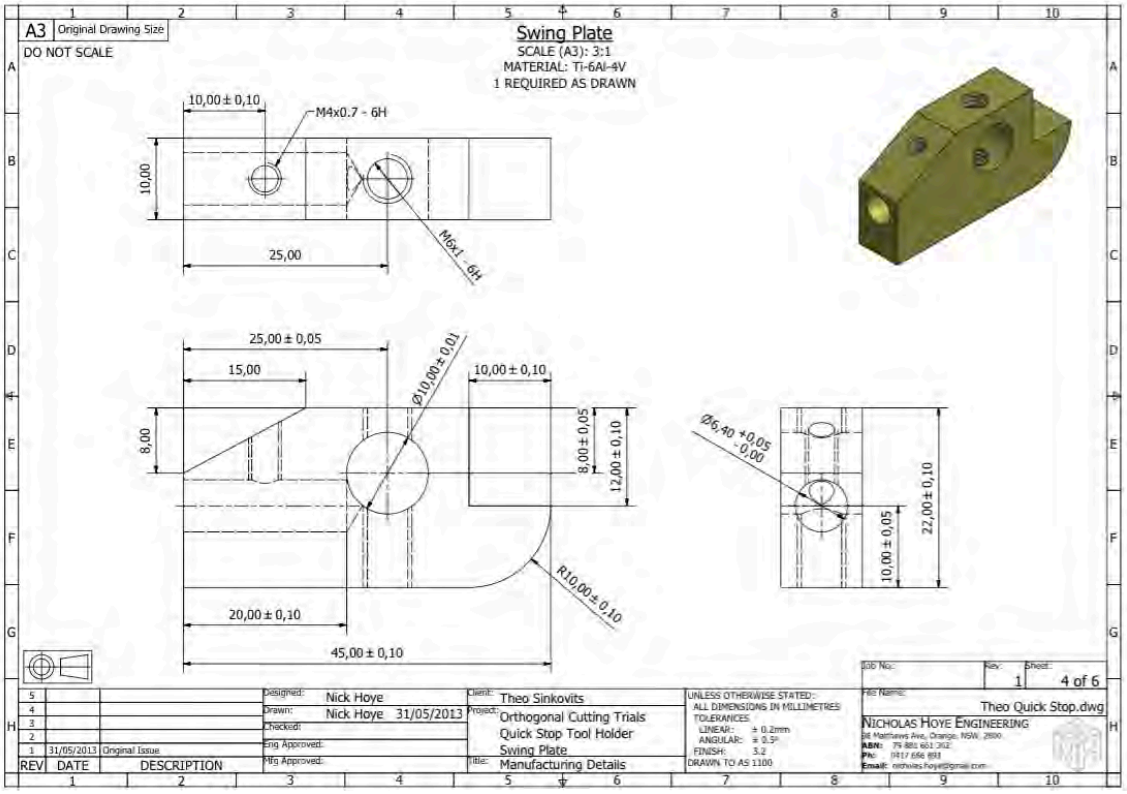
A3 Original Drawing Size
DO NOT SCALE
Swing Plate
SCALE (A3): 3:1
MATERIAL: Ti-6Al-4V
1 REQUIRED AS DRAWN
10,00 ± 0,10
M4x0.7 - 6H
10,00
25,00
M16x1 - 6H
25,00 ± 0,05
15,00
Ø10,00 +0,01 -0,00
10,00 ± 0,10
8,00
8,00 ± 0,05
12,00 ± 0,10
R10,00 ± 0,10
20,00 ± 0,10
45,00 ± 0,10
Ø6,40 +0,05 -0,00
22,00 ± 0,10
10,00 ± 0,05
Job No.: 1
Sheet: 4 of 6
File Name: Theo Quick Stop.dwg
Designed: Nick Hoye
Drawn: Nick Hoye 31/05/2013
Checked:
Eng Approved:
Mfg Approved:
Client: Theo Sinkovits
Project: Orthogonal Cutting Trials
Quick Stop Tool Holder
Swing Plate
Title: Manufacturing Details
UNLESS OTHERWISE STATED:
ALL DIMENSIONS IN MILLIMETRES
TOLERANCES:
LINEAR: ± 0.2mm
ANGULAR: ± 0.5°
FINISH: 3.2
DRAWN TO AS 1100
NICHOLAS HOYE ENGINEERING
REV DATE DESCRIPTION
1 31/05/2013 Original Issue

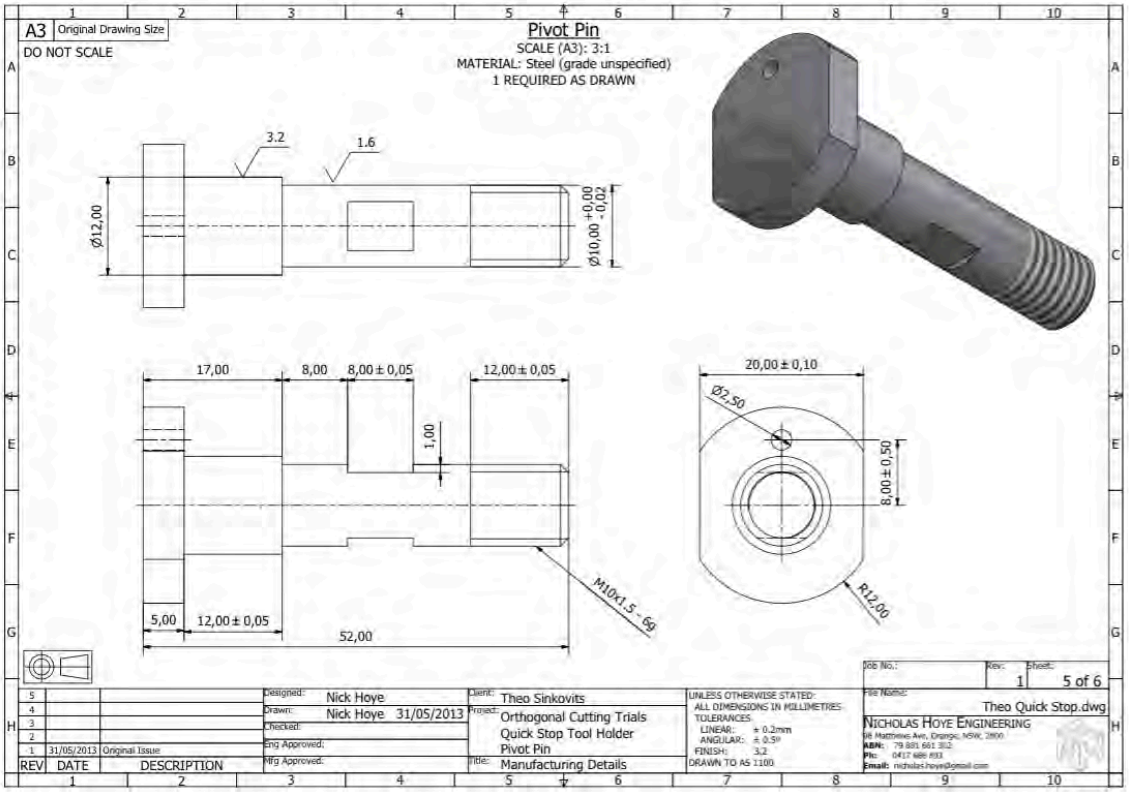
A3 Original Drawing Size
DO NOT SCALE
Pivot Pin
SCALE (A3): 3:1
MATERIAL: Steel (grade unspecified)
1 REQUIRED AS DRAWN
3.2
1.6
Ø12,00
Ø10,00 +0,00 -0,02
17,00
8,00
8,00 ± 0,05
12,00 ± 0,05
1,00
M10x1.5 - 6g
5,00
12,00 ± 0,05
52,00
20,00 ± 0,10
Ø2,50
8,00 ± 0,50
R12,00
Job No.: 1
Sheet: 5 of 6
File Name: Theo Quick Stop.dwg
Designed: Nick Hoye
Drawn: Nick Hoye 31/05/2013
Checked:
Eng Approved:
Mfg Approved:
Client: Theo Sinkovits
Project: Orthogonal Cutting Trials
Quick Stop Tool Holder
Pivot Pin
Title: Manufacturing Details
UNLESS OTHERWISE STATED:
ALL DIMENSIONS IN MILLIMETRES
TOLERANCES:
LINEAR: ± 0.2mm
ANGULAR: ± 0.5°
FINISH: 3.2
DRAWN TO AS 1100
NICHOLAS HOYE ENGINEERING
REV DATE DESCRIPTION
1 31/05/2013 Original Issue

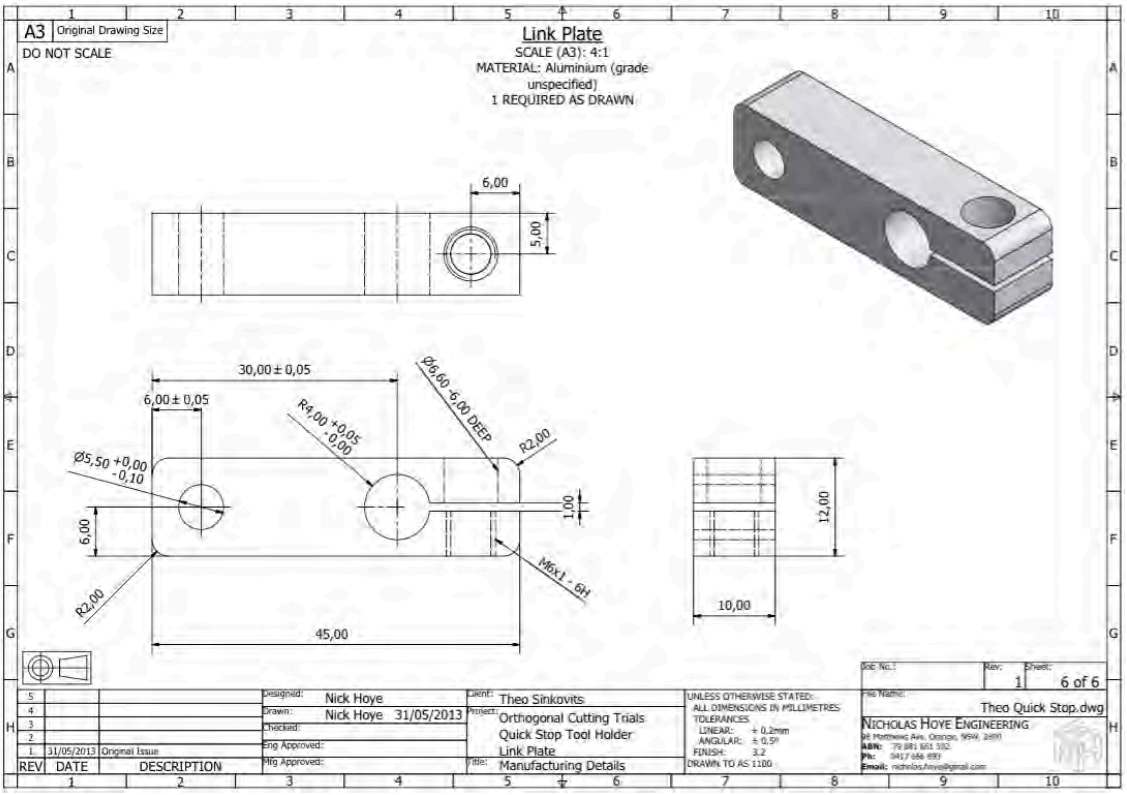
A3 Original Drawing Size
DO NOT SCALE
Link Plate
SCALE (A3): 4:1
MATERIAL: Aluminium (grade unspecified)
1 REQUIRED AS DRAWN
6,00
5,00
30,00 ± 0,05
6,00 ± 0,05
R4,00 +0,05 -0,00
Ø9,60 -5,00 DEEP
R2,00
Ø5,50 +0,00 -0,10
6,00
1,00
M6x1 - 6H
R2,00
45,00
12,00
10,00
Designed: Nick Hoye
Drawn: Nick Hoye 31/05/2013
Checked:
Eng Approved:
Mfg Approved:
Client: Theo Sinkovits
Project: Orthogonal Cutting Trials
Quick Stop Tool Holder
Link Plate
Title: Manufacturing Details
UNLESS OTHERWISE STATED:
ALL DIMENSIONS IN MILLIMETRES
TOLERANCES
LINEAR: ± 0.2mm
ANGULAR: ± 0.5°
FINISH: 3.2
DRAWN TO AS 1100
Job No.:
Rev: 1
Sheet: 6 of 6
File Name: Theo Quick Stop.dwg
NICHOLAS HOYE ENGINEERING
REV DATE DESCRIPTION
1 31/05/2013 Original Issue